

REPORT DOCUMENTATION PAGE			Form Approved OMB NO. 0704-0188	
<small>Public reporting burden for this collection of information is estimated to average 1 hour per response, including the time for reviewing instructions, searching existing data sources, gathering and maintaining the data needed, and completing and reviewing the collection of information. Send comment regarding this burden estimate or any other aspect of this collection of information, including suggestions for reducing this burden, to Washington Headquarters Services, Directorate for Information Operations and Reports, 1215 Jefferson Davis Highway, Suite 1204, Arlington, VA 22202-4302, and to the Office of Management and Budget, Paperwork Reduction Project (0704-0188), Washington, DC 20503.</small>				
1. AGENCY USE ONLY (Leave blank)	2. REPORT DATE 31 March 1997	3. REPORT TYPE AND DATES COVERED <i>Final</i>		
4. TITLE AND SUBTITLE  Augmentation of Research at the Center of Excellence in Rotorcraft Technology (CERT)		5. FUNDING NUMBERS  <i>DAH04-94-G-0072</i>		
6. AUTHOR(S): D.P. Schrage, Principal Investigator, et.al				
7. PERFORMING ORGANIZATION NAMES(S) AND ADDRESS(ES)  Georgia Institute of Technology School of Aerospace Engineering 275 Ferst Drive, NW Atlanta, GA 30332-0150		8. PERFORMING ORGANIZATION REPORT NUMBER  E16-X35		
9. SPONSORING / MONITORING AGENCY NAME(S) AND ADDRESS(ES)  U.S. Army Research Office P.O. Box 12211 Research Triangle Park, NC 27709-2211		10. SPONSORING / MONITORING AGENCY REPORT NUMBER  <i>ARO 32323.8-EG-RW</i>		
11. SUPPLEMENTARY NOTES  The views, opinions and/or findings contained in this report are those of the author(s) and should not be construed as an official Department of the Army position, policy or decision, unless so designated by other documentation.				
12a. DISTRIBUTION / AVAILABILITY STATEMENT  Approved for public release; distribution unlimited.				
13. ABSTRACT (Maximum 200 words)  Rotorcraft technology is one of the most challenging, multidisciplinary and interdisciplinary problems in engineering. For its sustained advancement requires a critical mass of researchers conducting interdisciplinary research in the four critical rotorcraft disciplines: aerodynamics, rotor dynamics & aeroelasticity, structures & materials, and flight mechanics & controls. To support and sustain this research requires a combination of analysis capabilities and experimental facilities, including the necessary research instrumentation. The Georgia Tech CERT has accumulated this critical mass of researchers and developed the necessary facilities with previous Army and Georgia Tech investments. The unique capabilities of rotorcraft (vertical flight & lifting capability, ability to operate from unprepared surfaces, low speed agility & maneuverability, etc.) make them essential weapon & support systems for the U.S. Army and other military services in the foreseeable future. Therefore, the problem studied is to sustain the advancement of rotorcraft technology by conducting leading edge research using sufficient research instrumentation for the direct benefit of future rotorcraft, as well as technology upgrades for existing rotorcraft.				
14. SUBJECT TERMS			15. NUMBER OF PAGES	
			16. PRICE CODE	
17. SECURITY CLASSIFICATION OR REPORT UNCLASSIFIED	18. SECURITY CLASSIFICATION OF THIS PAGE UNCLASSIFIED	19. SECURITY CLASSIFICATION OF ABSTRACT UNCLASSIFIED	20. LIMITATION OF ABSTRACT  UL	

19970514 065

THIS QUANTITY PREPARED 4

**AUGMENTATION OF RESEARCH AT THE  
CENTER OF EXCELLENCE IN ROTORCRAFT TECHNOLOGY  
(CERT)**

**FINAL PROGRESS REPORT**

**AUTHORS:**

Principal Investigator: Dr. Daniel P. Schrage  
Other Authors: Dr. L.N. Sankar, Dr. N. Komerath, Dr. D.A. Peters, Dr. D.H. Hodges,  
Dr. G.A. Kardomateas, Dr. E.A. Armanios, Dr. A.J. Calise, Dr. S.V. Hanagud, Dr. R.G. Loewy,  
and Dr. J.V.R. Prasad

31 March 1997

U.S. ARMY RESEARCH OFFICE  
4300 S. MIAMI BOULEVARD  
P.O. BOX 12211  
RESEARCH TRIANGLE, NC 27709-2211

**CONTRACT/GRANT NUMBER:**

DAAH04-94-G-0072  
Internal Project No.: E-16-X35

School of Aerospace Engineering  
Georgia Institute of Technology  
Atlanta, GA 30332-0150

## **FINAL REPORT**

### **AUGMENTATION OF RESEARCH AT THE GEORGIA TECH CENTER OF EXCELLENCE IN ROTORCRAFT TECHNOLOGY (CERT)**

**Contract Number DAA-H04-94-G-0072  
U.S. Army Research Office  
4300 S. Miami Blvd.  
Research Triangle Park, NC 276709**

#### **1. FORWARD:**

In response to recommendations from the U.S. Congress to provide increased funding for the U.S. Army Rotorcraft Centers of Excellence (RCOE) a proposal was submitted on 15 March 1994 and additional CERT augmentation funding was provided for funding in FY 94 and FY 95 for specific research tasks. Several no cost extensions have been provided to this grant as research requirements changed when the research, under both the existing CERT tasks and the augmented CERT tasks, were being conducted.

#### **2. BODY OF REPORT:**

Rotorcraft technology is one of the most challenging, multidisciplinary and interdisciplinary problems in engineering. For its sustained advancement requires a critical mass of researchers conducting interdisciplinary research in the four critical rotorcraft disciplines: aerodynamics, rotor dynamics & aeroelasticity, structures & materials, and flight mechanics & controls. To support and sustain this research requires a combination of analysis capabilities and experimental facilities, including the necessary research instrumentation. The Georgia Tech CERT has accumulated this critical mass of researchers and developed the necessary facilities with previous Army and Georgia Tech investments. The unique capabilities of rotorcraft (vertical flight & lifting capability, ability to operate from unprepared surfaces, low speed agility & maneuverability, etc.) make them essential weapon & support systems for the U.S. Army and other military services in the foreseeable future. Therefore, the problem studied is to sustain the advancement of rotorcraft technology by conducting leading edge research using sufficient research instrumentation for the direct benefit of future rotorcraft, as well as technology upgrades for existing rotorcraft.

#### **3. SUMMARY OF MOST IMPORTANT RESULTS:**

Seven CERT Augmentation Tasks were funded. Each of these tasks has one or two Principal Investigators (P.I.'s) who conducted and managed the tasks. Therefore, the final report documenting the most important results for each task was prepared by the P.I.'s and are attached as Appendix 1.

#### **4. LIST OF ALL PUBLICATIONS AND TECHNICAL REPORTS:**

These publications and technical reports are documented by the P.I.'s in their individual task reports in Appendix 1.

#### **5. LIST OF ALL PARTICIPATING SCIENTIFIC PERSONNEL:**

All participating scientific personnel are identified in the P.I.'s reports in Appendix 1.

## APPENDIX 1



**CERT AUGMENTATION PROJECT**  
**FINAL REPORT FOR TASK RUA-1**  
**Computational Fluid Dynamic Studies of Highly Maneuverable Rotorcraft**

Principal Investigator: L. N. Sankar  
Graduate Research Assistants: Ashok Bangalore, Justin Russell

1. Research Summary:

The main objective of this research work is to numerically investigate the aerodynamic performance characteristics of rotor blades with high lift devices such as leading edge slats. A multizone three dimensional unsteady compressible Navier-Stokes solver capable of analyzing flow over single/multi-element rotor blades undergoing arbitrary motion was developed. The rotor wake is captured from first principles without any need for external wake models. Following several two/three dimensional validation studies, the Navier-Stokes solver was applied to two rotor systems (VR7, UH-60A) with and without leading edge slats. The leading edge slat was shown to be beneficial in improving the thrust and lowering the torque at high collective pitch angles under hovering conditions. Under high speed forward flight condition, the leading edge slat eliminated the occurrence of the dynamic stall on the retreating side. This resulted in a decrease of torque and a decrease of pitching moment variation leading to lower power consumption and lesser pitch link loads.

The secondary objective of the present work is to use distributed computing strategy to compute the rotor flowfield using a network of workstations. The main advantage of using this approach is to reduce the computation time by effective utilization of high speed workstations in a network environment. In this approach, the computational domain is divided in to multiple zones or blocks and each block of flowfield is computed using one or two workstations constituting the parallel virtual machine environment. The present solver was successfully ported to a distributed computing environment. Both steady and unsteady flow applications were analyzed using the parallel strategy. Good speedup was obtained in both the cases and the throughput was comparable to supercomputer performance.

This work is believed to be the first of its kind to address the aerodynamic issues of slats on rotor blades under hover and forward flight conditions.

2. Technology Transfer: 2-D, and 3-D single- and multi-element rotor codes were developed as part of this research. These codes were transferred for in-house use to McDonnell Douglas helicopter Co. for their active flap investigations. A version of the 2-D code was made available to Chip Berezin of Sikorsky Aircraft, and was subsequently applied under a Sikorsky sponsored grant to problems of interest to Sikorsky.
3. Publications:

The following publications resulted out of this effort:

Refereed Publications:

1. Bangalore, A. and Sankar, L. N., "Numerical Analysis of Aerodynamic Performance of Rotors with Leading Edge Slats," Journal of Computational Mechanics, Vol. 17, pp. 335-342, 1996.
2. Bangalore, A., Latham, R. L. and Sankar, L. N., "Numerical Simulation of Viscous Flow over rotors using a Distributed Computing Strategy," AIAA Journal, Vol. 34, No. 10, October 1996, pp. 2189-2190.
3. Bangalore, A. and Sankar, L. N., "Forward Flight Analysis of Slatted Rotors using Navier-Stokes methods," accepted for publication in the AIAA Journal, 1997.

Conference Proceedings and Publications:

1. Bangalore, A. and Sankar, L. N., "Numerical Analysis of Aerodynamic Performance of Rotors with leading Edge Slats," AIAA paper 95-1888, Proceedings of the AIAA 13th Applied Aerodynamics Conference, June 19-22, 1995
2. Srinivasan, G. R. and Sankar, L. N., "Status of Euler and Navier-Stokes CFD Methods for Helicopter Applications," Proceedings of the 2nd International Aeromechanics Specialists Conference, Birdeport, CT, October 11-13, 1995.
3. Bangalore, A., Latham, R.L. and Sankar, L.N. "Numerical simulation of viscous flow over rotors using a distributed computing strategy", AIAA Paper 95-0575, 33rd AIAA aerospace sciences meeting, Reno, NV, January 1995.
4. Bangalore, A. and Sankar, L. N., "Forward Flight Analysis of Slatted Rotors using Navier-Stokes methods," AIAA Paper 96-0675.

Ph. D. Dissertation:

Bangalore, A., "Computational Fluid Dynamics Studies of High Lift Rotor Systems using Distributed Computing," Georgia tech, May 1995.

**INTRODUCTION TO THE RESEARCH TOPIC**

Next generation combat helicopters are expected to have high maneuverability, agility and good handling qualities. Highly maneuverable rotorcraft are particularly desirable in deep penetration operations, air to air combat situations and nap of the earth operations. The maneuverability and agility of the rotorcraft gets limited due to the retreating blade stall under high speed forward flight situation. The first step for achieving higher maneuverability is to improve the aerodynamic performance of the

main rotor, in particular, to increase the maximum thrust generated by the rotor and reduce or eliminate the retreating blade stall under maneuvering conditions.

Development of advanced rotorcraft airfoils has been an active topic of research for the past two decades. During late 1970's, Dadone<sup>1</sup>, Noonan<sup>2-3</sup>, McVeigh<sup>4</sup> and others designed rotorcraft airfoil sections to achieve high maximum lift coefficients ( $C_{lmax}$ ) and low zero lift drag coefficients ( $C_{do}$ ). The airfoils used in rotorcraft such as Hughes HH-02, Vertol VR-7, VR-12 and Sikorsky SC-1095 have shown significantly higher  $C_{lmax}$  and lower  $C_{do}$ <sup>5</sup> and good high speed characteristics. Helicopters such as the Boeing Chinook, Sikorsky Blackhawk (UH-60A) and the Apache use these airfoil sections on their rotors. However, the army's future needs require significant improvement in lift above the level of the current airfoils. Further dramatic improvement in airfoil lift capability without considerable compromises in pitching moment or drag divergence characteristics may be unrealistic for conventional airfoils<sup>6</sup>. In order to meet the enhanced thrust requirements, the rotor is expected to generate higher thrust levels without any major increase in blade weight. An increase in the blade area of the present day single element rotors causes an increase in the blade weight and decreases the useful payload. An increase in the camber of the airfoils results in undesirable drag divergence characteristics and higher pitching moment levels leading to higher control loads. Highly cambered single element airfoils also have poor dynamic stall characteristics which lead to structural vibration problems. The rotor blade with a leading edge slat is expected to achieve higher thrust levels compared to a single element airfoil without much increase in blade weight<sup>7</sup>.

Realizing the limitations of single element airfoils, researchers at the Aeroflightdynamics Directorate and Aerostructures Directorate began work on multi-element airfoils. Several two-dimensional studies done on rotorcraft airfoil sections with leading edge slats have been reported in the open literature. Carr and McAlister<sup>5</sup> have experimentally studied the dynamic stall characteristics of a Boeing vertol airfoil with and without slat, and demonstrated that the deployment of the slat shrinks the hysteresis loop and increases the average lift levels during the oscillation cycle. Noonan et al<sup>6</sup> have experimentally studied the aerodynamic performance characteristics of a slotted rotorcraft airfoil at different Mach numbers ranging from 0.2 to 0.8. Their studies indicate that the use of a slotted airfoil leads to significant improvements in  $C_{lmax}$  with minimum adverse impact on drag and pitching moment characteristics. Yung Yu et al.<sup>7</sup> have presented the potential of improving the lift, drag and moment characteristics of airfoil sections on rotor blades with high lift devices such as slats, deformable leading edges and upper surface blowing. They showed that airfoil-slat configurations have better lift and drag characteristics both in steady and unsteady flight than single element airfoils.

Wang and Wu<sup>8</sup> investigated the aerodynamic characteristics of airfoil-slat combinations using an incompressible flow solver. Tuncer and Sankar<sup>9</sup> have studied the dynamic stall characteristics of a VR-7 slat/airfoil configuration using a multi-zone Navier-Stokes solver. In the case of a single airfoil, the vortex induced suction and vortex shedding is responsible for high fluctuating aerodynamic loads and subsequent stall of the airfoil. In the case of slatted VR-7 airfoil, the suction peak at the leading edge of the main airfoil is significantly reduced and the formation of a strong vortex is not observed. The slatted airfoil did not experience a massive flow separation and also a shrinkage of the dynamic stall hysteresis loop was confirmed.

Recently, the present authors<sup>10</sup> studied two rotor configurations (VR7, UH-60A) with leading edge slats under hover using three-dimensional unsteady compressible Navier-Stokes methods. In the case of a VR7 rotor blade, a full span leading edge slat was employed and was shown that at high collective pitch settings the blade stall angle was increased leading to higher thrust and reduced torque. A partial span slat was used in the case of UH-60A rotor blade and at moderate collective pitch angles the slat was seen to improve the hover performance of the baseline rotor.

### **BENEFITS OF SLATTED ROTORS**

The primary benefit of a leading edge slat on a rotor blade is to improve the aerodynamic performance of the rotor under hover and forward flight conditions. The maximum thrust generated by the rotor under hover is limited by the blade stall. High lift devices such as leading edge slats delay the blade stall and increase the maximum thrust generated by the rotor. Thus an increase in useful payload in hover and climb can be realized. The leading edge slat does not add a significant amount of blade weight, particularly if the slats are deployed permanently to reduce the complexity of the actuators and active control devices.

In high speed forward flight situations, the maximum thrust on the retreating blade falls because of the decrease in dynamic pressure and also the occurrence of dynamic stall due to the changes in blade pitch. The thrust achievable is thus limited throughout the forward speed range. Maximum thrust possible on the advancing side increases but is unrealizable because of the retreating blade restriction. As the advancing blade tip Mach number approaches unity, the lift generated is restricted by shock-induced flow separation. Drag divergence and pitching moment divergence also limit the maximum speed achievable. Thus the envelope is bounded by a limit on thrust from retreating blade stall and a limit on forward speed from advancing blade Mach effects<sup>11</sup>. Figure 1 illustrates a typical rotor thrust limit envelope.

In addition to the above effects, the retreating blade stall leads to large, highly unsteady pitching moments. These pitching moment variations lead to high control loads and vibration levels. The blade torsional moments may also increase and in some cases lead to stall flutter.

Based on the two dimensional studies<sup>5-9</sup> and also the three dimensional hover calculations<sup>10</sup>, it may be expected that a leading edge slat will reduce or eliminate the dynamic stall on the retreating side. Thus, the thrust limit imposed by the blade stall could be increased by using a slat. The sectional drag levels may also be reduced on the retreating side lowering the torque. The slat also reduces the pitching moment oscillations due to the dynamic stall and reduces the pitch link loads and vibration levels. These beneficial effects of a slat must, of course, be weighted against any adverse effects on the advancing side. To date, such a comprehensive study has not been done.

With these considerations, the present study is aimed at numerically evaluating the aerodynamic performance of rotor blades with partial span leading edge slats under forward flight conditions. A numerical methodology is developed in the present work to analyze multi-element rotor blades because of the unavailability of flow solvers capable of analyzing rotor-slat configurations. The details of the present numerical method and the results obtained to date are discussed in the later sections.

### **NUMERICAL FORMULATION**

The 3-D unsteady compressible Reynolds averaged Navier-Stokes equations are solved numerically by using a time marching scheme. This involves solving the governing equations at each time step by marching in time from an initial flow condition with appropriate boundary conditions. A hybrid Alternating Direction Implicit (ADI) scheme<sup>12</sup> is used in the present work and is described in this section. The hybrid implicit scheme has been validated for a number of fixed wing and rotary wing configurations both in steady and unsteady flight conditions<sup>13-16</sup>.

The partial derivatives of the flux terms in the governing equations are calculated using finite difference approximations. The inviscid flux terms are calculated using a third order upwind scheme and the viscous stress terms are calculated using standard central difference representations. The time derivative is approximated using a two point first order backward difference.

The finite difference representation of the governing Navier-Stokes equations at time level 'n' is

$$\Delta q^{n+1} / \Delta \tau + \delta_{\xi} F^{n+1} + \delta_{\eta} G^n + \delta_{\zeta} H^{n+1} = (\delta_{\xi} R + \delta_{\eta} S + \delta_{\zeta} T)^n$$

where  $\Delta q^{n+1}$  is the change in  $q$  during adjacent time levels and  $\Delta t$  is the time step. The operators  $\delta_{\xi}$ ,  $\delta_{\eta}$  and  $\delta_{\zeta}$  are the standard central difference operators. The viscous terms are evaluated explicitly and the inviscid flux vectors  $F$  and  $H$  are calculated

implicitly at time level  $n+1$ . The spanwise derivative  $\delta_\eta G^n$  is evaluated explicitly. The inviscid flux terms are calculated using a finite-volume based third order upwind scheme. The details of the upwind formulation is given by Roe<sup>17</sup>. A two factor approximate factorization is used to factorize the implicit coefficient matrix operator into two operators which results in block tri-diagonal matrices. The factorized system of equations are solved using the Thomas algorithm.

### **BOUNDARY CONDITIONS**

The boundary conditions for a two or four bladed rotor in forward flight is different from the hover boundary conditions. In hover, the rotor wake remains close to the rotor and is convected only in the downward direction. In the forward flight condition, the rotor wake is convected aft due to the forward speed and also down due to the induced velocity. The flowfield is no longer symmetric in the case of forward flight as each blade encounters a varying freestream with the azimuth and the effective pitch of each blade changes with the azimuth depending on the flight condition. Hence, all the blades should be solved at each time step with appropriate boundary conditions. The blade grids of adjacent blades are patched and the flow data is transferred between the blade grids at each time step.

Figure 2 shows a top view of the four bladed rotor under forward flight and the different kinds of computational boundaries. The farfield boundaries are located at about one rotor radius from the blade surface. The one-dimensional approximate Riemann boundary conditions are applied at the far-field boundaries. The flow velocity is checked to determine whether it is an inflow or an outflow boundary. Depending on the type of the boundary the flow quantities are either prescribed or extrapolated from interior.

For viscous flows, the no-slip boundary condition is applied at the body surface on all the blades. The pressure on the surface is obtained by solving the normal momentum equation and the density is extrapolated from the interior grid point in the normal direction. The velocities of the grid points are due to the blade motion, the forward flight velocity and the cyclic pitching rate. The flap and lead-lag motions are not included in the present calculations. However, similar terms could be added in the three coordinate directions to represent the flap and lead-lag motions.

### **MULTI-ZONE METHODOLOGY**

Multiple grid blocks are used to construct simple structured grids around complex configurations such as multi-element airfoils/rotor blades. It becomes virtually impossible to generate single block smooth structured grid around multi-element configurations such as a partial span slatted rotor blade. By making use of multiple grid blocks, it is easier to construct the zonal grids around each component of the airfoil/rotor. In the case of a multi-bladed, multi-element rotor multiple grid blocks are used both in

the radial direction as well as in the azimuthal direction. Each blade grid consists of multiple zones in the radial direction depending on the number of airfoil elements. For example, three zones are used for a two element airfoil and in general 'n+1' zones are used for a 'n' component airfoil. The adjacent grid blocks are patched in the sense that there is a one to one correspondence between the grid points of adjacent blocks without any stagger. However, this multi-zone interpolation technique can also be used for staggered grid blocks.

Several multi-block strategies are reported in the literature. An overset grid methodology (CHIMERA) was developed by Steger et al<sup>18</sup>, and has been used in many fixed wing and helicopter aerodynamic applications. This method consists of simple structured grids overlapping in an arbitrary manner. The transfer of flow data between adjacent grid blocks requires complex data structures and grid connectivity techniques and may become computationally very expensive.

In the present study, highly unsteady flow occurring over a four-bladed rotor under high speed forward flight condition is solved using this multi-zone methodology. The zonal interface boundaries are updated at each time step explicitly and if the boundary conditions are not handled properly, there may be false reflections from the interface contaminating the temporal behavior. In the past this methodology was validated for an unsteady flow over a fighter wing<sup>14</sup> with experimental data and the temporal behavior of the flow was captured well. Figure 3 shows a zonal interface in the azimuthal direction between two adjacent blade grids in forward flight situation.

The zonal interface is shown by the surface ABCD. Consider any grid point 'i' on the zonal interface ABCD. The corresponding grid points in the interior of the blocks 1 and 2 are 'i+1' and 'i-1' respectively. The unknown flow vector 'q' at the grid point 'i' is evaluated by using the following interpolation

$$q_i = \frac{\Delta s_1 q_{i+1} + \Delta s_2 q_{i-1}}{\Delta s_1 + \Delta s_2}$$

where x,y and z are the Cartesian co-ordinates of the grid points and  $\Delta s_1$  and  $\Delta s_2$  are the distances between 'i+1'; 'i' and 'i-1'; 'i', respectively.

## **RESULTS AND DISCUSSION**

In this section, all the flow solutions obtained to date using the multi-zone three-dimensional unsteady Navier-Stokes solver are presented. The details of the computational grids used in the multi-element rotor airfoil/blade calculations with illustrations are first described. Some two dimensional case studies are next presented and compared with experimental data. Next, high speed forward flight solutions are presented for a four-bladed UH-60A rotor and compared with experiments. Then, some

results are presented for a UH-60A rotor with partial span slat and compared with the baseline rotor results.

### **Computational Grid**

Figure 4 shows a typical three zone H-grid around a slatted airfoil. This grid is generated using a Thomson-Thames-Mastin<sup>19</sup> technique. The grid is dense near the body surface and also in the front and aft wakes. The number of zones in the normal direction is 'n+1' where 'n' is the number of airfoil components. As shown in Figure 4, there are three zones in the normal direction for a two component airfoil. The farfield boundaries are at distance of six chord lengths from the body surface. A typical two component airfoil grid consists of 120 points in the streamwise direction, 40 points in the normal direction in the top and bottom zones and 30 points in the middle zone. This type of multizone H-grid was successfully used in computing flow over a five component Boeing 737 airfoil<sup>20</sup> in a previous study.

The forward flight calculations for a four bladed single/multi-element rotor are done using H-O type grids around each rotor blade. In the forward flight situation, each blade undergoes a different pitching motion and experiences different flow conditions. The computational grid has to include all the blades and the flow data has to be transferred between each blade at each time step of the solution process. A H-O type grid is generated around each blade and connected at the zonal interfaces. The top view of all the blade grids at a particular azimuth location is shown in Figure 5. At each time step, each blade grid is rotated in pitch within the flow solver and also in the azimuthal direction. The flow solver ensures that the zonal interfaces connecting any two adjacent blade grids are patched or aligned at each time step for efficient transfer of flow data.

### **SC1095 Slat Studies**

The objective of the present work is to evaluate the use of a high lift device such as a leading edge slat for a highly twisted realistic rotor (UH-60A) blade. The design of a slat section for the existing SC1095 airfoil for a range of Mach numbers and Reynolds numbers involves an elaborate analysis of the high lift airfoil with different slat shapes and orientations. A detailed three-dimensional optimization study is desirable but is not feasible due to enormous amount of computer resources required. As a first step, SC1095+slat configuration was analyzed in two dimensional mode with a fixed slat shape at two different slat orientations and at low subsonic Mach numbers.

In the present study, a partial span leading edge slat is proposed in the inboard portion of the UH-60A rotor blade as an attempt to delay the retreating side blade stall in high speed forward flight condition. Locally, low subsonic flow and high angle of attack flow is usually experienced at the inboard portions of the blade. A slat in these regions is expected to be effective in reducing the separation and improving the flow quality.

The airfoil profile of the slat is identical to the shape of the main airfoil, with a reduced chord and thickness distribution. The chord length of the slat is 10% of that of



the main airfoil. As shown in Figure 6,  $X_s$  is the distance of the quarter chord point of the slat from the leading edge of the main airfoil normalized with respect to the main chord.  $Z_s$  is the vertical shift in the quarter chord point of the slat from the leading edge point of the main airfoil and  $\delta_s$  is the angle of rotation of the slat pivoted at the quarter chord point and is measured in anticlockwise direction.

The slatted SC1095 airfoil is analyzed using the multizone Navier-Stokes solver at two subsonic Mach numbers of 0.2 and 0.38 at a Reynolds number of 2.2 Million. The sectional lift and drag coefficients are computed for a range of angles of attack and are compared with the load values of the SC1095 baseline computations. Figure 7 shows the sectional lift and drag coefficients of baseline and slatted sections of SC1095 airfoil plotted against angle of attack for a Mach number of 0.2. Two slat angles  $\delta_s$  ( $25^\circ$ ,  $34^\circ$ ) as defined in Figure 6 are selected for comparison purposes. In both the cases the parameters  $X_s$  and  $Z_s$  are 0.06c and 0.008c respectively.

Figures 7 and 8 show that at both the slat orientations the stall angle is increased. There is an increase in the lift values and a decrease in the drag coefficients at higher angles of attack when compared to the baseline values. At lower angles of attack below 8 degrees, the lift values of the slatted and baseline airfoils are practically the same, however the drag coefficients of the slatted airfoils are higher than the baseline values. This is because there is a mild separation on the lower surface of the slat at lower angles of attack. As the angle of attack is increased, the presence of the slat energizes the flow on the upper surface of the main airfoil thus delaying the stall. Also, it is seen that as the slat angle is increased from 25 degrees to 34 degrees in the anticlockwise direction, the percentage of lift increase with respect to the baseline airfoil increases and a higher percentage of reduction in drag coefficients is observed at higher angles of attack. Conversely, at lower angles, an increase in slat angle results in a decrease in lift and an increase in drag compared to the baseline data. To obtain a true optimum slat geometry for a desired range of Mach numbers and angles of attack, a parametric study needs to be done by varying the slat shape, horizontal and vertical distances ( $X_s$ ,  $Z_s$ ) and the slat angles.

Figure 9 shows a typical streamline pattern observed in the simulations for the baseline and slatted airfoils at 12.5 degrees of angle of attack and a freestream Mach number of 0.2. As expected, there is massive separation on the upper surface of the baseline airfoil while there is no separation in the case of slatted airfoil. The Baldwin-Lomax turbulence model<sup>21</sup> was used in all the calculations.

From the above two dimensional analysis, the benefits of the proposed slat for the SC1095 airfoil was confirmed. This slat section with a  $\delta_s = 34^\circ$  orientation was then incorporated in to the three-dimensional UH-60A rotor blade.

#### **UH-60A baseline rotor**

The aerodynamic environment of UH-60A rotor in high speed forward flight is significantly complicated compared to the hover case<sup>10</sup>. Some prominent flow features include the dynamic stall on the retreating blade, transonic flow on the advancing blade with shock formation and shock/boundary layer interaction, highly unsteady trailing wake system, tip vortices with varying strengths intersecting the blades to name a few. The present three dimensional unsteady Navier-Stokes solver has the capability to analyze all of the above physical flow phenomena, and in particular, capture the rotor wake from first principles.

The schematic of the model UH-60A rotor blade geometry is shown in Figure 10. The flow condition simulated in this calculation is high speed forward flight with an advance ratio ( $\mu$ ) of 0.3 and a tip Mach number of 0.628. The model rotor was trimmed to zero first harmonic flapping in the experiments<sup>22</sup>. Figure 11 shows the geometric pitch time history. This pitch distribution is taken out of Lorber's<sup>22</sup> data. This pitch distribution includes the built-in structural twist distribution, cyclic and collective pitch and torsional deflections around the azimuth. The collective pitch is 8.8 degrees. This pitch data is converted in to a table of sectional angle of attack (minus the inflow) values at all the azimuthal and spanwise locations. At each time step of the solution process, different spanwise sections of the rotor blade is rotated in pitch according to the tabular data.

The computational grid used in this calculation consists of four H-O blade grids. Each block spans a quarter of the azimuth (i.e. 90 degrees) and the adjacent blocks are patched at the zonal interfaces. Each blade grid consists of 90 points in the azimuthal direction, 43 points in the spanwise direction and 80 points in the normal direction. The total number of grid points (including all four blades) is 1,238,400 points. At each time step, the blade grids rotate in the azimuthal direction and also rotate in pitch according to the pitch distribution (Figure 11). The rotation of each blade grid in pitch is done in such a way that no shearing of the zonal interfaces is allowed. In other words, the zonal interfaces remain aligned at each time step even though the interior of the grid rotates with different pitch amplitudes. The time step ( $\Delta t$ ) taken in the present calculation is 0.01 which corresponds to an azimuth of 0.023 degrees for the chosen tip Mach number.

The forward flight simulation generates a huge amount of flow information. Only a representative sample of surface pressures and sectional loads are presented here. Figure 12 shows the surface pressures plotted in the first quadrant ( $\psi = 0$  to 90 degrees) at 77.5%R and 94.5%R radial locations. The pressure values are nondimensionalized with respect to the local dynamic pressure. The computed pressures match fairly well with the experimental data except that the suction peak is overpredicted.

Figures 13 show the surface pressures in the second quadrant ( $\psi = 90$  to 180 degrees). The tip region experiences negative loads in the second quadrant between  $\psi = 100 - 170$  degrees. At  $\psi = 100$  degrees a shock is formed on the lower surface near the tip region as a result of the negative pitch distribution (Figure 13b). The computed

pressures match well in the regions where the flow is smooth with no discontinuities but match poorly in the shock regions. This may be due to inadequate number of grid points in the boundary layer and also the present algebraic turbulence model may affect the shock location and movement.

The retreating side surface pressures at 40% radial location and  $\psi = 190, 220, 270$  and  $320$  degrees are shown in Figures 14. The leading edge peak is largely underpredicted in all the retreating side azimuthal locations. This may be due to inadequate grid points in the leading edge region. Even though the coefficient of pressure is vastly different between the computation and experiment the actual pressure difference may be less because the local dynamic pressure at 40% location on the retreating side is very low. The dynamic stall effect is seen in the upper surface pressures between  $\psi = 220$  and  $300$  degrees. The bumps in the surface pressures on the upper surface indicate the vortices and was also observed in the pressure contours at these azimuthal locations. The lower surface pressure indicates smooth attached flow in these azimuths ( $220 - 300$  degrees) as the blade is constantly increasing in pitch.

The prediction of the three dimensional dynamic stall vortex formation and movement is believed to be a very challenging task using the present day Navier-Stokes solvers. The present calculation does not adequately quantify the dynamic stall effects. This may be due to the coarseness of the grid and the algebraic turbulence model. It is hoped that with refined grid and better turbulence models (like  $k-\epsilon$ ) this phenomena could be analyzed more quantitatively. It is to be noted that the computed pressures are the unsteady values obtained at that particular instant of time whereas the experimental values are time averaged over several rotor revolutions.

The computed surface pressures are integrated along the radius to obtain the sectional force coefficients all along the azimuth. Figure 15 shows the normal force coefficient time history at 67.5%, 77.5%, 87% and 92% radial locations respectively. The experimental data is taken out of Lorber's data<sup>22</sup>. The force coefficients closely follow the pitch distribution (Figure 11) along the azimuth. The inboard load predictions are underpredicted between  $\psi = 200$  to  $260$  degrees. The normal force coefficients in the outboard regions compare better with the experimental values. The computed loads are plotted after each blade has travelled one full revolution. The experimental values are time averaged over several rotor revolutions. The flow in the inboard regions of the blade take longer time to develop fully in the computations. That is, each blade should experience the same flow environment at any particular azimuthal location. This is because the convection velocity is less in the inboard regions when compared to the tip region. In a time marching scheme, using a constant time step, for one rotor revolution of computation, the number of chords travelled by the tip region is more when compared to the inboard region. The force coefficients are normalized with respect to the local dynamic pressure which includes the forward flight velocity.

The 'dip' in the force coefficient around an azimuth of 260 degrees is believed to be due to the shedding of the dynamic stall vortex. In the tip region, beyond  $r/R = 0.87$ , the dynamic stall effect is not seen in the load plots. The plots show that the computed values are lower than the experimental predictions in the second quarter. The negative and positive load regions around the azimuth are predicted well in the computations. An observation of the vertical velocity contours showed that the tip vortices from the blades dissipated due to the grid coarseness and numerical dissipation. However, the convection of the tip vortices under the influence of the forward velocity was visible and the potential locations for the blade vortex interactions could be approximately identified.

The present simulation is believed to be the first in its kind to simulate a four blade rotor in forward flight condition without any external wake inputs. This computational tool is very useful in analyzing the retreating blade stall phenomena and the advancing side transonic effects. At present the computational grid is too coarse to quantify any blade vortex interaction effects.

### **UH-60A Slatted rotor**

The schematic of the UH-60A rotor blade with a partial span leading edge slat is shown in Figure 10. The main objective of the slat in the forward flight situation is to reduce or eliminate the dynamic stall phenomena occurring on the retreating blade. The slat spans upto 60% radius from the root of the blade. The location of the slat was chosen such that the slatted portion of the blade experienced high angle of attack subsonic flow. However, the analysis could be performed with the slat in any portion of the blade span using the present solver. The slat was not included near the tip region as it was not known a priori the transonic effects of the slat on the rotor performance. As explained earlier, detailed two dimensional load studies were done on the slatted section under subsonic flow conditions to determine the "optimum" slat orientation with respect to the main airfoil.

The four bladed H-O grid is used in the computation as shown in Figure 5. This grid may not be the most efficient grid in capturing the rotor wake in a forward flight situation because the grid is dense only near the tip region and is coarse away from the tip region. In a forward flight situation, unlike the hover case, the rotor wake is convected aft of the rotor blade. With the present form of the grid, the tip vortices move away from the dense portions of the grid. A drawback of using the structured grids, as in the present case, is that it is very hard, if not impossible to adapt the grid locally. Unstructured grids may be very useful in these situations where the grid adaption near the vortex regions becomes very easy. Such an unstructured grid approach is being pursued by Strawn<sup>23</sup>.

Figures 17 show the surface pressures on the retreating side of the azimuth at  $\psi = 190, 230, 260$  and  $290$  degrees for the slatted rotor blade. Figure 16 shows the corresponding retreating blade surface pressures at 55% radial location for the baseline rotor. These azimuthal and radial locations are chosen to show that there is a reduction of

dynamic stall due to the slat on the retreating side. At  $\psi = 190$  degrees, both the baseline and the slatted rotors (Figures 16-17) show smooth flow with no separation at the 55% radial location. For the baseline case, we start to observe the bumps on the upper surface pressure distribution, indicative of the dynamic stall vortex, at  $\psi = 230$  degrees. The corresponding pressure plot at  $\psi = 230$  degrees for the slatted rotor shows no bumps in the pressure distribution and indicates that there is no separation. This fact was confirmed by observing the pressure contours for both the cases. Figure 16 shows the pressure distribution for the baseline rotor at  $\psi = 260$  degrees with large undulations on the upper surface pressure indicative of large separation regions. The slat is shown to reduce this separation, resulting in a smooth pressure distribution. By the time the blade reaches  $\psi = 290$  degrees, the flow recovers from the stall and seems to be well behaved at this particular radial location.

The surface pressures are integrated along the radius of the blade to obtain the sectional force coefficients (normalized with respect to the local dynamic pressure) and are plotted along the azimuth at 36%, 43%, 55% and 87% radial locations as shown in Figure 18. The slatted rotor load values are plotted with the baseline values for comparison purposes. In the inboard regions ( $r/R = 0.36, 0.43$  and  $0.55$ ) the baseline  $C_n$  values show a sharp decrease indicative of the dynamic stall vortex shedding. This phenomena was also seen in the sectional pressure distributions as explained in the previous paragraph. The pitch distribution (Figure 11) shows a constant increase in pitch upto an azimuth of 300 degrees in the inboard portion of the blade whereas the corresponding  $C_n$  plots show a sharp dip around  $\psi = 260$  degrees. This 'dip' in the force coefficient is not seen in the outboard regions near the blade tip (Figure 18). The force coefficient in the slatted rotor case shows a smaller dip in the inboard regions near  $\psi = 260$  degrees. The slope of decrease of the normal force coefficient is more gradual than that of the baseline case. This decrease in  $C_n$  in the case of the slatted rotor around  $\psi = 260$  degrees is believed to be due to the change in local dynamic pressure in that azimuthal region and not due to the shedding of the dynamic stall vortex. This observation is based on the fact that no apparent separation was observed on the upper surface of the slatted blade on the retreating side of azimuth.

An increase in  $C_n$  is observed in the slatted portions of the blade ( $r/R < 60\%$  radius) at an azimuth of 300 degrees where the blade pitch reaches a maximum value (Figure 18). In the tip region of the blade where there is no slat, the force coefficients of the slatted and the baseline rotors are almost identical in their behavior along the azimuth. Another feature observed is that the slatted force coefficient in the second quadrant ( $\psi = 90 - 180$  degrees) is lower than the corresponding baseline values at some radial locations ( $r/R = 0.43, 0.55$ ). This is due to the fact that the pitch distribution assumes a minimum in the second quadrant and the slat may be causing an additional download on the rotor blade. These force coefficients are plotted after the rotor blade has rotated one full revolution. In the present study due to the enormous amount of computer time involved in the computation, the solution process was stopped after one revolution. It should be noted that the pitch distribution is obtained from the trim condition of the

baseline rotor. The trim condition obviously changes for the slatted rotor and should be calculated in an iterative process in future studies.

Figure 19 shows the variation of sectional drag coefficients of the baseline and slatted UH-60A rotors with the azimuth at different radial sections. These coefficients are normalized with respect to the local dynamic pressure which is a function of the local radius, angular rotation and the azimuth. At almost all the radial stations (43%, 55%, 67% and 87%) shown in Figure 18 the drag coefficients in the baseline and slatted rotor cases are almost identical on the advancing side (up to  $\psi = 180$  degrees).

There are significant differences between the baseline and the slatted rotor cases on the retreating side. In the inboard regions ( $r/R < 67\%$ ), the drag values are higher in the case of the baseline rotor between  $\psi = 180$  degrees and  $\psi = 260$  degrees. In particular, a sharp dip is observed near  $\psi = 250$  degrees. This phenomena was also observed in the sectional normal force coefficients. This is due to the movement and shedding of the dynamic stall vortex. This sharp dip in the drag at  $\psi = 250$  degrees is not observed in the slatted rotor case and the drag values are lower compared to the baseline case. However, the drag values in the fourth quadrant ( $\psi = 270 - 360$  degrees) show that the slatted rotor causes a higher drag in the inboard regions than the baseline rotor. This additional drag is a lift dependent drag due to the slat as is seen in the sectional force coefficient plots (Figure 18). As was explained earlier, the partial span slat on the UH-60A rotor blade extends upto 60% radius. Even in the outboard regions of the blade (beyond 60% radius), where there is no slat the drag values of the slatted rotor is less than the baseline rotor. This may be due to the centrifugal pumping effect of the inboard slat.

The sectional moment coefficient at different radial sections for the baseline and the slatted rotor cases are plotted in Figure 19. These coefficients were calculated by numerical integration of the surface pressures. Since the surface pressures were stored only at selected azimuth locations, the sectional moment coefficients are shown only at those locations. The moment coefficients between the slatted and the baseline rotors are significantly different on the retreating side. The movement of the dynamic stall vortex in the baseline rotor case causes rapid changes in the pitching moment and is observed in the Figure 20. In the slatted rotor case, there is no formation of the dynamic stall vortex and the corresponding pitching moment variation is not seen. In the outboard regions, the dynamic stall is not observed due to the negative twist of the blade. The reduction of the pitching moment variation due to the slat is very beneficial in reducing the pitch link loads and the structural vibration levels.

### **CONCLUDING REMARKS**

The present Navier-Stokes methodology is believed to be the first in its kind to be capable of analyzing unsteady three dimensional viscous compressible flows over complex geometries which include rotor+slat/flap configurations undergoing arbitrary

unsteady motion. The solver is capable of capturing rotor wakes from first principles without relying on external wake models. This wake capturing capability is very useful in the analysis of rotor blades with complex shapes (e.g., slatted UH-60A rotor) where there is no wake experimental data available a priori.

The forward flight analysis of the four bladed UH-60A rotor with and without slat has been successfully performed using the present method. The rotor wake was captured well. Pressure and load comparisons with experiments were done for the baseline UH-60A rotor. The leading edge slat eliminated the retreating blade dynamic stall. The unsteady variations of the sectional loads and the pitching moments of the baseline rotor on the retreating side was not observed in the case of the slatted rotor. The slat appears to be very beneficial in the reduction of blade vibration levels and pitch link loads. In this particular forward flight condition, the adverse effects on the advancing side due to the slat were not significant.

### REFERENCES

1. Dadone, L., " Helicopter Design DATCOM, Vol I - Airfoils, " NASA CR - 153247, 1976.
2. Noonan, K. W. and Bingham, B. J., "Aerodynamic Characteristics of Three Helicopter Rotor Airfoil Sections from Model Scale to Full Scale at Mach Numbers from 0.35 to 0.9, " NASA Technical Paper 1701, AVRADCOM TR-80-B-5, 1980.
3. Noonan, K. W. and Bingham, B. J., " Two dimensional Aerodynamic Characteristics of Several Rotorcraft Airfoils at Mach Numbers from 0.35 to 0.9, " NASA TM-X-73990, 1977.
4. McVeigh, M. A. and McHugh, F. J., " Recent Advances in Rotor Technology at Boeing Vertol , " Presented at the 38th Annual American Helicopter Society Forum, May 1982.
5. McAlister, K.W., Pucci, S.L., McCroskey, W.J. and Carr, L.W., "An Experimental study of Dynamic Stall on Advanced Airfoil Sections, Volume 2: Pressure and Force Data, " NASA TM 84245, September 1982.
6. Noonan, K. W, Allison, D.O and Stanaway, S., "Investigation of Slotted Rotorcraft Airfoil at Mach Numbers Ranging from 0.2 to 0.88 at Full Scale Reynolds Numbers, " presented at the AHS Aeromechanics Specialists Conference, San Francisco, CA, January 1994.
7. Yu, Y., Lee, S., McAlister, K.W. and Tung, C., "High Lift Concepts for Rotorcraft Applications, " presented at the 49th American Helicopter Society Annual Forum, St.Louis, MO, May 1993.

8. Wang, C.M., Wu, J. C. and Tung, C., "A Numerical Study of General Viscous Flow Around Multi-element Airfoils, " AIAA Paper 90-0572.
9. Tuncer I. and Sankar, L.N., "Unsteady Aerodynamic Characteristics of a Dual Element Airfoil Configuration," AIAA Paper 92-2508, Proceedings of the AIAA 33rd Structures, Structural Dynamics and Materials Conference, Dallas, TX, April 1992.
10. Bangalore, A. and Sankar, L. N., " Numerical Analysis of Aerodynamic Performance of Rotors with Leading Edge Slats, " AIAA 95-1888, to be presented at the 13th AIAA Applied Aerodynamics Conference, June 1995.
11. Seddon, J., Basic Helicopter Aerodynamics, AIAA Education Series, 1990.
12. Beam, R and Warming, R.F., " An implicit finite difference algorithm for hyperbolic systems in conservation law form, " *Journal of Computational Physics*, Vol 22. Sept 1976
13. Wake, B.E. and Sankar, L.N., " Solution of Navier-Stokes equations for the flow over a rotor blade, " *Journal of the American Helicopter Society*, April 1989.
14. Bangalore, A., Tseng, W and Sankar, L.N., " A Multizone Navier-Stokes Analysis of Dynamic Lift Enhancement concepts, " AIAA paper 94-0164, Reno,NV, Jan 1994.
15. Bangalore, A., Phaengsook, N. and Sankar, L.N. , " Application of a Third Order Upwind Scheme to Viscous Flow Over Clean and Iced Wings, " AIAA paper 94-0485, Reno,NV, Jan 1994.
16. Bangalore, A., " Computational Fluid Dynamic Studies of High Lift Rotor Systems Using Distributed Computing, " Ph.D Thesis, Georgia Institute of Technology, June 1995.
17. Roe, P.L., " Approximate Reimann solvers, Parameter vectors and difference schemes, " *Journal of Computational Physics*, 43, 357-372, 1981.
18. Benek, J. A., Buning, P. G. and Steger, J. L., "A 3-D Chimera Grid Embedding Technique, " AIAA Paper 85-1523, 1985.
19. Thompson, J. F., Thames, J. P. and Mastin, C. W., " Automatic Numerical Generation of Body-Fitted Curvilinear Coordinate System for Field Containing any Number of Arbitrary Two-dimensional Bodies, " *Journal of Computational Physics*, Vol. 15, 1974.
20. Sankar, L.N., Phaengsook, N. and Bangalore, A., "Effects of Icing on the Aerodynamic performance of High Lift Airfoils , " AIAA paper 93-0026, Jan 1993.



21. Baldwin, B.S. and Lomax, H., "Thin layer approximation and algebraic model for separated turbulent flow, " AIAA Paper 78-0257, Jan 1978.

22. Lorber, P. F., "Aerodynamic Results of a Pressure Instrumented Model Rotor Test at the DNW, " *Journal of the American Helicopter Society*, Vol. 36, No. 4, October 1991.

23. Strawn, R.J and Barth, J.T., " A finite-volume euler solver for computing rotary-wing aerodynamics on unstructured meshes, " presented at the 48th Annual forum of the American Helicopter Society, Washington D.C, June 1992.

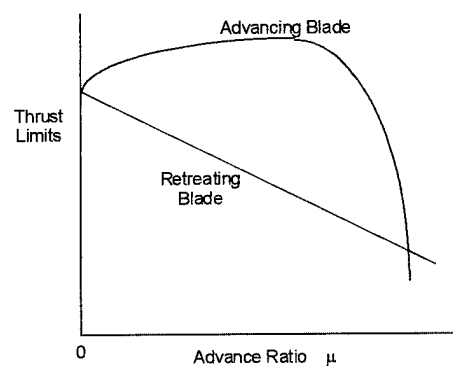


Figure 1 : A typical rotor thrust limit envelope

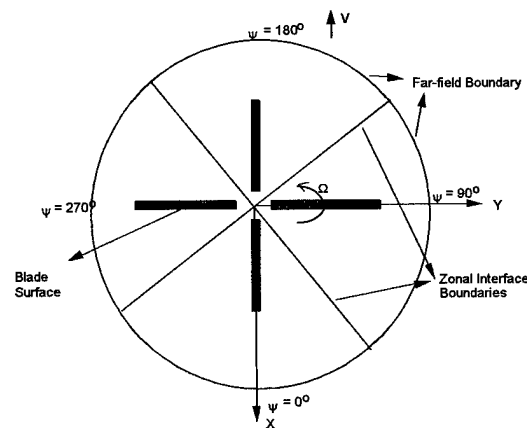


Figure 2 : Schematic of a four-bladed rotor in forward flight

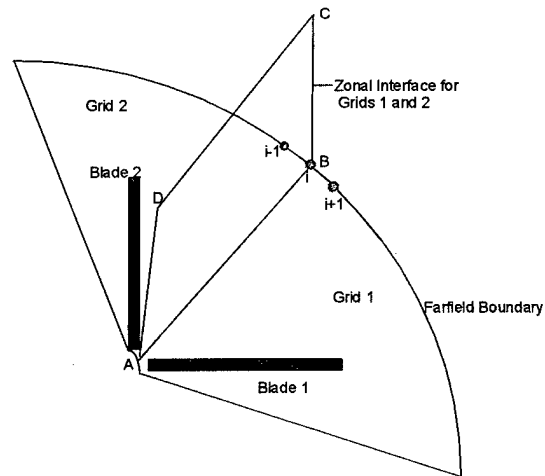


Figure 3 : Schematic showing the zonal interface connecting two H-O grids

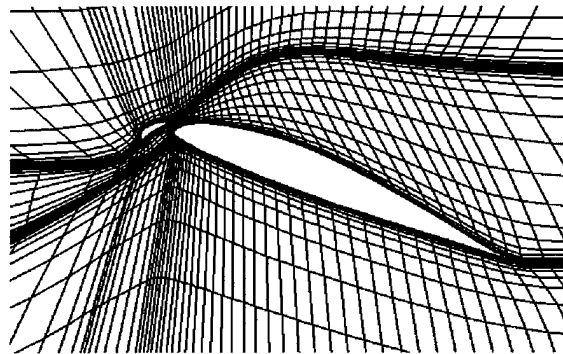


Figure 4. Two-dimensional multizone H-grid

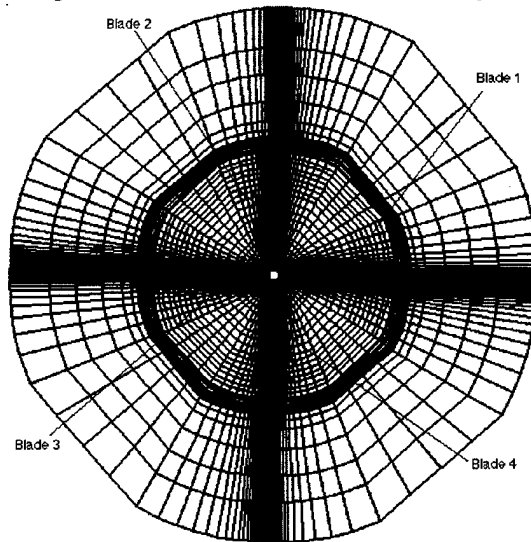


Figure 5 : Top view of a four-bladed multizone H-O grid in forward flight

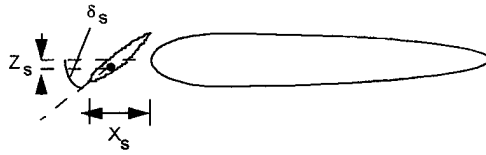


Figure 6 : Schematic of SC-1095 Slatted airfoil

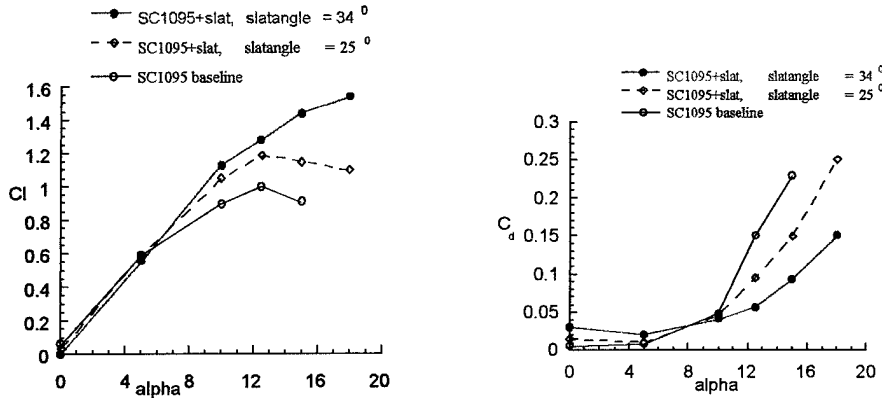


Figure 7 : Lift and Drag coefficients vs  $\alpha$ , Baseline and Slatted SC-1095 airfoils,  $M_\infty = 0.2$ ,  $Re = 2.2$  Million

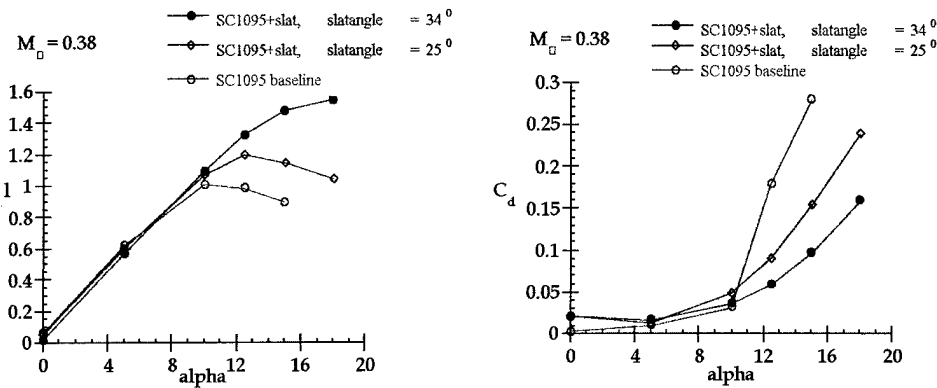


Figure 8 : Lift and Drag coefficients vs  $\alpha$ , Baseline and Slatted SC-1095 airfoils,  $M_\infty = 0.38$ ,  $Re = 2.2$  Million

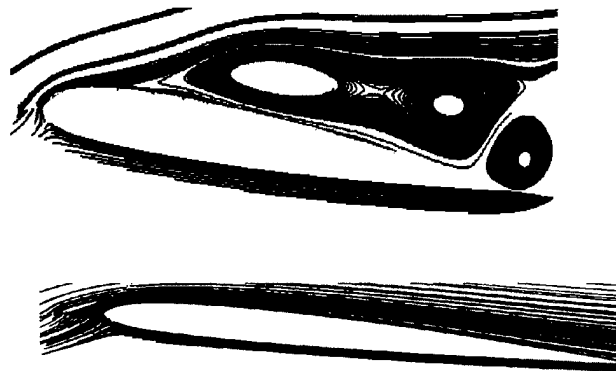


Figure 9: Streamline Pattern over Baseline and Slatted SC-1095 airfoils,  $\alpha = 12.5$  degrees,  $M_\infty = 0.2$ ,  $Re = 2.2$  Million

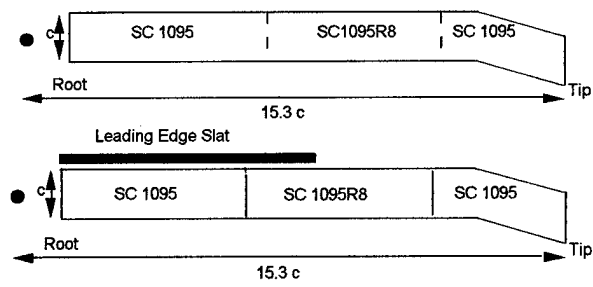


Figure 10 : Schematic of Baseline and Slatted UH-60A rotor blades

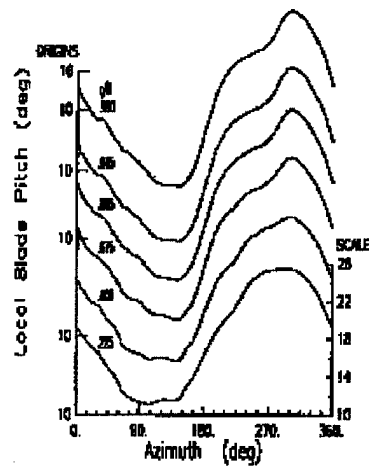


Figure 11 : Geometric Pitch vs azimuth at different radial stations

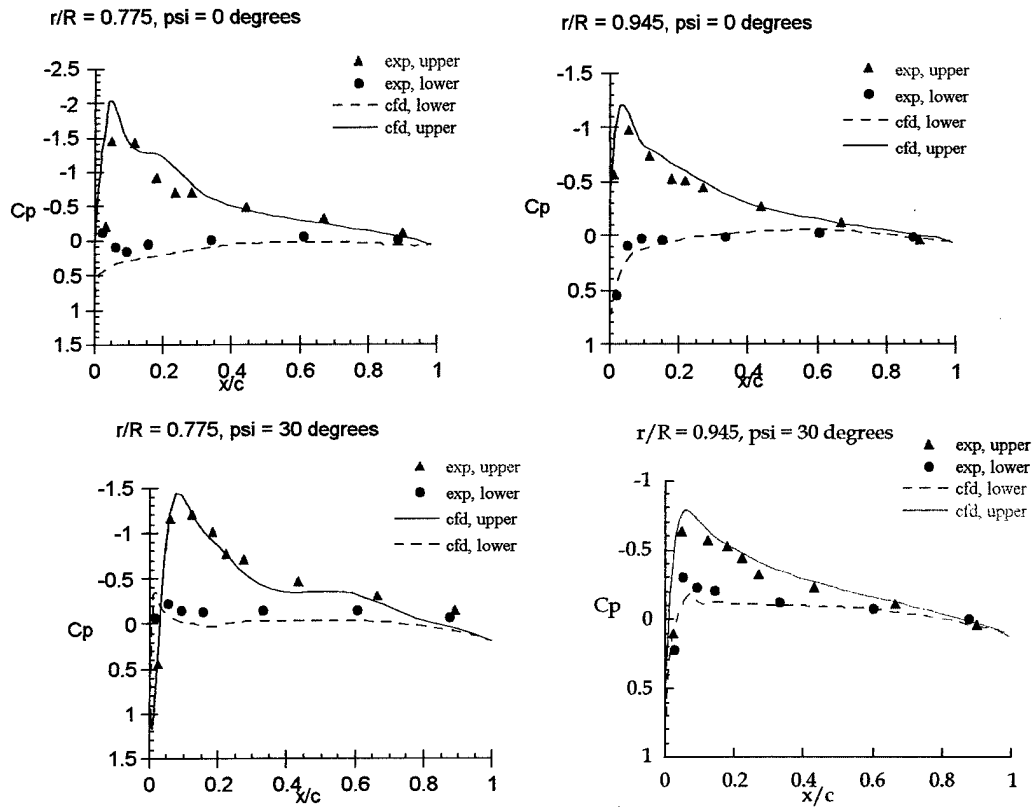


Figure 12 : Surface pressure distribution, First quadrant,  $M_{tip} = 0.628$ , advance ratio = 0.3, UH-60A baseline rotor

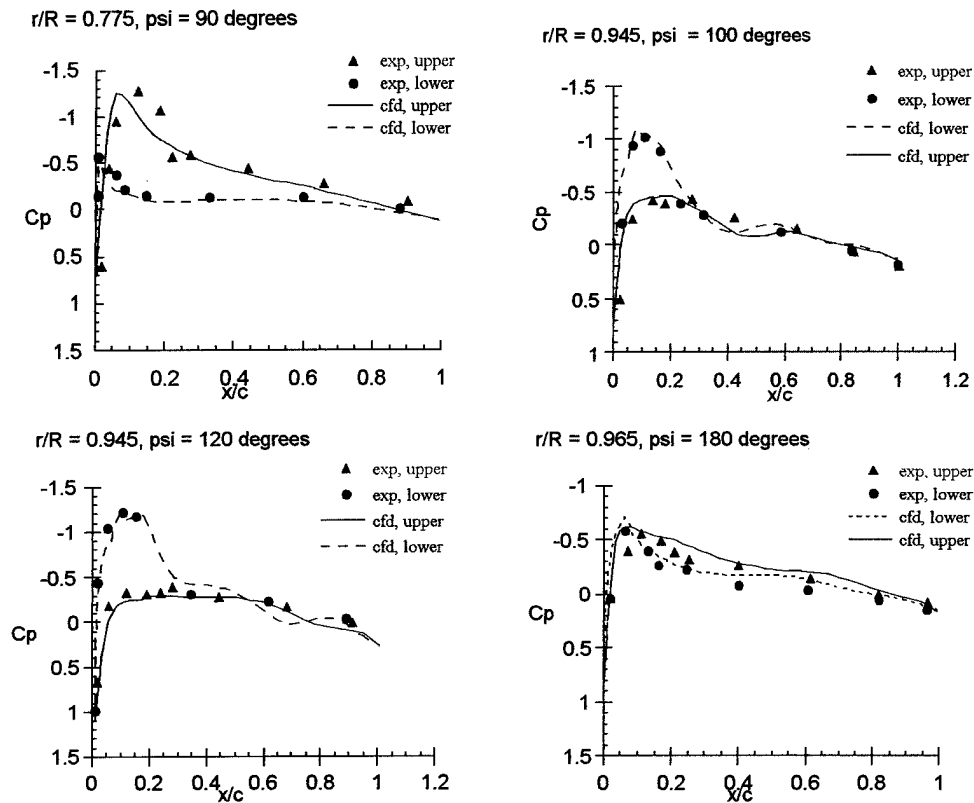


Figure 13 : Surface pressure distribution, second quadrant,  $M_{tip} = 0.628$ , advance ratio = 0.3, UH-60A baseline rotor

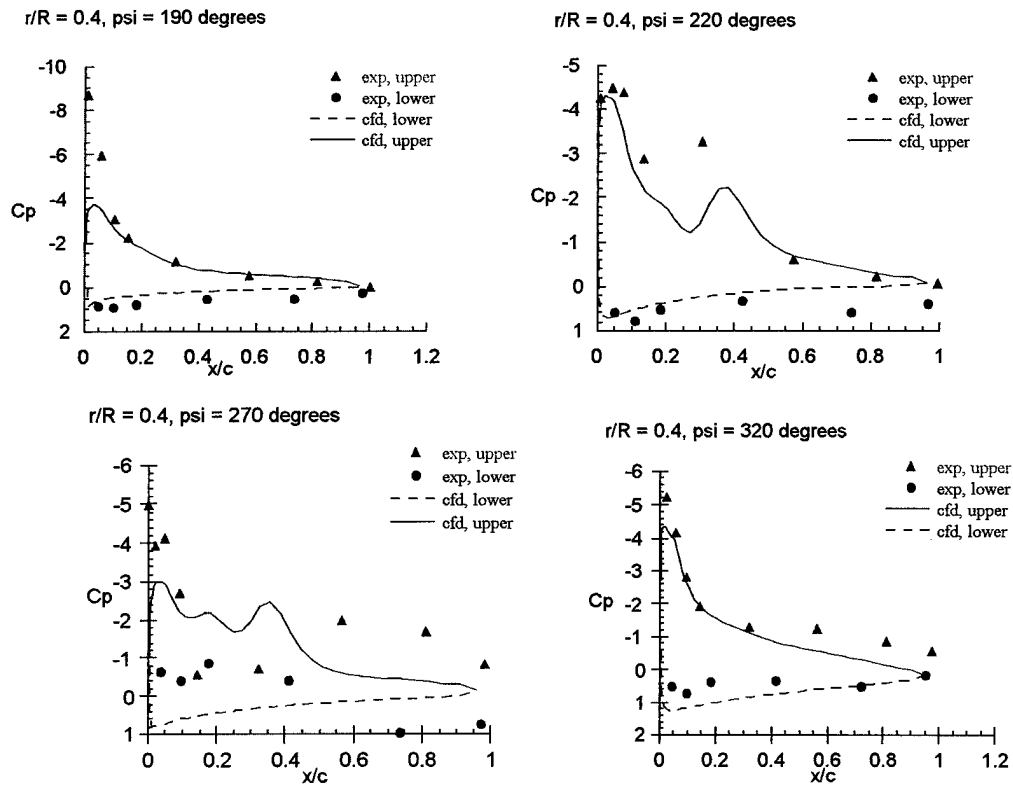


Figure 14 : Surface pressure distribution, retreating side,  $M_{tip} = 0.628$ , advance ratio = 0.3, UH-60A baseline rotor

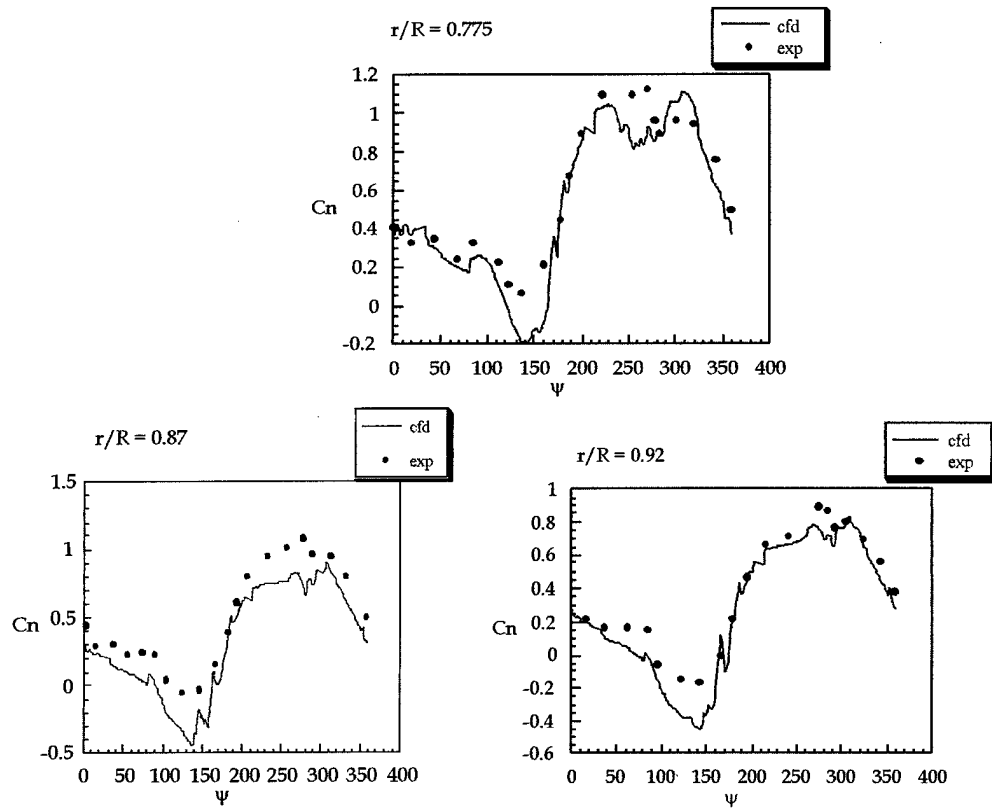


Figure 15 : Sectional normal force coefficient (nondimensionalized with local dynamic pressure) vs azimuth, UH-60A baseline rotor



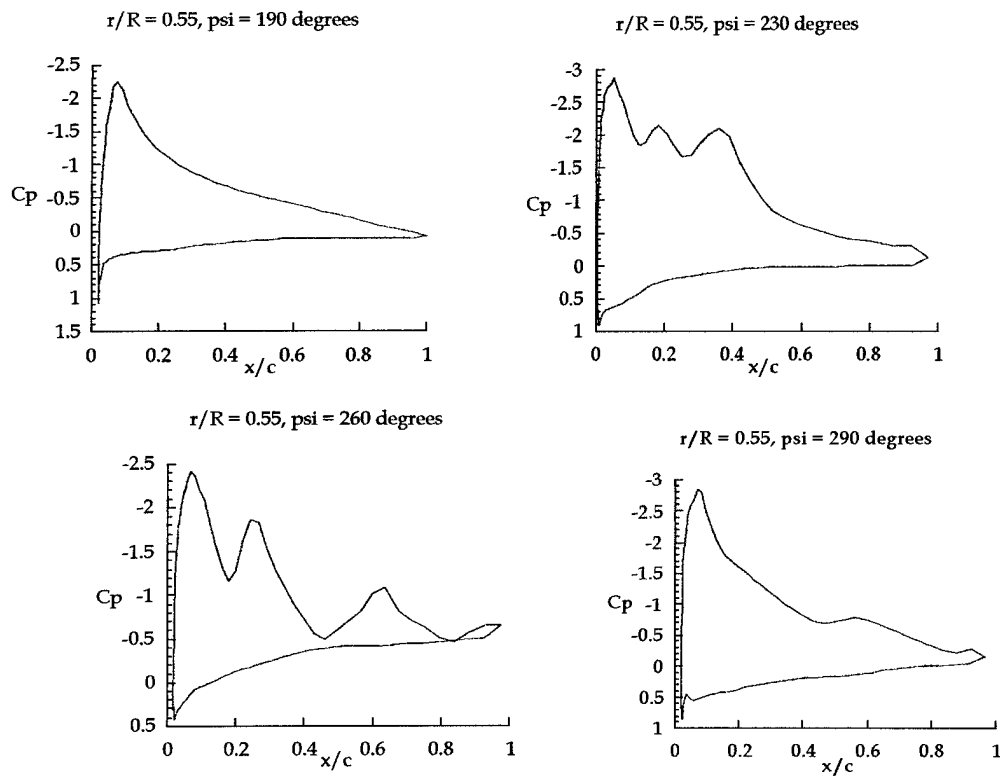


Figure 16 : Surface pressure distribution, 55 % radial station, retreating side,  $M_{tip} = 0.628$ , advance ratio = 0.3, UH-60A baseline rotor

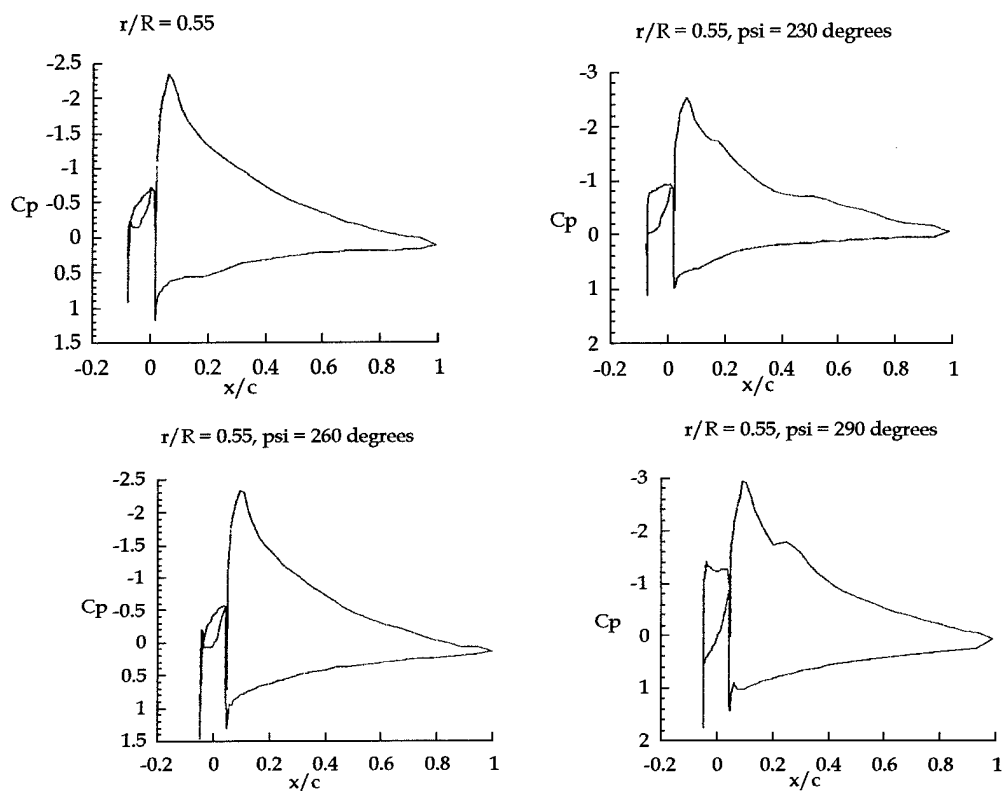


Figure 17 : Surface pressure distribution, 55 % radial station, retreating side,  $M_{tip} = 0.628$ , advance ratio = 0.3, UH-60A slatted rotor

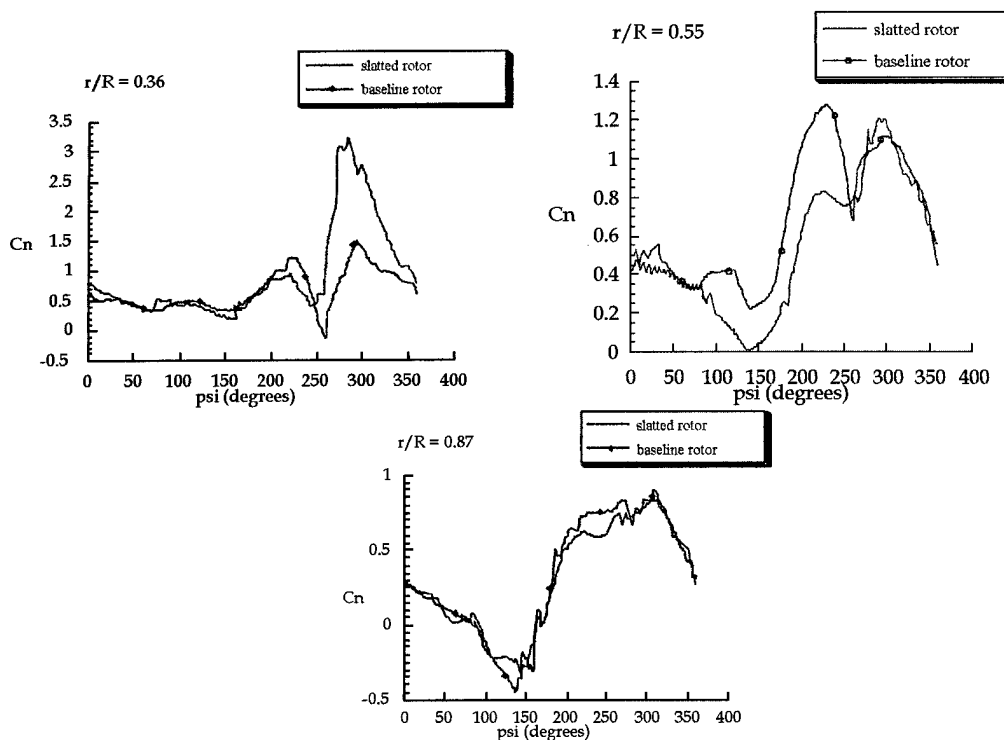


Figure 18 : Sectional normal force coefficient (nondimensionalized with local dynamic pressure) vs azimuth, UH-60A baseline and slatted rotors,  $\mu = 0.3$

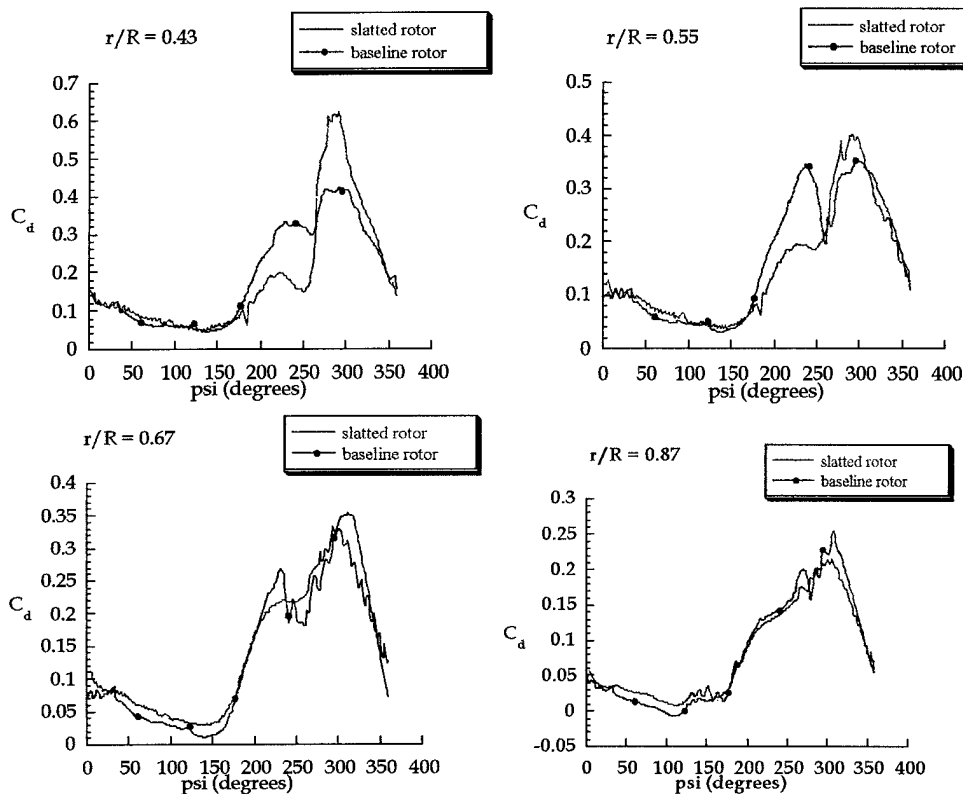


Figure 19 : Sectional drag coefficient (nondimensionalized with local dynamic pressure) vs azimuth, UH-60A baseline and slatted rotors;  $\mu = 0.3$

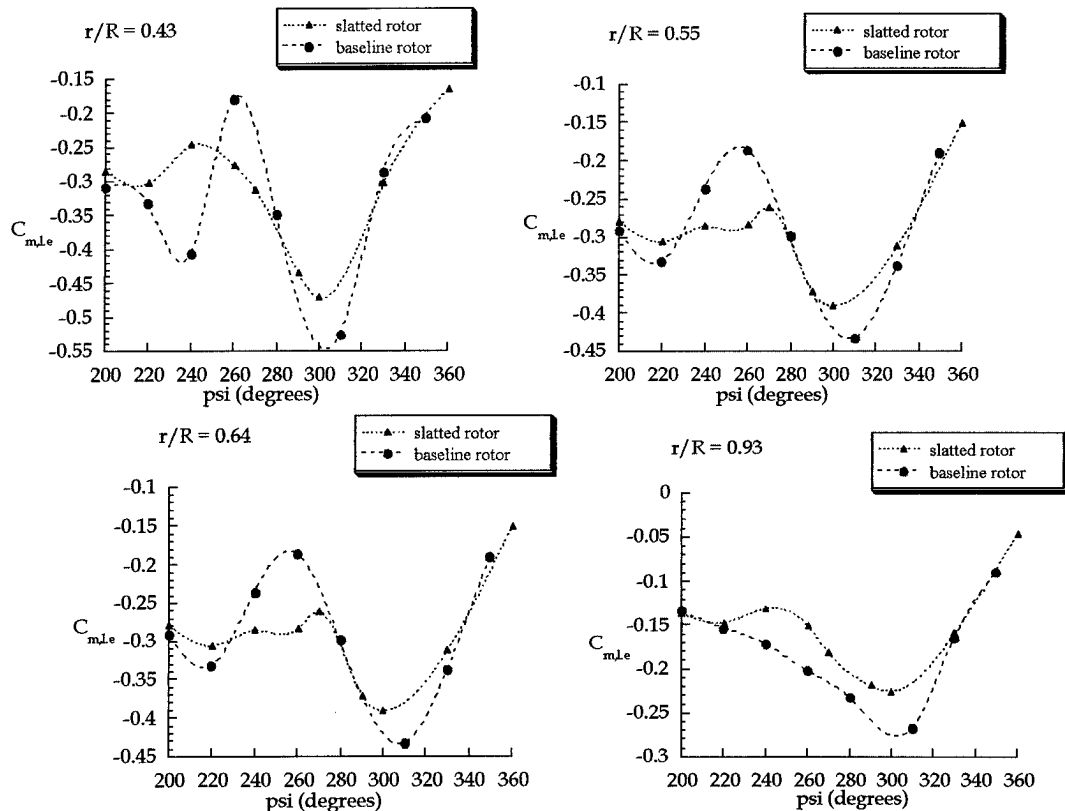


Figure 20 : Sectional moment coefficient (nondimensionalized with local dynamic pressure) on the retreating side, UH-60A baseline and slatted rotors

*Final Report*

*E16-X35 Task RUA-2*

## Flow Diagnostics for Rotorcraft Executing Maneuvers

Submitted to  
U.S. Army Research Office

Urmila C. Reddy, Robert B. Funk, Narayanan M. Komerath  
School of Aerospace Engineering  
Georgia Institute of Technology  
Atlanta, GA 30332-0150

Army Technical Monitor:  
Dr. Thomas L. Doligalski

GITAER-EAG-97-3

March 1997

## CONTENTS

1. Abstract	1
2. Introduction	3
3. Previous work	5
4. Tomographic Reconstruction	7
5. Spatial Cross-correlation Velocimetry	13
6. 3D Vector Field Reconstruction	20
7. Conclusions	26
8. References	27
9. Figures	

## 1. ABSTRACT

To quantify flows encountered by rotorcraft during maneuvers, rapid measurements of scalar and vector fields are needed over large volumes. The techniques used must be compatible with the requirements of large test facilities. This 2-year project studied methods for acquiring and reconstructing fully resolved, four-dimensional, spatio-temporal measurements of vector flow properties in unsteady periodic flows, such as those around rotorcraft. The project thus involved both the theoretical studies needed for algorithm development and image extraction, and the solution of hardware problems required to enable multi-dimensional velocity field measurement in large low-speed flows typical of rotorcraft. The effort started with a survey of theoretical formulations for tomographic reconstruction of  $n$ -dimensional scalar fields from  $(n-1)$ -dimensional projections. The Filtered Back Projection algorithm for reconstruction of scalar quantities has been developed and tested on a uniform density field within an elliptic boundary. This led to the 3D reconstruction of velocity fields from 2-D velocity fields acquired by Spatial Correlation Velocimetry (SCV). The extension to three dimensions is done using a stacking of 2D data planes and interpolating between planes using physical laws. This has been numerically demonstrated, its accuracy validated, and it is now being used in reconstructing the velocity field of a wing-rotor interaction experiment in a low-speed wind tunnel.

SCV computes a planar vector field by cross-correlating two images of the flow acquired with a known time difference. Extension of this planar imaging velocimetry technique to whole-field measurements is described. The 2D projection data is obtained by recording light intensity patterns on a CCD array whereas the reconstruction to three-dimensions uses known properties of the flow. The problem of obtaining the third component normal to the 2D planes was tackled here by using the equation of mass conservation for incompressible flows. The method has been validated using a test case where the velocity field is obtained from a known solution of the Navier Stokes equations for rotating flow above a stationary ground plane.

SCV measurements using a pulsed laser sheet were demonstrated under the previous Rotorcraft Center project. Here, SCV has been successfully applied to white light sources and extended to large areas. Experiments were performed at the exit of a low-speed wind tunnel, where the accuracy of the measurements was demonstrated by comparison with readings from a standard point velocity probe. These experiments used a set of 300 Watt halogen lamps with sheet-generating optics.

The post-processing algorithm has been modified to handle highly deterministic image fields which are encountered in heavily-seeded flow regions. Digital noise removal routines have been added to eliminate periodic noise due to interference from the various components of the imaging system. Tests have been conducted for two configurations: an isolated rotor in the 16' AeroTech hover facility, and a rotor - fixed wing configuration in forward flight in the 7' x 9' wind tunnel. Sample results for the two component velocity field in several parallel planes are shown. The complete 3D velocity field measurement is underway.

The technology developed under this project has enabled extension to systems which have been successfully used in large industry and government test facilities. During 1996, the technique has been used at the Bell Helicopter Textron Whirl Cage, in the 30' x 30' settling chamber of the Ames AFDD tunnel, and in the 60' diameter hover chamber of the Boeing VTOL tunnel. To put in perspective the nature of these advances, the total system hardware cost of the equipment used in these experiments (which was shipped to and from the sites each time) was less than the cost of a single-component low-power laser Doppler velocimeter of the type used in undergraduate lab classes, and less than the cost of one of the cameras used in typical bench-scale Particle Image Velocimetry experiments.



## **2. INTRODUCTION**

The measurement of velocity fields is critical to understanding and predicting the aerodynamics of rotorcraft. Traditional velocimetry techniques used intrusive probes e.g. hot-wire and hot-film anemometry. However the use of intrusive probes is undesirable due to interference with the flow being measured and the inability to measure reversed flow. More recent laser-based non intrusive techniques such as Laser Doppler Velocimetry (LDV) and Particle Image Velocimetry (PIV) are now widely used. The former is a pointwise technique whereas the latter is a planar technique. Point wise techniques are not amenable to full field measurements in unsteady flows where periodicity cannot be assumed. The desire to overcome this limitation and get quantitative results from flow visualization data led to the development of planar velocimetry techniques that allow for the study of both steady and unsteady flows.

Most problems of interest in modern fluid dynamics involve three-dimensional, three-component velocity fields. Very few such techniques exist for measuring such flows rapidly. Being intrinsically a 3D imaging process, holography offers a great scope for measuring 3D velocity fields. Particle holography offers an enormous information capability. At present, the use of holographic imaging over large volumes in the vibrating environment of a rotorcraft test facility poses an expensive engineering problem. In addition, the storage and retrieval of holographic data poses a major challenge, which is being addressed by researchers in the computer industry. Pending the development of efficient techniques for these, it remains difficult to use holography for large-area measurements in rotorcrafts flows.

Another 3D technique in use is tomography. Tomography refers to the cross-sectional imaging of an object from either transmission or reflection data collected by illuminating the object from different directions. Fundamentally, tomographic imaging deals with reconstruction of a property field(usually density) from a set of its projections (data collected by detectors outside the field) as illustrated in Fig. 1. The impact of this technique in diagnostic medicine has been revolutionary. The first medical application utilized x-rays for forming images of tissues based on their x-ray attenuation coefficient. When x-rays pass through matter, they are attenuated roughly in proportion to the density of that matter. Thus if we record the intensity of x-rays that have passed through an object we get a projection of the mass density. In computed tomography, the spatial variation of x-ray absorption in a thin slice or cross-section of the sample is recorded for various projection directions or views, the number of which depends on the ultimate resolution desired. The different views are combined via a reconstruction algorithm, and the two-

dimensional map of the x-ray absorption across the slice is obtained. The three-dimensional distribution of the absorption in the sample is recovered by stacking successive slices. There are numerous non-medical imaging applications that lend themselves to the methods of computerized tomography. Researchers have already applied this methodology to mapping of underground resources, cross-sectional imaging for non-destructive testing, 3D imaging with electron microscopy, design and measurement of industrial systems, 3D flow visualization and imaging etc.

In recent years there has been a growing interest in tomographic reconstruction of vector fields. The primary driving force has been the realization that certain applications such as ultrasonic imaging, flow imaging and ocean acoustic tomography have measurements that are inherently line integrals of the inner(dot) product of the vector field. Simple stacking procedures cannot be used for 3D vector fields - additional information about the flow being imaged is needed. The key to vector tomography is the decomposition of the field into its irrotational and solenoidal components. Standard line integral measurements can be used to recover the solenoidal component in 2D vector fields. The irrotational component can be reconstructed only if the fluid is incompressible and no sources or sinks are assumed to exist. For 3D vector fields one additional constraint is necessary to obtain the third component. Researchers have concluded that for complete reconstruction of 3D vector fields either *a priori* information about the field (source free, curl free) is needed or two different types of projections must be available. Under these circumstances scanning of multiple planes is a tractable alternative (illustrated in Fig. 2) , but once again an offset in time requires identical flow events in repetitive runs. Since the rotor and rotor/body flows investigated by the authors have this periodicity, measurement of multiple planes of two component velocity fields using a correlation method (SCV) was used as a precursor to the complete 3D three component velocity field measurement. The later was achieved computationally by using a known property of the flowfield - incompressibility. In future applications to non-periodic flowfields, it is basically possible to perform high-speed scanning of the flowfield using multiple sheets, and storage of this "slice" information within a time which is shorter than the smallest time scales of interest. This would enable stacking of essentially instantaneous 2-D velocity fields.

This project provided the opportunity to study tomographic reconstruction techniques, with a view to future incorporation into scalar and vector field measurements. At the end of this 2-year period, the efforts under the tomography and those under the hardware experiments using image velocimetry still appear to be parallel. This parallelism is essential until some hardware advances from the computer and electronics industry become commonly available.

### **3. PREVIOUS WORK**

Applications of these 2D/3D reconstruction methods are many and varied. Sato and Shiraki [1] have used tomographic methods to study the planar flow velocity distribution in a water tank. Pulsed sound waves were used to obtain information on the flow velocity components in different directions (projection data) and then a 2D velocity field was reconstructed using a pseudo inverse matrix method. Reference [2] deals with density field reconstructions of the flow over a free flying supersonic cone at different angles of attack. The projection data were recorded using five interferometers around the object in flight.

Liu, Merzkirch and Oberste-Lehn [3] used the convolution backprojection algorithm for obtaining a 3D density distribution of a steady, laminar, axisymmetric helium jet exhausting vertically into ambient air. Speckle photographic recordings were used because they provided a high number of data points in each projection. The noise in the experimental data was smoothed by a cubic spline technique. They obtained good reconstructions with just 12 projections in the 0-180° range.

The 3D density field around a helicopter rotor blade was reconstructed by Hesselink and Snyder [4] using parallel beam projections of laser light. Density was determined from the refractive index field obtained by using a pulsed ruby laser holographic interferometer. Forty projections taken at two degree intervals were sufficient to give reconstructions with only 0.4% deviation from the original image. They conclude that among the various reconstruction algorithms the convolution back projection method provides the best results and is computationally efficient.

The problem of reconstructing 2D vector fields throughout a bounded region  $D$  from the line integrals of velocity (projections) through  $D$  was investigated by Norton [5]. By means of a vector projection slice theorem, he showed that only the solenoidal component of a 2D velocity field can be uniquely reconstructed from projections whereas the irrotational component cannot. However when the fluid is incompressible and source-free the latter vanishes and the vector field can be completely reconstructed. In a later paper Norton [6] showed that the irrotational component of a vector field can be recovered from measurements on the boundary. Braun and Hauck [7] confirmed Norton's results and imaged simple flowfields in laboratory experiments. They investigated tomographic reconstruction of fluid velocity using ultrasonic time-of-flight measurements. Winters and Rouseff [8] focused on the direct reconstruction of fluid vorticity instead of velocity. This is advantageous because in many areas of fluid dynamics vorticity is the fundamental

descriptor of the flow. They presented a new discrete vorticity inversion algorithm based on filtered backprojection.

Tomographic reconstruction of 3D vector fields using inner product probes was investigated by Prince [9]. He shows that one set of measurements is required to reconstruct an irrotational field, two are required to reconstruct a solenoidal field and special probes are required to reconstruct arbitrary fields. A convolution-backprojection algorithm has also been developed for vector field reconstruction [10].

Meng and Hussain [11] used Holographic Particle Velocimetry (HPV) where 3D information is recorded instantaneously from a well seeded flow. Autocorrelation was used for double-exposed holograms, each hologram being reconstructed separately. Cross-correlation was used for single-exposure holograms, requiring two holograms that are recorded at different instants in the same time series. However both these operations were performed as 2D operations giving only two velocity components. They proposed an orthogonal view of the recording supplying the third component. This is somewhat redundant since the 3D information is already recorded within one view but is often difficult to extract. Huang, Slepicka and Cha [12] developed Holographic Diffraction Image Velocimetry (HDIV) which can measure 3D three component velocity fields. They used off-axis holography where multiple scenes can be separately recorded on a single holographic plate and then independently reconstructed, by employing an individual reference beam for each scene. However HDIV processing is rather involved, including holographic recording, image calibration and 3D image correlation.

#### 4. TOMOGRAPHIC RECONSTRUCTION

There are two basic types of tomographic techniques -- the conventional straight ray tomography and diffraction tomography. The following work deals only with straight ray tomography. Mathematical algorithms for tomographic reconstructions are based on projection data. Projections are a set of measurements of the integrated values of some parameter of the object. They can represent, for example, the attenuation of x-rays through an object as in conventional x-ray tomography, the decay of radioactive nucleoids in the body as in emission tomography, or refractive index variations as in ultrasonic tomography.

If these integrated values are along straight lines through the object, the projections obtained are referred to as 'line integrals'. Two possible types of projections are *parallel beam projections* and *fan beam projections*. The former is a collection of parallel ray integrals obtained by moving the source and detector along parallel lines on either sides of the object. If a single source is placed in a fixed position relative to a line of detectors, the line integrals are measured along fans and this is called fan beam projection. These two projection types are illustrated in Fig. 3.

Mathematically, a line projection is simply the radon transform of the 2D object function. If  $f(x,y)$  is a 2D object function, its Radon transform is given by:

$$R[f(x,y)] = \int_{-\infty}^{\infty} \int_{-\infty}^{\infty} f(x,y) \delta(x \cos \theta + y \sin \theta - t) dx dy$$

Where  $x \cos \theta + y \sin \theta - t = 0$  is the parametric equation of the line along which the projection is taken.

The key to tomographic imaging is the Fourier Slice Theorem (illustrated in Fig. 4) which relates the measured projection data to the 2D Fourier transform of the object function. This theorem is stated as follows:

*The Fourier transform of a parallel projection of an image  $f(x,y)$  taken at an angle  $\theta$  gives a slice of the two-dimensional transform  $F(u,v)$  subtending an angle  $\theta$  with the  $u$ -axis.*

By taking projections of an object function at several angles and transforming each of these we can determine the values of  $F(u,v)$  on radial lines. If an infinite number of projections are taken then  $F(u,v)$  will be known at all points in the  $u$ - $v$  plane (frequency domain).

Knowing  $F(u,v)$  the object function can be recovered by performing the inverse Fourier transform. In practice only a finite number of projections of an object can be taken.

## **2D Reconstruction methods**

Reconstruction techniques fall into two broad categories namely, frequency domain interpolation schemes and the space domain interpolation schemes. In the theory described so far the interpolation is in the frequency domain. The 2D inverse FFT is performed assuming all values in-between the discrete slices to be zero in the frequency domain.

It is usually more accurate to carry out interpolation in the space domain than in the frequency domain. This is used in the filtered back projection algorithm. In actual application the simple inverse transform of the 2D FFT does not yield good results. So the filtered back projection algorithm is used. A brief explanation of this method follows.

Consider a single projection and its Fourier transform. By the Fourier Slice Theorem this projection gives the values of the object's two-dimensional Fourier transform along a single line in the frequency domain. In a simple reconstruction the other projections are assumed to be zero and the 2D inverse Fourier transform is performed. This means that accurate reconstructions can be obtained theoretically by using an infinite number of projections. In practice, however only a limited number of projections can be recorded.

In order to better approximate the ideal case a simple weighting in the frequency domain is used. The simplest way to do this is to take the object's Fourier transform and multiply it by a weighting function (that resembles a wedge with apex at the origin of the frequency domain). For e.g. if there were  $K$  projections in 180 degrees then at a given frequency each wedge has a width of  $2\pi|w|/K$  where  $|w|$  is the absolute value of frequency. The effect of weighting by  $2\pi|w|/K$  is to make the discrete transform a better approximation to the infinite frequencies.

The weighted projection has the same 'mass' as the pie shaped wedge and therefore gives a much more accurate reconstruction than the simple inverse Fourier transform. The filtered projection will make the same contribution to the reconstruction of all points on a line. Therefore, in the reconstruction process each filtered projection is smeared back or 'backprojected' over the image plane. Hence the name 'filtered backprojection method' or FBP in short. The final reconstruction is found by adding together the 2D inverse Fourier transform of each weighted projection.

There are two advantages of this method over a frequency domain interpolation scheme. Firstly the reconstruction procedure can be started as soon as the first projection has been measured. This can speed up the reconstruction procedure and reduce the amount of data that must be stored at any one time. Secondly, simple linear interpolation is often

adequate for the backprojection algorithm while more complicated approaches are needed for the direct Fourier inverse schemes.

### **Scalar Field Reconstruction**

The Filtered Backprojection technique described earlier was applied to the simple case of an elliptic object function. The object function is defined as:

$$f(x,y) = \rho \quad \text{for } \frac{x^2}{A^2} + \frac{y^2}{B^2} \leq 1$$

$$= 0 \quad \text{outside the ellipse}$$

Therefore, the function to be reconstructed is an ellipse with major axis 'A' and minor axis 'B' and centered at (0,0). The analytic expression for the line projection of an ellipse is taken from Kak and Slaney [13] and is given below:

$$P_{\theta}(t) = \frac{2\rho AB}{k(\theta)^2} \sqrt{k(\theta)^2 - t^2} \quad \text{for } |t| \leq k(\theta)$$

$$= 0 \quad \text{for } |t| > k(\theta)$$

where  $k(\theta)^2 = A^2 \cos^2(\theta) + B^2 \sin^2(\theta)$

$\theta$  is the projection angle and  $k(\theta)$  is the projection half-width as shown in Fig. 5.

### **Results and discussion**

Parallel beam reconstructions using the FBP scheme were performed and studied[13]. The code was run for several cases. In all cases the value of the object function in the elliptical boundary was 1.0. The ellipse to be reconstructed has a major axis of 10 and a minor axis of 5. The computational domain is extended beyond the boundaries of the ellipse to a circular grid whose radius was equal to the semi-major axis of the ellipse. This gives some idea of the far field reconstruction. An ideal reconstruction would be an elliptical region with density of 1.0 throughout and a density of zero outside the boundary of the ellipse. However, due to various reasons described below the reconstructed image differs from the ideal. Input parameters such as sampling interval and number of projections were varied and their effect on the reconstructed image studied.

**Case 1:** constant sampling interval and changing number of projections : The number of grid points for each projection angle was kept constant and the number of projections varied. Increasing the number of projections resulted in a more accurate reconstruction of

the object function. The average value was 0.55 for 64 projections, 0.58 for 128 projections and about 0.6 for 256 projections with 64 grid points.

Note : It is essential to have the number of grid points and the number of projections as powers of 2. This is because the Fast Fourier Transform algorithm used for Fourier transforming requires this.

Case 2: constant number of projections and changing grid size : For a given number of projections the sampling interval was varied to see its effect on the accuracy of reconstruction. The smaller the sampling interval (close grid spacing) the closer was the object function value to the ideal value of 1.0. The thin streaks surrounding the ellipse are caused due to insufficient number of projections and are called Moiré patterns.

In both of the above cases it is seen that streaks may be light or dark. This is because the sampled projection can be considered as the sum of two parts -- the true projection and the error term. A positive error in a projection causes a light streak when the data are backprojected. Likewise negative errors lead to dark streaks. An analysis performed by Kak & Slaney [14] of the optimum number of rays and projections required concludes that the number of projections should be roughly equal to the number of rays. Fig. 6, 7 and 8 show reconstructed images for different grid resolutions where the number of rays equal the number of projections. The reconstructed ellipse for the case with 256 projections and 256 rays is a reasonably good approximation to the ideal case.

In all these cases projections were taken only between 0 to 180° due to the symmetric nature of the ellipse. Any projections taken for 180-360° would only overlap the ones already taken. From this one would expect symmetric reconstructions for the upper and lower halves of the ellipse. The reconstructed image improved with increase in grid points as well as the number of projections as expected.

## **Reconstruction Errors**

### *Sampling errors*

According to the sampling theory of signal processing, there exists a critical sampling rate, which is equal to twice the highest spatial frequency in the Fourier transform domain of the sampled object. This means that data must be sampled at a certain minimum rate for the original signal to be represented accurately. This is called the Nyquist rate.

The sequence of numbers used to approximate a continuous function will represent the function accurately only if they are sampled at Nyquist rate if not higher. If the sampling frequency is lower than the Nyquist rate (undersampling) some of the information



in the original data is smeared by replications of the signal at other frequencies and the original signal is lost. Such errors are known as 'aliasing'. Aliasing is one of the artifacts that may occur in the reconstructed image and it is of great impact on the reconstruction accuracy.

#### *Interpolation error*

Since only a finite number of projections can be taken, the Fourier transform of the function is known only along a finite number of radial lines. There is an error involved in interpolating between these radial lines to points on an elliptical or square grid (in the object domain). Since the density of the radial points becomes lesser as we move away from the center, the interpolation error also becomes larger. So there is a greater error in the calculation of the high frequency components in an image than in the low frequency ones. This results in some image degradation. In the present case a circular grid was chosen even in the object space and therefore this type of interpolation between radial lines was not necessary.

However, in the FBP scheme the effect of all projections has to be summed up at every grid point. Linear interpolation is used to obtain the contribution of each projection at that point. Thus there is interpolation between grid points along one ray. Since grid spacing increases away from the center this interpolation error is also higher at the boundary of the ellipse and once again high frequency components in the image suffer greater degradation than the low frequency components. The high frequency components are along the boundary of the ellipse and this is maximum error in the reconstructed images.

#### *Zero-padding*

It is possible to produce smoother looking outputs by zero-padding the data before taking the FFT. Padding a sequence of data with zeros increases the resolution in the frequency domain. So, by zero padding the data to twice its length the display resolution can be greatly increased. In the case of the elliptical object function the projection function was analytically obtained and not measured. Therefore the number of data points could be increased at will and there was no need to zero-pad the data.

#### *Filter function*

The filter function used in the numerical simulation described is the absolute value of the frequency. Usually in commercial applications the filter function is the product of a window function and the absolute value of frequency. The choice of the window function depends on the specific application. A few common window functions used in FBP are Butterworth, Hann, Hamming, Parzen or rectangular. Many authors such as Baba and Murata [15] have proposed variations on the standard filter functions of the filtered backprojection algorithm.

The current status of the tomography work is that the reconstruction techniques are available and amenable to efficient implementation on computer systems employing multidimensional Fourier Transforms. Advances are needed in the ability to acquire vector and scalar data over large volumes rapidly, and to store this information efficiently. The next section deals with a simple, inexpensive and efficient implementation aimed at acquiring such multidimensional velocity fields in large rotorcraft facilities.

## **5. SPATIAL CORRELATION VELOCIMETRY**

Spatial Correlation Velocimetry (SCV) is a planar velocimetry technique that has been developed and continues to be refined at Georgia Tech. The basic premise is that most of the energy of the flow is contained in larger "packets" or eddies of fluid. Even in highly turbulent flow the size of these "packets" is much larger than the size of the individual particles. These "packets," imaged twice with a sufficiently small time delay, remain largely undistorted, exhibiting a spatial displacement that can be determined computationally.

By the late 1980s, Particle Image Velocimetry techniques had been demonstrated, but the thinking at the time was that it

- a) required coherent illumination
- b) required high-power pulsed lasers
- c) post-processing used laborious point-wise techniques using lasers

The automation of the post-processing was then a development challenge, but the path being taken was using autocorrelations of the fringe patterns formed during the post-processing of double-exposed particle field images. Adrian [16, 17] had shown that the computation of these autocorrelations could be performed efficiently. The use of direct cross-correlation of images had been considered and ruled out as computationally prohibitive [18]. Note that a 2-D cross correlation is vastly more computation-intensive than the autocorrelation, where only the diagonal elements of the computation arrays need be considered.

Our patent [19], which originated under ARO Rotorcraft Center support, showed that direct cross-correlation could be performed efficiently using images taken with separate cameras, over areas of arbitrary size, without being able to resolve scattering at the particle size scale, without the and without the use of coherent illumination.. The initial demonstrations were done using a 16MHz MC68020-based Macintosh II computer [20]. This opened the way to computing velocity fields with arbitrary time resolution, using essentially the same video imaging parameters as were used in flow visualization [21,22]. The demonstration of velocimetry from images taken with two different cameras [23] broke through the obstacle of using high-speed motion picture cameras (or high-speed framing cameras with their resolution constraints). The system used in our recent industry experiments consisted of intensified cameras of the relatively inexpensive class used in security system.

The methodology is as follows - A light sheet is used to illuminate a single plane in a flow field. Intensified cameras are used to image seeding moving through this light sheet.

Two images separated by a small time are digitized from the two cameras. The two images are then sub-divided into small sub-image regions and a spatial cross-correlation is performed on the corresponding sub-image regions from each image. Digitized images from these cameras have dimensions of 640x480 pixels. Sub-image areas are normally 64x64 pixels. The amount of error is proportional to the size of the sub-image, so by keeping the sub-image size small error at the edges of the sub-image can be minimized. However the sub-image size must be large enough to accomodate a cognizable flow feature.

This cross-correlation is done computationally by performing a 2D fast Fourier transform(FFT) on each sub-image, then calculating a cross-spectra, and finally performing an inverse 2D FFT on the cross-spectra resulting in a cross-correlation function. This is illustrated in Fig. 9 as having a single distinct peak. The displacement of the peak of the cross-correlation function from the origin indicates the spatial shift in the seeding patterns from one image to the next. Knowing the time between the images and the physical dimensions of the imaged plane allows calculation of the velocity in that sub-image region. The calculation is repeated for each sub-image area to determine velocities in the imaged plane.

## **Post-processing**

### *Intensity criterion*

If adequate seeding exists in all parts of the image, this method will give an instantaneous picture of velocities in the imaged plane. In the larger area case, it is difficult to keep seeding in all areas at all times. An intensity criterion is then used to validate the computed vectors. If the average intensity of a sub-image area surpasses a user defined threshold it is assumed adequate seeding fills the sub-image area and the vector is valid.

### *Peak ratio criterion*

Another criterion used to eliminate unreliable vectors, is the ratio of the second largest and largest peak in the cross-correlation function. If the ratio exceeds a threshold value then there are two equally probable values for velocity at the same point! Therefore neither of them can be reliable. A good measure of the reliability of computed vectors must incorporate both the image intensity and peak-ratio criterions.

It was demonstrated in [24] that the presence of noise in images (ie. low signal-to-noise ratio or SNR) only lowers the primary peak and enhances the secondary peaks but does not substantially alter their positions. This means that low seeding concentration areas of the image (low SNR) must have a higher peak ratio than well-seeded areas (high SNR). This is borne out by the experimental results.

This brings us to the effect of image over-exposure on peak ratio i.e. investigating the possibility that there is too much seeding or that the shutter was open long enough to blur the image. Too much as well as too little seeding concentration and shutter exposure time lead to the same problem -- insufficient intensity patterns in the image. Therefore in both these cases SNR decreases and the peak ratio rises. Hence there is a good chance of peak ratio being exceeded in areas where there is too 'good' smoke.

#### *Distortion correction:*

Relative distortion between images causes errors in the displacement computed using SCV. This is because SCV in its present form computes only translational correlation. Flow or image distortion is not accounted for. Image distortion is corrected in the following manner. A rigid grid board covering the entire image area is recorded on both cameras and correlated. If the cameras are perfectly aligned and there is no relative distortion due to the lenses this correlation must yield all zero vectors. So any vectors obtained are due to alignment and distortion errors. These are therefore subtracted from the actual flow vectors.

#### *Moving window averaging*

Moving window averaging enables a large improvement in the statistical accuracy of the vector computed. This method simply involves computing vectors in overlapping sub-images i.e. sub-image centers are shifted only by a few pixels in both directions. All vectors in a given area are then averaged to obtain a more stable vector plot. For example choosing 64X64 non-overlapping sub-images in a 640X448 image gives 70 vectors (at 64 pixels apart) per image. If overlapping sub-images at 8 pixels apart are chosen we have 3577 vectors per image! These can then be averaged to the desired spacing. For e.g. averaging all vectors in non-overlapping boxes of 32 X 32 pixels gives 300 statistically stable vectors per image. Another useful technique is simple ensemble averaging (averaging corresponding vectors in several images) which improves accuracy in case of steady state or periodic flows.

#### *Noise smoothing*

There are many sources of noise in SCV. A main source is the entrance and exit of particles from the area of interest. This means that since corresponding sub-images are correlated (same location) all particles in sub-image 1 are not found in sub-image 2. Some new ones have entered and others have left in the time between images. Each of these phenomena will appear as noise and cause a reduction in the correlation between images. Therefore there is an error in the measured displacement which can be minimized by correlating with a shifted sub-image. Other sources of noise include the imaging system, aberrations of the lenses or noise in the image recording medium. Very often images

contain background noise due to interference from various types of electrical and electronic devices which comprise the imaging system. These include the basic image acquisition system itself i.e. cameras and VCRs as well as peripheral devices such as frame code generators, video mixer, video title maker, computer etc.

Methods for detecting, recording, storing and digitizing intensity patterns all contribute noise to the data. Since the actual flow patterns contain an infinite number of intensity values the digitization process results in a certain amount of image smearing because the actual intensity values are truncated to fit the available digitization resolution.

There are two ways of eliminating noise -- a) through hardware and b) through software. For best results both methods have to be combined. The first approach involves proper connections between different devices and the use of terminators wherever needed. This can only minimize electronic noise but cannot eliminate it. The second method involves the addition of noise smoothing routines in the software. This successfully eliminates periodic noise patterns often visible in low intensity images.

*Out-range pixel smoothing* is a nonlinear operation and is useful in reducing impulsive or salt-and-pepper noise. This is based on the assumption that most flow images are random with no preferred periodicity. If for any reason the image itself is spatially periodic the application of this technique will increase the error as useful data is eliminated. Therefore it is important to establish periodic components as noise spectra before applying the smoothing routines.

Initially the FFTs of both images are taken. Then a window slides along the image FFTs and the average of the pixel values excluding the pixel being processed is obtained. The window is usually a square of four to eight pixels. If the difference between the average and the value of the FFT magnitude for the pixel being processed exceeds a specified threshold then the current pixel value is replaced by the average, thus smoothing the peak. If the difference does not exceed the threshold then the peak is not of significant magnitude to be smoothed and is left as it is. Noise peaks are identified as those that are reasonably sharp and consistent in all the images. Usually the FFTs being complex have both magnitude and phase. While the magnitude at a noise peak is smoothed as described above the phase is preserved (due to lack of a better alternative). Because it is difficult to determine the best parameter values in advance it is useful to process an image using several different window sizes and threshold values and select the best result.

### **White light, large area experiments**

Over the past few years the SCV technique has advanced from very slow flows in water channels to instantaneous velocity fields in fully unsteady and turbulent air flows around a plunging wing and a complex dual wing configuration[25].

#### *The flowfield at the exit of a 3.5' x 3.5' wind tunnel*

The accuracy of the velocity measurements using the white light system is demonstrated over the speed range from 0 to 19 m/s by comparing instantaneous velocity vectors to the time-averaged velocity measured by a TSI Velocicalc™ probe placed downstream of the exit of a 3.5' x 3.5' wind tunnel[26]. The schematic of the setup is shown in Fig. 10(a). The vectors corresponding to the location of the probe were then taken from a series of images for each speed. The average velocity calculated by the SCV technique from 10 images is compared to the Velocicalc™ probe values in Fig. 10(b). The agreement is excellent. The range of velocities from the images used for averaging at each location are all within 10% of the probe measurements.

#### *3D Rotor flows*

Another configuration tested was the wake of a rotor in forward flight in a 2.1 X 2.5 m wind tunnel[27]. Here the challenge was to capture and analyze a sufficient number of velocity fields to resolve the periodic variation of the velocity field. This experiment also involved a wide range of spatial and temporal scales of velocity variation, as well as a highly three-dimensional flowfield with strong out-of-plane velocities.

Strobed white light SCV was first tested on a 3-bladed 30" rotor in hover in an indoor facility. Flow was seeded using commercial fog fluid emerging from two plastic ducts under the fan. Two strobe lights pulsing at camera framing speed (29.97 Hz) were used to generate 1" thick white light sheets perpendicular to the blade surface. The duration of the light pulse was much lesser (microseconds) and the strobe frequency ensured that there was only one pulse per shutter exposure. Each of these light sheets was synchronized with an intensified PULNIX camera. Sample velocity fields from this flowfield at various rotor azimuths are shown in Fig. 11.

### **Cross Spectral Velocimetry**

The cross-correlation of two periodic functions is periodic so that a unique peak cannot be identified. The Fourier spectrum is ideally suited for describing the directionality of periodic or almost periodic two-dimensional patterns in an image. It is important to remember that the spectrum of a real image is symmetric about the origin, so only half of

the frequency plane is unique and needs to be considered. Thus, every periodic pattern is associated with only one peak in the spectrum, rather than two. Three features of the Fourier spectrum are exploited here

- prominent peaks in the spectrum give the principle direction of the texture patterns
- the locations of the peaks in the frequency plane give the fundamental spatial period of the patterns
- by eliminating any periodic components we are left with non-periodic image elements which can then be described by statistical techniques.

In case of periodic functions the cross-spectra will have definite peaks corresponding to the primary spatial frequencies in the image. Velocity magnitude is obtained from the phase of the cross spectra at this peak frequency. For example a phase of 360 degrees means a displacement equal to the wavelength corresponding to the peak frequency ( $l = 1/f$ ). Direction is given by the two components of the peak frequency i.e. if  $f_1$  and  $f_2$  are the two primary frequency components in the horizontal and vertical directions respectively, then velocity direction is given by the angle  $\tan^{-1}(f_2/f_1)$  made with the positive  $f_1$  axis. The sign of velocity is given by the sign of the phase of cross-spectra at the peak frequency.

There is a limitation on the amount of displacement that can be measured using this method. It is obvious that displacements greater than one wavelength cannot be measured due to uncertainty in the number of wavelengths traversed. This restricts the method to low frequency periodic functions i.e. functions where there is approximately one cycle in one sub-image (usually a square of side 64 pixels). An alternative is to re-size the sub-image to equal one wavelength of the fundamental frequency.

In locating the primary peak in a 2D cross-spectral function the maximum peak is chosen and not the sharpest peak. However the accuracy of the computed displacement depends on the sharpness of the maximum peak and the relative magnitude of the secondary peaks. The sharper the primary peak the more accurate is the computed vector. This is because the method essentially approximates the image to a purely periodic function with a single sharp frequency peak (basically a delta function). The error is directly proportional to the magnitude and number of secondary cross-spectral peaks.

Often, peak ratios in the cross-correlation function exceed the threshold value when the cross-correlation function is periodic and more than one cycle exists in one sub-image. The height of the peak in every cycle of the function is roughly the same since a periodic function merely repeats itself once every cycle. In such cases where there is a clearly identifiable periodicity in the cross-correlation (this is only possible when individual image spectra are periodic) the following approach is used. For sub-images where the peak ratio



does not exceed the threshold value specified the vector is computed the usual way from the cross-correlation function. However when the ratio exceeds the threshold, instead of discarding the vector the cross-spectra is computed and scrutinized for a dominant frequency. If there is a single dominant frequency the cross-spectral technique described above is used to obtain the displacement. If there is no dominant frequency then the vector has neither a cross-correlation peak nor a cross-spectral peak and is therefore discarded.

#### *2D sine wave test case*

The method was tested using two 2D sine functions (variation need not be sinusoidal), one displaced with respect to the other by a known amount. The cross-correlation of two sine functions is also a sinusoidal function and the multiple peaks (all of approximately same height) do not allow computation of velocity by the SCV technique. If the two sine waves have the same frequency, it will correspond to the peak frequency in the cross-spectra. Displacement computed for such single frequency noise-free sine wave images was within 99% of the exact values.

In order to better simulate the multiple frequencies obtained in actual flow images two 2D sine waves of different frequencies and amplitudes were superimposed. In this case there are two discrete frequencies in the image. The primary frequency was chosen such that the corresponding wavelength is equal to the size of the sub-image i.e. one cycle in one sub-image. For a sub-image of size 64 X 64 pixels this corresponds to 0.0156 cycles/pixel. The secondary frequency in the image was six times the primary - 0.0936 cycles/pixel. The cross spectra has two discrete frequencies - only the primary frequency is used to compute displacement as long as the secondary peak is sufficiently small in comparison (peak ratio criterion).

Since the displacement is computed using only the primary frequency the presence of secondary frequencies increases the deviation from exact values. The method can be made more accurate by taking into account the effect of more and more frequencies in the algorithm. When multiple frequencies are considered the contribution of each to the displacement must be appropriately weighted. Ideally of course there are an infinite number of continuous frequencies in an image. This test case proves that the method works very well as long as there is a single well defined frequency in the image.

## 6. 3D VECTOR FIELD RECONSTRUCTION

The march toward higher dimensional data is motivated by several factors, the first and foremost being the fundamental nature of fluid motion. The conventional way to image a three-dimensional field is by stacking 2D reconstructions (in x-y plane) at different heights along the z-axis. The problem of reconstructing the 3D field therefore reduces to the reconstruction of a set of 2D fields. This however is not sufficient to reconstruct vector fields where a third out-of-plane component exists.

Although SCV is currently capable of measuring only the two components of velocity that lie in the plane of illumination, there are possibilities for extension to a 3D technique. One method would be to use two light sheets perpendicular to each other, each sheet with its own imaging system. These sheets could then be swept through the flow with images being recorded at each location. Not only would this process eliminate SCVs unsteady capabilities but it also entails a substantial increase in experimental time and cost. Precise alignment of the light sheets is also likely to be a problem.

Since all the rotorcraft experiments at Georgia Tech. are in the low subsonic regime a computational method applicable only to incompressible flows is used. The method is based on the solution of the incompressible continuity equation. A second order finite difference scheme is used to compute the change in third component between successive 2D data planes. One sided difference was used at the edge points and central difference for the interior points. These differentials are then integrated to obtain the third component. The integration requires two boundary planes to be specified with reasonable accuracy.

A pulsed vertical white light sheet is stepped rapidly normal to itself, and several images captured at each location. The two velocity components in the plane of the image are obtained using SCV at several closely spaced locations in the plane. The third component is the velocity component perpendicular to these 2D data planes. The continuity equation applied at each of these points yields the differential change in the third component from one plane to the next. Integrating these differentials yields the third velocity component in the entire volume. To integrate the continuity equation using a first order difference scheme, one boundary plane wherein all three velocity components are known is required. For a second order scheme two such adjacent boundary planes are required. We propose to obtain this boundary data by stepping the light sheet horizontally in the farfield where the velocity gradients are relatively less or stepping it out vertically to a wall which forces the component perpendicular to the wall to be zero at the wall. This data along with the 2D

planar velocity data is fed into the TVC (third velocity component) solver to obtain the azimuth resolved 3D velocity field.

### **Third Velocity Component solver**

Since our primary interest is in low-speed air flows, we use a method for the computation of the third velocity component based on satisfying the continuity equation. A second order TVC (Third Velocity Component) solver has been developed. The solver steps across the flow, starting from two boundary planes where the component of velocity normal to the plane is known (usually zero or constant), so that all components and their gradients can be specified in these planes. In the wind tunnel this is done simply by going away from the rotor wake region and, where necessary, going near the tunnel walls.

### **Test Case for 3-D Reconstruction: Rotating Flow Above a Ground Plane**

A test case of rotating flow interacting with ground was chosen to validate the TVC algorithm. This problem is one of the few 3D flows with an exact solution to the Navier-Stokes equation. It was chosen because the flow contains some of the elements of a helicopter ground effect flow, though the axial flow is in the opposite direction. Also missing are the strong tip vortices and vortex sheets. However, we do have a swirling flow, a rapidly varying axial velocity profile and a large radial variation near the ground plane. Fluid at large distances from the ground is in equilibrium under the influence of centrifugal force and radial pressure gradient and is assumed to rotate like a rigid body. In the boundary layer, viscous forces attenuate the outward centrifugal force and there is a radial inflow as shown in the schematic in Fig. 12. The secondary flow upwards ensures that continuity is satisfied.

The Navier-Stokes equations in cylindrical coordinates are used to analyze this problem. For an axially symmetric flow these equations are as follows.

$$\frac{\partial u}{\partial r} + \frac{u}{r} + \frac{\partial w}{\partial z} = 0 \quad (1)$$

$$u \frac{\partial u}{\partial r} + w \frac{\partial u}{\partial z} - \frac{v^2}{r} = -\frac{1}{\rho} \frac{\partial p}{\partial r} + \nu \left[ \frac{\partial^2 u}{\partial r^2} + \frac{\partial}{\partial r} \left( \frac{u}{r} \right) + \frac{\partial^2 u}{\partial z^2} \right] \quad (2)$$

$$u \frac{\partial v}{\partial r} + w \frac{\partial v}{\partial z} - \frac{uv}{r} = \nu \left[ \frac{\partial^2 v}{\partial r^2} + \frac{\partial}{\partial r} \left( \frac{v}{r} \right) + \frac{\partial^2 v}{\partial z^2} \right] \quad (3)$$

$$u \frac{\partial w}{\partial r} + w \frac{\partial w}{\partial z} = -\frac{1}{\rho} \frac{\partial p}{\partial z} + \nu \left[ \frac{\partial^2 w}{\partial r^2} + \frac{1}{r} \frac{\partial w}{\partial r} + \frac{\partial^2 w}{\partial z^2} \right] \quad (4)$$

The boundary conditions are:

$$z=0: u=0; v=0; w=0 \quad \text{and} \quad z=\infty: u=0; v=r \omega$$

where  $u$  is the radial velocity,  $v$  is the tangential velocity and  $w$  is the axial velocity. At large distances from the ground the flow is rotating at a constant angular velocity  $\omega$ . Introducing the dimensionless coordinate  $\zeta = z \sqrt{\frac{\omega}{\nu}}$  and assuming that the velocity components have the form:  $u = r\omega F(\zeta)$ ;  $v = r\omega G(\zeta)$ ;  $w = \sqrt{\nu\omega} H(\zeta)$ , we obtain a system of ordinary differential equations given below.

$$\begin{aligned} F^2 - G^2 + HF' - F'' + 1 &= 0 \\ 2GF + HG' - G'' &= 0 \\ 2F + H' &= 0 \end{aligned} \quad (5)$$

with the boundary conditions:

$$\zeta = 0 : F = 0; G = 0; H = 0$$

$$\zeta = \infty : F = 0; G = 1$$

This system of equations was first solved by U.T. Bödewadt[28] in a very laborious way by means of a power series expansion. This was corrected by J.E. Nydahl[29] and it is his solution tabulated in Schlichting[30] that has been used to generate the desired velocity field. The axial velocity component depends only on the distance from the ground.

A Cartesian coordinate system was chosen so that the code is not restricted to cylindrical flows. The velocity components in a plane are given by:

$$\begin{aligned} v_x &= u \cos \theta - v \sin \theta \\ v_y &= u \sin \theta + v \cos \theta \end{aligned} \quad (6)$$

A second order difference was used to discretize the continuity equation -- central difference at all interior points and one sided difference at the boundaries. The third component was calculated using a backward difference scheme. The first order scheme requires one boundary plane to be specified.

$$w_{i,j,k} = w_{i,j,k-1} + \frac{dw}{dz}(z_{i,j,k} - z_{i,j,k-1}) \quad (7)$$

A second order scheme requires two boundary planes as shown below:

$$w_{i,j,k} = \frac{w_{i,j,k-1}(\Delta z_{-2})^2 - w_{i,j,k-2}(\Delta z_{-1})^2 - \frac{dw}{dz}(\Delta z_{-2})(\Delta z_{-1})(\Delta z_{-2-1})}{(\Delta z_{-2})(\Delta z_{-1})(\Delta z_{-2-1})} \quad (8)$$

where

$$\Delta z_{-1} = z_{i,j,k-1} - z_{i,j,k}$$

$$\Delta z_{-2} = z_{i,j,k-2} - z_{i,j,k}$$

$$\Delta z_{-2-1} = z_{i,j,k-2} - z_{i,j,k-1}$$

### Implementation

The solution from Schlichting[30] was used to generate 27 slices of 2D velocity data (a 41 x 31 grid of radial and azimuthal velocity components) parallel to the ground. The 3D vector field obtained from this solution in two planes parallel to the ground is shown in Fig. 13. For testing the TVC solver only two components were taken from the known solution and the third was computed. The farfield angular velocity specified was 1050 RPM. The distances are non-dimensionalized by the square root of the ratio of kinematic viscosity to the farfield angular velocity. The normalizing factor for the axial velocity component is the square root of their product. The radial and tangential components are normalized by the angular velocity in the farfield at the same radial station. The axial velocity (perpendicular to the ground) varies only with distance from the ground. Hence the plots shown for the reconstructed axial velocity are one dimensional - the x-axis being height from the ground and the y-axis being the axial velocity averaged at all grid points at the same height. The non-dimensionalized radial and tangential components are also functions of only distance from the ground.

### *Boundary Conditions*

A comparison of the exact and calculated axial velocity component at varying distances from the ground is shown in Fig. 14. Fig. 14(a) shows the comparison with two boundary planes specified at the ground. The solid line denotes the solution obtained by numerically solving the Navier-Stokes equations. The dotted line is the axial velocity profile obtained using a second order finite difference scheme with two boundary planes specified.

When the two boundary planes are chosen in the farfield, there is a very good match with the exact solution except for a small region near the ground where the gradient in the axial velocity profile is steep as seen in Fig. 14(b). Therefore better reconstructions are obtained by specifying boundary conditions in regions of relatively low gradient in the third component. In order to check the applicability of the method to the reconstruction of any component of the flow the radial and tangential velocities were reconstructed from 2D data planes of the other two components. A comparison of the exact and calculated profiles is shown in Fig. 15.

### *Addition of random noise*

In the earlier comparisons the two inplane components were exact values. To simulate experimental data, random noise upto 30% of the exact values was added to the radial and tangential components. The resulting axial velocity profile closely matches the zero noise solution. The SCV technique itself is quite robust to experimental noise. Although the presence of noise reduces the maximum correlation coefficient between the two images its position (which determines the vector) remains largely unaltered.

It was found that adding as much as 25% random measurement noise to the data still gives good reconstruction for both the nearfield (Fig. 16(a)) as well as farfield (Fig. 16(b)) boundary cases. This is a reasonable level of accuracy for experimental data even without phase averaging. This shows the robustness of the method in handling experimental error in the measurement of the inplane components. However the accuracy of the two component velocity data and the boundary data planes is critical for accurate 3D reconstructions. The table shows the non-dimensionalized RMS. (root mean square) of the deviation from the exact solution for the farfield boundary planes case. The third column shows this RMS. error as a percentage of the non-dimensionalized farfield axial velocity (1.3494). Noise levels were gradually increased from 0 to 30% but the RMS. error remained within 5% of the farfield axial velocity. Thus the TVC solver can handle substantial levels of experimental noise in the two-component velocity data.

Random noise added	RMS. error	Percentage error
0%	0.02628	1.95%
5%	0.02702	2.00%
10%	0.02857	2.12%
15%	0.03080	2.28%
20%	0.03358	2.49%
25%	0.03678	2.72%
30%	0.04030	2.99%
35%	0.04408	3.27%
40%	0.04803	3.56%
45%	0.05214	3.86%
50%	0.05636	4.18%

### *Interpolation*

When experimental data is used with the TVC solver, interpolation routines become a necessity. In regions where experimental data is not available or not reliable, in-plane velocities can be interpolated. The computation of the third component involves computing velocity gradients from velocity values at surrounding grid points. Therefore even a single data value missing at one grid location stalls the solution process. Interpolation is also required between planes to increase the resolution of the 2D velocity data in parallel planes. A second order interpolation scheme is required since a first order interpolation scheme would only enhance the error in the second order finite difference scheme being used. Second order polynomial interpolation was chosen as the most suitable.

## **7. CONCLUSIONS**

Tomographic techniques for reconstruction of flowfields have been studied. A test case of a uniform density field showed the computational efficiency and accuracy of the Filtered Back Projection algorithm. It was found that for a well balanced reconstruction the number of projections should be roughly equal to the number of sampling points per projection. As a first step in the reconstruction of vector fields a finite differencing technique which reconstructs a periodic 3D vector field from 2D planar velocity field projections has been developed. This 3D technique was validated using a test case of swirling flow near a ground, a known velocity field. The results demonstrate the robustness of the method in the presence of upto 25% experimental noise in the measurement of the two inplane velocity components. Spatial Cross-correlation Velocimetry is used to obtain this inplane 2D velocity data. This planar velocity technique has been successfully employed for large area velocity measurements in 3D periodic flows using both laser and white light sheets. A white light sheet illumination system developed under this project has led to the application of large-area velocimetry to the flowfield of a fan, as well as to large-scale rotorcraft flowfields in industrial and government test facilities.



## 8. REFERENCES

- 1) Sato and Shiraki, 'Tomographic observation of flow in a water tank,' Journal of Acoustical Society of America, Vol.76, No.5, Nov. 1984
- 2) Komissaruk, Mende and Popov, 'Tomographic study of a supersonic object in free flight', SPIE Vol.1843, 1991
- 3) Liu, Merzkich and Oberste-Lehn, 'Optical tomography applied to speckle photographic measurement of asymmetric flows with variable density,' Experiments in Fluids, 1989
- 4) Hesselink and Snyder, 'Three-dimensional tomographic reconstruction of the flow around a revolving helicopter rotorblade; A numerical simulation', Proceedings of the Third International Symposium on Flow Visualization, Ann Arbor, Michigan, Sept. 1983.
- 5) Stephen J. Norton, 'Tomographic reconstruction of 2-D vector fields: application to flow imaging,' Geophysical Journal, Vol.97, 1988.
- 6) Stephan J. Norton, 'Unique tomographic reconstruction of vector fields using boundary data,' IEEE Transactions in Image Processing, Vol. 1, 1992.
- 7) Braun and Hauck, 'Tomographic Reconstruction of Vector Fields', IEEE Transactions On Signal Processing, Vol.39, No.2,1991
- 8) Winters and Rouseff, 'Tomographic reconstruction of stratified fluid flow,' IEEE Transactions On Ultrasonics, Ferroelectrics And Frequency Control, Vol.40, No. 1, 1993.
- 9) Jerry L. Prince, 'Tomographic reconstruction of 3D vector fields using inner product probes', IEEE Transactions On Image Processing, Vol.3, No.2,1994.
- 10) Jerry L. Prince, 'A convolution backprojection formula for three-dimensional vector tomography,' IEEE International Conference On Image Processing, Vol.2,1994.
- 11) Meng and Hussain, 'Holographic particle velocimetry: a 3D measurement technique for vortex interactions, coherent structures and turbulence,' Fluid Dynamics Research, Vol.8, 1991.
- 12) Huang, Slepicka and Cha, 'Cross-correlation of three-dimensional images for three-dimensional three-component fluid velocity measurements,' SPIE, Vol. 2005, 1993.
- 13) Reddy, U.C., "Tomographic Reconstruction of Flowfields from projections", AIAA Southeastern Regional Student Conference, Decatur, Georgia, April 95.
- 14) Kak and Slaney, Principles of Computerized Tomographic Imaging, Piscataway, NJ: IEEE, 1988
- 15) Baba N. and Murata K., 'Filtering for image reconstruction from projections,' Journal of the Optical Society of America, Vol. 67, 1977.

- 16) Adrian, R.J., Yao, C-S., "Method and Apparatus for Measuring the Displacements of Particle Images for Multiple Exposure Velocimetry" U.S. Patent 4729109
- 17) Reuss, D.L., Adrian, R.J., Ladreth, C.C., "Two-Dimensional Velocity Measurements in a Laminar Flame Using Particle Image Velocimetry", Combustion Science and Technology, October 1989, pp. 73-83.
- 18) Smith, C.A., Lourenco, L.M.M., Krothapalli, A., "The Development of Laser Speckle Velocimetry for the Measurement of Vortical Flow Fields". AIAA 86-0768CP, March 1986.
- 19) Komerath, N.M., and Fawcett, P.A., "Spatial Cross-Correlation Velocimeter" U.S. Patent No. 5,249,238, September 1993.
- 20) Komerath, N.M., Fawcett, P.A., Ballarini, D., "Planar Velocimetry Using Digital Cross-Correlations". Developments in Theoretical and Applied Mechanics, Vol. XV, March 1990, p. 471 - 478.
- 21) Komerath, N.M., and Fawcett, P.A., 'Planar velocimetry by spatial cross correlation: Theoretical basis and validation', AIAA Paper 90-1634, 21st Fluid Dynamics, Plasma Dynamics and Lasers conference, Seattle 1990.
- 22) Fawcett, P.A. and Komerath, N.M., 'Spatial correlation velocimetry in unsteady flows,' AIAA 91-0271, 29th Aerospace sciences meeting, Reno, NV, 1991.
- 23) Fawcett, P.A., Funk, R., Komerath, N.M., "Quantification of Canard and Wing Interactions Using Spatial Correlation Velocimetry". AIAA Paper 92-2687, 10th Applied Aerodynamics Conference, Palo Alto, CA, June 1992.
- 24) Fawcett, P.A., 'An Investigation On Planar Velocimetry By Spatial Cross Correlation,' Ph.D. Thesis, School of Aerospace Engineering, Georgia Institute of Technology, 1992.
- 25) Funk, R.B., 'Transient interaction between a rotor wake and a lifting surface,' Ph.D. Thesis, School of Aerospace Engineering, Georgia Institute of Technology, 1995.
- 26) Griffin, M.H., Funk, R.B. and Komerath, N.M., 'Wind turbulence measurement over large areas using spatial correlation velocimetry', Proceedings of the Silver Symposium of the Society of Test Engineers, Washington DC, Aug. 1994.
- 27) Komerath N.M., Fawcett, P.A., Funk, R.B., Reddy, U.C., "Large-Area Velocity Measurement in Low-Speed Flows", ICIASF, Wright-Patterson AFB, Ohio, 1995.
- 28) Bödewadt, U.T., Die Drehströmung über festem Grund. ZAMM 20, 241-253 (1940).
- 29) Nydahl, J.E., 'Heat transfer for the Bödewadt problem,' Dissertation, Colorado State University, Fort Collins, Colorado 1971.
- 30) Hermann Schlichting, Boundary Layer Theory, McGraw-Hill Book Company, Seventh edition.

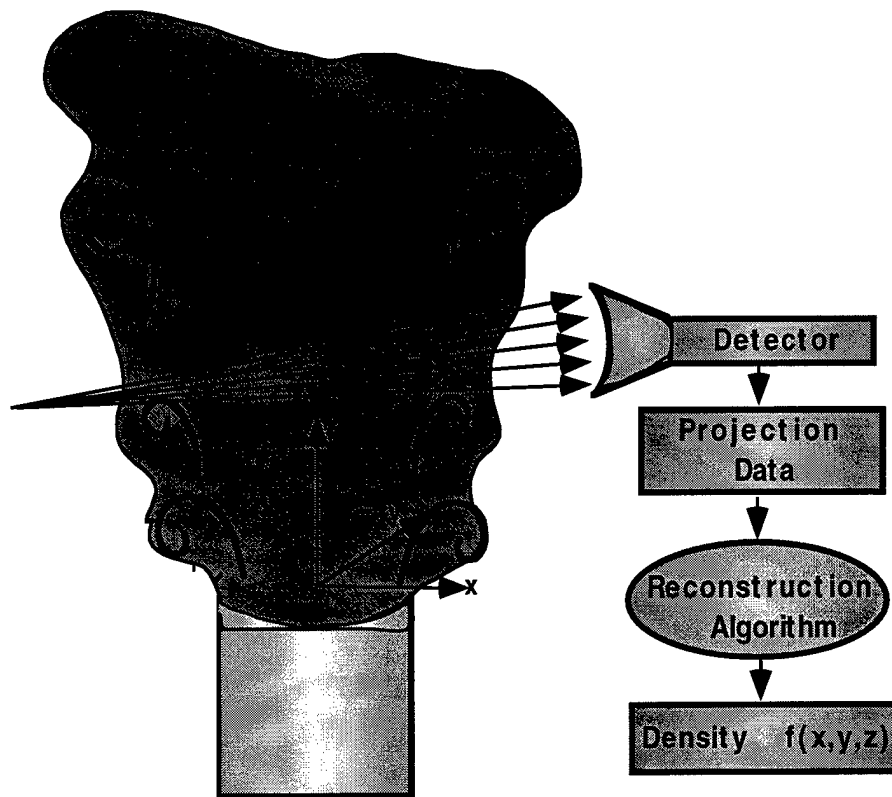


Fig. 1: Tomographic Reconstruction of Flowfields

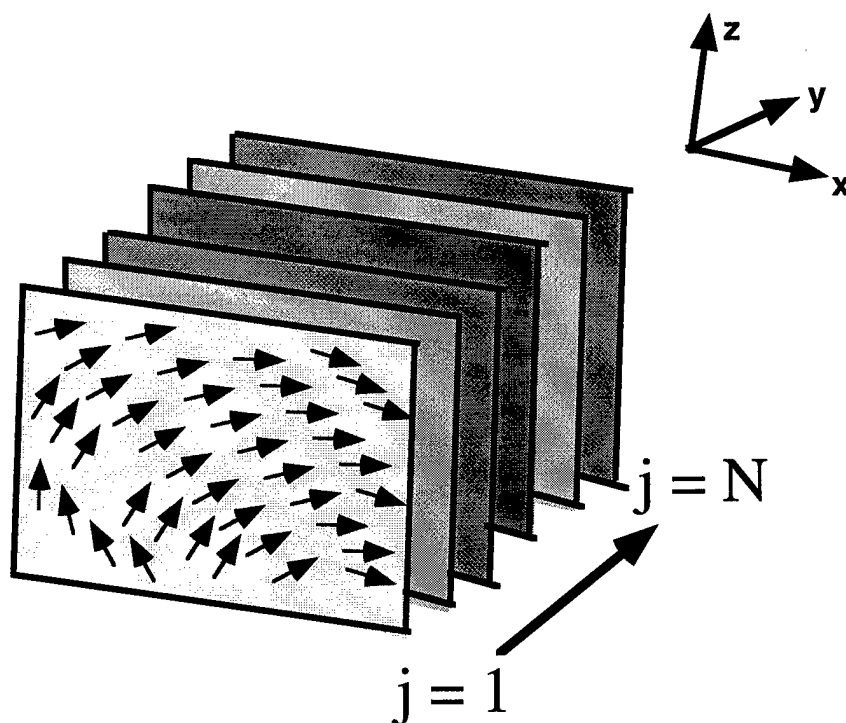


Fig. 2: Scanning multiple planes for 3D reconstruction

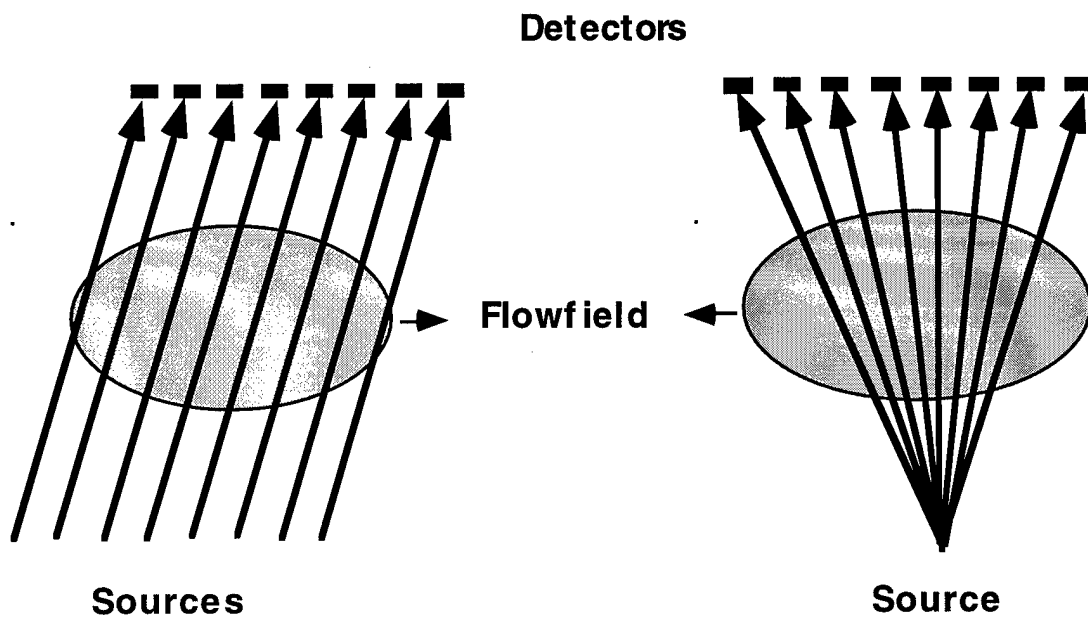


Fig. 3: Parallel beam and Fan beam projections

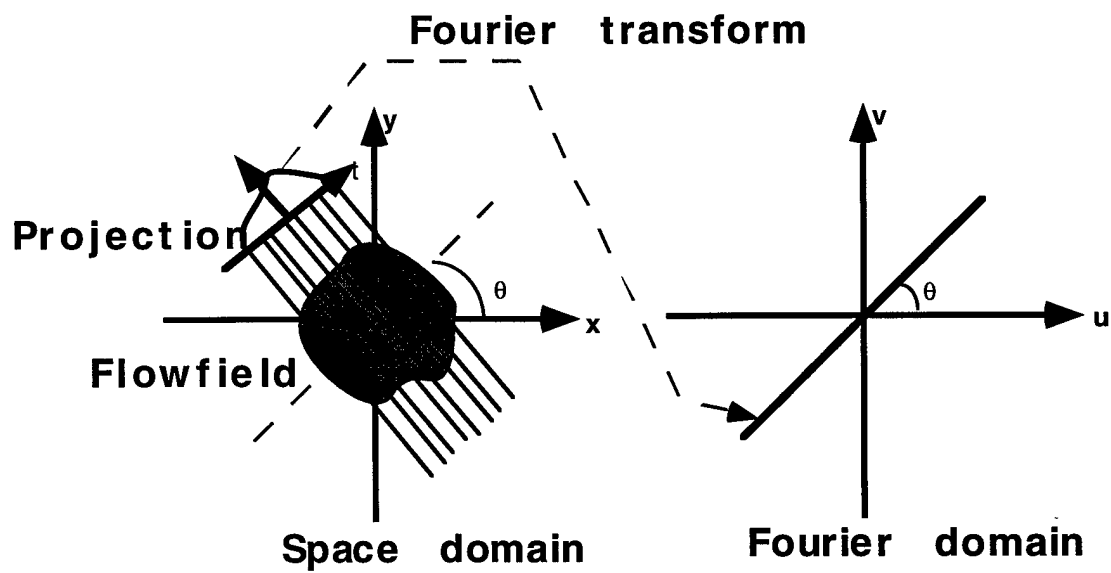


Fig. 4: Fourier Slice Theorem

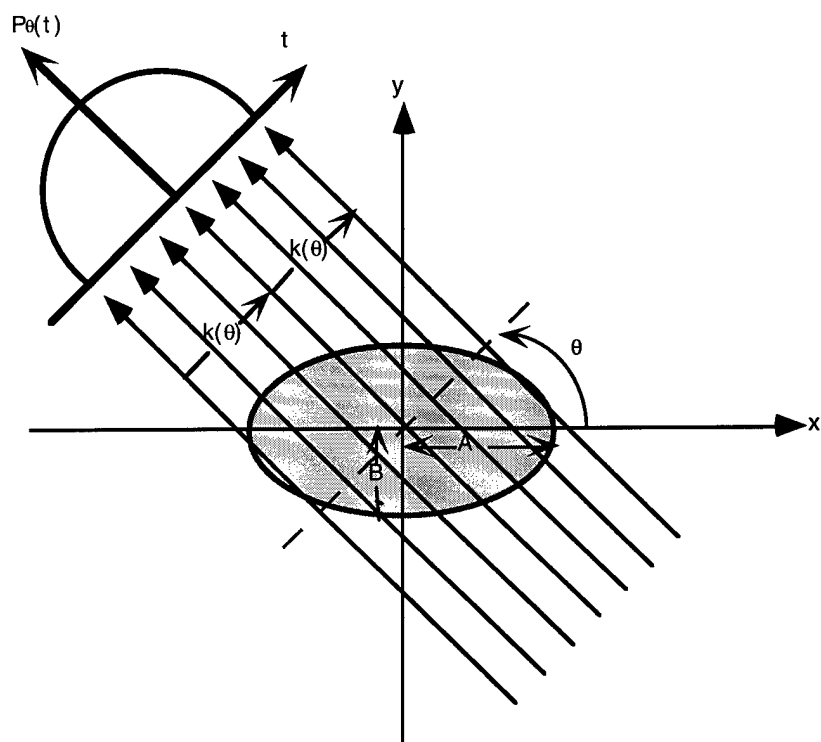


Fig. 5: Reconstruction of a uniform density elliptic field

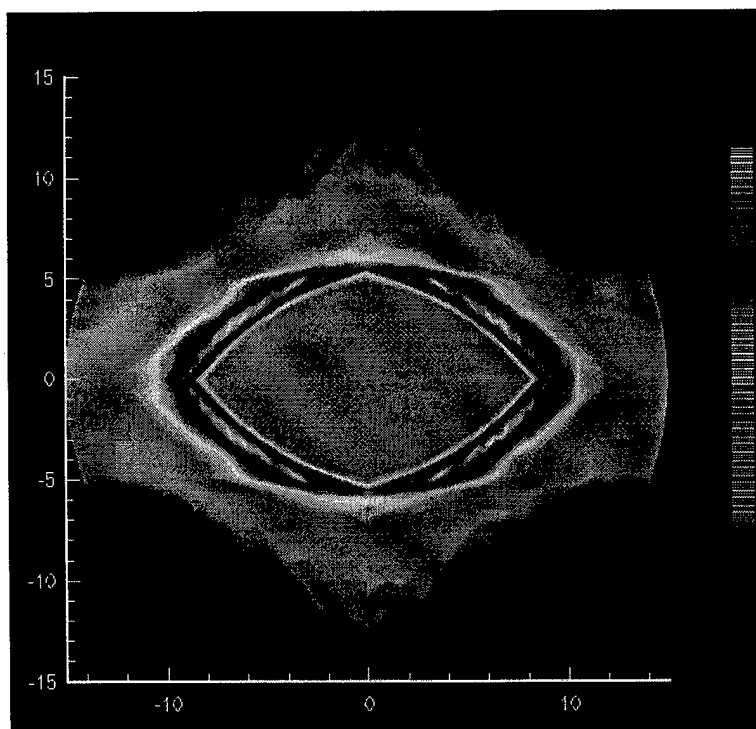


Fig. 6: 64 projections and 64 rays

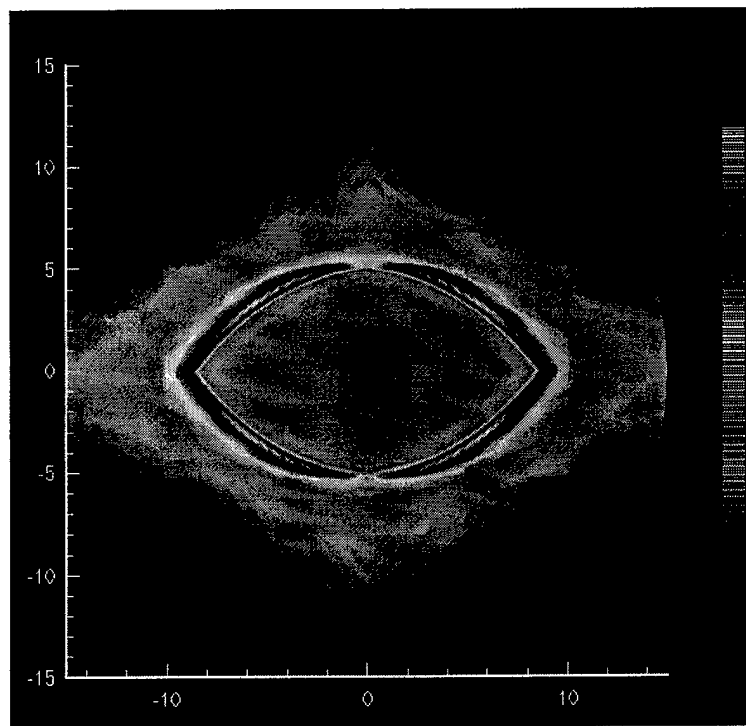


Fig. 7: 128 projections and 128 rays

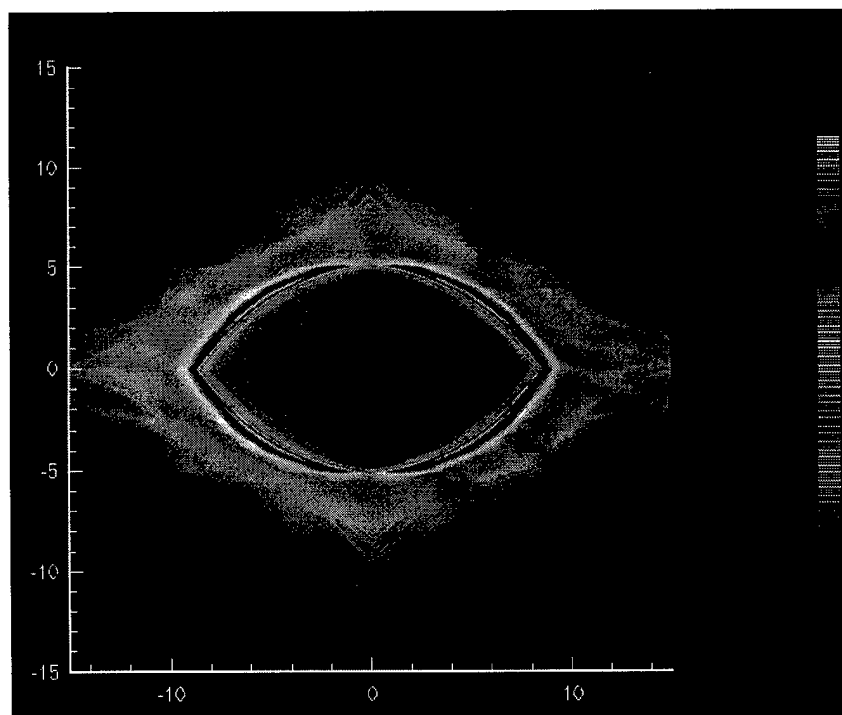


Fig. 8: 256 projections and 256 rays

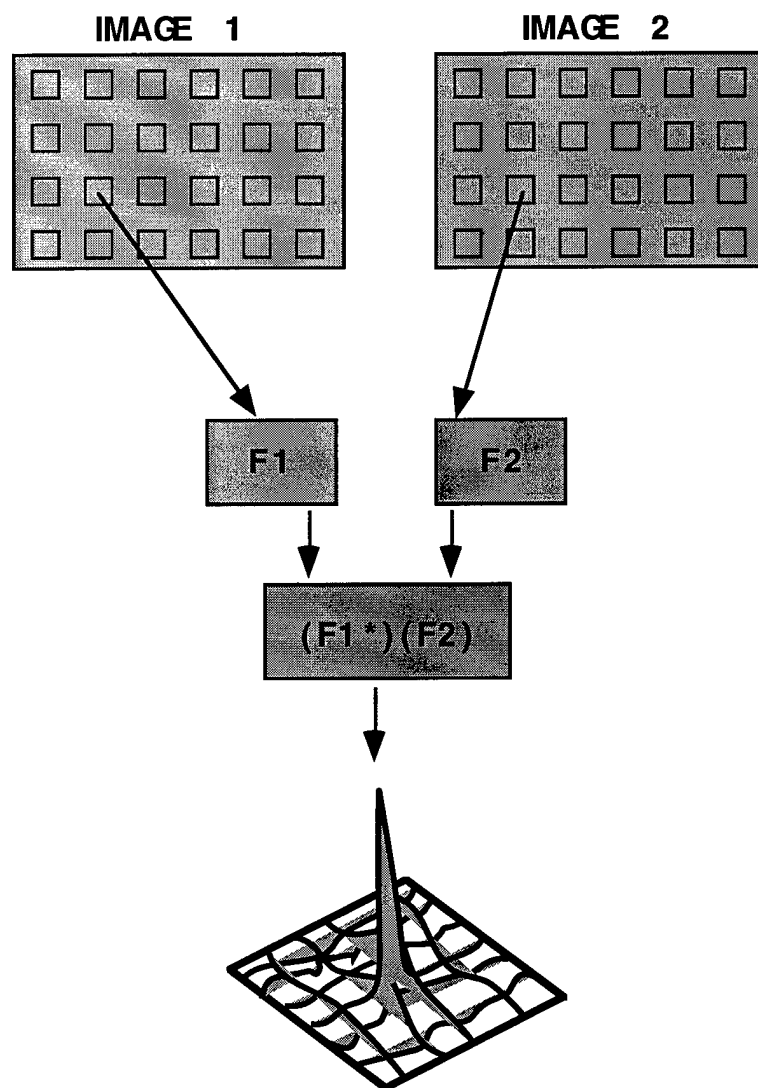


Fig. 9: The SCV technique

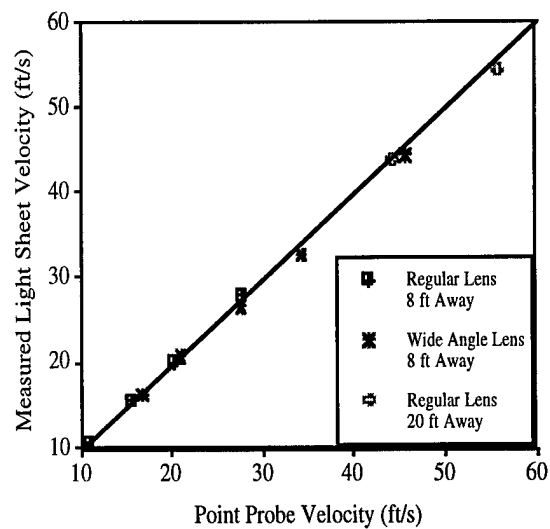
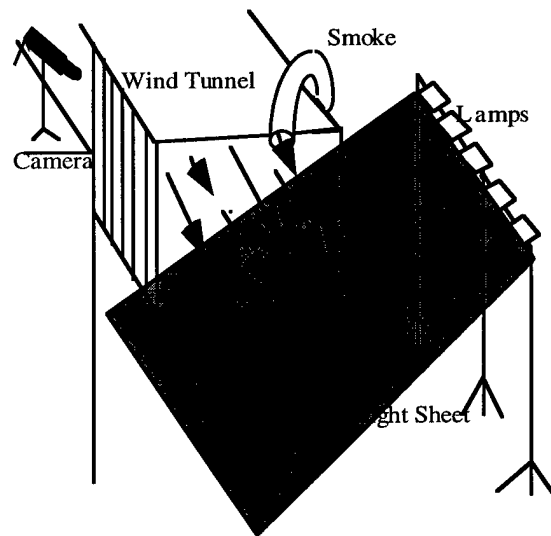


Figure 10: Velocity field at the exit of a 42" x 42" wind tunnel. (a) Configuration (b) Calibration against TSI Velocicalc point velocity sensor. From Griffin, Funk & Komerath [22].



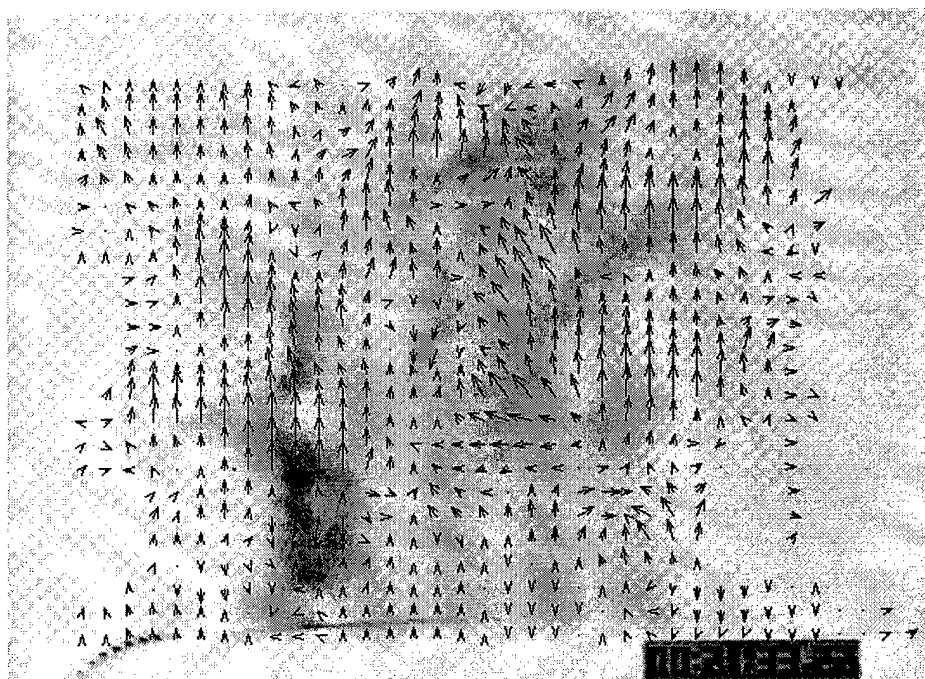


Fig. 11(a)

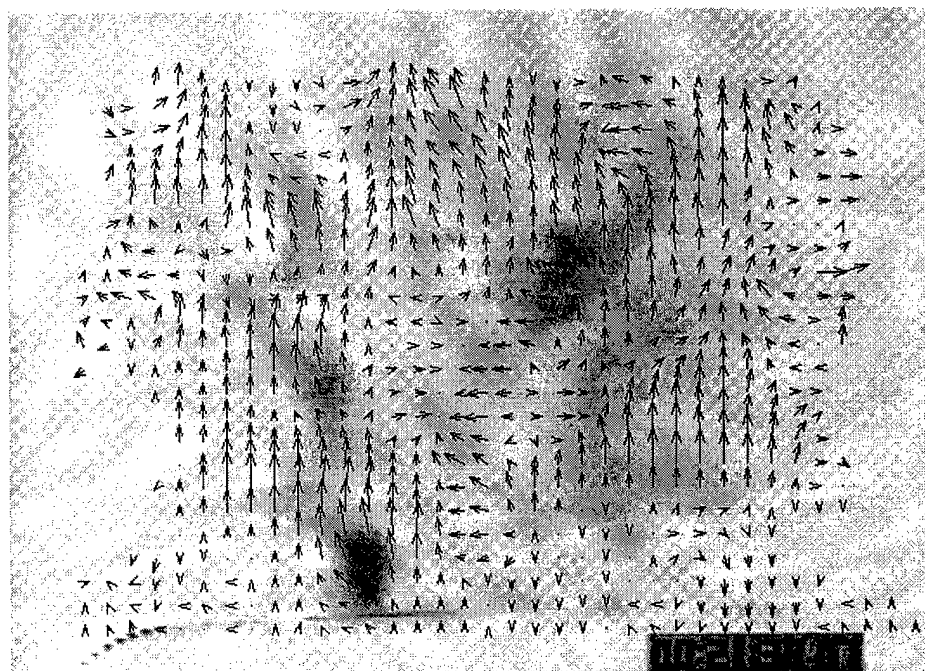


Fig. 11(b)

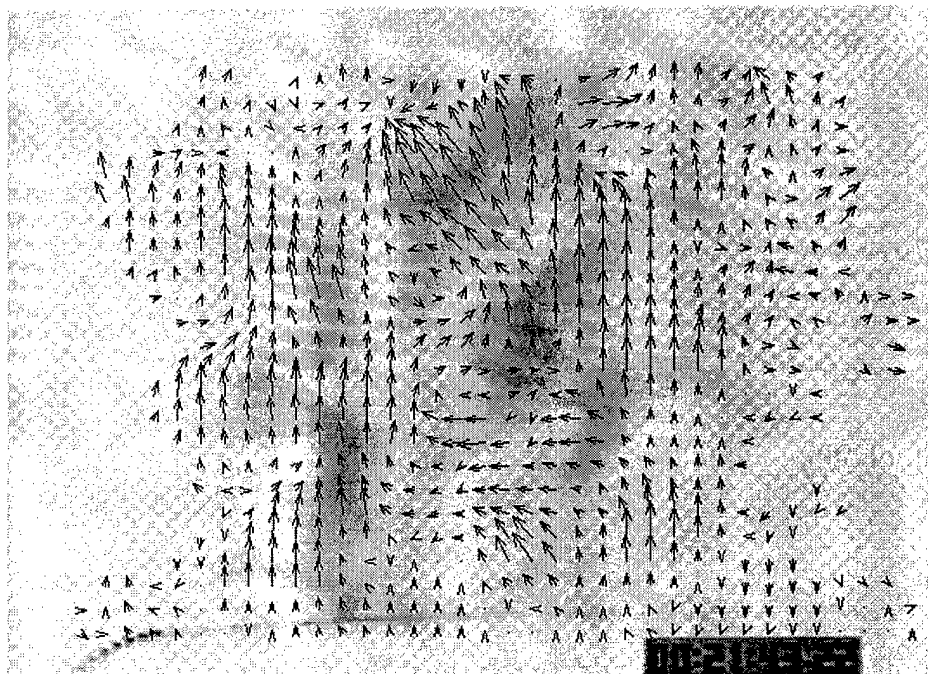


Fig. 11(c)

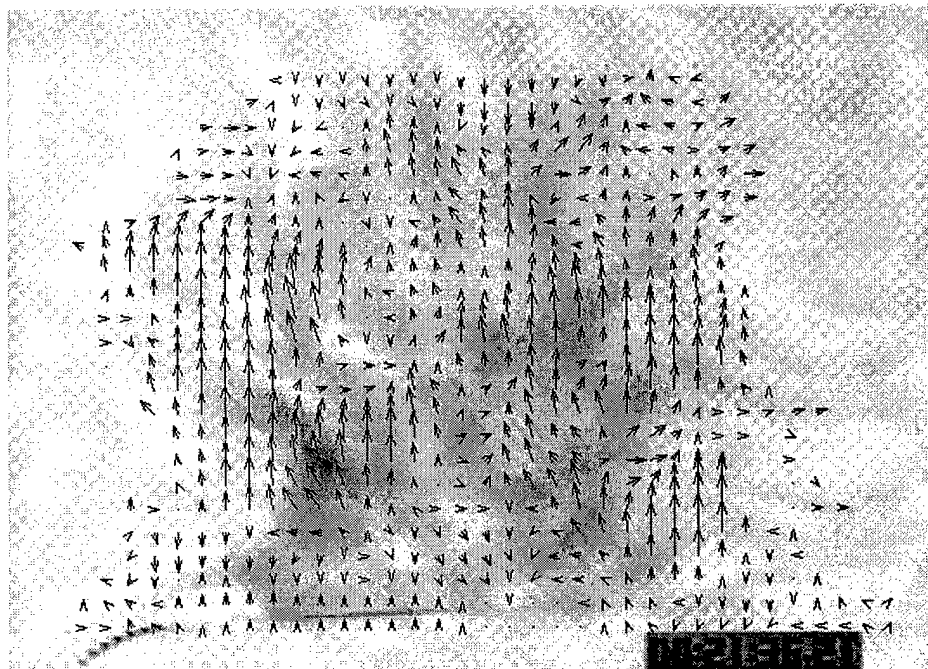


Fig. 11(d)

Fig. 11 : Instantaneous velocity vectors for the isolated rotor configuration at different rotor azimuths

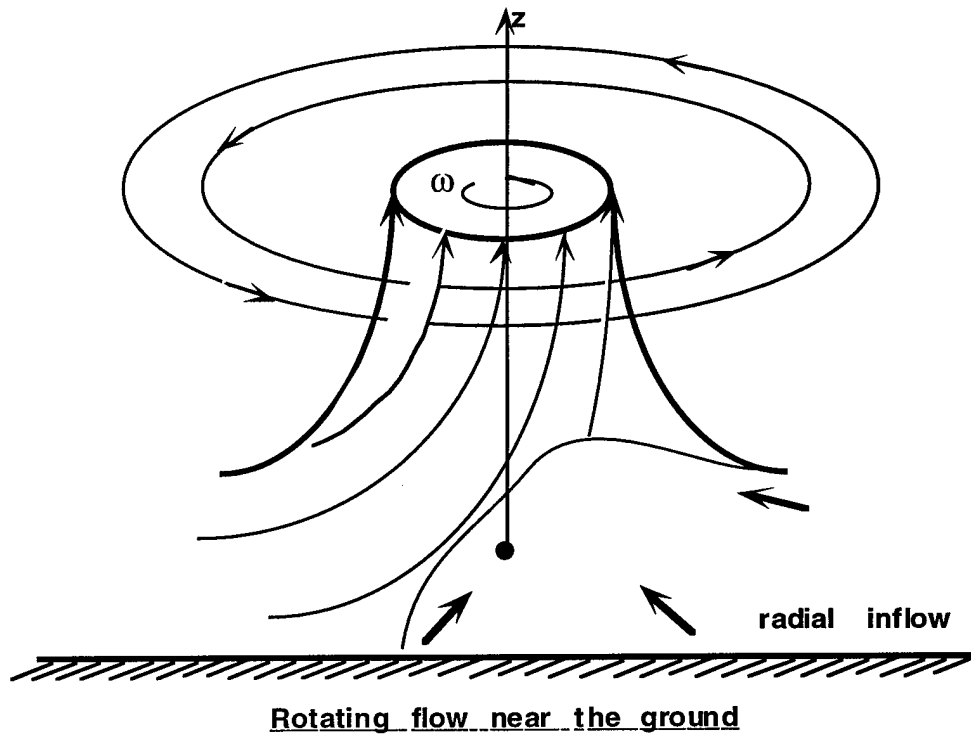


Fig. 12: Swirling flow in the presence of a ground

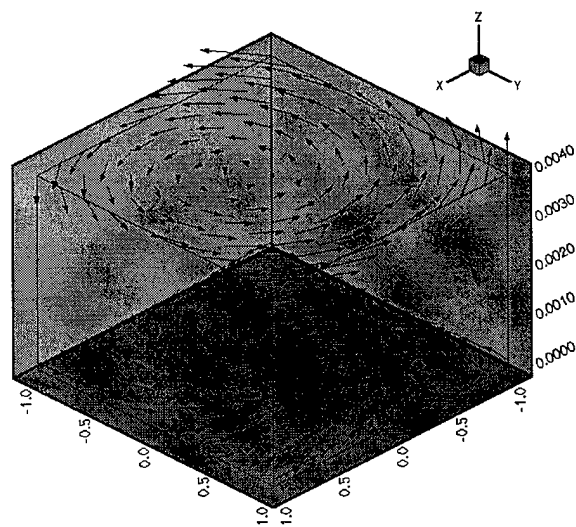


Fig. 13: Vector field in two planes obtained from Navier-Stokes solution

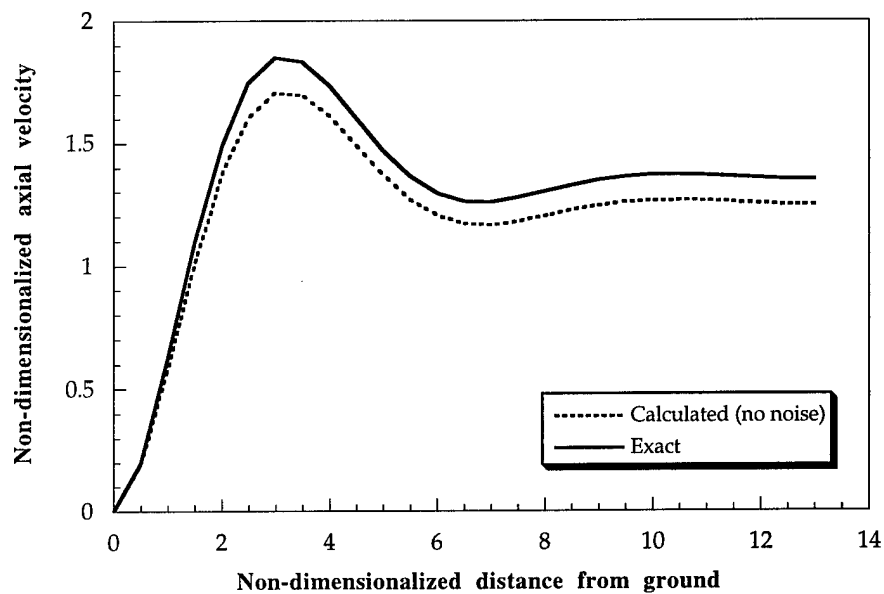


Fig. 14(a): Comparison of exact and calculated axial velocity profile with ground boundary planes specified

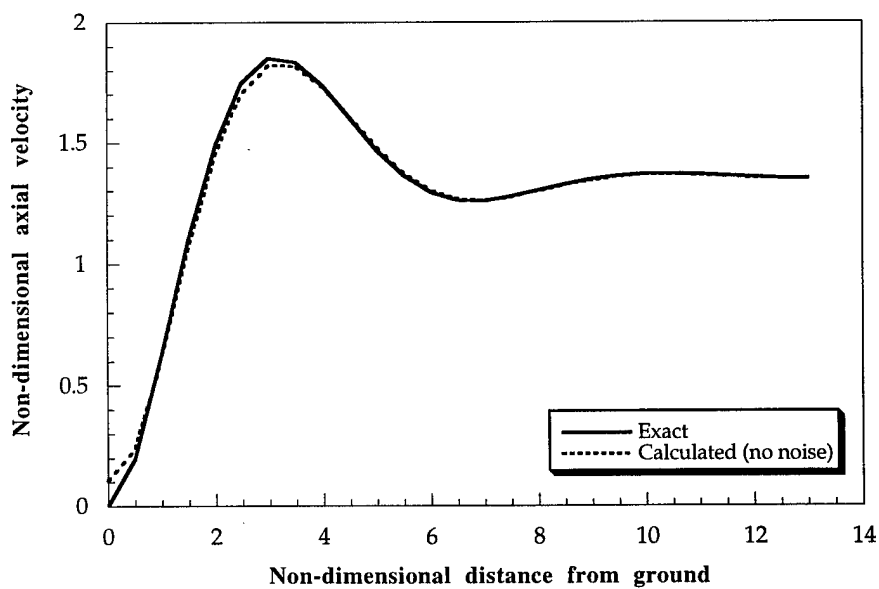


Fig. 14(b): Comparison of exact and calculated axial velocity profile with farfield boundary planes specified

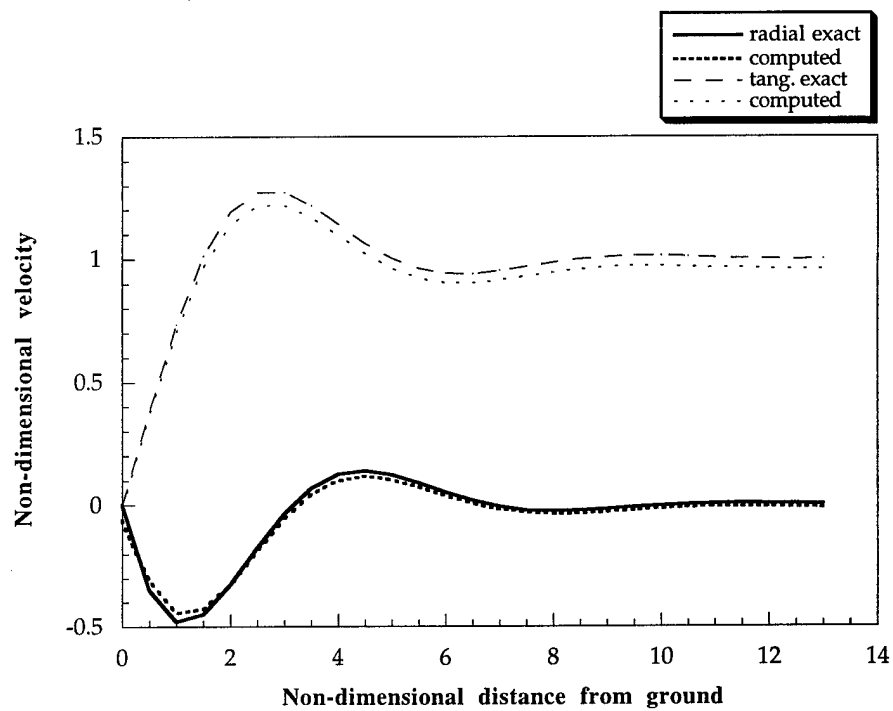


Fig. 15: Radial and Tangential components

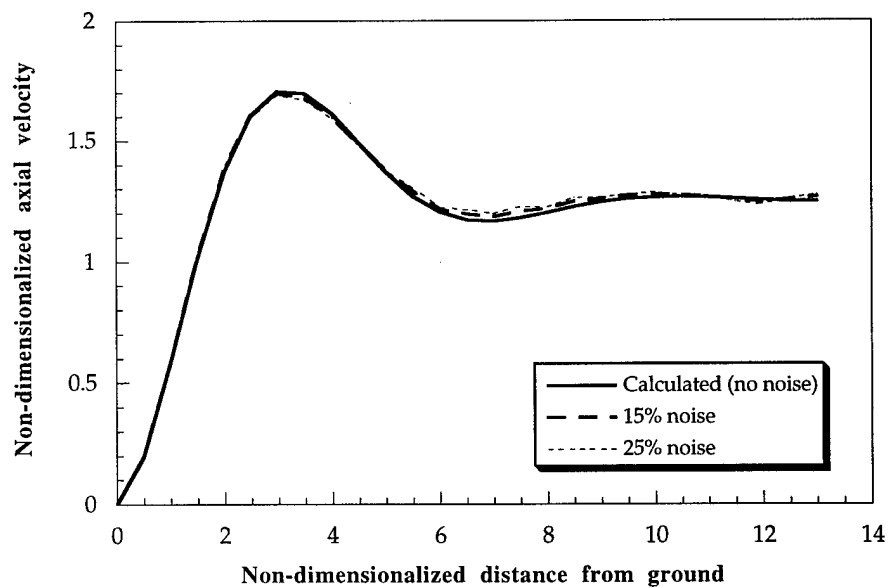


Fig. 16(a): Axial velocity profile with random noise addition using ground boundary planes

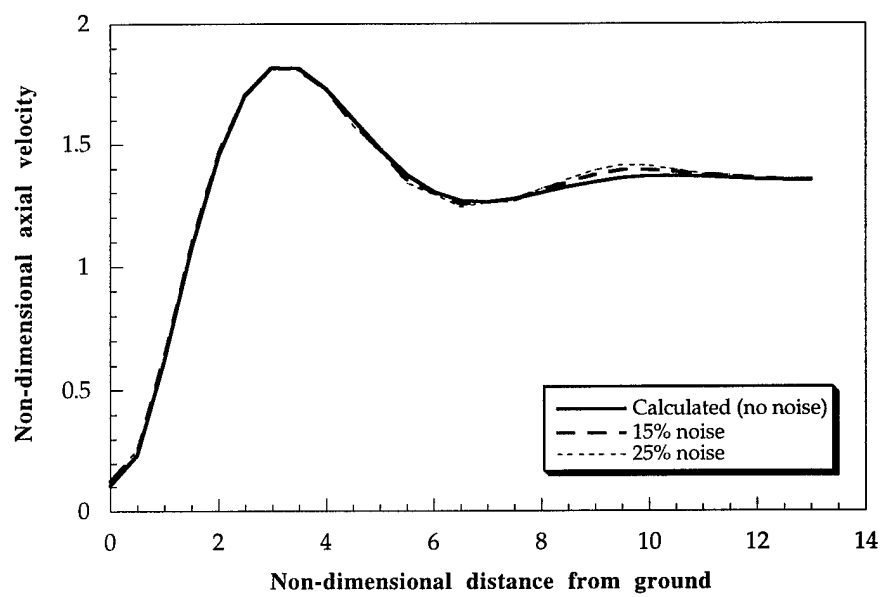


Fig. 16(b): Axial velocity profile with random noise addition using farfield boundary planes

**RSI2. Thin-Walled Composite Beams with Optimum Couplings**  
**Co-PI's: E. Armanios, V. Berdichevsky, D. Hodges, N. Komerath, and M. Kamat**

**Problem Studied**

The primary objective of this research is to enable the implementation of elastic tailoring concepts and take advantage of their benefits in achieving enhanced performance at lower manufacturing and operational costs. To this end, a constrained optimization scheme is developed for obtaining thin-walled closed sections single and two-celled composite beams with optimum extension-twist and bending-twist couplings subject to constraints on natural frequencies and hygrothermal deformation. The optimum designs were verified through manufacturing and testing.

**Final Report:**

This report is an overview of the research performed in this task. It describes the motivation, major accomplishments, the lessons learned and future investigation which stems from its findings.

**Motivation**

The motivation for achieving optimally coupled thin-walled composite beams stems from the additional design flexibility they offer, the reduction in part counts and associated lower manufacturing and maintenance costs as well as increase in performance and life. To this end, three major tasks have been undertaken. The first, is the development of a constrained optimization scheme for obtaining thin-walled composite beams with maximum extension-twist and bending-twist couplings within dynamic, hygrothermal and manufacturing constraints. The second, is the manufacturing of these optimally coupled beams in order to verify their tolerance in meeting the hygrothermal constraints and their response within manufacturing variabilities in material properties and measured mechanical constants. The third, is testing their extension-twist coupling and verifying their optimality.

A detailed description of the optimization scheme, the manufacturing and testing is provided in Appendix which is part of the Ph.D. thesis in Ref. 1.

**Major Accomplishments**

The design of thin-walled, closed section composite beams has been treated in a multidisciplinary approach including analysis, manufacturing and testing.

From the analytical standpoint a gradient based constrained optimization scheme has been developed for obtaining maximum coupling subject to practical design considerations. The stacking sequence for producing the maximum extension-twist coupling of Circumferentially Uniform Stiffness (CUS) single and two-celled beams, and bending-twist coupling in Circumferentially Antisymmetric Stiffness (CAS) single-celled beams have been determined. Constraints have been imposed using the Sequential Unconstrained Minimization Technique. For single-celled cross sections, the hygrothermal deformation of the beam is minimized and the first two natural frequencies of each mode shape are distinct from a single specified frequency. The two-celled beam have been constrained so that only one form of coupling is present.

The sensitivity of the optimum designs to variations in material properties, as determined by test data, and ply angles associated with manufacturing tolerances, has been investigated for both single and two-celled beams. A statistical technique was used to model the variability which might be expected in a manufacturing environment. This provides a practical tool allowing a designer to build factors of safety into a design, or to establish requirements for a manufacturing process.

From the manufacturing and testing stand points, nine different CUS beams have been made in an attempt to verify the optimality of the predicted solutions. Two beams manufactured at the local optimum solution have coupling within 1.6% of the predicted value. Two beams made with stacking sequences perturbed three degrees from the local optimum show the expected changes in coupling. Five beams manufactured at or near the global optimum have coupling that is approximately twenty percent less than predicted, but show the appropriate small decrease in coupling as the stacking sequence is shifted. Beams with both stacking sequences show the expected behavior with regard to hygrothermal twisting curvature.

A simple manufacturing technique for two-celled beams has been developed, and one beam made with a web in the center of its cross section. It has been tested and found to have extension-twist compliance within 6.2 % of the predicted value. The testing for both single and two-celled beams was performed using the custom patent pending apparatus of Ref. 2.

In summary, the analysis, manufacturing and testing performed in this task provides a tool that facilitates design of elastically tailored, thin-walled, closed section beams. A gradient based search algorithm has been shown to work well with the selected beam theory [3] developed under an earlier CERT Grant. It has been shown that, whether in an unconstrained situation or in the face of multiple constraints on structural behavior, certain configurations exist that maximize elastic coupling. These conclusions have been verified with both finite element and experimental techniques.

### **Lessons Learned and Future Investigation**

Among the findings of this research task, a number of lessons have significant implications. The first, is that the hygrothermally constrained optima for the CUS single-celled beam are very close to the unconstrained optima, so that the magnitude of coupling obtained drops only by approximately three percent. In each case of wall thickness varying from two to eight plies, the constrained global solution incorporates two ply angles. A constrained local optimum exists with only one ply angle. The difference in coupling magnitude between these solutions is about ten percent. The second, is the fact that the same stacking sequence that maximizes extension-twist coupling in a CUS beam also maximizes bend-twist coupling in CAS beam because both result from local extension-shear coupling within the beam walls.

The third, is the finding that the coupling and hygrothermal twist show most sensitivity to the shear modulus,  $G_{12}$ , and the transverse Young's modulus,  $E_{22}$ , of the material. Also variations in the thermal and hygroscopic properties of the composite effect the resultant twist without changing the coupling produced. The magnitudes of coupling for both global and local optima are approximately equally sensitive to variability in material properties and ply angles. However, the constrained hygrothermal twisting curvature of the global optimum has 70% more sensitivity. In addition, the simplicity of manufacturing the local solution makes it a desirable configuration. It could be practical in any situation with a combination of constraints and loading that do not prohibit an unidirectional



configuration. Finally, the results of the sensitivity analysis as applied to two-celled beams indicate that the global optimum of extension-twist coupling is insensitive, with a standard deviation approximately one percent of the mean. However, the bending-twist coupling which is constrained by the optimization to be zero, has an extremely high level of sensitivity.

The results achieved in this work points to the need for further inquiries. In the experimental category, one area is the manufacturing of several two-celled beams to verify the optimality of the predicted stacking sequence. More development of the manufacturing technique and investigation of configurations with off-center web are needed. Further investigation of two-celled solutions is warranted. Stacking sequences representing local optima should be investigated for sensitivity of the constrained forms of coupling. Also, other configurations may be found that are easily manufactured and lower levels of sensitivity than the configuration of two independent cells with overwrap that is considered in this work. Testing of dynamic characteristics of the single-celled beams to verify the theory and finite element results presented in the literature is necessary before the natural frequency constrained optimization presented in this work can be applied with confidence. An effort towards developing an efficient prediction methodology for natural frequencies and mode shapes for thin-walled closed composite beams was undertaken in Ref. 4.

In the area of optimization, it would be a straightforward process to include additional constraints such as strength, stiffness, and buckling load. Achieving a specified level of torsional rigidity is a practical design issue for implementation of extension-twist coupling in rotor blade design, where a lower bound on torsional rigidity is required to maintain aeroelastic stability. This could be included in the optimization scheme either as a constrain requiring the level of torsional rigidity to be above a specified value, or by reformulating the objective function to maximize the ratio of coupling compliance to torsional compliance. The need for preserving a lower bound on torsional stiffness in order to achieve acceptable stability characteristic was highlighted in Ref. 5. This issue was discussed with Dr. Mark Nixon.

The effect of damage on the coupling properties of the beams should be investigated. This is key in practical implementation since demonstration of damage tolerance is required, particularly so for an airfoil relying on coupling for performance. Finally, relaxing the thin-walled assumptions and the inclusion of sandwich and hybrid constructions is a much needed extension. A finite element discretization of the cross section has been developed in the VABS code [6]. A parallel effort should be undertaken in order to develop a simplified model suitable for constrained optimization where a large number of configurations need to be evaluated quickly and economically.

## References

- [1] Lentz, K. W., " Optimum Coupling in Thin-Walled, Closed Section Composite Beams," Ph. D. Thesis, School of Aerospace Engineering, Georgia Institute of Technology, February 1997.
- [2] Armanios, E. A. and Hooke, D. A., "Rotational Displacement Apparatus with Ultra-low Torque and High Thrust Capability," Patent Pending, US Patent and Trademark Office Serial No. 08/562,586.
- [3] Berdichevsky, V., Armanios, E. A. and Badir, A., "Theory of Anisotropic Thin-walled Closed-cross-section Beams," *Composites Engineering*, Vol. 2, Nos. 5-7, pp. 411-432, 1992.

[4] Dancila, D. and Armanios, E., "The Influence of Coupling in the Free Vibration of Thin-Walled Closed-Section Beams," *36th AIAA/ASME/ASCE/AHS/ASC Structures, Structural Dynamics and Materials (SDM) Conference*, New Orleans, LA, Part 4, AIAA-95-1411-CP, pp. 2106-2115.

[5] Nixon, M. W., "Aeroelastic Response and Stability of Tiltrotors with Elastically-Coupled Composite Rotor Blades," Ph. D. Thesis, Department of Aerospace Engineering, University of Maryland, 1993.

[6] Cesnik, Carlos E. S.; and Hodges, Dewey H., "VABS: A New Concept for Composite Rotor Blade Cross-Sectional Modeling," *Journal of the American Helicopter Society*, vol. 42, no. 1, Jan. 1997, pp. 27 - 38.

### **External Interactions**

The optimization scheme and results have been discussed with Dr. Mark Nixon at ARL, NASA Langley. The constrained optimization scheme developed in this work is ideally suited for meeting a lower bound on torsional rigidity. An increase in torsional stiffness was recommended in Mark Nixon's Ph.D. work for acceptable stability characteristics. The optimum configurations obtained in this work indicate a potential for achieving rotor blade sections with increased torsional stiffness.

### **Publications During the Grant Period:**

#### **Refereed journals:**

Armanios, E. A., and Badir, A. M., "Free Vibration Analysis of Anisotropic Thin-Walled Closed-Section Beams," *AIAA Journal*, Vol. 33, No. 9, September, 1995.

Hooke, D. A. and Armanios, E. A. "Design and Evaluation of Three Methods for Testing Extension-twist-Coupled Laminates," *Composite Materials: Testing and Design* (Twelfth Volume) ASTM STP 1274, C. R. Saff and R. B. Deo, Eds. American Society for Testing and Materials, 1996, pp. 340-357.

#### **Meeting Papers:**

Dancila, D. and Armanios, E., "The Influence of Coupling in the Free Vibration of Thin-Walled Closed-Section Beams," *36th AIAA/ASME/ASCE/AHS/ASC Structures, Structural Dynamics and Materials (SDM) Conference*, New Orleans, LA, Part 4, AIAA-95-1411-CP, pp. 2106-2115.

Armanios, E. A., Kamat, M. P., and Lentz, W. K., "Optimum Coupling in Composite Thin-Walled Closed Section Beams," *COMPOSITES '95 : Recent Advances in Japan and the United States*, I. Kimpara, H. Miyairi & N. Takeda, Ed., *Proc. Japan -U.S. CCM-VII*, pp. 683-691.

Lentz, W. K. and Armanios, E. A., "Constrained Optimization of Thin-Walled Composite Beams with Coupling," *37th AIAA/ASME/ASCE/AHS/ASC Structures, Structural Dynamics and Materials (SDM) Conference*, Salt Lake City, UT, Part 4, AIAA-96-1582, pp. 2326-2334.

**Ph.D. Thesis:**

Hooke, D. A., " Design and Evaluation of Test Apparatuses and Methods for Extension-Twist Coupled laminates," Ph. D. Thesis, School of Aerospace Engineering, Georgia Institute of Technology, October 1996.

Lentz, K. W., " Optimum Coupling in Thin-Walled, Closed Section Composite Beams," Ph. D. Thesis, School of Aerospace Engineering, Georgia Institute of Technology, February 1997.

**Master's Special Problem:**

Charlotte, Marshall, " Alternate Method for Determining the Coefficient of Thermal Expansion," School of Aerospace Engineering, Georgia Institute of Technology, March 1996.

**Undergraduate Special Problem:**

Melitas, Nicholas, " A New Method for Measuring Thermal Expansion Coefficients in Composites," School of Aerospace Engineering, Georgia Institute of Technology, November 1996.

## **APPENDIX**

# **Optimum Coupling in Thin-Walled, Closed Section Composite Beams**

A Thesis Presented to  
the Academic Faculty

by

W. Karl Lentz

Advised by Dr. Erian A. Armanios

In Partial Fulfillment of the Requirements for the Degree  
Doctor of Philosophy

School of Aerospace Engineering  
Georgia Institute of Technology  
February 1997

# Chapter 1 - Introduction & Previous Work

---

## 1.1 Introduction

Elastically tailored thin-walled laminated composites provide flexibility to meet design requirements efficiently. Coupling between deformation modes such as extension-twist, bending-twist, extension-flap bending, extension-sweep bending, and flap-sweep bending is created by an appropriate selection of fiber orientation, stacking sequence, materials, and geometric parameters. These mechanical couplings can be tailored to produce favorable static and dynamic response.

Elastically tailored composites have many diverse applications. In the field of aeronautics, forward swept wings such as those of the X-29 utilize bending-twist coupling to help in preventing divergence. Extension-twist coupling may be used to enhance aeroelastic stability and improve aerodynamic efficiency of rotors on helicopters or tilt-rotor aircraft. Thermal sensitivities in conjunction with elastic coupling may be used to control the angle of attack of fan or turbine blades. In the field of recreational equipment, bending-twist coupling can be used to control the feel of a golf club and to enhance the size and location of the sweet spot of a tennis racket.

The mechanism which produces both extension-twist and bending-twist elastic couplings in thin-walled beams is local extension-shear coupling in the wall. This coupling occurs because of the anisotropy of the material. Consider an orthotropic laminate with the principal axes of the material ( $1,2$ ) at an angle with respect to the axes of the laminate ( $x,y$ ), as is shown in Figure 1.1. The fine lines indicate the fiber orientation. Applying a tensile load,  $F$ , to the laminate will produce a shearing motion, as

illustrated by the dashed lines in the figure. If a beam is constructed from walls having this tension-shear coupling property, then the beam will also have coupling properties.

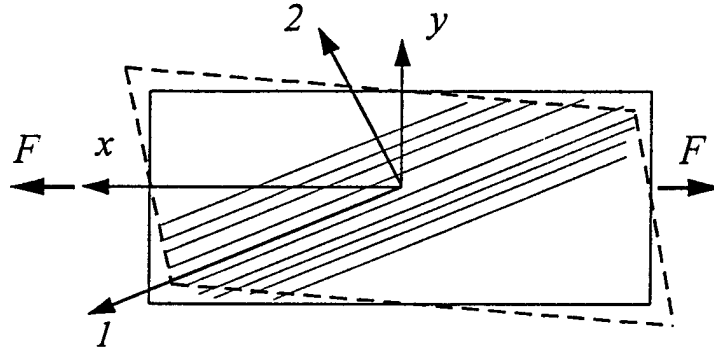


Figure 1.1: Illustration of Tension-Shear Coupling in a Laminate.

For a given closed cross section, extension-twist coupling can be created by a layup which provides a Circumferentially Uniform Stiffness (CUS). Such a configuration is achieved by wrapping the composite layup using a winding technique, and is illustrated in Figure 1.2. Again in this figure, the fine lines indicate the fiber orientation. Application of the tensile load,  $T$ , causes each wall of the beam to try to deform in shear as did the laminate in Figure 1.1. The net result on the beam is a twisting deformation distributed along the length of the beam, denoted by  $\phi$ .

Bending-twist coupling is created by a Circumferentially Antisymmetric Stiffness (CAS) layup. A CAS beam has a  $(+\theta_i)$  layup on one side of the cross section mid-plane, and  $(-\theta_i)$  on the other side, as illustrated in Figure 1.3. Application of the bending moment,  $M$ , causes the top half of the beam to be in tension and the bottom half in compression. The laminates forming the walls experience a shear deformation in

response to the loading, and the resultant beam deformation is a twist. It should be noted that this definition of the CAS configuration is slightly different from that presented in earlier work. This definition is correct at the ply level: each ply changes angle at the mid-plane. The previous definition was more practical from a manufacturing point of view and maintained the antisymmetry about the mid-plane at the level of reduced beam stiffnesses.

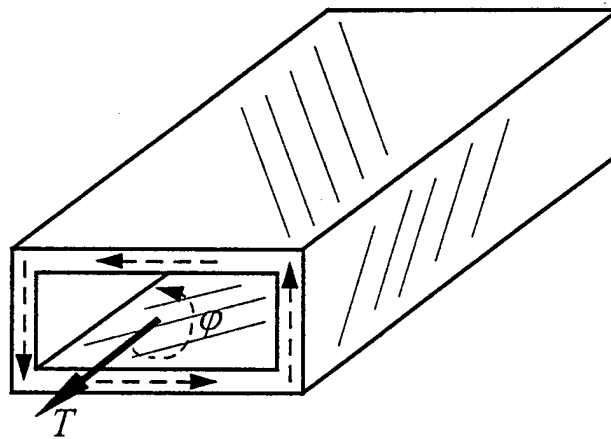


Figure 1.2: Illustration of Extension-Twist Coupling in CUS Beam.

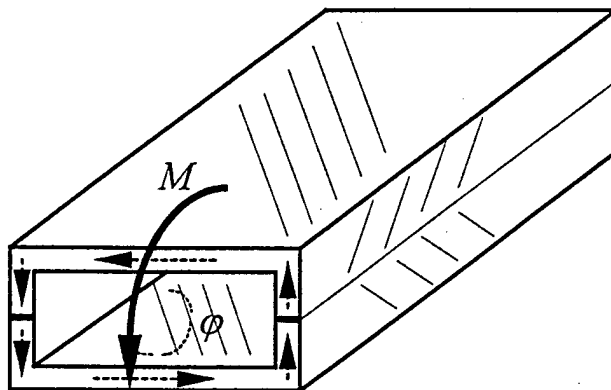


Figure 1.3: Illustration of Bending-Twist Coupling in CAS Beam.



The CUS and CAS configurations provide simple means to obtain desired elastic coupling of thin-walled closed section beams. The question remains as to the stacking sequences which maximize the extension-twist in the CUS case and bending-twist coupling in the CAS case.

## ***1.2 Beam Theories***

A brief review of the available thin walled beam theories, with emphasis on those designed to predict mechanical coupling, is presented in the following. One of these theories is selected for the optimization in this work. This review is followed in Section 1.3 by a history of some prior structural optimization work involving thin walled, closed section beams. And finally, previous experimental work related to coupled deformations is summarized in Section 1.4.

Many researchers have developed ways to analyze thin-walled composite beams to incorporate all forms of coupling. Many of these are based on a finite element approach (FEM). The FEM approach is impractical for consideration in this work because of the necessity for the optimization routine to solve the problem repeatedly for many different beam configurations. The computational effort required is prohibitively high, therefore only closed form approaches are discussed here. In addition, a prerequisite for the finite element analysis is a definition of a configuration which is arrived at by other means. In this regard, closed form solutions are appealing due to their small computational effort and ability to help in defining the configuration by isolating the effect of parameters that control the behavior.

Smith and Chopra<sup>1</sup> and, more recently, Kim and White<sup>2</sup> present very good reviews of the literature. In particular, Smith and Chopra compare existing analytical and finite element approaches concerning box beams, the type of beam most commonly analyzed.

They also present an analytical solution based on a Newtonian approach to the problem, whereby applied forces are reacted by stresses in the beams. This method assumes a displacement field of a thin-walled isotropic beam with shear deformation, with no justification for this assumption presented. A discussion on the importance of warping of the cross section to torsional displacements, and on the necessity of considering transverse shear effects is presented. The result is a solution which is in closed form, however the displacement field does not account for the effects of material anisotropy.

Rehfield<sup>3</sup> was one of the first to use such a displacement field. Rehfield, et al<sup>4</sup> present some discussion of the nonclassical effects in thin-walled composite beams. In particular, these researchers conclude that torsional warping is an important consideration because it contributes to a significant end effect. It is also shown that bending-transverse shear coupling is important in CUS beams because its inclusion leads to added flexibility in bending.

The work of Reissner and Tsai<sup>5</sup> presents a closed form analysis of thin-walled shells which is applicable to open or closed cross sections. The specification of the boundary conditions is the only difference between the two formulations. The basis of the work is an exact solution to the equilibrium, compatibility, and constitutive equations of a shell. The authors do not present expressions for the stiffness coefficients of the structure, and coupling between in-plane strains and curvature are neglected.

Kim and White<sup>2</sup> develop a theory which applies to both thin- and thick-walled beams of arbitrary cross section, accounting for primary and secondary warping effects and transverse shear of the cross section and of the beam wall. This theory also assumes a displacement field, where the out-of-plane warping is described by a cubic function of the cross-sectional coordinates. This is a different assumption from that made by Smith and Chopra, but again no justification is presented. The method of Kim and White also yields a closed form solution with inherent inaccuracies resulting from the assumed displacement field, and also includes thick-walled considerations.

Bauchau *et al*<sup>6</sup> use variational principles to establish a method of accounting for warping of the cross section in thin-walled beams. Two models are used, with assumed displacement fields differing only in the treatment of torsion-related warping. St. Venant warping and warping generalized by a series representation, are compared. The assumption of St. Venant torsion related warping is not justified in this work, and including only this warping term ignores the effects of anisotropy. The series approach is capable of representing arbitrary warping, but its form will not show the relation between the warping and other deformation modes.

Barbero *et al*<sup>7</sup> consider not only membrane stresses but also flexural stresses in the walls. Their theory thus applies to moderately thick-walled beams. The position of the neutral axis is defined in such a way that deformations may be completely described by axial, bending, and shear stiffness coefficients, i.e. no explicit coupling stiffness is required. A shear correction factor is determined from energy equivalence of shear strain energy predicted by Timoshenko theory and that obtained from the shearing stress distribution. A rotation of the cross section out of its original plane is assumed in the displacement field, but warping of the cross section is not considered.

More recently, Rand and Barkai<sup>8</sup> have presented a formulation applying to thin-walled or solid composite beams. These investigators again assume a displacement field. In this case, the traditional cross-sectional displacement are considered, along with a warping function which can only take into account out-of-plane warping. Furthermore, in some cases of interest in this work, i.e. thin-walled beams with coupling, the form of this warping function must be assumed.

Several investigators have considered the dynamic behavior of thin-walled composite beams. An excellent review of the literature is provided by Hodges, *et al*.<sup>9</sup> In addition to techniques applying to other composite structures, two methods of determining the sectional stiffness coefficients for thin-walled closed section beams are

compared. One is based on the work of Rehfield<sup>3</sup>, and the other is a finite element method. This work also compares two methods for determining the natural frequencies and mode shapes: a simple mixed finite element approach and a numerical integration method. Both are numerical in nature and are not considered for application in this work.

McGee<sup>10,11</sup> has considered the dynamic behavior of pretwisted beams. A multifilament model is used to derive closed form expressions for the torsional natural frequencies and mode shapes of beams with helical pretwist. The effects of elastic warping and warping-pretwist coupling are identified. Only beams with open cross sections are considered, and the analysis is limited to torsional behavior.

Song and Librescu<sup>12</sup> have studied the importance of transverse shear and primary and secondary warping of the cross section when considering natural frequencies of thin- and thick-walled composite beams. These investigators have used unidirectional stacking sequences with the CUS beam configuration and illustrated the effect of changing the ply angle on natural frequencies. Again a displacement field is postulated, based on an isotropic case. Instead of St. Venant torsion, the warping function is assumed to be a function of the axial coordinate of the beam. A secondary warping of points off the mid-line contour is also assumed. No justification of these assumptions or verification of the theoretical results is presented.

Bank and Kao<sup>13,14</sup> also investigated the dynamics of CUS box beams. They used a Timoshenko-type model of the beam using a transformed shear coefficient and demonstrated the ability to tailor the natural frequencies of the beam. The effectiveness of a Timoshenko-type theory is shown to be dependent on the technique used to determine the constants in the governing equation. The theory is derived for beams composed of orthotropic panels with principal axes aligned with the axes of the beam. This means that no coupling can occur.

Tutuncu and Winckler<sup>15</sup> have presented an overly simplified method for dealing with hygrothermal effects. These researchers treat a composite tube as a laminate that is wrapped into the shape of a tube. Classical Laminate Theory (CLT) for plates is used as the analytical model, with changes in wall curvatures assumed to be zero. The paper addresses torsional hygrothermal displacements (determined from in-plane shear deformation  $\epsilon_6$ ) with no mention of warping or transverse shear. Kollar<sup>16</sup> has developed an approximate method of dealing with a cylindrical shell subjected to a constant linear temperature and moisture gradient through the thickness.

The overwhelming majority of papers in the literature begin by assuming a displacement field. As a consequence, their results are not consistent and lead to errors, differing in magnitude in different loading situations. Berdichevsky *et al*<sup>17</sup> and Badir<sup>18</sup> have developed a closed form analysis based on a variational, asymptotic approach. Their formulation does not assume a displacement field a priori, but rather the displacements are derived in the asymptotic analysis. In addition to a torsion related warping term, the axial displacement has additional components which are referred to as axial related warping and bending related warping. The constitutive equations contain only the four main displacements of classic beam theory: extension, torsion, and bending in two planes. The theory does implicitly account for the contributions of warping of the cross section and transverse shear to these four deformation modes. The closed form expressions for coupling stiffnesses are simple enough to provide physical understanding of the quantities, and are computationally efficient. Explicit contributions of variables provide an ideal guide to the optimization. In addition, the theory has been extended to include hygrothermal effects<sup>19</sup> and dynamic behavior,<sup>20,21</sup> and by Badir<sup>22</sup> to include the static behavior of two-celled beams.

This theory presents a complete and accurate representation of the beam deformation which applies for any beam configuration. It is simple, closed form, and has been verified by comparison with the test data and finite element work of other

researchers.<sup>17,18,20</sup> For these reasons the variational asymptotic formulation has been chosen for use in this work.

### ***1.3 Structural Optimization***

While much work has been done in the field of structural optimization, only a very small portion of this work pertains directly to thin-walled composite beams. Some of the relevant work is reviewed in the following.

Barbero<sup>23</sup> has performed a parametric study of box beams and I-beams with the objective of maximizing the buckling load. In this work, both web and flange crippling behavior are studied. The variables considered are fiber volume fraction, and a single lamination angle within the flange or the web. Caprino and Langella<sup>24</sup> considered optimizing a beam to produce the highest possible fundamental frequency for application to robotics. Only beams of circular cross section with no elastic couplings and specific stacking sequences are considered. Rayleigh's energy method is used to provide an expression for the fundamental frequency in terms of geometric and material parameters. Neither of these works uses a formal optimization scheme.

Tutuncu and Winckler<sup>15</sup> optimized the hygrothermal performance of a composite tube. As mentioned previously, the analytical model used in this work is simply Classical Laminate Theory for plates. These researchers sought to maximize the thermal twist of the tube per unit temperature change. As a constraint, the change in torsional stiffness of the tube due to hygrothermal degradation of the transverse and shear moduli is minimized. A  $\pm 45^\circ$  bimaterial solution is proposed such that the torsional strength is fiber dominated but there is a mismatch in thermal expansion coefficients leading to shear deformation in the wall. Optimization is carried out by plotting a ratio of hygrothermal twist to change in torsional rigidity over all choices of ply angles.

Peck and Bauchau<sup>25</sup> have performed a structural optimization of beams with initial curvature. A strength of material approach is used to model the stresses in flanges and webs of beams subjected to bending in the plane of the initial curvature. The analytical model does not include coupling effects and focuses on curling of beam flanges. The objective is to maximize a measure of load carrying ability subject to a failure constraint based on the Tsai-Wu First Ply Failure criterion. A generalized reduced gradient based optimizer is used to select variables such as flange lengths and thicknesses, web thicknesses, and certain properties of the stacking sequence. The optimizer is only allowed to use ply angles of 90,  $\pm 45$ , and 0 degrees.

Ganguli and Chopra<sup>26</sup> have applied a gradient based optimization scheme to the design of advanced geometry helicopter rotors. The authors use an analytical model based on an assumed displacement field. Shear degrees of freedom are eliminated from the constitutive relation using the technique of static condensation. This model and an aeroelastic analysis are applied to a rotor that is discretized into finite elements. An optimization algorithm is then applied with three ply angle degrees of freedom and various geometrical degrees of freedom. The goal is reduction of the vibratory hub loads and vibratory bending moments. An initial guess configuration is the only basis for comparison between different optimum configurations.

A comprehensive review of structural optimization with frequency constraints, not focusing on composites, is presented by Grandhi.<sup>27</sup> The author discusses various problem statements, sensitivity analyses, constraint approximations, algorithms, and frequency-related problems. It is noteworthy that the type of frequency constraint applied in this work is not among those discussed. Also, the structural goal mentioned alongside the optimization of dynamic behavior for different applications is minimum weight, not any specific behavior such as stiffness or strength.

The unconstrained optimization of thin-walled beams of rectangular and elliptic cross section is a part of this thesis research, and has been presented by Armanios *et al.*<sup>28</sup>

In this study, the stacking sequences which produce maximum extension-twist coupling of a CUS beam and maximum bending-twist coupling of a CAS beam are determined. The robustness of these solutions is evaluated by observing the effect of variations in material properties and ply angles on the values of coupling.

Several optimization techniques exist which could be applied to the structural optimization problem at hand. The concept of a genetic algorithm<sup>29</sup> is becoming widely used in the field of composites. An initial population of laminate configurations is generated at random or by the user. A weighting function is assigned to each laminate as a measure of its desirability. Laminates with high weighting functions are then "mated," new laminates being created with mixed characteristics of the "parents." This process continues until the improvement from one generation to the next drops below a specified level. A mechanism called mutation is used to aid in the optimization process so that a laminate may be created with properties not derived from either parent. The disadvantages of this technique are the computational effort involved, and the requirement that a small number of ply orientations may be allowed.

A gradient based search algorithm<sup>30-32</sup> has been selected for this work. This method involves minimizing (or maximizing) a function which expresses the desirability of a design in terms of several variables, usually the ply orientations. The values of the function and its gradient are evaluated for an initial configuration. The gradient determines the direction in which the routine will step, altering the stacking sequence so the value of the objective function decreases as desired. The routine concludes when a point of zero gradient is reached, indicating that a minimum, maximum, or inflection point has been reached. It is necessary to run the routine several times with different initial guesses to insure that the global optimum is found. A key advantage of this method is the ability to add design constraints using penalty functions. The penalty function causes the magnitude of the objective function to be higher in areas where the constraint is not meant.



#### 1.4 Experimental Work

Very little work has been done on the experimental analysis of thin-walled composite beams. Chandra and Chopra<sup>33</sup> have investigated the static extension-twist coupling of two celled helicopter rotors. No details of the testing technique are presented. Bauchau *et al*<sup>6</sup> performed an experimental investigation of a box beam with two graphite/epoxy walls, two aluminum c-section walls, and an aluminum honeycomb core. The torsional behavior of this beam is investigated, but coupling behavior is not considered. Bank, Smith<sup>34</sup> have investigated the behavior of cantilevered I-beams subjected to tip loads and tip moments. Bending-twist coupling is measured. No details of the technique used to measure twist are presented. Bending deflections are measured using dial gauges placed along the length of the beam.

Kosmatka *et al*<sup>35</sup> have investigated the dynamic behavior of beams with an initial twist. Modal analysis was performed on five specimens with different stacking sequences. Results indicate that the natural frequencies of the first three bending modes and the first torsion mode are very dependent on the ply orientation for both cantilevered and free boundary conditions. Coupled natural frequencies are not considered.

Chandra, *et al*<sup>36</sup> performed an investigation of the behavior of CUS and CAS box beams subjected to static loading. The beams were tested in a unique fixture, and distributions of deflections along the span of the beam were established. The fixture held the beams in a cantilevered configuration, with loading applied by a system of pulleys and weights. A thrust bearing is used to allow the loaded end of a CUS beam to twist. The bending slope and twist are measured using an optical system consisting of a light beam and mirrors located on the beam walls. The results of the testing are very precise, but the loading technique places limits on the amount of load that can be applied. Also, the friction of the thrust bearing is dependent on the magnitude of load, introducing nonlinearity into the measurements.

Nixon<sup>37</sup> has performed a series of tension and torsion tests on circular cylindrical CUS beams. A thrust bearing is used to allow "free" rotation of one end of the test specimen. It is stated that this thrust bearing had negligible torsional resistance under axial load, but no quantitative evidence is presented to support this statement. However, the work of Hooke and Armanios<sup>37</sup> indicates that thrust bearings introduce friction varying with applied axial load. Twist measurements are made using arms extending from a diameter of the specimen and linear variable displacement transducers (LVDT's). The effect of the end of the arm moving in a circular path was corrected for. Sixty strain gauge rosettes were attached to each specimen to provide information on the distribution of strain in the beam.

Hooke and Armanios<sup>37</sup> have investigated three means of performing extension-twist testing of laminates. A thrust bearing apparatus is tested and found to follow trends predicted by a finite element method. However, friction with increasing axial load was found and was modeled as an effective torsional spring. A rotating frame apparatus is tested and found to have a parasitic inertial effect due to a rotating end mass. An improved thrust bearing apparatus is also designed, manufactured, and verified. The main improvement consists of accuracy unaffected by the magnitude of the load. The restraining moment of a traditional thrust bearing apparatus is significantly reduced. This improved thrust bearing apparatus has been selected for experimental testing of extension-twist coupled beams.

It is clear after a review of the existing literature that a need exists for a validated design tool for thin-walled composite beams with coupling. This statement is true of single-celled beams, and the gap in the literature is wider for two-celled beams. The optimization routine developed in this thesis research is the required tool, allowing a designer to create a beam tailored to produce a high value of elastic coupling but still meeting other practical requirements relating to manufacturability and dynamic behavior.

A systematic experimental investigation of thin-walled closed cross section beams is an important part of the work, as well. It is necessary to validate the optimization routine and the theory it is based on, from verification of the optimality of the beams to comparison of their coupling properties with the theoretical prediction. The results will also contribute greatly to the sparse experimental data available in the literature, providing a database for thin-walled closed section composite beams. An investigation of the sensitivity of the global and local optima to the scatter in measured elastic constants and manufacturing variability of fiber placement is performed. This investigation establishes bounds for optimum design achieved practically and are a basis for establishing adequate safety margins.

## Chapter 2 - Problem & Research Overview

---

Based on the survey of previous research efforts presented in Chapter 1, it is concluded that design engineers do not have the tools and information that will allow them to create optimum elastically tailored composite beams for various applications. Various researchers have addressed parts of the problem, but no comprehensive treatment of the problem exists. This work attempts to fill this gap in the literature by addressing five separate elements: analysis with a proven theoretical model, application of a constrained optimization scheme, manufacturing, experimental testing, and finite element verification.

The existence of an optimum design of a thin-walled closed section composite beam may be ascertained by formulating the problem as one of constrained optimization. This work addresses the optimal design of a single-celled beam with maximized extension-twist or bending-twist coupling and little or no hygrothermal warping, and while avoiding a specified natural frequency. Both rectangular and elliptical cross sections with a variety of aspect ratios are considered. Beam wall thicknesses ranging from two plies to eight plies have been considered, each a degree of freedom for the optimizer.

The robustness of the optimum design configurations are assessed by investigating their sensitivity to variations in material constants and manufacturing tolerances expressed by variations in fiber angles. A stochastic method is used to represent the variabilities that might be expected in a manufacturing environment. Each material property and ply angle is treated as an independent random variable, leading to a distribution of resultant beam properties. Cost considerations are also examined, as determined by the ease of manufacturing of beams with various configurations.

A second objective is the optimization of two-celled beams consisting of a rectangular cross section and a single web. The constraint imposed on the two-celled beam is that only one form of coupling is exhibited. This poses an interesting problem in the case of a beam with an off-center web as fiber placement becomes a tool to remove undesired coupling introduced by the geometry. These beams consist of walls and web of eight-ply thickness, and a total of twelve degrees of freedom. Care has been taken to allow the optimization to select from a set of configurations practical for manufacturing. The robustness of these solutions in the face of variability of input parameters has been addressed in a similar manner to that applied to single-celled beams.

Experimental work has been done to verify the results of the theory and the optimization scheme. Several CUS box beams have been manufactured near the configuration predicted to be the constrained global optimum for an eight-ply beam, and several more near a constrained local optimum of interest. Not only are beams made with the optimum sequence to verify the properties at optimum, but beams are made with stacking sequences perturbed from optimum to verify the expected drop in coupling. The manufacturing technique involves wrapping around mandrel, followed by removal of the mandrel and curing inside a female mold.

Manufacturing of two-celled beams required development of a new technique. Three two-celled beams were manufactured. Each successive beam displayed a higher level of quality, reflecting evolving and improving manufacturing techniques. The final iteration involved two mandrels, with pressure plates over the composite to insure good surface finish. Only the last beam was of high enough quality to be tested. At this point lack of material availability precluded further manufacturing.

The ABAQUS finite element analysis (FEA) has been used for comparison with the experimental results and theoretical predictions for both the single-celled and two-celled cases. The stacking sequences of the optimum configurations and

the magnitude of coupling at each optimum have been investigated for the CUS unconstrained solutions and the two-celled solution. It should be noted that this finite element work and the experimental work provide first verification of the analytical work of Badir<sup>22</sup> in the area of two-celled beams.

## Chapter 3 - Analytical Model, Optimization

---

This chapter provides the background information on the beam theory used to develop the optimization in this work. The static theory of both single- and two-celled beams is covered, as well as the extensions to include hygrothermal deformations and dynamic response of single-celled beams. This is followed by a discussion of the optimization technique used, focusing on the formulation of the objective function and inclusion of the constraints.

### 3.1 Review of Analytical Model

The coupling response of a single-celled beam is predicted from the variational asymptotic anisotropic beam theory of Ref. 17. Closed form expressions for the displacement field are obtained and the influence of the material's anisotropy is explicitly identified. A summary of governing equations is presented for convenience.

#### 3.1.1 Displacement Field

The displacement field is analytically determined to be

$$\begin{aligned} u &= U_1(x) - y(s)U_2'(x) - z(s)U_3'(x) + G(s)\varphi'(x) + \\ &\quad g_1(s)U_1'(x) + g_2(s)U_2''(x) + g_3(s)U_3''(x) \\ v &= U_2(x)\frac{dy}{ds} + U_3(x)\frac{dz}{ds} + \varphi(x)r_n \\ w &= U_2(x)\frac{dz}{ds} + U_3(x)\frac{dy}{ds} - \varphi(x)r_t \end{aligned} \tag{1}$$

where  $u$ ,  $v$ , and  $w$  are the axial and two transverse displacements,  $U_1(x)$ ,  $U_2(x)$ , and  $U_3(x)$  are average displacements along the coordinates, and  $\phi(x)$  is the twist angle. The primes in Eqn. 1 indicate differentiation with respect to the axial coordinate,  $x$ . The coordinate system and associated kinematic variables appear in Figure 1. In the expression for axial displacement, the term  $G(s)\phi'(x)$  is similar to the classical torsion-related warping. The remaining three terms represent warping of the cross section due to axial tension,  $g_1(s)U_1'(x)$ , due to bending about the  $z$ -axis,  $g_2(s)U_2''(x)$ , and due to bending about the  $y$ -axis,  $g_3(s)U_3''(x)$ . These last three terms vanish for materials that are orthotropic or whose properties are antisymmetric with respect to the middle surface of the beam wall.

### 3.1.2 Constitutive Relationships

Closed form expressions for the compliance coefficients in terms of material and geometric parameters are provided through the constitutive relationships<sup>18</sup>

$$\begin{Bmatrix} U_1' \\ \phi' \\ U_3'' \\ U_2'' \end{Bmatrix} = \begin{bmatrix} S_{11} & S_{12} & S_{13} & S_{14} \\ S_{12} & S_{22} & S_{23} & S_{24} \\ S_{13} & S_{23} & S_{33} & S_{34} \\ S_{14} & S_{24} & S_{34} & S_{44} \end{bmatrix} \begin{Bmatrix} T + T^{(nm)} \\ M_x + M_x^{(nm)} \\ M_y + M_y^{(nm)} \\ M_z + M_z^{(nm)} \end{Bmatrix} \quad (2)$$

where  $T$ ,  $M_x$ ,  $M_y$ , and  $M_z$ , denote the axial force, torsional moment, and bending moments about  $y$  and  $z$  axes, respectively. The  $(nm)$  superscript refers to non-mechanical stress resultants. The deformation-related variables  $U_1'$ ,  $\phi'$ ,  $U_3''$  and  $U_2''$  represent the axial strain, twist rate and bending curvatures associated with the  $xz$  and  $xy$  planes, respectively. The compliance coefficients,  $S_{ij}$ , are the inverse of the stiffness coefficients,  $C_{ij}$ , which are given for convenience in Appendix A. They are defined in terms of contour integrals and Classical Lamination Theory in-plane stiffnesses,  $A_{ij}$ .<sup>39</sup>



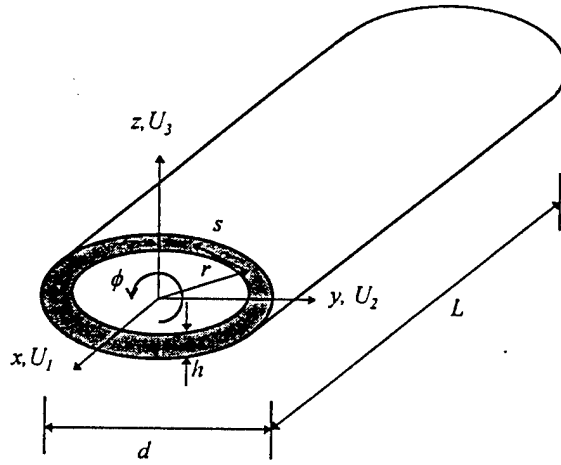


Figure 3.1: Coordinate System and Kinematic Variables

The compliance coefficients of particular interest in this work are those controlling extension-twist coupling and bending-twist coupling. In the case of a CUS beam the coupling of interest is extension-twist coupling, given by the  $S_{12}$  compliance. The stiffness matrix for a CUS configuration is reduced to the form

$$\begin{bmatrix} C_{11} & C_{12} & 0 & 0 \\ C_{12} & C_{22} & 0 & 0 \\ 0 & 0 & C_{33} & 0 \\ 0 & 0 & 0 & C_{44} \end{bmatrix} \quad (3)$$

The extension-twist compliance is found by inverting the 2x2 upper left corner of the stiffness matrix to be

$$S_{12} = -\frac{C_{12}}{C_{11}C_{22} - C_{12}^2} = \left(\frac{1}{A_e}\right)\left(\frac{B}{B^2 - AC}\right) \quad (4)$$

Here  $A_e$  is the area enclosed by the cross section and  $A$ ,  $B$  and  $C$  represent the reduced axial, coupling and shear stiffnesses, respectively. Note that the only dependence of the compliance on the cross-section geometry is on the enclosed area. Therefore the stacking sequence which optimizes the extension-twist coupling is independent of the shape of the cross-section. This implies that development and verification can be done on a simple cross-section and then generalized to more complex shapes necessary for applications such as airfoils. The final expression of Eqn. 3 has been simplified by the fact that these stiffnesses are constant around the cross section in the CUS configuration. They can, in general, vary along the circumferential direction and are given by

$$A(s) = A_{11} - \frac{(A_{12})^2}{A_{22}} \quad B(s) = 2\left[A_{16} - \frac{A_{12}A_{26}}{A_{22}}\right] \quad C(s) = 4\left[A_{66} - \frac{(A_{26})^2}{A_{22}}\right] \quad (5)$$

For a beam with the CAS configuration, the bending-twist coupling is of interest and is given by the  $S_{23}$  compliance coefficient. The stiffness matrix simplifies to

$$\begin{bmatrix} C_{11} & 0 & 0 & 0 \\ 0 & C_{22} & C_{23} & 0 \\ 0 & C_{23} & C_{33} & 0 \\ 0 & 0 & 0 & C_{44} \end{bmatrix} \quad (6)$$

and the bend-twist coupling is found by inverting the 2x2 submatrix in the center to be

$$S_{23} = -\frac{C_{23}}{C_{22}C_{33} - C_{23}^2} = \left(\frac{1}{A_e} \frac{\int z ds}{\int z^2 ds}\right)\left(\frac{B_t}{B_t^2 - AC}\right) \quad (7)$$

where the  $t$  associated with the line integral and appearing as a subscript indicates the top half ( $z>0$ ) of the cross section. This appears because the reduced axial and shear stiffnesses are constant around the cross section, while the coupling stiffness has opposite signs on opposite sides of the  $y$  axis.

Comparing Eqns. (4) and (7) reveals that the same stacking sequence will maximize the coupling in both the CUS and CAS cases. This is because both forms of coupling result from local extension-shear coupling in the wall of the beam.

### 3.1.3 Equations of Motion

The equations of motion for free vibration analysis have been derived in Ref. 20 using the variational asymptotic approach and Hamilton's principle. Closed form expressions for the natural frequencies are available for the two cases of interest, CUS and CAS. In both cases the vibration modes are dependent on the anisotropic parameters of the material. The effect of coupling on the natural frequencies is presented in Ref. 21.

The equations of motion for the generally anisotropic case are

$$\begin{aligned}
 C_{11}U_1'' + C_{12}\phi'' + C_{13}U_3''' + C_{14}U_2''' - m_c\ddot{U}_1 &= 0 \\
 C_{12}U_1'' + C_{22}\phi'' + C_{23}U_3''' + C_{24}U_2''' - I\ddot{\phi} - S_z\ddot{U}_3 + S_y\ddot{U}_2 &= 0 \\
 C_{13}U_1''' + C_{23}\phi''' + C_{33}U_3'''' + C_{34}U_2'''' + S_z\ddot{\phi} + m_c\ddot{U}_3 &= 0 \\
 C_{14}U_1''' + C_{24}\phi''' + C_{34}U_3'''' + C_{44}U_2'''' - S_y\ddot{\phi} + m_c\ddot{U}_2 &= 0
 \end{aligned} \tag{8}$$

where the inertial parameters are defined by

$$m_c = \oint \rho h(s) ds \quad I = \oint \rho (y^2 + z^2) h(s) ds \quad (S_y, S_z) = \oint \rho (z, y) h(s) ds \quad (9)$$

and  $\rho$  is the mass per unit length of the beam. The boundary conditions at the ends of the beam require prescribing one of each of the following pairs.

$$T \text{ or } U_1, \quad M_x \text{ or } \varphi, \quad M_y \text{ or } U_3', \quad M_y' \text{ or } U_3, \quad (10)$$

$$M_z \text{ or } U_2', \text{ and } M_z' \text{ or } U_2$$

The general case is simplified greatly in each of the two configurations of interest. For the CUS case the system of equations reduces to

$$\begin{aligned} C_{11}U_1'' + C_{12}\varphi'' - m_c\ddot{U}_1 &= 0 \\ C_{12}U_1'' + C_{22}\varphi'' - I\ddot{\varphi} &= 0 \end{aligned} \quad (11)$$

$$C_{33}U_3'''' + m_c\ddot{U}_3 = 0$$

$$C_{44}U_2'''' + m_c\ddot{U}_2 = 0$$

where the first two equations govern the extension-twist coupled mode, and the last two equations represent the two uncoupled bending modes. The natural frequencies of extension-twist coupling for a cantilevered beam are given by

$$\omega_n = \frac{n\pi\lambda}{2L} \quad (12)$$

where

$$\lambda^2 = \frac{2\alpha}{\beta \pm \sqrt{\beta^2 - 4\alpha m_c I}} \quad (13)$$

and

$$\alpha = C_{11}C_{22} - (C_{12})^2 \quad \beta = C_{11}I - C_{22}m_c \quad (14)$$

The natural frequencies for bending about the y axis are given by

$$\omega_n = k_n^2 \sqrt{\frac{C_{33}}{m_c}} \quad (15)$$

and the natural frequencies for bending about the z axis are given by

$$\omega_n = k_n^2 \sqrt{\frac{C_{44}}{m_c}} \quad (16)$$

where the  $k_n$  are the roots of the transcendental equation

$$\cos(kL)\cosh(kL) = -1 \quad (17)$$

Note that the solutions for these uncoupled bending modes have the same form and characteristic equation as classic beam bending.

For beams with the CAS configuration the equations of motion reduce to

$$C_{11}U_1'' - m_c \ddot{U}_1 = 0 \quad C_{22}\phi'' + C_{23}U_3''' - I\ddot{\phi} = 0 \quad (18)$$

$$C_{23}\phi'''' + C_{33}U_3'''' + m_c\ddot{U}_3 = 0 \quad C_{44}U_2'''' + m_c\ddot{U}_2 = 0$$

The characteristic equation for a cantilevered CAS beam is expressed<sup>21</sup>

$$\alpha y^3 + \beta y^2 + \gamma y + \delta = 0 \quad (19)$$

where

$$y = \lambda^2$$

$$\delta = -\omega^4 \text{Im}_c$$

$$\alpha = C_{22}C_{33} - C_{23}^2 \quad (20)$$

$$\gamma = -C_{22}\omega^2 m_c$$

$$\beta = C_{33}I\omega^2$$

and  $\lambda$  is the space domain eigenvalue. This system is solved by the quasi-decoupled method given by Ref. 21. The resultant approximate natural frequencies are

$$\omega^2 = \frac{-(C_{22}m_c\lambda^2 - C_{33}I\lambda^4)}{2m_cI} \pm \frac{\sqrt{(C_{22}m_c\lambda^2 - C_{33}I\lambda^4)^2 + 4m_cI(C_{22}C_{33} - C_{23}^2)\lambda^6}}{2m_cI} \quad (21)$$

where  $\lambda = \pm ik_1$ ,  $\lambda = \pm ik_3$  and

$$k_1 = \frac{(2m+1)\pi}{2L} \quad m=0,1,2,\dots \quad (22)$$

and  $k_3$  is a solution of the beam bending characteristic Eqn. (17).

The frequency of uncoupled axial vibration is

$$\omega_n = \frac{n\pi}{2L} \sqrt{\frac{C_{11}}{m_c}} \quad (n=1,3,5,\dots) \quad (23)$$

This is of the same form as that of an isotropic beam. Uncoupled bending about the  $z$  axis is described by Eqns. (16) and (17).

### 3.1.4 Hygrothermal Behavior

The theory of Refs. 17 and 18 has been extended in Ref. 19 to include hygrothermal effects. Material anisotropy has a significant effect on the hygrothermal stresses. The parameters of the beam may be selected in such a way as to produce a finite value of a compliance coefficient while one or more of the hygrothermal stress resultants is minimized. Ideally, a beam can be manufactured to possess a desired mechanical coupling while experiencing little or no hygrothermal deformation.

The hygrothermal stress resultants are given by

$$\begin{aligned} T^{(nm)} &= -\frac{1}{2} \left[ \oint A^{(nm)} ds - \oint \frac{BC^{(nm)}}{C} ds + \frac{\oint \frac{B}{C} ds \oint \frac{C^{(nm)}}{C} ds}{\oint \frac{1}{C} ds} \right] \\ M_x^{(nm)} &= -\frac{1}{2} \frac{\oint \frac{C^{(nm)}}{C} ds}{\oint \frac{1}{C} ds} A_e \\ M_y^{(nm)} &= \frac{1}{2} \left[ \oint A^{(nm)} z ds - \oint \frac{BC^{(nm)}}{C} z ds + \frac{\oint \frac{B}{C} z ds \oint \frac{C^{(nm)}}{C} ds}{\oint \frac{1}{C} ds} \right] \end{aligned} \quad (24)$$

$$M_z^{(nm)} = \frac{1}{2} \left[ \oint A^{(nm)} y ds - \oint \frac{BC^{(nm)}}{C} y ds + \frac{\oint \frac{B}{C} y ds \oint \frac{C^{(nm)}}{C} ds}{\oint \frac{1}{C} ds} \right]$$

The non-mechanical reduced stiffnesses denoted with a superscript  $(nm)$  appearing in these equations are expressed as

$$A^{(nm)} = 2 \left[ \frac{A_{12}}{A_{22}} (\Psi_\alpha + \Psi_\beta) - (\Gamma_\alpha + \Gamma_\beta) \right] \quad C^{(nm)} = 4 \left[ \frac{A_{26}}{A_{66}} (\Psi_\alpha + \Psi_\beta) - (\Omega_\alpha + \Omega_\beta) \right] \quad (25)$$

where

$$\Psi_\alpha = \Delta T \sum_{k=1}^n (\bar{Q}_{12} \alpha_x + 2\bar{Q}_{26} \alpha_{xy} + \bar{Q}_{22} \alpha_y) h_k$$

$$\Psi_\beta = \Delta H \sum_{k=1}^n (\bar{Q}_{12} \beta_x + 2\bar{Q}_{26} \beta_{xy} + \bar{Q}_{22} \beta_y) h_k$$

$$\Gamma_\alpha = \Delta T \sum_{k=1}^n (\bar{Q}_{11} \alpha_x + 2\bar{Q}_{16} \alpha_{xy} + \bar{Q}_{12} \alpha_y) h_k$$

(26)

$$\Gamma_\beta = \Delta H \sum_{k=1}^n (\bar{Q}_{11} \beta_x + 2\bar{Q}_{16} \beta_{xy} + \bar{Q}_{12} \beta_y) h_k$$

$$\Omega_\alpha = \Delta T \sum_{k=1}^n (\bar{Q}_{16} \alpha_x + 2\bar{Q}_{66} \alpha_{xy} + \bar{Q}_{26} \alpha_y) h_k$$

$$\Omega_\beta = \Delta H \sum_{k=1}^n (\bar{Q}_{16} \beta_x + 2\bar{Q}_{66} \beta_{xy} + \bar{Q}_{26} \beta_y) h_k$$



Here  $\Delta T$  is the change in temperature,  $\Delta H$  is the change in moisture percentage, and  $h_k$  is the thickness of the  $k^{\text{th}}$  ply. The  $\bar{Q}_{ij}$  are the transformed ply stiffnesses,  $\alpha_x$  and  $\alpha_y$  are the coefficients of thermal expansion in the axial and circumferential directions, respectively, and similarly for the hygroscopic expansion coefficients,  $\beta_x$  and  $\beta_y$ . All of these stress resultants vanish for any CAS configuration as a result of the antisymmetric stiffness distribution with respect to the cross section coordinate system. Therefore no hygrothermal deformations will be introduced during manufacturing or in subsequent application. For the CUS case, the stress resultants reduce to

$$T^{(nm)} = -\frac{1}{2}A^{(nm)}l \quad M_x^{(nm)} = -\frac{1}{2}C^{(nm)}A_e \quad M_y^{(nm)} = M_z^{(nm)} = 0 \quad (27)$$

Here  $l$  is the perimeter of the cross section. The only nonzero off-diagonal compliance coefficient is  $S_{12}$ , so in the absence of any mechanical loading the only hygrothermal deformation produced in a CUS beam is the twist rate,  $\phi'$ . This parameter will be referred to as  $k_{xy}^{(nm)}$  and is determined by simplifying Eqn. (1) to be

$$k_{xy}^{(nm)} = S_{12}T^{(nm)} + S_{22}M_x^{(nm)} \quad (28)$$

This is the quantity that will be minimized while the coupling is maximized.

The theoretical development is very similar for a beam with cross section divided by a single web, making a two-celled cross section<sup>22</sup>. See Figure 3.2 for an illustration. The displacement field obtained for the beam has the same form as that given for a single-celled beam in Eqn. (1). The constitutive relationship can also be expressed in the form shown in Eqn. (2). The compliance coefficients for the two-celled beam are described in terms of contour integrals over segments of the cross section and by the CLT in-plane stiffnesses  $A_{ij}$ . The stiffness coefficients for two-celled beams are referred to as  $K_{ij}$  and are given for convenience in Appendix B.

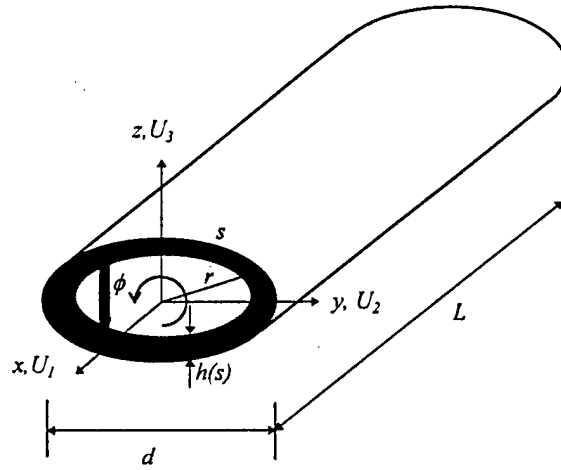


Figure 3.2: Two-Celled Beam

Unlike single-celled beams, a simple method of constructing a beam with only one form of coupling does not exist for two-celled beams. Therefore the optimization is constructed with the goal of maximizing a specific form of coupling while constraining to zero all other forms.

### 3.2 Discussion of Optimization Technique

A Sequential Unconstrained Minimization Technique (SUMT)<sup>31</sup> has been used to perform the optimizations in this work. The development of the optimization scheme is shown for maximization of the magnitude of the extension-twist compliance coefficient of a CUS beam,  $S_{12}$ , while minimizing the magnitude of the hygrothermal twist,  $k_{xy}^{(nm)}$ , and restricting selected natural frequencies. The magnitude of bending-twist coupling of a CAS beam is maximized by the same stacking sequence that maximizes the extension-twist coupling of a CUS beam. Recall that a CAS beam will not experience hygrothermal

deformation, so the hygrothermal constraint is not applied. A similar development is used for the optimization of the two-celled beams, with specific differences noted in the following discussion.

The problem is changed from one of maximization to minimization through the transformation

$$\begin{aligned} \text{Maximize: } |S_{12}(\theta_i)| &\rightarrow \\ \text{Minimize: } f(S_{12}) &= \text{Exp} \left[ - \left( \frac{S_{12}}{(S_{12})_o} \right)^2 \right] \end{aligned} \quad (29)$$

where  $f(S_{12})$  is the objective function. The subscript  $o$  represents a value at the stacking sequence used as an initial guess, and is used to non-dimensionalize the objective function. If the initial guess is a stacking sequence that has zero coupling, then a small value is arbitrarily used as the initial coupling. The same procedure applies for a CAS beam, replacing  $S_{12}$  with  $S_{23}$ .

The system is constrained for practical reasons to ply angles ranging from  $-90^\circ$  to  $+90^\circ$ . To remove this constraint, a new variable  $y_i$  is defined as

$$y_i = \cos^{-1} \left( \frac{\theta_i}{\pi} \right) \quad (30)$$

where the  $i$  subscript indicates the  $i^{\text{th}}$  ply of the stacking sequence. The objective function is now  $f(S_{12}(y_i))$ ,  $i=1 \dots n$ , or simply  $f(y_i)$ .

The hygrothermal and natural frequency constraints are removed by defining a modified objective function with a positive penalty parameter. The constraint on hygrothermal twist is easily removed with the exterior penalty method by multiplying the

square of the twisting curvature by the penalty parameter,  $\lambda$ . As in the objective function, the constraint is non-dimensionalized using the value corresponding to the initial guess. The resulting modified objective function is

$$f^* = f + \lambda \left( \frac{k_{xy}^{(nm)}}{\left(k_{xy}^{(nm)}\right)_o} \right)^2 \quad (31)$$

If the initial guess happens to be a stacking sequence that has no hygrothermal twisting curvature, then an arbitrary small value of coupling is used. For a two-celled beam, the undesirable forms of coupling are non-dimensionalized and constrained in this manner.

The constraint on the natural frequencies is met by preventing any beam natural frequency from being within a given percentage of a single specified frequency. For the purpose of this investigation, only the first two natural frequencies of each mode shape are considered. In the case of a CUS beam the modes are bending in two planes and extension-twist coupled vibration. For a CAS beam the modes are bending, extension, and bending-twist coupled vibration. The constraint function is stated as

$$g_i = (nf_i - sf)^2 - a^2 sf^2 \geq 0 \quad i = 1, \dots, 6 \quad (32)$$

where  $nf_i$  are the six natural frequencies of the beam,  $sf$  is the specified frequency to be avoided, and  $a$  gives the minimum difference allowed between any natural frequency and the specified frequency as a fraction of the specified frequency. This constraint is not well behaved at the boundary of the feasible and infeasible regions. Initial attempts to use a simple interior penalty method resulted in the solution jumping into the infeasible region. For this reason a quadratic extended interior penalty method is used to keep the intermediate solutions in the feasible region during the iterations. The constraint function is redefined as

$$p_i^* = \begin{cases} 1/g_i & \text{for } g_i \geq g_0 \\ 1/g_0 [3 - 3(\frac{g_i}{g_0}) + (\frac{g_i}{g_0})^2] & \text{for } g_i < g_0 \end{cases} \quad (33)$$

where  $g_0$  is a small transition parameter and is chosen to be the inverse of the penalty parameter,  $\lambda$ . The modified objective function is stated as<sup>32</sup>

$$f^* = f + \frac{1}{\lambda^2} (p_1^* + p_2^* + p_3^* + p_4^* + p_5^* + p_6^*) \quad (34)$$

The two constraints may be applied simultaneously to the CUS beam by stating the modified objective function as

$$f^* = f + \lambda k_{xy}^{(nm)^2} + \frac{1}{\lambda^2} (\sum p_i^*) \quad (35)$$

A Quasi-Newton optimization method is used, with the general iteration procedure stated as<sup>29</sup>

$$\begin{aligned} \{y\}_k &= \{y\}_{k-1} + \alpha \{s\}_{k-1} \\ \{s\}_{k-1} &= -H_{k-1}^{-1} \{\nabla f^*\} \end{aligned} \quad (36)$$

where  $H$  is the Hessian matrix of  $g$ , and  $\alpha$  is determined so as to minimize  $g$  along the Newton direction  $\{s\}_{k-1}$ . As  $f^*$  involves exponential and trigonometric functions it is highly nonlinear. This nonlinearity is the motivation for using a Quasi-Newton method, in which the explicit calculation of the inverse of the Hessian matrix is avoided. In this study, the well-known Broyden-Fletcher-Goldfarb-Shanno (BFGS) update method is used to approximate the inverse Hessian matrix during the minimization.

## Chapter 4 - Results and Discussion

---

The results of the optimization routine are presented in tabular and graphical format, along with discussion. Evaluation of the stability and robustness of the solutions is also considered.

### *4.1 Results of Optimizations*

The optimization has been carried out using the material properties of Fiberite T300/954-3 graphite/cyanate composite shown in Table 4.1. The density is provided by the manufacturer. The elastic constants have been experimentally determined by Palmer.<sup>40</sup> The coefficients of thermal expansion (CTE's) have been determined by manufacturing bimaterial strips composed of one strip of unidirectional composite bonded to one of metal with known properties. Applying a known temperature change to these strips and observing the resultant deformation allows the CTE to be calculated. This procedure has been used with longitudinal strips and transverse strips to obtain the two coefficients,  $\alpha_1$  and  $\alpha_2$ . A further test with a  $\pm 45^\circ$  composite strip was used to verify the results. The hygroscopic coefficients used are representative properties of graphite/epoxy composites.<sup>41</sup> A temperature decrease of  $130^\circ\text{C}$  and a hygroscopic increase of 0.4% moisture weight are used to model the cure cycle for the hygrothermal optimization.

Table 4.1: Material Properties

Ply Thickness	0.0762 mm
$E_{11}$	135.6 GPa
$E_{22}$	9.96 GPa
$\nu_{12}$	0.3
$G_{12}$	4.2 GPa
$\alpha_1$	$4.34(10^{-6}) \text{ C}^{-1}$
$\alpha_2$	$37.0(10^{-6}) \text{ C}^{-1}$
$\beta_1$	0
$\beta_2$	$5.56(10^{-3}) \text{ } \epsilon/\% \text{ wght}$
$\rho$	$1415 \text{ kg/m}^3$

The first beam geometry considered has a rectangular cross section with major dimension 3.18 cm and an aspect ratio of 0.792. The length of the beam is 45.7 cm. Results of the unconstrained optimization of beams with the CUS configuration are shown in Table 4.2. Ply angles are given in degrees, and the units of coupling are  $(\text{MN m})^{-1}$ . Note that reversing the sign of the ply angles will reverse the direction of the coupling. Two solutions of interest are shown. One is obviously the global optimum solution. The values referred to as Local Optimum are actually one of many local optima found for each wall thickness. The reason for the inclusion of these sequences in the table is their simplicity, being made with a unidirectional stacking sequence. The ability to create a near-optimum beam using only a single ply angle has obvious manufacturing advantages over any multi-angle sequence. Strength constraint for the case of combined loading or end restraint may require addition of fibers at different orientations. Irrespective of the number of plies, there is always a local optimum with every ply at an angle of  $28.45^\circ$ . These solutions have coupling values ranging from 2.2% to 3.2% lower than the global optimum. The only exception is the two-ply case, where the simple optimum is the global optimum and using two ply angles actually reduces the maximum coupling.

Table 4.2: Unconstrained Optimization of Rectangular Cross Section CUS Beam.

Number of Plies	Global Optimum		Local Optimum		Coupling
	Layup	Coupling	Layup	Coupling	Decrease
2	$[28.45_2]$	-278.0	$[28.45_2]$	-278.0	-
3	$[-77.17/26.98_2]$	-189.37	$[28.45_3]$	-185.30	2.2%
4	$[-83.54/30.70_3]$	-143.10	$[28.45_4]$	-138.98	2.9%
5	$[-83.55/30.55_4]$	-114.76	$[28.45_5]$	-111.18	3.1%
6	$[-83.55/30.42_5]$	-95.68	$[28.45_6]$	-92.65	3.2%
7	$[-83.54/30.30_6]$	-82.00	$[28.45_7]$	-79.41	3.1%
8	$[-83.53/30.19_7]$	-71.70	$[28.45_8]$	-69.49	3.1%

The same beam has been optimized while subjected to only the hygrothermal constraint. Several stacking sequences exist for wall thicknesses of two to eight plies having nonzero extension-twist coupling combined with no hygrothermal twist to specified accuracy. Each of these is an optimum of the modified objective function. For the beam and hygrothermal parameters given, the optimum end-to-end twist values are less than two hundredths of a degree for ply angles accurate to the hundredth of a degree. The global optimum stacking sequences are shown with the associated wall thicknesses and compared to the simple local constrained optima in Table 4.3. Again, irrespective of the number of plies, there is always a local optimum with every ply at the same angle. Consideration of the hygrothermal constraint has changed this angle from  $28.45^\circ$  to  $37.84^\circ$ . These simple solutions have coupling values ranging from 10.5% to 11.2% lower than the global optimum. Clearly, the difference between the local and global optima is much greater in the constrained case than in the unconstrained case. Note that the two ply case now has a global solution using two different ply angles.



Table 4.3: Constrained Optimization of Rectangular Cross Section CUS Beam.

Number of Plies	Global Optimum		Local Optimum		Coupling
	Layup	Coupling	Layup	Coupling	Decrease
2	[-81.84/30.48]	-275.75	[37.84 <sub>2</sub> ]	-246.7	10.5%
3	[-77.17/26.98 <sub>2</sub> ]	-182.818	[37.84 <sub>3</sub> ]	-164.49	10.0%
4	[-81.84 <sub>2</sub> /30.48 <sub>2</sub> ]	-137.872	[37.84 <sub>4</sub> ]	-123.37	10.5%
5	[-79.04 <sub>2</sub> /28.73 <sub>3</sub> ]	-111.007	[37.84 <sub>5</sub> ]	-98.70	11.1%
6	[-81.84 <sub>3</sub> /30.48 <sub>3</sub> ]	-91.915	[37.84 <sub>6</sub> ]	-82.25	10.5%
7	[-79.86 <sub>3</sub> /29.33 <sub>4</sub> ]	-79.353	[37.84 <sub>7</sub> ]	-70.50	11.2%
8	[-78.33 <sub>3</sub> /28.13 <sub>5</sub> ]	-69.193	[37.84 <sub>8</sub> ]	-61.69	10.9%

Finally, the global constrained and global unconstrained optima are compared in Table 4.4. The drop-off in coupling magnitude caused by constraining the hygrothermal deformations is 0.8% to 3.9%.

Table 4.4: Global Optima of Rectangular Cross Section CUS Beam.

Number of Plies	Unconstrained Global Optimum		Constrained Global Optimum		Coupling
	Layup	Coupling	Layup	Coupling	Decrease
2	[28.45 <sub>2</sub> ]	-278.0	[-81.84/30.48]	-275.75	0.8%
3	[-83.50/30.87 <sub>2</sub> ]	-189.37	[-77.17/26.98 <sub>2</sub> ]	-182.818	3.5%
4	[-83.54/30.70 <sub>3</sub> ]	-143.10	[-81.84 <sub>2</sub> /30.48 <sub>2</sub> ]	-137.872	3.7%
5	[-83.55/30.55 <sub>4</sub> ]	-114.76	[-79.04 <sub>2</sub> /28.73 <sub>3</sub> ]	-111.007	3.3%
6	[-83.55/30.42 <sub>5</sub> ]	-95.68	[-81.84 <sub>3</sub> /30.48 <sub>3</sub> ]	-91.915	3.9%
7	[-83.54/30.30 <sub>6</sub> ]	-82.00	[-79.86 <sub>3</sub> /29.33 <sub>4</sub> ]	-79.353	3.2%
8	[-83.53/30.19 <sub>7</sub> ]	-71.70	[-78.33 <sub>3</sub> /28.13 <sub>5</sub> ]	-69.193	3.5%

Figure 4.1 illustrates the distribution of hygrothermal twist and extension-twist coupling over the entire range of ply angles for a two ply CUS beam. The units of coupling are (MN m)<sup>-1</sup> and the units of twist are rad/m. The two peaks labeled with the

letter *a* are the unconstrained global optima. The four peaks labeled with the letter *b* are the unconstrained local optima. Figure 4.2 focuses on the region of ply angles near the global optimum. The constrained global optimum of  $[-81.84/30.48]$  is located at the middle of the plot. Notice that it is located very near a peak in extension-twist coupling, which corresponds to the unconstrained global optimum. This results in a coupling value near the maximum possible and a low slope indicating a lack of sensitivity to slight variations in the ply angles. Figure 4.3 is a similar illustration of the region near the local optimum. Again the constrained optimum is at the center of the plot, near a peak in coupling. The slope on the coupling plot appears steeper in the local case than the global, indicating a less robust solution. However, the global optimum appears more sensitive when the hygrothermal twisting curvature is considered. This issue is considered further in the following section.

For this CUS beam, optimization has been done including both the hygrothermal and natural frequency constraints simultaneously. As expected, when one of the natural frequencies is within the infeasible region, the final solution is moved just into the feasible region. It is necessary to use initial guesses with natural frequencies above and below the specified frequency to see which side of the infeasible region produces a solution with higher coupling magnitude. With an infeasible region stretching five percent of the specified frequency in either direction from the specified frequency, the maximum drop in coupling magnitude observed in a series of trial was three percent.

A CUS beam with elliptical cross section has also been considered. All results show the same trends, with only the magnitude of coupling and twist affected by the change in geometry. All of the optimum stacking sequences remain the same. Rectangular and elliptical CAS beams have been investigated, as well. All of the optimum stacking sequences for the unconstrained case remain the same as for the CUS beam, as expected. Recall that application of the hygrothermal constraint has no effect because CAS beams do not experience any hygrothermal deformation.

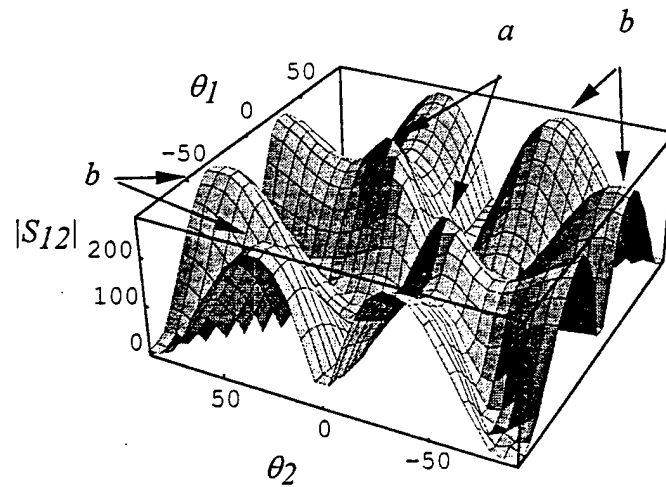
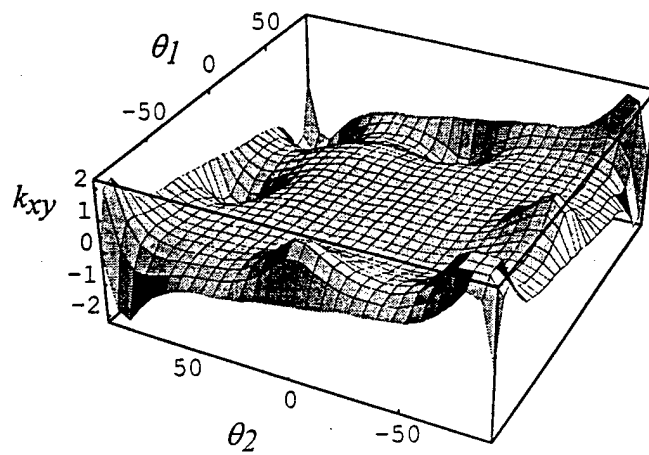


Figure 4.1: Distribution of Twist and Coupling over Entire Range of Ply Angles.

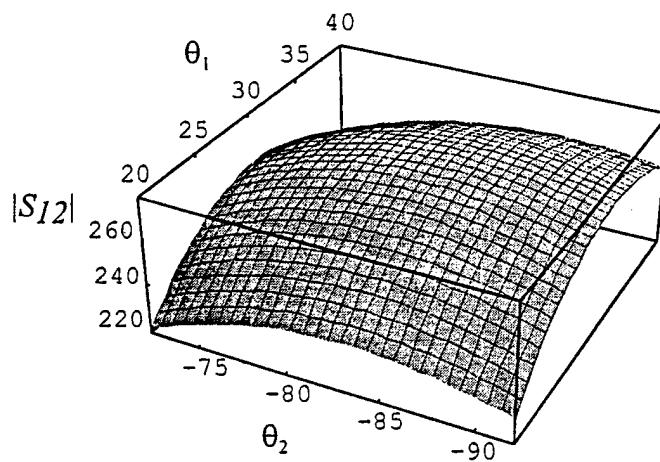
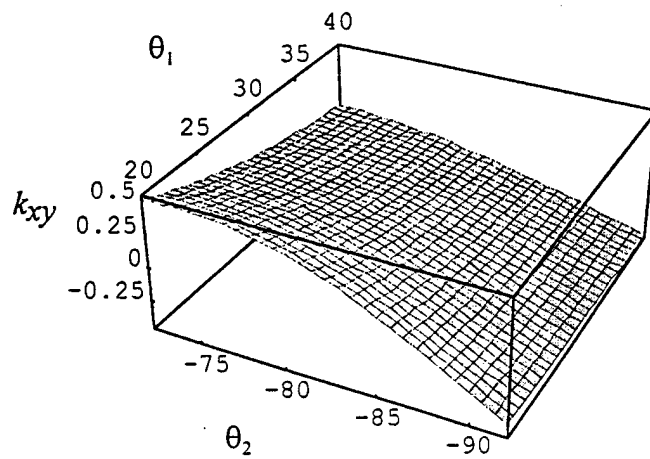


Figure 4.2: Distribution of Twist and Coupling in Vicinity of Global Optimum.

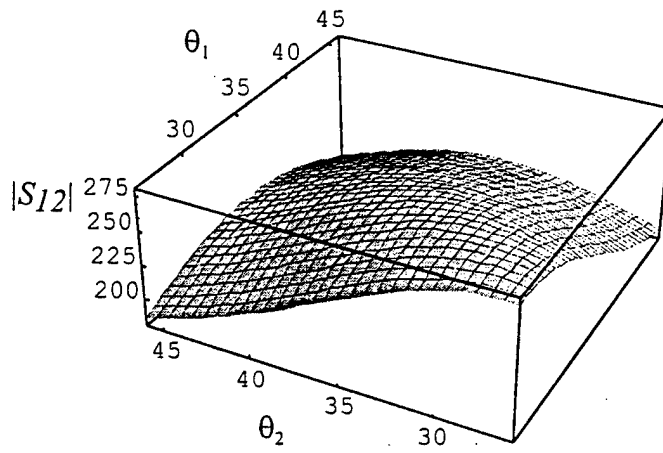
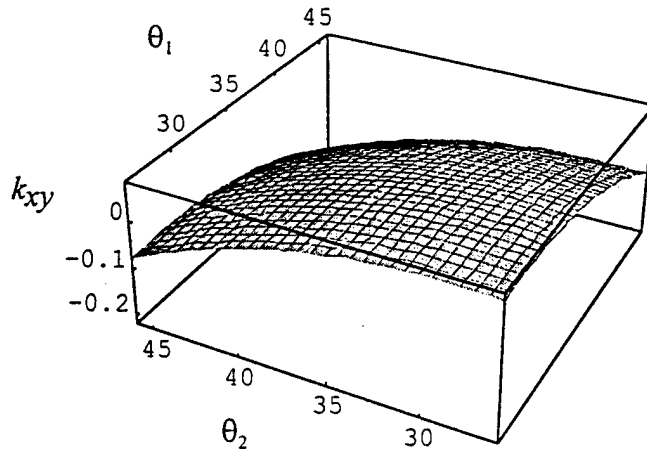


Figure 4.3: Distribution of Twist and Coupling in Vicinity of Local Optimum.

The results of the optimization of two-celled beams are shown in Table 4.5 below. The beams are of a specialized construction because of the intention to experimentally verify the results. Each of the walls and the web are eight plies thick. The left and right cells are formed independently by wrapping four plies. The two cells are placed together with one wall from each cell in contact with the other. This shared wall is now the web. Over-wrapping the joined, two-celled structure with four more plies completes the construction. The results shown in Table 4.5 are for a beam with the web in the center of the cross section.

Table 4.5: Results of Two-Celled Optimization, Centered Web.

Left Cell	Right Cell	Overwrap	E-T Coupling
83.7 <sub>4</sub>	83.7 <sub>4</sub>	-29.2 <sub>4</sub>	61.5
85.9/86.1 <sub>2</sub> /84.8	86.5/86.0/85.3/85.2	-31.3/-32/-31.5 <sub>2</sub>	61.1
83.4 <sub>4</sub>	83.4 <sub>4</sub>	83.4/-29.3 <sub>3</sub>	58.9
82.9 <sub>4</sub>	82.9 <sub>4</sub>	82.9 <sub>2</sub> /-29.5 <sub>2</sub>	54.2
69.9/-80.5/-81.9/-83.6	88.6/88.2/86.0/85.3	36.2/35.8/34.4/37.3	53.0

As Table 4.5 indicates, many optima are available for this construction. Only the five optima producing the highest magnitudes of extension-twist coupling are shown. Conveniently, the global optimum is also the simplest, with each of the three portions of the beam being unidirectional. In most of the optima, the stacking sequences of the interior cells are identical. It is interesting to note that in cases when the web is not located in the center of the cross section it is possible to eliminate the extension-bend coupling this geometry induces by simply selecting the proper stacking sequence.

The largest coupling value of 61.5 (MN m)<sup>-1</sup> may be compared to the value for unconstrained optimization of a CUS beam with eight plies of 71.7 (MN m)<sup>-1</sup>. This is a

drop-off in coupling of 14.2%, and is accompanied by a decrease in extensional compliance of 10.6%. Therefore, a single celled beam not only provides the higher value of coupling, but also the higher ratio of coupled deformation to uncoupled response. This can be important in an application such as an airfoil on a racing car. Bend-twist coupling could be a passive means of controlling angle of attack, but the airfoils are constrained by the rules of competition to meet minimum bending stiffness requirements.

#### ***4.2 Stability and Robustness of Solutions***

An investigation of the effect of variations in material properties on the values of coupling and associated hygrothermal twisting curvature of the rectangular CUS beam has been carried out. The material property considered is perturbed by ten percent in each direction and the maximum changes in coupling and hygrothermal twisting curvature of the global optimum solution are recorded. The results of the study can be seen in Table 4.4. The values in the coupling column represent the range of percent change in coupling over all wall thicknesses. The values of hygrothermal twist listed are in rad/km, and are the absolute values of the deviation in twist from zero. It can be seen that among the mechanical properties the system has the greatest sensitivity to variations in  $G_{12}$  and  $E_{11}$ . This result is expected because the beam coupling phenomena results from local extension-shear-coupling within the wall.

Table 4.4: Material Property Sensitivity

Property	$S_{12}$	$k_{xy}$
$E_{11}$	1.0 -1.7	2.4-3.4
$E_{22}$	1.6-3.4	0.2-0.7
$\nu_{12}$	0.06-0.09	0.5-0.6
$G_{12}$	7.5-10.5	2.0-3.1
$\alpha_1$	-	1.7-3.0
$\alpha_2$	-	3.2-5.6
$\beta_2$	-	1.5-2.6

The sensitivity of the optimal stacking sequences to changes in ply angles has also been investigated for the rectangular CUS box beam. A close inspection of Figures 4.1, 4.2, and 4.3 appears to show higher coupling gradients in the region of the local optimum, indicating that the local optimum is more sensitive than the global optimum to changes in ply angles. This is an important practical consideration because any manufacturing technique, particularly a hand layup, will not place the plies at precisely the angle desired. Figure 4.4 summarizes the investigation of the constrained optima of a two ply beam. For a two-ply laminate, one of the ply angles has been varied plus-or-minus three degrees. The percent change in the magnitude of extension-twist coupling is plotted versus the variation from the predicted optimal angle. The figure clearly indicates that the local optimum is more sensitive than the global optimum. Comparing the gradients of hygrothermal twisting curvature for the two optima, it is seen that the global optimum is more sensitive to changes in ply angles. The two considerations must be balanced in light of particular design requirements.



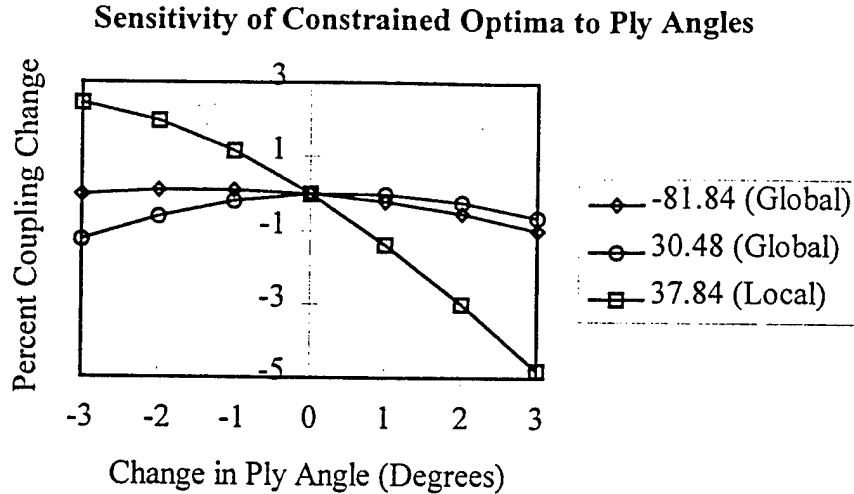


Figure 4.4: Sensitivity of 2-Ply Constrained Optima to Changing One Ply Angle.

To further study the apparent difference in sensitivity between the two optima a statistical approach has been employed. This technique allows the investigation of beams with arbitrary wall thickness and the simultaneous effects of variations in all material properties and ply angles. The method attempts to accurately reflect the variability expected in a manufacturing environment. Each input parameter has been treated as an independent random variable with normal distribution. The ply angles have been assumed to have a mean equal to the optimum predicted angle and standard deviation of three degrees. The mean value of each material property is that given previously in Table 4.4. The deviations of most material properties have been determined experimentally by manufacturing and testing 22 coupon specimens. A summary of the properties determined from this testing is given in Table 4.5. A complete listing of all experimental data from this study is given in Appendix C. The thermal and hygroscopic expansion coefficients are more difficult to measure, and therefore the deviations are assumed to be 4.0% of the respective mean values. This value is chosen using the rationale that the

coefficients are largely driven by matrix properties, as are the transverse modulus and the shear modulus. Therefore a similar percent deviation is selected.

Table 4.5: Deviations in Material Properties.

Property	Average	Deviation	% Deviation
$E_{11}$ (Gpa)	135.7	2.65	1.95
$E_{22}$ (Gpa)	9.408	0.369	3.92
$\nu_{12}$	0.3191	0.0695	21.8
$G_{12}$ (Gpa)	4.860	0.2140	4.40

The coupling and hygrothermal twisting curvature of an eight ply CUS beam have been calculated in six hundred independent trials based on the global optimum, and six hundred based on the local optimum, each time sampling every material property and ply angle from the respective normal distributions. The results are shown as bar graphs in Figures 4.5 and 4.6. These figures indicate that the conclusions based on variation of ply angles in a two ply beam, reached from Figures 4.1, 4.2, and 4.3, may not be generalized to the manufacturing of any CUS beam. The local minimum of hygrothermal twisting curvature is more robust, as seen before, but the global optimum distribution of coupling is nearly identical to that of the local optimum. The standard deviation of coupling at the global optimum is actually 4.2% higher than that of the local optimum. In addition, the standard deviation of hygrothermal twisting curvature at the global optimum is 70% higher. Thus it would appear that unless the extra ten percent of coupling is an absolute necessity the local optimum is a better sequence for manufacturing single celled beams with coupling.

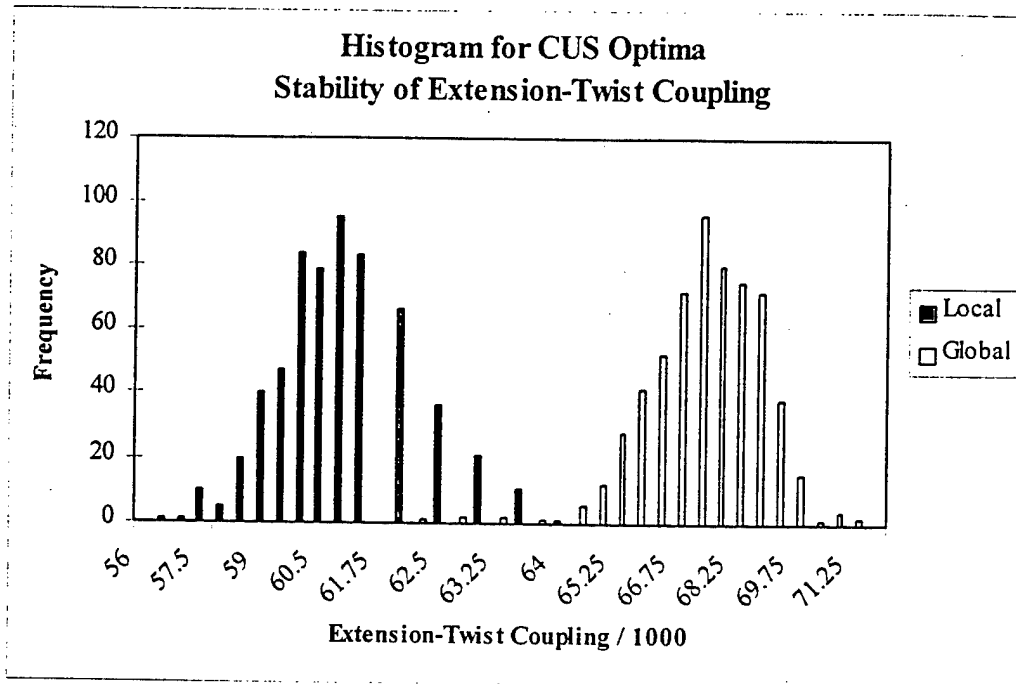


Figure 4.6: Histogram of Extension-Twist Coupling of CUS Beam.

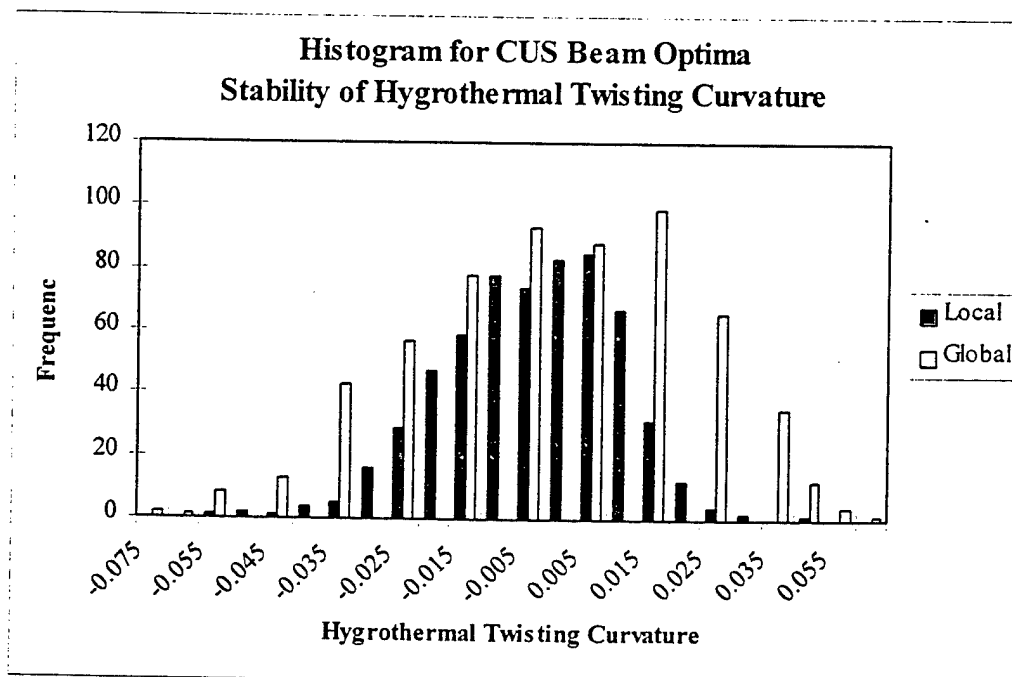


Figure 4.7: Histogram of Hygrothermal Twisting Curvature of CUS Beam.

A similar statistical analysis method has been used to investigate the sensitivity of the two-celled optima. Instead of minimization of the hygrothermal twisting curvature, in this case the undesirable forms of coupling, bending-twist coupling and bending-extension coupling, are minimized. Each input variable is again considered to be from a normal distribution and six hundred independent trials are computed, as in the single-celled case. The resulting histogram of maximum extension-twist coupling is shown in Figure 4.7, while the histograms of undesirable couplings are shown in Figures 4.8 and 4.9. The standard deviation in extension-twist coupling is  $801.6 \text{ (MN m)}^{-1}$ , approximately 40% less than the single celled optima. The minimization of bend-twist coupling is extremely sensitive to variation, with a standard deviation of  $21,847 \text{ MN}^{-1}$  about the target of zero.

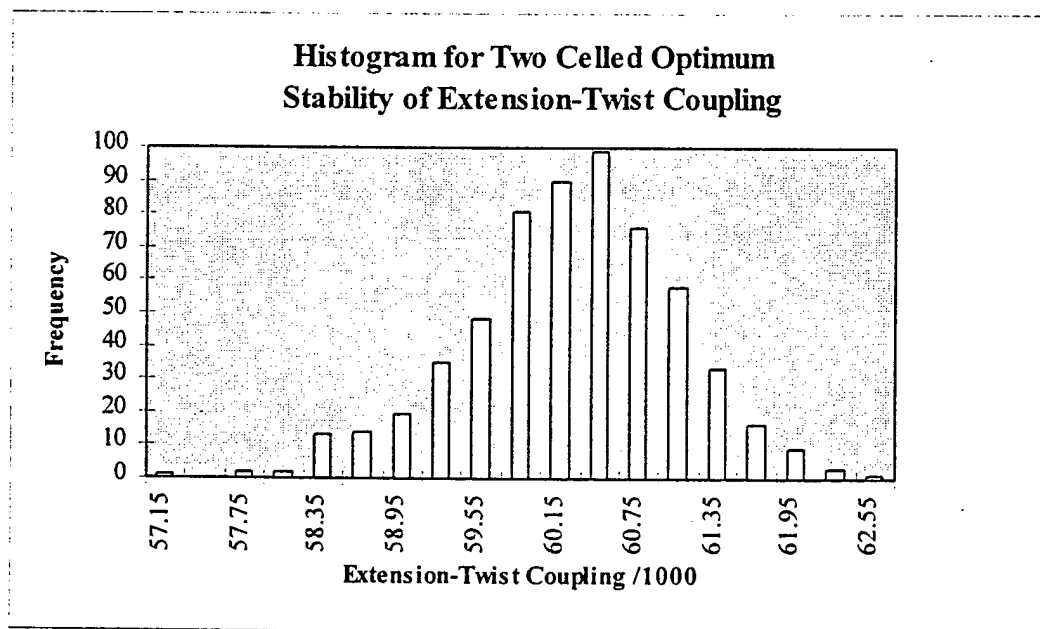


Figure 4.8: Histogram of Extension-Twist Coupling of Two-Celled Beam.

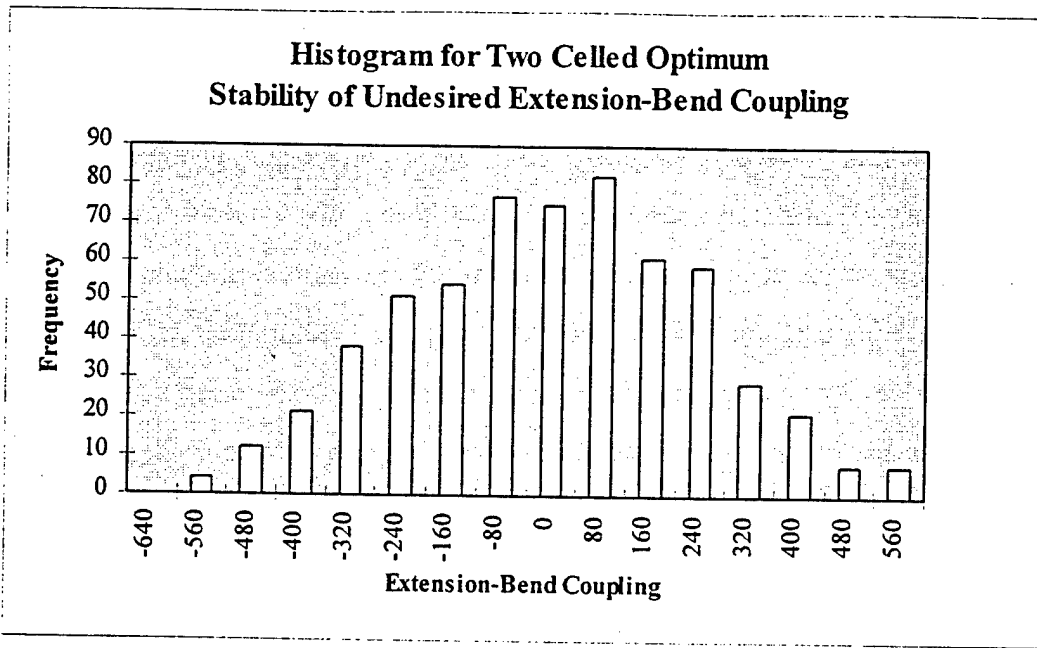


Figure 4.9: Histogram of Extension-Bend Coupling of Two-Celled Beam.

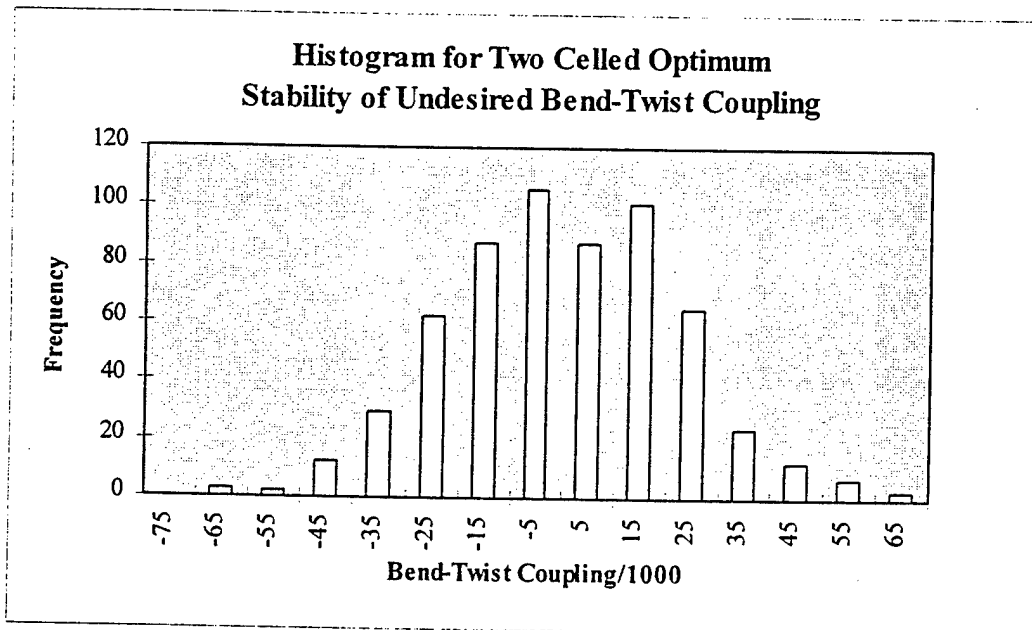


Figure 4.10: Histogram of Bend-Twist Coupling of Two-Celled Beam.

## Chapter 5 - Experimental & FEM Verification

---

The experimental plan is presented, along with a discussion of results from testing of all specimens manufactured.

### *5.1 Experimental Plan*

Beam specimens have been manufactured to verify the results of the optimization routine. An initial attempt to make high quality single-celled beams was made using a mold consisting of an aluminum channel section mated with a flat piece of aluminum plate to form an external mold. The edges of the channel section were machined into ridges, and matching grooves were machined into the plate. The two pieces then fit together without slipping. The mold pieces may be seen in Figure 5.1. The first step in the manufacturing process was wrapping layers of prepreg around a wooden mandrel. Upon completion of the wrapping process, the mandrel was removed and the composite tube inserted into the aluminum channel section. Including a layer of Teflon film between the mandrel and the composite facilitates the removal of the mandrel. This Teflon layer was left inside the composite tube to provide a smooth surface finish. A similar layer of Teflon was wrapped around the outside of the tube before insertion into the mold to make it easier to remove the beam from the mold after curing. The entire assembly was then vacuum bagged by inserting a tube of bagging material through the center of the assembly, slipping another over the outside, and sealing the ends.

The beam was then cured in an autoclave using the cure cycle illustrated in Figure 5.2. A photo of the autoclave is included in Figure 5.3.

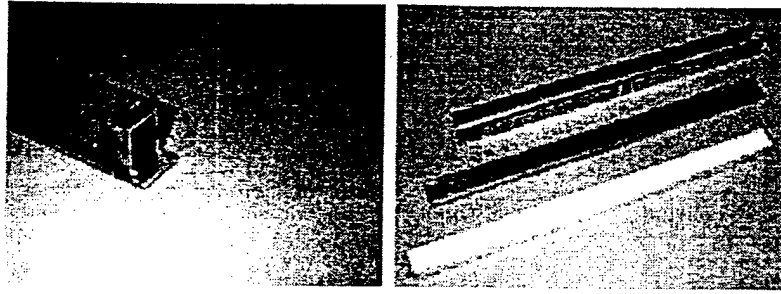


Figure 5.1: Photographs of Initial Single-Celled Beam Mold.

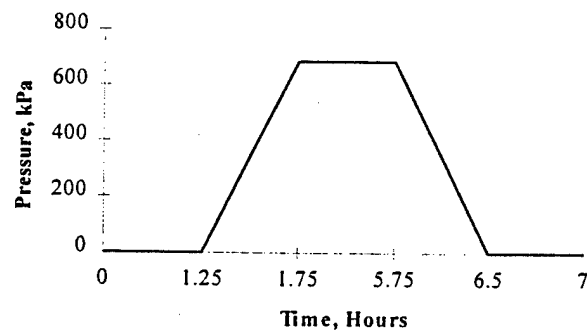
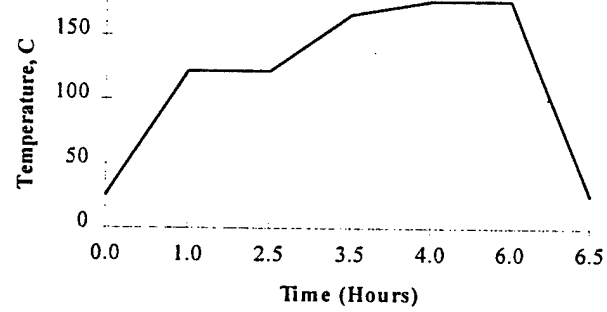


Figure 5.2: Cure Cycle.

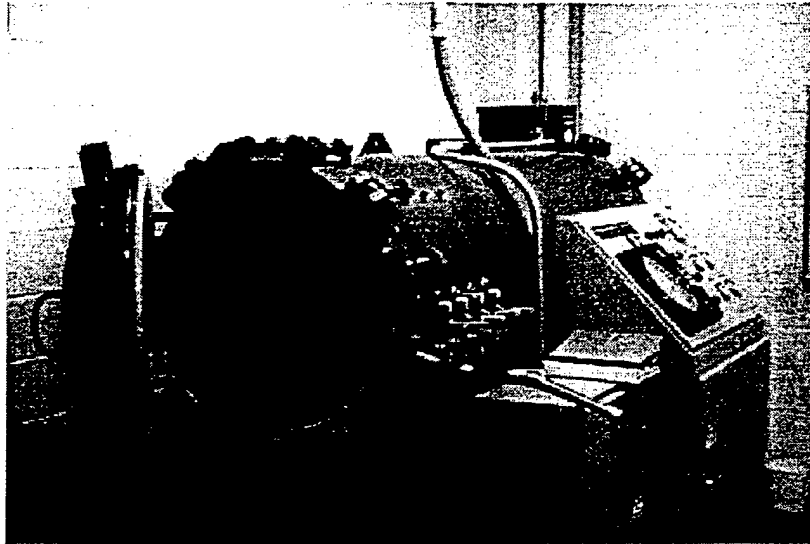


Figure 5.3: Autoclave Used for Curing All Specimens.

The main difficulty encountered during the manufacturing of this beam was determining the correct size of the mandrel. The prepreg is extremely difficult to wrap tightly around the mandrel so that the beam formed is somewhat larger than the mandrel. When the mandrel is too small, the perimeter of the composite box section formed is too small and the corners of the mold are not filled in. The corners of the resultant beam are rounded, pockets of resin are present in the corners, and delaminations exist within the composite in the region near the corners. When the mandrel is too big, the composite no longer fits well within the mold, and the two sections of the mold do not mate as intended. The manner of determining the correct mandrel size was simply trial-and-error. A photo of a beam specimen is shown in Figure 5.4.



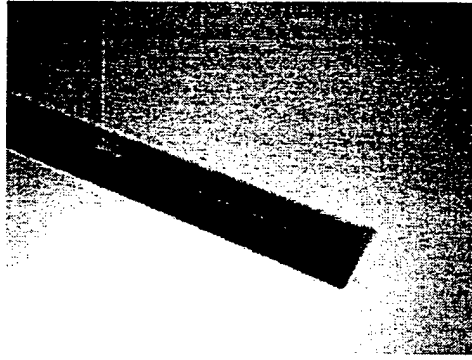


Figure 5.4: Photograph of Single-Celled Beam Specimen.

No matter what size mandrel was used, the pockets of resin in the corners were not eliminated. The eight layers of composite were too stiff for the pressure to force into the corners. For this reason a second, similar, mold was manufactured. This one has its split just above the mid-plane. The same technique of using mating ridges and grooves is employed to align the two halves. All four corners are machined with a  $3/16$ " radius fillet. The manufacturing process used with this mold is the same as detailed above with two exceptions. The first is that peel-ply is used as the layer between the wooden mandrel and the inner ply of composite to improve flow of resin into the breather/bleeder cloth. Also, a release agent is applied to the mold instead of using a Teflon layer on the outside. This mold is shown with a sample beam in Figure 5.6. Beams produced with this mold show a much higher quality. The only problem being very small ridges of composite are formed and cured in the gap between the two mold sections.

Another difficulty encountered during manufacturing was cutting and laying up the prepreg at the correct angles. It is estimated that the resultant ply angles were within three degrees of the intended angles. As seen in Section 4.2, this has a small effect on the coupling and hygrothermal twisting curvature of the beam. It also should be noted that the physical dimensions of the beams constructed do not exactly match the values used in the optimization because of the necessity of redesigning and building a second mold. The actual major cross section dimension is 3.20 cm instead of 3.18 cm, and the aspect ratio is

0.791 instead of 0.792. The effect of this change in geometry on the predicted results is small, reducing the peak coupling magnitude by approximately 1.1%.

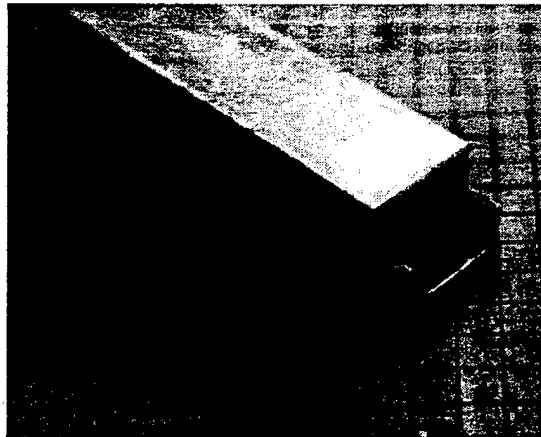
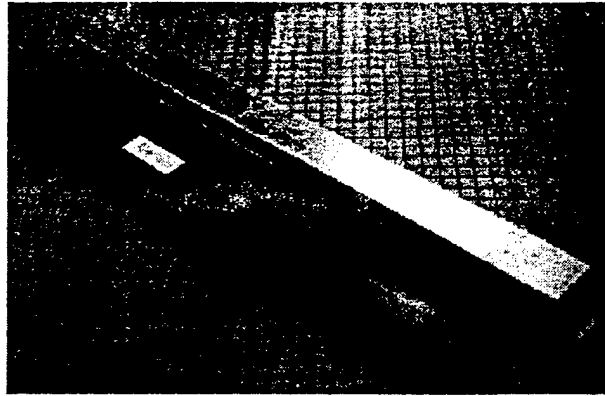


Figure 5.5: Photographs of Final-Mold for Single-Celled Beams, Sample Beam.

The beams with two-celled cross-sections have been manufactured using a completely different process. Layers of composite were cured over two aluminum, box-shaped molds. To facilitate a tight fit, the composite was wrapped around a round mandrel with a circumference slightly smaller than the perimeter of the box-shaped molds. The wrapped tube was slid off the round mandrel and over the mold. These wrapped molds were then placed back-to-back so that the adjacent faces of the composite tubes formed the web of the beam. The process was completed by and over-wrapping the

assembly with the final plies. Again it has been necessary to use trial-and-error to determine the correct size of the mandrel used for laminating the composite. Curing was done with the aluminum mandrels in place. Pressure plates on the four outside faces of the beam insure a smooth surface and prevent the two mandrels from becoming misaligned when vacuum is applied. Use of release agent allowed the two mandrels to be removed with little difficulty from the cured, two-celled beam. Photographs of the mold and a finished beam are shown in Figure 5.5.

Like the single-celled beams from the second mold, the dimensions of the two-celled beams do not exactly match the values used in the optimization. The major dimension is 3.38 cm instead of 3.18 cm and the aspect ratio is 0.797 instead of 0.792. This change in geometry lowers the predicted value of coupling at the optimum configuration from  $61.55 \text{ (MN m)}^{-1}$  to  $54.13 \text{ (MN m)}^{-1}$ . Unfortunately, only one two-celled beam was manufactured to a sufficient level of quality before the supply of T300 composite was exhausted.



Figure 5.6: Photographs of Sample Beam, Mold for Two-Celled Beams.

The lack of any twist when a CUS beam is removed from the mold after curing verifies that the constraint regarding hygrothermal warping has been successfully met. Measured values of this hygrothermal twisting curvature for all manufactured box beams are shown in Table 5.1. Note that the numbers in the Predicted Value column have bee

computed using the actual geometry of the manufactured beams, not the geometry assumed in the optimization. Nine eight-ply CUS beams have been manufactured. The beams denoted B1G and B2G have the global optimum stacking sequence, but were made using the first box beam mold. They are resin rich and have accumulations of resin in the corners of the cross section. Beam B3G was manufactured in the second mold with the global optimum stacking sequence. Beams B4G and B5G have stacking sequences that vary slightly from the global optimum. Every ply angle in the sequence has been shifted three degrees. In beam B4G, the plies were shifted from  $28.1^\circ$  to  $31.1^\circ$  and from  $-78.3^\circ$  to  $-75.3^\circ$ . In beam B5G the plies were shifted from  $28.1^\circ$  to  $25.1^\circ$  and  $-78.3^\circ$  to  $-81.3^\circ$ . Beams B1L and B4L have been manufactured with the local optimum stacking sequence, B1L without the use of peel ply. It therefore has a higher resin content than the other local optimum beams. Beams B2L and B3L were made with the local optimum ply angle shifted by three degrees. In beam B2L the angle is  $34.8^\circ$ , and in beam B3L the angle is  $40.8^\circ$ .

Table 5.1: Out-of-Mold End-to-End Twist for All Box Beams.

Beam	Twist (deg)	Length (m)	Twist/Length (rad/m)	Analytical Prediction
B1L*	13.0	0.452	0.501	0.000
B2L	12.0	0.456	0.460	0.044
B3L	13.5	0.448	0.526	0.060
B4L	7.0	0.445	0.275	0.000
B1G**	2.3	0.454	0.086	0.000
B2G**	2.5	0.456	0.096	0.000
B3G	2.0	0.454	0.077	0.000
B4G	2.0	0.451	0.077	0.005
B5G	3.3	0.451	0.126	0.002

\* Made with second mold, without peel ply. Resin rich.

\*\* Made with initial mold. Pockets of resin in corners.

It is noteworthy that the beams constructed at or near the global optimum solution have very little twist, while those at or near the local optimum have twist roughly five

times greater. As discussed in Section 4.2, this contradicts the result expected from variation in material properties and ply angles about the assumed mean values. This leads to the possible conclusion that the values of the hygrothermal properties used, the assumed temperature at which the resin cures, the assumed change in moisture content, or a combination of these parameters are inaccurate.

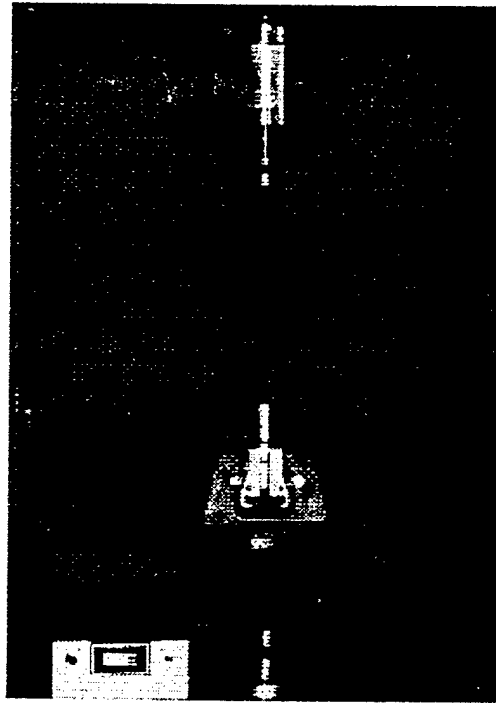


Figure 5.7: Photo of Extension-Twist Testing Setup.

## ***5.2 Measured Values***

The value of extension-twist coupling in each beam is measured using the patent-pending apparatus of Ref. 38 mounted on an Instron test machine. This device was developed with testing of laminates with extension-twist coupling, and consists essentially of an air bearing with an optical encoder attached to the piston. The piston of the bearing is free to rotate within the housing, driving the optical encoder. One end of the specimen is clamped into the test machine, and the other is attached to the piston of the bearing. Load is applied by controlling the flow of air through the bearing, and is

indicated by the load cell of the Instron. Unfortunately, the gears driving the optical encoder contained some backlash that easily accounted for when measuring laminates with large end-to-end twist. The amount of backlash was approximately equal to the total twist in the much stiffer beams measured in this work, necessitating the use of a laser technique.

A small laser was mounted to the torsionally free end of the beam, pointed at a chalkboard approximately 5 meters away. Movements of the light on the chalkboard were converted into angles of rotation of the end of the beam using simple trigonometry. This technique is estimated to be accurate to within one tenth of a degree. Figure 5.7 contains a photograph of the transducer (without the laser) mounted in the test machine, testing a coupon specimen. The fixtures attaching the specimens to the testing equipment were steel plugs inserted into the ends of the beams. Clamps were then applied to the outside of the beam to prevent it from slipping on the fixture. The fixtures used for testing two-celled beams have a slot machined through the center of the insert to match the thickness of the web.

The source of air for the air-bearing transducer was a typical shop air compressor. A faucet-type valve on the compressor controlled the amount of air flowing through the bearing, and hence the applied axial load. Due to the limited supply of air, it was necessary to apply the maximum amount of load at the start of a test, and take measurements as the load was decreased to zero. The time to apply the maximum load of 1.2 kN was approximately one second. The load was then gradually decreased to zero over a period of about fifteen seconds.

Table 5.2: Measured Extension-Twist Coupling for CUS Box Beams.

Beam	Experimental	Analytical	Difference
B1G	56.1	68.3	17.9%
B2G	55.7	68.3	18.4%
B3G	54.0	68.3	20.9%
B4G	50.0	67.2	25.6%
B5G	54.1	67.1	19.4%
B1L	60.3	60.9	1.0%
B2L*	70.6	65.0	-8.6%
B3L	62.4	55.8	-11.8%
B4L	61.9	60.9	-1.6%

\* This beam cracked during testing.

A sample of the test data is shown in Figure 5.8. The data is very much linear throughout the test range, indicating that the testing equipment is performing without slippage in the linear elastic regime of the material. Data for all of the single-celled beams tested is presented in Appendix D. A comparison of measured coupling values with predicted values for each beam is shown in Table 5.2. Note that the predicted values are computed with the actual beam geometry, not the geometry assumed in the optimization routine. This explains the difference between the values for optimum configurations listed here and those in Tables 4.2, 4.3, and 4.4.

The global optimum beams do not agree well with the prediction, with an average difference between experimental and predicted values of 20.4 percent. Recall that these are constrained optima, and are not the sequence corresponding to the top of the peak in coupling. The only verification seen in this data is that beams B4G and B5G have slightly lower coupling than the beams with optimum configuration. The two beams constructed with the local optimum ply sequence have couplings within 1.6 percent of the predicted value. Beam B2L was observed to be cracked after testing, so that beam provides no information. The other beam with shifted ply angle has coupling approximately the same as the two beams with the optimum angle. The coupling of beam

B3L is actually 0.8 and 3.5 percent higher those with the optimum ply angle when it should be lower.

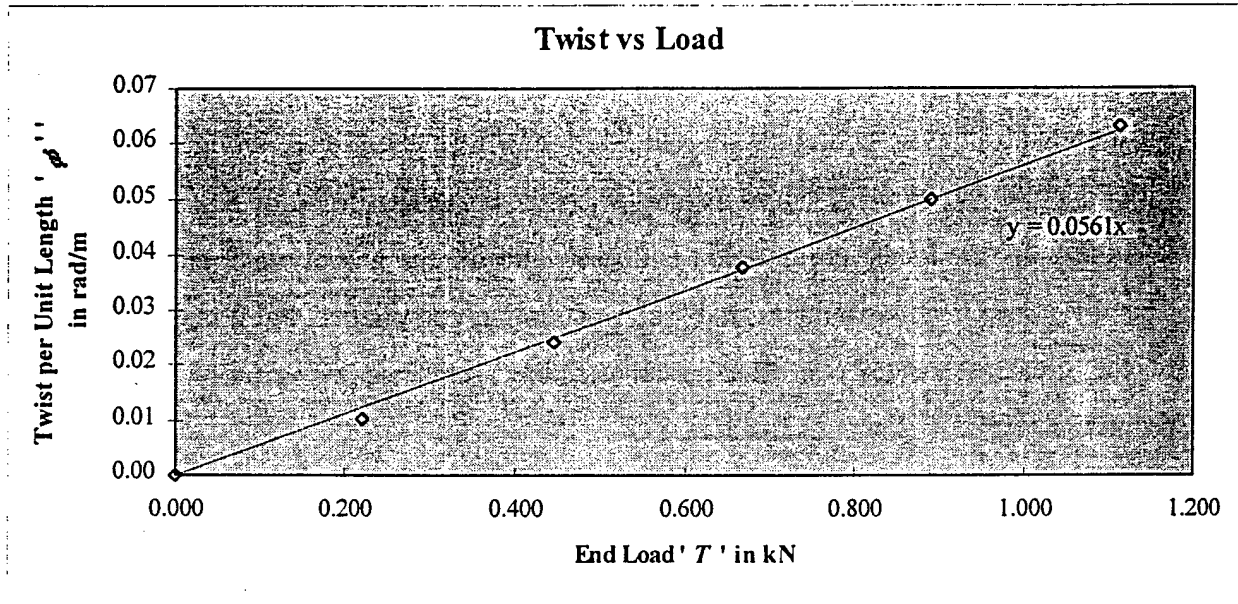


Figure 5.8: Sample CUS Extension-Twist Test Data.

The discrepancies between the theoretical predictions and measured values for the beams with the global optimum sequence are explained by the difference in the material properties used in the analysis. The coupons used for material property testing were manufactured in an aluminum mold with aluminum pressure plates. Therefore resin was only able to bleed out at the edges and ends of the laminate. As described previously, the beams were manufactured with a layer of peel ply on the inside surface. Visual inspection of the coupons and beams confirms the expected result, that the coupons have a higher resin content than the beam walls. Clearly this difference in fiber and matrix volume fraction implies a difference in material properties, particularly those most dependent on the matrix properties such as  $E_{22}$  and  $\alpha_2$ . Given this variability, it is surprising that the beams manufactured at the local optimum had the predicted properties.



To test whether variability in material properties affects the stiffness of the global stacking sequence more than the local, the extensional compliance of the beam has been measured by attaching strain gauges to the sides of one local and one global optimum beam. This practical indicator is the only property besides extension-twist coupling that can be easily measured. The predicted values of extensional compliance are  $1036 \text{ MN}^{-1}$  for the local optimum configuration and  $742.6 \text{ MN}^{-1}$  for the global configuration. The experimentally determined values are shown by the curve fits in Figure 5.9. The percent difference for the local configuration is 2.25%, and for the global configuration 5.06%. This difference is not as large as that seen in coupling compliance, but it is an indication of the greater sensitivity of the global stacking sequence to variation in material properties caused by lower resin content.

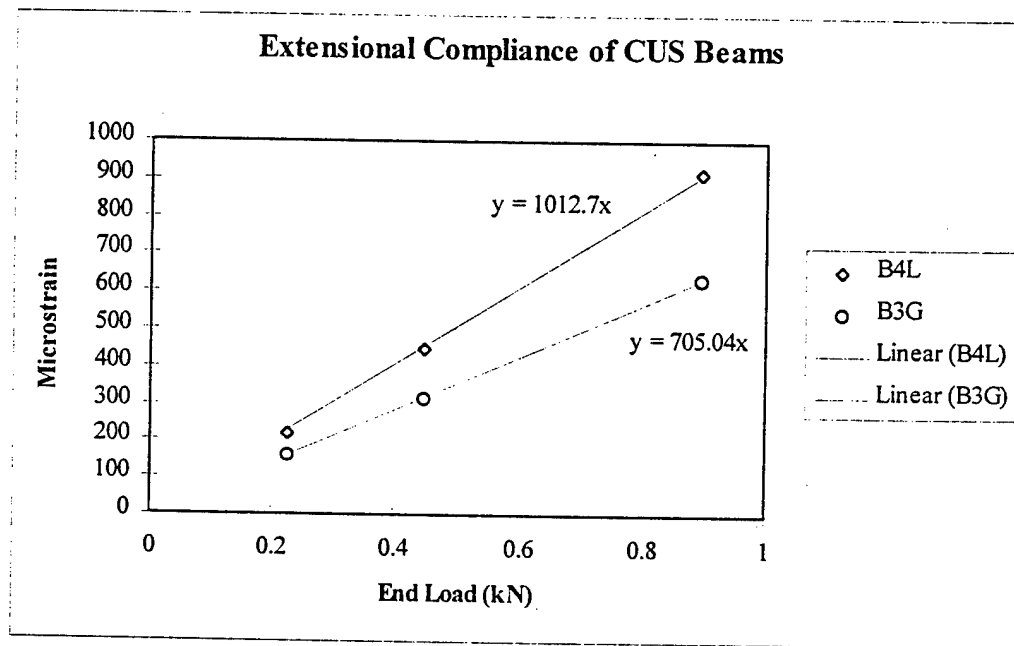


Figure 5.9: Comparison of Extensional Compliance of CUS Beams.

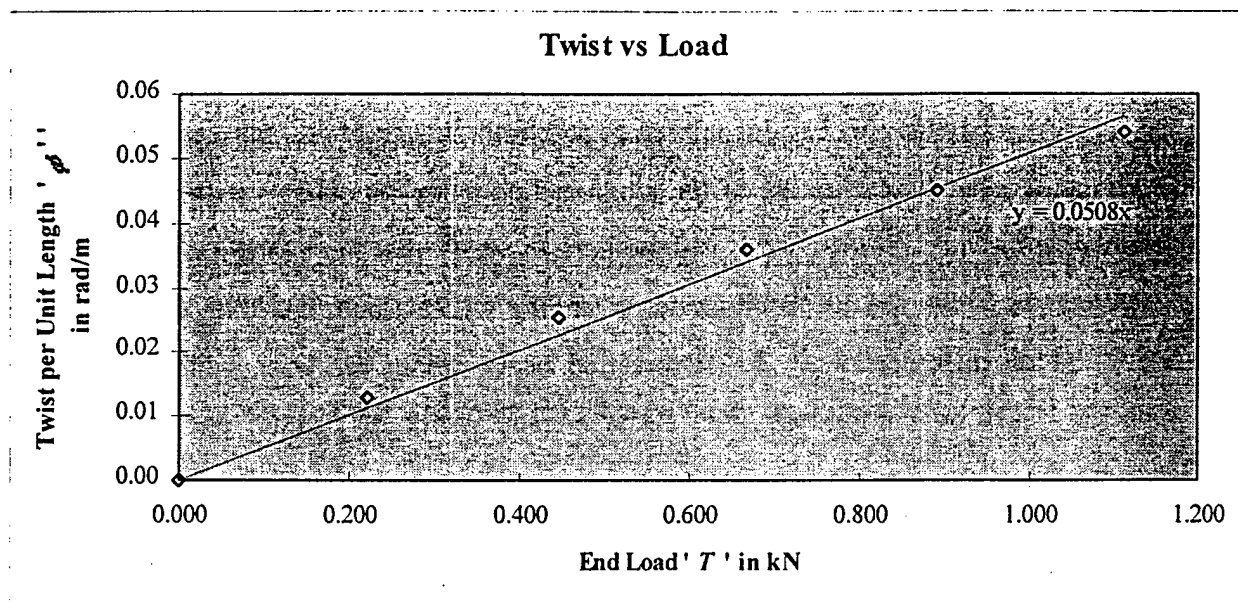


Figure 5.10: Two-Celled Extension-Twist Test Data.

The two-celled beam has also been tested for its coupling compliance. The data is plotted in Figure 5.10. Taking into account the actual geometry of the manufactured specimen and recalculating the value of extension-twist coupling at the optimum stacking sequence yields  $54.1 \text{ (MN m)}^{-1}$ . The measured value of coupling compliance is  $50.8 \text{ (MN m)}^{-1}$ , which is 6.15% below the predicted value. This can be partly due to the fact that the surface of the beam is not perfectly smooth. Some wrinkling is present at the corners because the plug was not the correct size to match the mandrel. The difficulty in constraining the bend-extension coupling to zero may also contribute. (See Section 4.2) The fixture for measuring extension-twist coupling constrains the ends of the beam against rotation in bending. If the beam has some bending-twist coupling but is restrained from bending by the fixture, then the resultant twisting deformation would likely be affected.

### 5.3 Finite Element Verification

The commercial finite element package ABAQUS has been used to verify that the sequences predicted to be unconstrained optima do result in maximum coupling. Although the analytical model of the single-celled beam has been verified using finite element techniques, further work is done here to verify that the specific combination of material properties and the configurations leading to maximum coupling do not lead to undiscovered discrepancies. The two-celled beam model has been validated for two specific cases by comparison with finite element work of Gandhi and Lee<sup>42</sup>, but a systematic verification has not been undertaken. This work provides more evidence of the accuracy of the model.

The CUS box beam and two-celled beam configurations used as the representative beam throughout this work has been used in the case of single-celled beams. The values of extension-twist coupling predicted by the finite element code are within 0.50% of the prediction, and the predicted optimum angles have been verified to within three tenths of a degree. A summary of finite element analyses run in the vicinity of each optimum is presented in Table 5.3. In addition to those presented, a selection of other single- and two-celled cases has been run to verify the accuracy of both  $S_{11}$  and  $S_{12}$ . In general,  $S_{11}$  values are within 1.5% and  $S_{12}$  values are within 0.5%. Sample ABAQUS input and output files are presented in Appendix E.

The models of both the single- and two-celled beams maintain the same cross-section dimensions as those used in the optimization (Section 4.1). For convenience, the length is made one meter, divided into 150 elements. The CUS box beam has 18 elements per cross section: five on each long side and three on each short side. A wire mesh illustration of the single-celled finite element model is shown in Figure 5.11. The two-celled beam has four elements comprising each of the four sides and the web, for a total of 20 elements per cross section. An illustration of the two-celled finite element model is shown in Figure 5.12. All elements are 4-node, doubly curved, reduced integration shell elements (ABAQUS S4R elements) using six degrees of freedom per

node. These elements allow the definition of a layered composite cross section. The total number of elements is 2700 for the CUS box beam, with 16,308 variables in the model. For the two-celled beam, the number of elements is 3000, and the number of variables is 17,214. In each case, an axial load of 1 kN is applied. The displacements of the tip of the beam are measured by averaging the displacement and rotation of the nodes comprising the end cross section. Simply dividing the displacement and rotation by the load yields the magnitudes of extensional and extension-twist compliance, respectively.

Table 5.3: Comparison of FEM and Analytical Results.

Configuration	Stacking Sequence	S12(FEM)	S12(Ana)	$\Delta$ %
1-Celled Local	28.25 <sub>g</sub>	69.153		
	28.45 <sub>g</sub>	69.157	69.490	0.48%
	28.65 <sub>g</sub>	69.157		
1-Celled Global	[30 <sub>7</sub> /-83.2]	71.321		
	[30.19 <sub>7</sub> /-83.53]	71.332	71.700	0.51%
	[30 <sub>7</sub> /-83.8]	71.326		
Two-Celled	[-83.7\83.7\29.2]	61.280	61.552	0.44%
	[-83.9\83.9\29.1]	61.285		
	[-84.0\84.0\29.0]	61.287		
	[-84.1\84.1\28.9]	61.286		

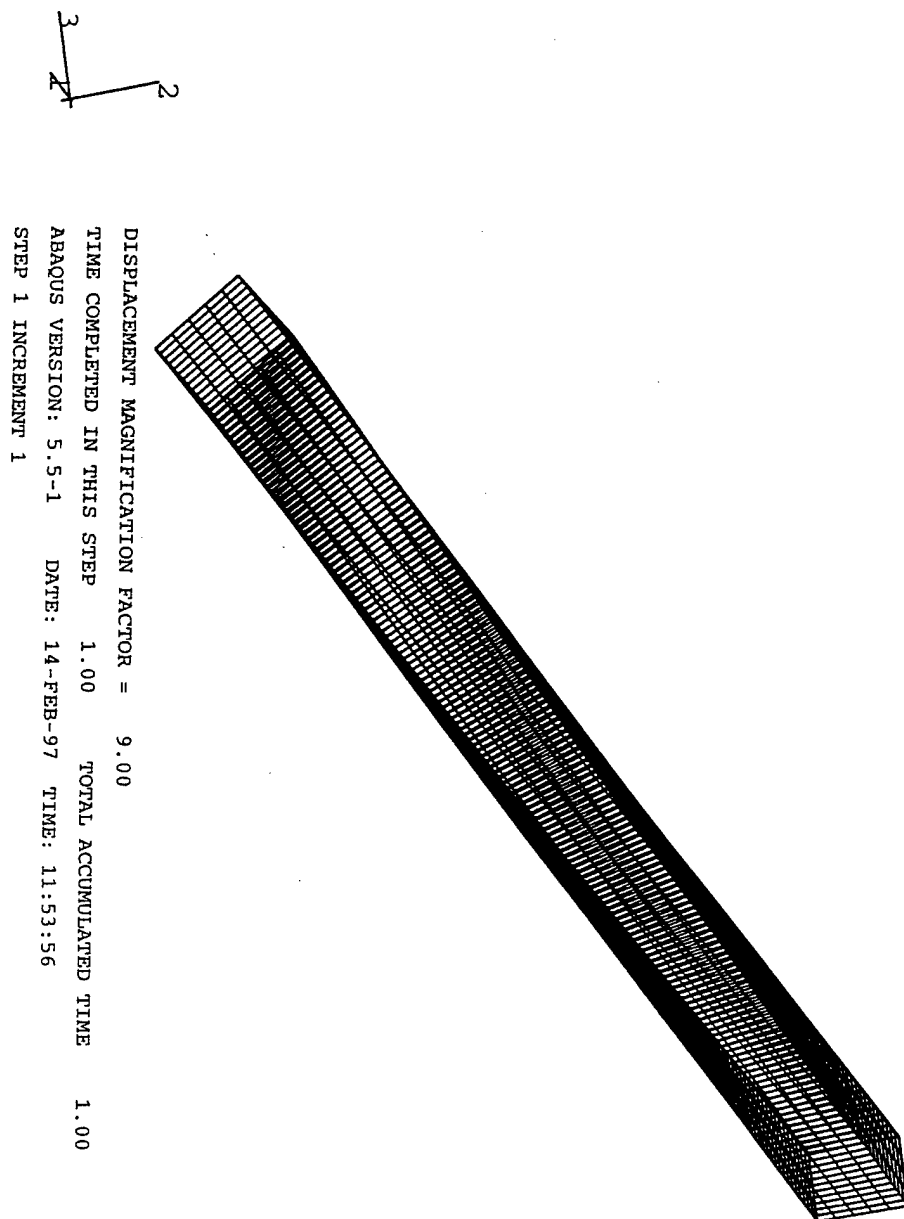


Figure 5.11: Finite Element Mesh for Single-Celled Beams.

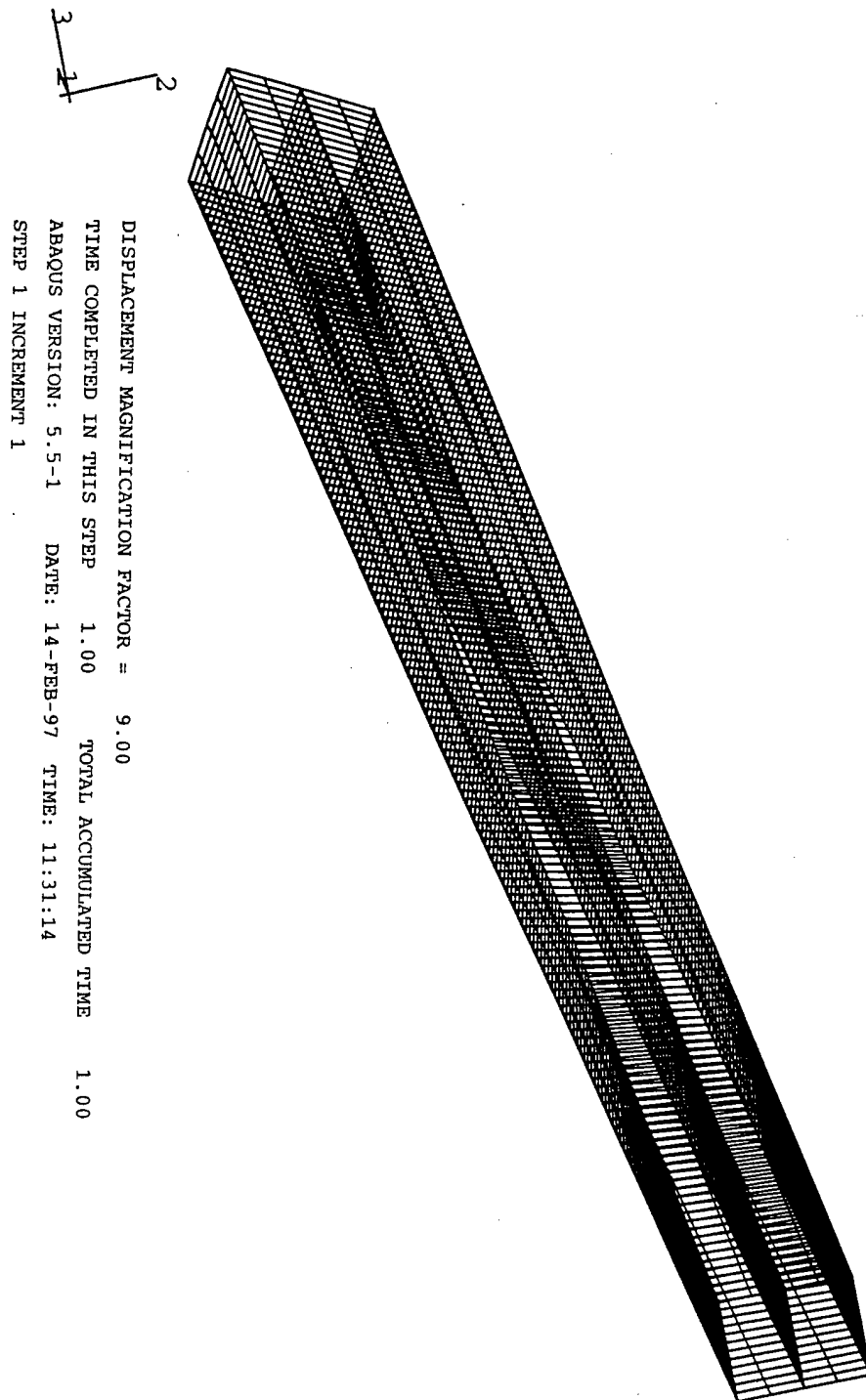


Figure 5.12: Finite Element Mesh for Two-Celled Beams.

## Chapter 6 - Conclusions & Recommendations

---

The design of thin-walled, closed section composite beams has been treated in a comprehensive manner. A gradient based constrained optimization scheme has been developed for obtaining the maximum coupling subject to practical design considerations. The stacking sequences for producing the maximum extension-twist coupling of CUS single-celled beams and two-celled beams, and bending-twist coupling in CAS single-celled beams have been determined. Constraints have been imposed using the Sequential Unconstrained Minimization Technique. For single-celled beams, the hygrothermal deformation of the beam is minimized through the use of an exterior penalty function. A second constraint imposed is that the first two natural frequencies of each mode shape are distinct from a single specified frequency. This constraint has been implemented by the use of an extended interior penalty function. The two-celled beams have been constrained so that only one form of coupling is present.

The results of the optimization of a CUS single-celled beam show that the hygrothermally constrained optima are very close to the unconstrained optima, so that the magnitude of coupling obtained drops only by approximately three percent. In each case of wall thickness varying from two to eight plies, the constrained global solution incorporates two ply angles. A constrained local optimum exists with only one ply angle. The difference in coupling magnitude between these solutions is about ten percent. The same stacking sequence that maximizes extension-twist coupling in a CUS beam also maximizes bend-twist coupling in a CAS beam because both result from local extension-shear coupling within the beam walls.

The sensitivity of the two optima of interest to variations in material properties and ply angles has been investigated. An important result of this work is the finding that

the coupling and hygrothermal twist of the beam show most sensitivity to the shear modulus,  $G_{12}$ , and the transverse Young's modulus,  $E_{22}$ , of the material. This result makes intuitive sense because the beam coupling results from local extension-shear coupling in the walls. As expected, variations in the thermal and hygroscopic properties of the composite effect the resultant twist without changing the coupling produced.

A statistical technique has been used to model the variability which might be expected in a manufacturing environment. This can be a practical tool allowing a designer to build factors of safety into a design, or to establish requirements for a manufacturing process. The results reveal that the magnitudes of coupling for the two configurations are approximately equally sensitive to variability in material properties and ply angles. However, the constrained hygrothermal twisting curvature of the global optimum has 70% more sensitivity. In addition, the simplicity of manufacturing the local solution makes it a desirable configuration. It could be practical in any situation with a combination of constraints and loading that do not prohibit a unidirectional configuration.

Nine different CUS beams have been made in an attempt to verify the optimality of the predicted solutions. Two beams manufactured at the local optimum solution have coupling within 1.6% of the predicted value. Two beams made with stacking sequences perturbed three degrees from the local optimum show the expected changes in coupling. Five beams manufactured at or near the global optimum have coupling that is approximately twenty percent less than predicted, but show the appropriate small decrease in coupling as the stacking sequence is shifted. Beams with both stacking sequences show the expected behavior with regard to hygrothermal twisting curvature. Beams with stacking sequences shifted from the optimum have increased twist. The beams constructed with the global optimum solution have significantly less coupling than those with the local solution. This unexpected behavior is attributed to material properties differing from those measured by testing of coupon specimens.



The constrained optimization scheme has also been applied to beams with two-celled cross sections. The constraint applied to the two-celled beams is that only one form of coupling may be present, in this case extension-twist coupling. The most interesting solutions to this problem are for beams with webs located away from the center of the cross section. Elastic tailoring can be used to reduce, and in many cases eliminate, the bend-extension coupling induced by this geometry. A limitation on the type of construction of the beam has been made so that experimental verification could be undertaken. In this situation, the global optimum solution is also the simplest to manufacture. A simple manufacturing technique for two-celled beams has been developed, and one beam made with a web in the center of its cross section. It has been tested and found to have extension-twist compliance within 6.2 percent of the predicted value.

The stochastic approach to assessing the sensitivity of the optimum configuration has been applied to the two-celled beam with centered web. Results indicate that the global optimum of extension-twist coupling is insensitive, with a standard deviation approximately one percent of the mean. The difficulty that may make the configuration impractical for many applications, arises because bending-twist coupling, which is constrained by the optimization to be zero, has an extremely high level of sensitivity.

A finite element method has also been used for comparison with the theoretical and experimental work. The three unconstrained optima primarily discussed in this work have been assessed. The results match the predicted values of extension-twist coupling to within one percent for both single- and two-celled beams. The extensional compliance of the beams has also been compared, and the FEM results agree with the theoretical prediction to within two percent. The predicted optimum stacking sequences are also verified to within three tenths of a degree.

This thesis provides a tool that facilitates design of elastically tailored, thin-walled, closed section beams. To address this need, a gradient based search algorithm

has been shown to work well with the selected beam theory. It has been shown that, whether in an unconstrained situation or in the face of multiple constraints on structural behavior, certain configurations exist that maximize elastic coupling. These conclusions have been verified with both finite element and experimental techniques.

The research presented here suggests several possibilities for continuation and expansion of the work. In the experimental category, one area is the manufacturing of several two-celled beams to verify the optimality of the predicted stacking sequence. More development of the manufacturing technique and investigation of configurations with off-center web are needed. Testing of dynamic characteristics of the single-celled beams to verify the theory and finite element results presented in the literature is necessary before the natural frequency constrained optimization presented in this work can be applied with confidence.

In the area of optimization, it would be a straightforward process to include additional constraints such as strength, stiffness, and buckling load. Achieving a specified level of torsional rigidity is a practical design issue for implementation of extension-twist coupling in rotor blade design, where a lower bound on torsional rigidity is required to maintain aeroelastic stability. This could be included in the optimization scheme either as a constraint requiring the level of torsional rigidity to be above a specified value, or by reformulating the objective function to maximize the ratio of coupling compliance to torsional compliance. Further investigation of two-celled solutions is warranted. Stacking sequences representing local optima should be investigated for sensitivity of the constrained forms of coupling. Also, other configurations may be found that are easily manufactured and lower levels of sensitivity than the configuration of two independent cells with overwrap that is considered here.

In the field of analytical research, a challenging topic for consideration is the effect of damage on the coupling properties of the beams. This is key in practical implementation since demonstration of damage tolerance is required, particularly so for

an airfoil relying on coupling for performance. In general, advancing the state of the art is necessary to allow design of practical rotorcraft airfoils, including torque tube, sandwich construction, weighted leading edge, and hybrid construction.

## References

---

- [1]. Smith, E. C. and Chopra, I., "Formulation and Evaluation of an Analytical Model for Composite Box-Beams," *Journal of the American Helicopter Society*, v36, n3, Jul 1991, pp. 23-25.
- [2]. Kim, C. and White, S. R., "Laminated Composite Thin- and Thick-Walled Beam Theory and Coupled Deformations," Recent Advances in Composite Materials, ASME Materials Division Publication, ASME, 1995, pp. 167-177.
- [3]. Rehfield, L. W., "Design Analysis Methodology for Composite Rotor Blades," *7th DoD/NASA Conference on Fibrous Composites in Structural Design*, AFWAL-TR-85-3094, Denver, CO, Jun 1985, pp. (V(a)-1)- (V(a)-15).
- [4]. Rehfield, L. W., Hodges, D. H., and Atilgan, A. R., "Some Considerations on the Nonclassical Behavior of Thin-Walled Composite Beams,"
- [5]. Reissner, E., and Tsai, W. T., "Pure Bending, Stretching, and Twisting of Anisotropic Cylindrical Shells," *Journal of Applied Mechanics*, v39, Mar 1972, pp. 148-154.
- [6]. Bauchau, O. A., Coffenberry, B. S., and Rehfield, L. W., "Composite Box Beam Analysis: Theory and Experiments," *Journal of Reinforced Plastics and Composites*, v6, n1, Jan 1987, pp. 25-35.

- [7]. Barbero, E.J., Lopez-Anido, R., and Davalos, J. F., "On the Mechanics of Thin-Walled Laminated Composite Beams," *Journal of Composite Materials*, v27, n8, 1993, pp. 806-829.
- [8]. Rand, O. and Barkai, S., "Analytic Insight into the Structural Couplings and Nonlinear Formulation of Solid and Thin-Walled Composite Blades," Annual Forum Proceedings of the American Helicopter Society, v2, 1996, pp. 927-941.
- [9]. Hodges, D. H., Atilgan, A. R., Fulton, M. V., and Rehfield, L. W., "Free Vibration Analysis of Composite Beams," *Journal of the American Helicopter Society*, v36, n3, Jul 1991, pp. 36-47.
- [10]. McGee, O. G., "Effect of Warping-Pretwist Coupling on the Natural Vibration of Torsionally Clamped-Pinned Thin-Walled Open-Profile Bars," *International Journal for Numerical Methods in Engineering*, v35, 1992, pp. 325-349.
- [11]. McGee, O. G., "Closed-Form Effects of Warping and Pretwist on the Torsional Vibration of Thin-Walled Open-Profile Cantilevers," Thin-Walled Structures, Elsevier Science Publishers Ltd., UK, 1992, pp. 217-244.
- [12]. Song O. and Librescu, L., "Free Vibration Analysis of Anisotropic Composite Thin-Walled Beams of Closed Cross-Section Contour," *Journal of Sound and Vibration*, v167, n1, 1993, pp. 129-147.
- [13]. Bank, L. C. and Kao, C. H., "The Influence of Geometric and Material Design Variables on the Free Vibration of Thin-Walled Composite Material Beams," *Journal of Acoustics, Stress, and Reliability in Design*, v111, n3, Jul 1989, pp. 290-297.

- [14]. Bank, L. C. and Kao, C. H., "Dynamic Response of Thin-Walled Composite Material Timoshenko Beams," *Journal of Energy Resources Technology*, v112, Jun 1990, pp. 149-154.
- [15]. Tutuncu, Winckler, "Thermally Induced Twist in Composite Tubes and their Applications to Helicopter Blades with Controllable Twist," *Journal of the American Helicopter Society*, v39, n1, Jan 1994, pp. 41-49.
- [16]. Kollar, L., P., "Approximate Analysis of the Temperature Induced Stresses and Deformations of Composite Shells," *Journal of Composite Materials*, v28, n5, 1994, pp. 392-414.
- [17]. Berdichevsky, V., Armanios, E. A. and Badir, A. M., "Theory of Anisotropic Thin-walled Closed-cross-section Beams," *Composites Engineering*, v2, n5-7, 1992, pp. 411-432.
- [18]. Badir, A. M., Analysis of Advanced Thin-Walled Composite Beams, Ph.D. Thesis Dissertation, Georgia Institute of Technology, 1992, Ch. 4,5.
- [19]. Badir, A. M., "Theory of Anisotropic Thin-Walled Closed-Section Beams with Hygrothermal Effects," *33rd AIAA/ASME/ASCE/AHS/ASC Structures, Structural Dynamics and Materials (SDM) Conference*, Dallas, TX, AIAA-92-2543-CP, pp. 1078-1092.
- [20]. Armanios, E. A., and Badir, A. M., "Free Vibration Analysis of Anisotropic Thin-Walled Closed-Section Beams," *AIAA Journal*, v33, n9, Sep 1995.
- [21]. Dancilla, D. S., and Armanios, E. A., "The Influence of Coupling on the Free Vibrations of Anisotropic Thin-Walled Closed-Section Beams," *36th*

*AIAA/ASME/ASCE/AHS/ASC Structures, Structural Dynamics and Materials (SDM) Conference*, New Orleans, LA, Part 4, AIAA-95-1411-CP, pp. 2106-2115.

[22]. Badir, A. M., "Analysis of Two-Cell Composite Beams," *36th AIAA/ASME/ASCE/AHS/ASC Structures, Structural Dynamics, and Materials Conference*, New Orleans, LA, Part 1, AIAA-95-1208-CP, pp. 419-424.

[23]. Barbero, E. J., "Optimization of Pultruded Composite Beams and Columns," How Concept Becomes Reality, *SAMPE Symposium and Exhibition*, v36, pt 2, 1991, pp. 1343-1359.

[24]. Caprino, G. and Langella, A., "Optimization of Robotic Arms Made of Composite Materials for Maximum Fundamental Frequency," *Journal of Composite Structures*, v31, n2, 1995, pp. 1-8.

[25]. Peck, A. W. and Bauchau, O. A., "On Design and Optimization of Curved Composite Beams," *American Helicopter Society 48th Annual Forum Proceedings*, v1, Jun 1992, pp. 647-660.

[26]. Ganguli, R., and Chopra, I., "Aeroelastic Optimization of an Advanced Geometry Composite Helicopter Rotor," *Annual Forum Proceeding of the American Helicopter Society*, v2, 1995, pp. 965-984.

[27]. Grandhi, R., "Structural Optimization with Frequency Constraints," *AIAA Journal*, v31, n12, 1993, pp. 2296-2303.

[28]. Armanios, E. A., Kamat, M. P., and Lentz, W. K., "Optimum Coupling in Composite Thin-Walled Closed Section Beams," COMPOSITES '95: Recent Advances in Japan and the United States, Kimpara, I., Miyairi, H., and Takeda, N., Ed.,

Proceedings of the 7th Japan-U.S. Conference on Composite Materials, Kyoto, Japan, pp. 683-691.

[29]. Kogiso, N. *et al*, "Genetic Algorithms wit Local Improvement for Composite Laminate Design," *Structures and Controls Optimization*, AD-Vol. 38, ASME 1993.

[30]. Kirsch, U., Structural Optimization, Springer-Verlag, Berlin, 1993.

[31]. Haftka, R.T. and Kamat, M. P., Elements of Structural Optimization, Martinus Nijhoff Publishers, 1985.

[32]. Fiacco, McCormick, Nonlinear Programming: Sequential Unconstrained Minimization Techniques, John Wiley, New York, 1960.

[33]. Chandra, R. and Chopra, I., "Structural Behavior of Two-Cell Composite Rotor Blades with Elastic Couplings," *AIAA Journal*, v30, n12, Dec 1992, pp. 2914-2921.

[34]. Bank, Smith, "Experimental Investigation of Bending and Twisting Coupling in Thin-Walled Composite Beams," *Proceedings of Ninth ASCE Conference on Engineering Mechanics*, 1992.

[35]. Kosmatka, J.B., Idosor, F. R., and Lake, R. C., "Experimental/Analytical Investigation of the Free Vibration Behavior of Composite Spars with Initial Twist," *36th AIAA/ASME/ASCE/AHS/ASC Structures, Structural Dynamics and Materials (SDM) Conference*, New Orleans, LA, AIAA-95-1233-CP, pp. 690-697.

[36]. Chandra, R., Stemple A. D., and Chopra, I., "Thin-Walled Composite Beams Under Bending, Torsional, and Extensional Loads," *Journal of Aircraft*, v27, n7, Jul 1990, pp. 619-626.



[37]. Nixon, M. W., "Extension-Twist Coupling of Composite Circular Tubes with Application to Tilt Rotor Blade Design," *28th AIAA/ASME/ASCE/AHS Structures, Structural Dynamics and Materials (SDM) Conference*, Washington D. C87-0772, pp. 295-303.

[38] Hooke, D. A. and Armanios, E. A., "Design and Evaluation of Three Methods for Testing Extension-Twist-Coupled Laminates," *Composite Materials: Testing and Design (Twelfth Volume) ASTM STP 1274*, C. R. Saff and R. B. Deo, Eds., American Society for Testing and Materials, 1996, pp. 340-357.

[39]. Agarwal, B. D. and Broutman, L. J., Analysis and Performance of Fiber Composites, John Wiley, New York, 1980.

[40]. Palmer, D. W., "The Effect of Internal Delaminations on Unsymmetric Laminated Composite Plates," Ph.D. Thesis Dissertation, Georgia Institute of Technology, 1995, Ch. 5, Appendix D.

[41]. Chawla, K. K., Composite Materials: Science and Engineering, Springer-Verlag, New York, 1987.

[42]. Ghandi, F., and Lee, S. W., "A Composite Beam Finite Element Model with p-Version Assumed Warping Displacement," *Composites Engineering*, v2, n5-7, 1992, pp 329-345.

**Augmentation Task RS13  
Fatigue Behavior of Composite Panels with Multiple Delaminations and/or  
Transverse Cracks**

**Co-PI's: G.A. Kardomateas, E.A. Armanios and D.P. Schrage**

**Other Participants: Andrew MaKeev (GRA) and Mina Pelegri (GRA)  
Participants not funded under task: Basharat Malik**

**Final Report**

**Problem Studied**

Ensuring the integrity of composite structures depends on the ability to predict their behavior in the presence of defects. An important type of defect in laminated composites is the delamination, i.e. local debonding at a layer interface; this may occur due to manufacturing imperfections or due to service loads which include impact, and vibrations excited by the rotary systems.

Not only single, but also multiple delaminations can occur at moderate spacings at the same layer interface, or at adjacent layer interfaces and these can affect the fatigue behavior of the composite due to possible interactions among them. Interactions may also arise from another type of defect that appears after a sufficient number of fatigue cycles, namely the transverse cracks. Before these multiple crack influences are understood, the delineation of the behavior of the simple single delamination is first needed.

The long term benefit to the rotorcraft community from this research would be the formulation of predictive capabilities to design composites for fatigue with the associated anticipated significant cost and time savings due to the elimination of unnecessary tests. Also, a cost-effective scheduling of inspection procedures and intervals would be possible if the fatigue failure of laminated composites is thoroughly understood. Ultimately, confident decision making could take place when inspections show damage in rotorcraft structures in service.

The research in this task consists of both experiments and analysis and includes a fracture mechanics formulation and a properly validated growth criterion through extensive testing, in order to predict the cyclic growth of the delaminations.

The objective of this work is to study the conditions for initiation and propagation of delaminations (inter-layer cracks) in laminated composite structures and apply these concepts in the prediction of the fatigue behavior. Topics include the energy release rate and the mixed mode stress intensity factors, the bridging of delaminations by fibers only partially pulled-out, and the interaction effects between neighboring delaminations and/or transverse cracks.

## Summary of Accomplishments

### *Fatigue Delamination Growth in Unidirectional Graphite/Epoxy and Glass/Epoxy Composites Under Constant Amplitude Loading*

A study was conducted into the fatigue growth of internal delaminations in unidirectional graphite/epoxy and glass/epoxy composite plates subjected to constant amplitude cyclic compression. Due to the compressive loading, these structures undergo repeated buckling/unloading of the delaminated layer, which opens the delamination and creates free surfaces. The cyclic load causes a reduction of the interlayer resistance. A noteworthy feature of the problem is that the state of stress near the delamination tip is of mixed mode, I and II.

Several configurations were studied with the delamination located at different depths (through the thickness) and with different applied maximum compressive displacements. The experimental data were correlated with the predictions from a combined delamination buckling/postbuckling and fracture mechanics model. A mode-dependent fatigue delamination growth law was suggested and used together with a derived initial postbuckling solution for the deformation pattern of the delaminated layer and the substrate; the latter does not impose any restrictive assumptions on the delamination thickness and plate length. Furthermore, the investigation includes the possibility of unstable delamination growth.

Five test configurations of each material were studied with different initial delamination lengths, delamination location through the thickness and applied maximum compressive strain. Therefore, these configurations exhibit different mode mixities and energy release rates at  $\epsilon_{\max}$ . It should be mentioned that the applied maximum strain,  $\epsilon_{\max}$ , is in all cases below the level which would cause growth of the delaminations in a monotonic test. It was found that the fatigue delamination growth is strongly affected by the relative location of the delamination through the plate thickness, the fatigue growth being slower for a smaller value of delamination thickness over plate thickness,  $h/T$  (delaminations located closer to the surface). On the other hand, delaminations located very near the surface, e.g.  $h/T = 2/30$ , did not grow even for a very large number of applied compressive cycles. Furthermore, the growth of the delaminations takes place under mixed mode conditions characterized by a relatively high value of the Mode II component, which is increasing as the delaminations grow.

A mode-dependent cyclic growth law was suggested, as follows:

$$\frac{da}{dN} = C(\psi) \frac{(\Delta \tilde{G})^{m(\psi)}}{1 - \tilde{G}_{\max}}.$$

This growth law is expressed in terms of the spread in the normalized energy release rate in the pre- and post-buckling state,

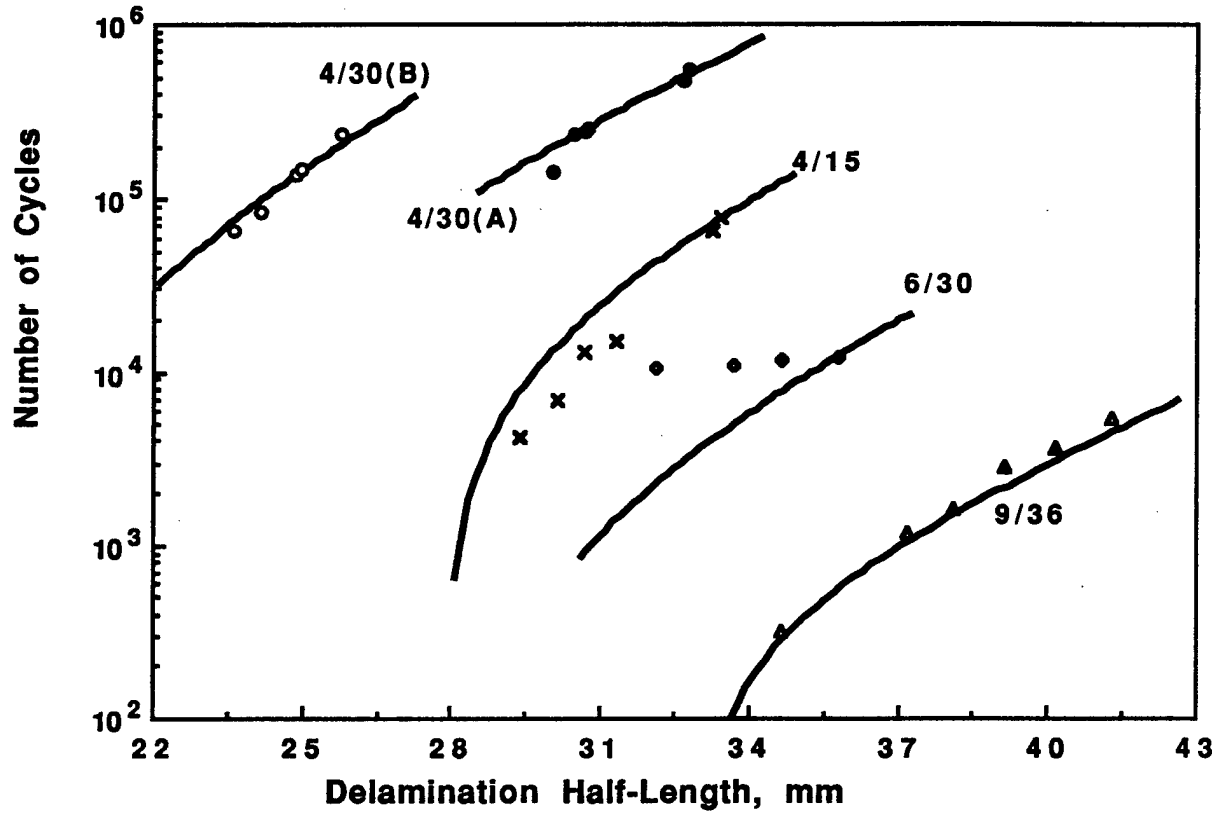
$$\tilde{G} = G/\Gamma_0(\psi) = \tilde{G}(\epsilon_0, \psi); \quad \psi = \tan^{-1}(K_{II}/K_I),$$

where  $\psi$  is the mode mixity and  $\Gamma_0(\psi)$  is the mode-dependent fracture toughness. Now the exponent and the constant are also mode-dependent:

$$m(\psi) = m_I [1 + (\mu - 1) \sin^2 \psi] ; \quad \mu = m_{II} / m_I$$

$$C(\psi) = C_I [1 + (\kappa - 1) \sin^2 \psi] ; \quad \kappa = C_{II} / C_I$$

This proposed fatigue growth law was shown to correlate well with the experiments, inspite of the different geometry (location of the delamination through the thickness, initial delamination length, plate thickness) and applied loading in each of the five delamination configurations for each material tested.



Fatigue delamination growth in unidirectional graphite/epoxy. 4/30 means a delamination between the fourth and fifth ply in a 30-ply construction. (A) and (B) denote same geometry but different peak load.

## *New Formulas for the Energy Release Rate and the Stress Intensity Factors in Laminated Composites with Arbitrary Stacking Sequence*

A set of new formulas for the total energy release rate and stress intensity factors was developed for general non-homogeneous laminated composite laminates. The total energy release rate was obtained by using J-integral for the separate models of plane stress, plane strain and cylindrical bending. Decomposition of it into Mode I and Mode II was based on the assumption of equivalent orthotropic properties through the laminate thickness. The process is straight forward and can be used to set criteria for delamination onset and growth.

Specifically, in terms of the constants  $\alpha_{id}$  and  $\alpha_{iu}$  which are obtained in terms of the material constants separately for plane stress or plane strain or cylindrical bending (Sheinman and Kardomateas, 1996), the energy release rate is:

$$G = \frac{1}{2} \left[ \frac{p_u^2}{R_1} + \frac{M_u^2}{R_2} + \frac{2G_{pm}}{\sqrt{R_1 R_2}} \right] \quad (1)$$

where

$$\frac{1}{R_1} = \alpha_{1d} + \alpha_{1u} - (\alpha_{2d} + \alpha_{3d})(h + zr_2 - zr_3) + \alpha_{4d}(h + zr_2 - zr_3)^2$$

$$\frac{1}{R_2} = \alpha_{4d} + \alpha_{4u}$$

$$G_{pm} = p_u M_u \sin \gamma$$

$$\sin \gamma = \sqrt{R_1 R_2} / 2 [\alpha_{2d} + \alpha_{2u} + \alpha_{3d} + \alpha_{3u} - 2\alpha_{4d}(h + zr_2 - zr_3)] \quad (2)$$

In the above expressions,  $zr_2$  and  $zr_3$  denote the distance from the reference lines of region 2 and 3 (Fig. 1),  $h$  is the delamination thickness and  $p_u$  and  $M_u$  are the stress resultants of the delaminated layer.

The energy release rate given by eq. (1) is the most general exact expression for any non-homogeneous anisotropic material. For homogeneous material (non-laminated or laminated with equal laminate properties), the coefficients are reduced exactly to the expression given by Suo and Hutchinson (1990).

The energy release rate can also be written as:

$$\begin{aligned}
G &= |G| e^{i\phi_1} \\
|G| &= \frac{1}{\sqrt{2}} \left| \frac{p_u}{\sqrt{R_1}} \mp i e^{i\bar{\gamma}} \frac{M_u}{\sqrt{R_2}} \right| \\
\phi_1 &= \arctg \left[ \frac{\mp M_u \cos \gamma}{p_u \sqrt{\frac{R_2}{R_1}} \pm M_u \sin \bar{\gamma}} \right] \\
\bar{\gamma} &= |\gamma|
\end{aligned} \tag{3}$$

The upper sign is for the case of  $G_{pm} > 0$  and the lower for  $G_{pm} < 0$

Regarding the stress intensity factors, these were found in the form:

$$\begin{aligned}
K_I &= \frac{\lambda^{3/8}}{\sqrt{2p_{11}n}} \left[ \frac{p_u}{\sqrt{R_1}} \cos \omega \pm \frac{M_u}{\sqrt{R_2}} \sin (\omega + \bar{\gamma}) \right] \\
K_{II} &= \frac{\lambda^{1/8}}{\sqrt{2p_{11}n}} \left[ \frac{p_u}{\sqrt{R_1}} \sin \omega \mp \frac{M_u}{\sqrt{R_2}} \cos (\omega + \bar{\gamma}) \right]
\end{aligned} \tag{4}$$

where

$[p] = [\bar{s}]^{-1}$  is the compliance matrix and

$$\lambda = p_{11} / p_{22}$$

$$\rho = \frac{2p_{12} + p_{33}}{2\sqrt{p_{11}p_{22}}}$$

$$n = \sqrt{\frac{1+\rho}{2}}$$

The upper sign in (4) is for the case of  $G_{pm} > 0$  and the lower for  $G_{pm} < 0$ .  $\omega$  is a function of the material and geometric parameters. It can be obtained by numerical solution of the integral equation for anisotropic plane elasticity problem (see Suo and Hutchinson, 1990). However, one may use the approximated expression  $\omega = 52.1 - 3h/H$ .

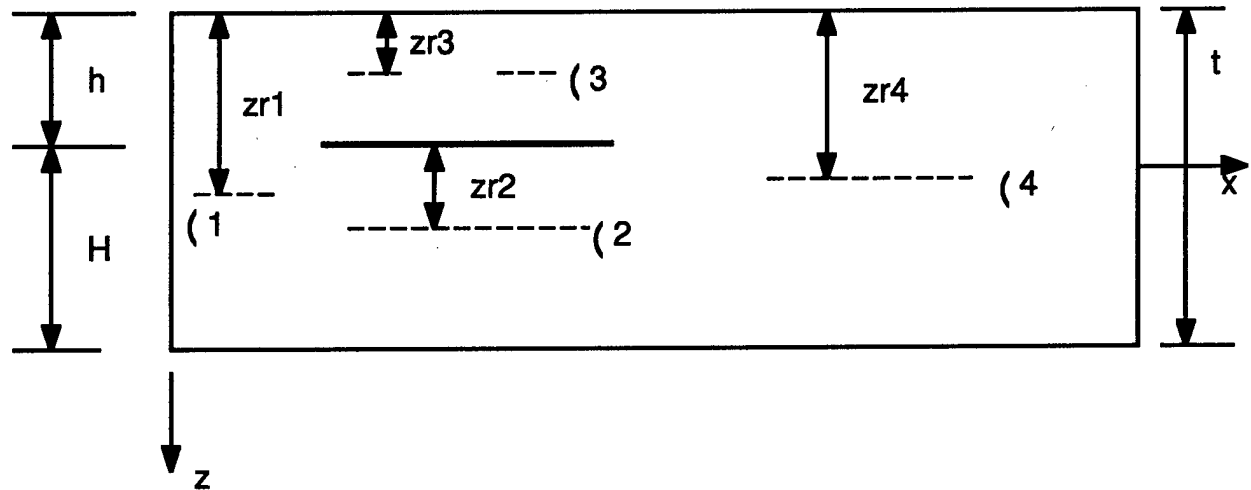


**Fig. 1 A Delaminated Plate**

### References

Suo, Z., and Hutchinson, J. W., 1990, "Interface crack between two elastic layers", *International Journal of Fracture*, Vol. 43, pp. 1-18.

Sheinman I. and Kardomateas G.A. (1996). "Energy Release Rate and Stress Intensity Factors for Delaminated Composite Laminates". In Press, *International Journal of Solids and Structures*.

### Publications during this period:

#### Referreed Journal:

Kardomateas G.A., Pelegri A.A. and Malik B., "Growth of Internal Delaminations Under Cyclic Compression in Composite Plates", *Journal of the Mechanics and Physics of Solids*, vol. 43, no. 6, pp. 847-868, 1995.

Sheinman I. and Kardomateas G.A., "Energy Release Rate and Stress Intensity Factors for Delaminated Composite Laminates", *International Journal of Solids and Structures*, vol. 34, No. 4, pp. 451-459, 1997.

Kardomateas G.A. and Malik B., (1996) "Fatigue Delamination Growth Under Cyclic Compression in Glass/Epoxy Composite Beam/Plates". In press, journal of *Polymer Composites*.

Kardomateas G.A. and Pelegri A.A., "Growth Behavior of Internal Delaminations in Composite Beam/Plates Under Compression: Effect of the End Conditions", *International Journal of Fracture*, vol. 75, pp. 49-67, 1996.

Sheinman I., Kardomateas G.A. and Pelegri A., "Delamination growth during pre-and post-buckling phases of delaminated composite laminates", in press, *International Journal of Solids and Structures*, 1997.

**Conference Presentations:**

Kardomateas, G.A., "Stable and Unstable Delamination Growth in Compressively Loaded Composite Plates", Proceedings, 36th AIAA/ASME/ASCE/AHS/ASC SDM Conference, New Orleans, LA, April 10-13, 1995, pp. 2690-2699.

Pelegri A.A., Kardomateas G.A. and Malik B.U. (1995) "The Fatigue Growth of Internal Delaminations Under Compression in Cross Ply Composite Plates", ASTM Sixth Symposium on Composites: Fatigue and Fracture, May 16-17, 1995, Denver, Colorado.

Kardomateas G.A. and Malik B. (1995) "Fatigue Delamination Growth Under Cyclic Compression in Glass/Epoxy Composite Plates", Proceedings, 1995 AHS National Technical Specialists Meeting on Rotorcraft Structures, Williamsburg, Virginia, Oct 30-Nov 2, 1995.

**Ph.D. Thesis**

**Basharat Malik**, Graduated in August 1995

Thesis: *Growth of Delaminations Under Cyclic Compression in Unidirectional Composite Plates.*



**Augmentation Task RS14:  
Sectional Analysis of Composite Rotor Blades  
Accounting for Realistic Blade Design Parameters**

**PI: Dewey H. Hodges**

Reporting Period: April 15, 1994 – December 31, 1996

## **Background**

At this time the rotorcraft industry does not exploit elastic couplings in its composite rotor blade designs. What has been talked about for two decades, to use elastically coupled blades to improve performance or to enhance the margin of stability, has still not been accomplished. The reasons for this lie mainly with the fact that the industry does not possess tools that allow accurate analysis of elastically coupled composite blades as beams. To actually make this feasible is the main goal of this research.

In this project, we continued the development of a general framework for modeling composite rotor blades. This framework extracts from a 3-D elasticity formulation two sets of analyses: one over the cross section, providing elastic constants that can be used in a suitable set of beam equations, and the other the beam equations themselves. The cross-sectional analysis, along with the accompanying engineering software VABS (Variational-Asymptotic Beam Section), provides an accurate beam representation of the blade structure, allowing a designer to take advantage of composite materials when designing rotor blades. VABS is able to take into consideration anisotropic, nonhomogeneous materials and to represent general cross-sectional geometries, requiring neither the costly use of 3-D finite element discretization nor the loss of accuracy inherent in any simplified representation of the cross section. The generality of the method and accuracy of the results obtained should increase confidence at the design stage that the structure will perform as expected and, consequently, should lower costs from experimental tests and further adjustments.

This problem is quite relevant for the rotor blade designer. Most of the structural members which make up rotor blades can be treated as beams (1-D), while some parts such as bearingless rotor flexbeams are more accurately modeled as plates or shells (2-D). Because of prior support from the U.S. Army, we started this project with theories in place for development of both 1-D (CERWAT through ARO) and 2-D (Army-Langley) models. In order to make these theories useful for industry and government (such as in 2GCHAS), they had to be extended in some areas and the extended theory fully implemented in VABS. This task was originally intended to address mainly the 1-D problem. There was some plate (2-D) work anticipated on this task as well, but Dr. Vladislav G. Sutyrin, a Post Doctoral Fellow who was to be the main resource for working on the plate problem, left Georgia Tech early in the project, in September 1994. Also, Mr. John S. St. Angelo, the graduate student who worked on the plate problem, had to leave Georgia Tech due to serious illness. Thus, we chose to substantially descope the plate work. It turned out that the beam-related work was much more labor intensive than we had anticipated, so the project man-power was well utilized.

## **Accomplishments**

Our computer program VABS has been under development for several years now with the ultimate objective of enabling the designer to determine from first principles the equivalent beam properties for a rotor blade with arbitrary cross-sectional geometry and material properties. VABS and its capabilities are described in Cesnik and Hodges (1997). The present project focused on three areas of improvements to VABS: (1) the extension of VABS to allow for arbitrary choices of reference line and reference cross section; (2) the treatment of large initial curvature and initial twist; and (3) the treatment of the trapeze effect. Finally, the accomplishments related to plates are noted.

*Choice of Reference Line and Cross Section in Beams:* In order to allow more flexibility to the designer, an analysis was developed that allows the removal of the assumption that the reference cross section should be orthogonal to the reference line. The new analysis and code allow an arbitrary choice of reference cross sectional planes. With an oblique reference cross section, a natural choice is given for the analysis of swept blades and/or blades with curved tips.

In order to have a non-orthogonal reference section, the changes started at the basic kinematics of the beam. For describing the kinematics with the new reference section, curvilinear nonorthogonal coordinates were introduced such that the axial coordinate is along the reference line and the other two are orthogonal coordinates in the plane of the oblique cross section. For the purpose of strain calculation the dextral triad given by unit vectors in the plane of and normal to the cross section has been introduced together with the dextral triad given by the unit vector along the tangent to the axial coordinate line and two other unit vectors given by a conveniently chosen, nonunique rotation matrix. The same considerations apply for the deformed state of the beam except for the introduction of warping expressed in the coordinate system of the cross section.

To preserve the assumption of the  $4 \times 4$  stiffness matrix formulation ("classical" theory, in the sense of this framework), where only "classical" degrees of freedom are taken into account (three displacements and one rotation about the reference line), the tensile strain of the normal cross section has been decomposed in the system of the oblique cross section resulting in a local non-independent shear strain. The angle between the tangent to the reference line and the base vectors in the plane of the cross section for the undeformed state has been preserved in the deformed state, so that the tangent has the same angle to the cross-sectional reference plane. Modified strain-displacement relations have been derived for the 1-D generalized strains. The 3-D strains were obtained in a similar form as the previous formulation for normal reference cross section.

This formulation has been implemented in VABS, where in order to minimize the modification of the existing 1-D code a similarity transformation of the stiffness matrix was performed. The modified version of VABS, including stress and strain recovery, has been tested for composite beams with success. The derivation and some results are reported in Hodges, Cesnik, Popescu, and Harursampath (1996). Excellent correlation with experimental data was achieved and is reported in Hodges, Shang, and Cesnik (1996).

The problem of allowing the designer the choice of an arbitrary reference line was studied. However, since the  $4 \times 4$  stiffness matrix formulation (classical beam theory) does not use the concept of the shear center of the beam, it turns out to be better to stay with the area centroid as the reference line. It was shown that at least a  $6 \times 6$  formulation is needed to have completely arbitrary choice of the reference line. Thus, this is being undertaken in work sponsored by NRTC.

*Large Curvature/Twist Effects:* The effect due to large initial twist and curvature (propfan, tilt rotor blades) in the cross-section analysis was addressed. As discussed in previous reports, the effects of initial twist and curvature not only appears in the 1-D beam equations, but also in the 2-D sectional analysis. A linear correction was already present in VABS. But that is not sufficient for highly twisted and/or curved rotors. A new stiffness matrix correction due to a second-order influence of these parameters was derived and implemented in VABS. The inadequacy of ignoring initial twist and curvature effects in the analysis was demonstrated, and the inadequacy of the first-order analysis was shown for some cases. The derivation and numerical results are reported in Cesnik, Hodges, and Sutyryn (1996).

*Trapeze Effect in Beams:* The final part of work that was to be undertaken in this project was the incorporation of nonlinear strain field effects, such as the trapeze effect. It is known that, for treatment of certain thin-walled beam cross sections, it is possible to find closed-form expressions for the asymptotically correct stiffnesses. We postulated that this might be possible for the trapeze effect as well. Thus, we started with a strip in order to make it more probable that we would understand what we were doing. It turned out to be quite a challenge within the rigorous framework, but a closed-form expression for the strain energy, including the trapeze effect, was finally developed for generally anisotropic strips. These results, including pretwist, are presented in Hodges, Harursampath, and Cesnik (1996) and are in preparation for submission to a journal. This result motivated us consider the thin-walled beam problem in more generality in later work.

Since VABS is for general cross-sectional geometries, where one does not take advantage of small parameters related to the thinness of the walls, we also needed a way to capture the trapeze effect in the general case. We proceeded by starting from 3-D elasticity and writing down all the terms that are of the order of strain to the third power in the strain energy for a long, prismatic beam. The classical warping displacement field is known, and all terms that multiply the perturbation of the warping actually cancel out. This leaves only known expressions that need to be evaluated numerically. While algebraically tedious, the calculation of trapeze effect contributions could be undertaken. The resulting methodology has been coded into VABS, and now it is possible to capture the trapeze effect for beams of arbitrary cross-sectional geometry with a numerical evaluation of the nonlinear stiffness effect. This derivation along with some results is part of a paper in preparation.

*Plates:* We shifted available resources to the beam problem, since it is far more challenging than we originally thought anyway and because of the departure of Dr. Sutyrin and the illness of Mr. St. Angelo. In spite of this, a significant breakthrough occurred regarding the development of laminated plate theory. For the first time it is understood how to derive the next approximation for laminated composite plates. First the conditions for having an asymptotically correct plate theory were developed. It was determined that a Reissner-like laminated plate theory that is asymptotically correct may not exist for certain layups. However, we discovered a way to get as close to optimality as desired. Our resulting plate theory provides excellent agreement with 3-D elasticity solutions – better than results for any published first-order shear deformation theory in the literature. In fact these results are even superior to those obtained from sophisticated higher-order and layerwise theories. This work appeared as Sutyrin and Hodges (1996).

### ***External Interactions***

Over the duration of the grant, we have been in touch with all four major helicopter companies (Dr. Jing Yen, Bell; Mr. Frank Tarzanin, Boeing; Mr. Jerry Miao, Sikorsky, and Dr. Friedrich Straub, McDonnell Douglas Helicopters) to offer them the VABS software and training on how to use it. Only Bell was interested in pursuing it further, and we visited them twice to follow up. (They are not currently using VABS, because it would require too much investment of manpower on their part. We are trying to address this in future work on a friendlier user interface.) VABS and the training was also offered to the windpower community through the U.S. Department of Energy (Dr. Gunjit Bir). Our most significant interaction was with Dr. Gene Ruzicka and Dr. M. J. Rutkowski of the 2GCHAS Project office, U.S. Army Aeroflightdynamics Directorate, Ames Research Center. Although the primary aspect of this interaction has been the nonlinear beam element of the 2GCHAS system, provided by the PI, there have also been discussions about VABS. The 2GCHAS beam element will take output from VABS as input. Some AFDD hardware needs to be modeled, and VABS will probably get a “workout” in the near future.

## ***Personnel Supported***

Dewey H. Hodges, Professor and PI

Carlos E. S. Cesnik, Post Doctoral Fellow (now Assistant Professor, MIT)

Vladislav G. Sutyrin, Post Doctoral Fellow (resigned September 30, 1994; now Assistant Professor, Wayne State University)

Bogdan Popescu, Graduate Research Assistant

Dineshkumar Harursampath, Graduate Research Assistant

John S. St. Angelo, Graduate Student (participated but not supported by this task; now on medical leave)

## ***Publications***

### Refereed Journals:

Cesnik, Carlos E. S.; and Hodges, Dewey H.: "Variational-Asymptotical Analysis of Initially Twisted and Curved Composite Beams," *International Journal for Engineering Analysis and Design*, vol. 1, no. 2, Apr. 1994, pp. 177 – 187.

Cesnik, Carlos E. S.; and Hodges, Dewey H.: "Stiffness Constants for Composite Beams Including Large Initial Twist and Curvature Effects," *Applied Mechanics Reviews*, vol. 48, no. 11, part 2, Nov. 1995, pp. S61 – S67.

Cesnik, C. E. S.; Hodges, D. H.; and Sutyrin, V. G.: "Cross-Sectional Analysis of Composite Beams Including Large Initial Twist and Curvature Effects," *AIAA Journal*, vol. 34, no. 9, Sept. 1996, pp. 1913 – 1920.

Cesnik, Carlos E. S.; and Hodges, Dewey H.: "VABS: A New Concept for Composite Rotor Blade Cross-Sectional Modeling," *Journal of the American Helicopter Society*, vol. 42, no. 1, Jan. 1997, pp. 27 – 38.

Hodges, Dewey H.: "Comment on 'Flexural Behavior of a Rotating Sandwich Tapered Beam' and on 'Dynamic Analysis for Free Vibrations of Rotating Sandwich Tapered Beams,'" *AIAA Journal*, vol. 33, no. 6, June 1995, pp. 1168 – 1170. (CERT related)

Hodges, D. H.; Shang, X.; and Cesnik, C. E. S.: "Finite Element Solution of Nonlinear Intrinsic Equations for Curved Composite Beams," *Journal of the American Helicopter Society*, vol. 41, no. 4, Oct. 1996, pp. 313 – 321.

Sutyrin, Vladislav G.; and Hodges, Dewey H.: "On Asymptotically Correct Linear Laminated Plate Theory," *International Journal of Solids and Structures*, vol. 33, no. 25, 1996, pp. 3649 – 3671.

## ***Publications (continued)***

### **Papers Presented at Conferences:**

Cesnik, Carlos E. S.; Sutyrin, Vladislav G.; and Hodges, Dewey H.: "Refined Theory of Twisted and Curved Composite Beams: The Role of Short-Wavelength Extrapolation," AIAA Paper 94-1451, *Proceedings of the 35th Structures, Structural Dynamics and Materials Conference*, Hilton Head, South Carolina, Apr. 20 – 22, 1994, pp. 1134 – 1143.

Cesnik, Carlos E. S.; and Hodges, Dewey H.: "Stiffness Constants for Composite Beams Including Large Initial Twist and Curvature Effects," *Applied Mechanics in the Americas (Proceedings of the 4th Pan-American Congress of Applied Mechanics*, Buenos Aires, Argentina, Jan. 3 – 6, 1995), vol. III, pp. 229 – 232.

Cesnik, C. E. S.; Hodges, D. H.; and Sutyrin, V. G.: "Stiffness Constants for Composite Beams Including Large Initial Twist and Curvature Effect," *Proceedings of the 36th Structures, Structural Dynamics and Materials Conference*, New Orleans, Louisiana, Apr. 10 – 12, 1995, AIAA Paper 95-1500, pp. 3106 – 3116.

Cesnik, Carlos E. S.; and Hodges, Dewey H.: "VABS: A New Concept for Composite Rotor Blade Cross-Sectional Modeling," *Proceedings of the 51st Annual Forum of the American Helicopter Society*, Fort Worth, Texas, May 9 – 11, 1995. Sutyrin, V. G.; and Hodges, D. H.: "On Asymptotically Correct Plate Theory," *Proceedings of the 36th Structures, Structural Dynamics and Materials Conference*, New Orleans, Louisiana, Apr. 10 – 12, 1995, AIAA Paper 95-1373, pp. 1800 – 1811.

Hodges, Dewey H.; Cesnik, Carlos E. S.; Popescu, Bogdan; and Harursampath, Dineshkumar: "Composite Beam Cross-Sectional Modeling Including Obliqueness and Trapeze Effects," *Proceedings of the 37th Structures, Structural Dynamics and Materials Conference*, Salt Lake City, Utah, Apr. 15 – 17, 1996, AIAA Paper 96-1469, pp. 1384 – 1397.

Hodges, Dewey H.; Harursampath, Dineshkumar; and Cesnik, Carlos E. S.: "Nonlinear Strain Field Effects in Anisotropic Strips," *Proceedings of Recent Developments in Solid Mechanics*, Rio de Janeiro, Brazil, July 31 – August 2, 1996, pp. 71 – 78 (Invited).

Sutyrin, V. G.; and Hodges, D. H.: "On Asymptotically Correct Plate Theory," *Proceedings of the 36th Structures, Structural Dynamics and Materials Conference*, New Orleans, Louisiana, Apr. 10 – 12, 1995, AIAA Paper 95-1373, pp. 1800 – 1811.

## **Rotor Technology Integration Task 3 (RTI - 3)**

### **Active Control of Blade Aerodynamics**

PIs: Dr. J.V.R. Prasad, Dr. L.N. Sankar  
GRAs: R. Norris, S-Y. Yi, K-K, Leung, S. Bae  
Contributed but not supported: R. Swaminathan

### **Introduction**

Current rotor designs necessarily represent a difficult trade-off between hover and high speed performance, and between performance and other design criteria such as vibration, noise, etc. Active control technology offers to improve rotor design by relaxing to some degree the trade-offs required. By introducing additional freedom for rotor control (i.e. active control of rotor speed, individual control of blade pitch, limited control of airfoil shape at least over some portion of blade span, and even control of span-wise blade properties) dramatic improvements in rotor vibration, performance and noise generation may be possible. Control inputs can even be tailored to specific operating conditions. For example, when in a highly populated area, one could actively reduce noise levels, at the price of performance, to meet noise regulations. Alternately, one could choose to maximize performance in flight regimes where higher noise levels are acceptable.

Most of the previous active control investigations were based on the use of numerical optimization techniques in conjunction with computational fluid dynamics analysis of rotor blade flow problem involving solution to a set of integral and partial differential equations. Instead, if a state-space modal representation of rotor blade aerodynamics were to be available, one could easily combine such models with state-space models of blade structure/controller for a systematic investigation of active control concepts taking into account aerodynamic/structure/control interactions in the study.

### **Problem Studied**

This task is aimed at exploring the potential for helicopter rotor vibration and /or noise reduction by means of active control of rotor blade aerodynamics. The proposed effort involves developing approximate state space models for predicting unsteady pressure fluctuations due to blade vortex interaction and combining such models with optimal control theory to investigate optimal control strategies for rotor vibration and/or noise reduction.

### **Progress During the Reporting Period**

During the reporting period, we have developed both 2-D and 3-D finite state models for the blade vortex interaction problem. The 2-D finite state model has been validated by comparing the predicted steady and unsteady aerodynamic results (e.g., induced velocity, airloads, etc.) with those from a 2-D Computational Fluid Dynamics (CFD) model developed at Georgia Tech for analyzing the BVI problem. The 2-D finite state model has been combined with optimal control theory for investigating optimal control strategies for reducing BVI effects. As an alternative, active controllers based on neural networks and fuzzy logic for reducing BVI effects have also been investigated. Also, a 3-D finite state model for the BVI problem has been developed and initial validation of the 3-D model has been carried out. One of the students who worked on the finite state modeling is currently continuing on for his Ph.D. program and he is working on extending the

optimal control results with 2-D models to the more general case using 3-D models. Brief descriptions of these accomplishments with illustrative results follow.

## 2-D and 3-D CFD models

Since the 2-D and 3-D CFD codes are used for validation of finite state models in this study, development and validation of CFD models for the BVI problem is carried out first. Two programs have been developed and tested, one is "ogrid.f", the other is "ufoil.f". The "ogrid.f" is used to generate an o-grid for "ufoil.f", and the "ufoil.f" applies the full potential equation for the calculation of the pressure coefficient distribution and the lift coefficient of a 2-D airfoil. For a rotor case, we have to modify the programs so that we can simulate an incoming vortex and flap motion capabilities. The new program has been named as "uflap.f". Also, an option to compute pressure fluctuations in the near field has been included. Validations using data for several cases involving different free stream Mach numbers and for two airfoils, NACA 0012 and NACA 64A006, have been carried out. For the 3-D case, two similar programs, "frflap-f" and "bviflap.f", have been developed and initial validations have been completed. They allow users to simulate a linear or sine flap motion with an incoming vortex. The program has been validated for some simple cases of flow over a rotor with a NACA 0012 airfoil section, but without flap motion and an incoming vortex.

## 2-D finite state model of BVI

The 2-D finite state model previously developed in the literature for predicting pressure distribution on an airfoil in a flow field has formed the basis for developing a finite state model for the BVI problem. By use of Glauert (for spatial distributions) expansions, the airload equations have been converted to ordinary differential equations. As this model formulation is based on thin airfoil theory, the model does not include thickness effects. Effects from both external vortex and shed wake on induced velocity are included in the model. The 2-D finite state model of BVI has been validated by comparing predicted airload distributions with those obtained using CFD analysis.

Figures 1 through 4 compare steady airloads predicted by the 2-D finite state model in the absence of an external vortex with those obtained using CFD analysis. Note that the CFD model takes thickness effects into account. Since the finite state model is based on thin airfoil theory, the predicted pressure distribution near the leading edge would not be realistic. However, the values for lift and moment coefficients at different angles of attack match very well with CFD results. Next, the unsteady airloads in the presence of an external vortex as predicted by the 2D finite state model are compared with those obtained using CFD analysis. A vortex of known strength is assumed to be moving with the free stream velocity. Figures 5 through 9 compare pressure variations at various points along the chord with panel 1 near the trailing edge and panel 20 near the leading edge. Both models predict the pressure peaks to occur roughly at the same time. However, significant differences are noted in the magnitude of pressure fluctuations. Some of the differences could be attributed to thickness effects. Also, the differences in magnitude of pressure fluctuations predicted by the two models seem to be more near the leading and trailing edges (see Figs. 5 and 9). Figures 10 and 11 compare lift and moment coefficient variations due to BVI, respectively, for small angles of attack as predicted by the two models. It is seen that there is reasonable agreement between these predictions at low angles of attack. However, for moderate to high angles of attack (see Figs. 12 through 16), CFD predictions of unsteady lift and moment coefficient variations due to BVI don't seem reasonable whereas finite state model predictions seem qualitatively correct.

## Airloads alleviation

The 2-D finite state model of BVI has been combined with optimal control theory to arrive at optimal open loop flap schedules required for reducing the effect of BVI on airloads. A quadratic performance index of the following form is used in this study:

$$J = \frac{1}{2} \int_0^{t_f} [w_1(C_l - C_{lss})^2 + w_2(C_m - C_{mss})^2 + w_3(C_d - C_{dss})^2 + w_4 u^2] dt$$

where  $u$  represents control input to the flap actuator and subscript 'ss' represents steady state value. The weightings  $w_1$ ,  $w_2$ ,  $w_3$  and  $w_4$  allow for either individual or combined control of  $C_l$ ,  $C_m$ , and  $C_d$ . A second order model with assumed stiffness and damping values for the flap actuator is used in this study. The aerodynamic model is represented in terms of 7 states. An optimal control formulation for minimizing the above performance index has resulted in 14 coupled first order differential equations with mixed boundary conditions and the resulting equations have been solved using a first order gradient method. Figures 17 through 21 present controlled airload variation for the case with  $w_1=1$ ,  $w_2=0$ ,  $w_3=0$  and  $w_4=0$ . It is seen from Fig. 18 that the optimal open loop flap schedule required is within  $\pm 2.5^\circ$  while suppressing the BVI effect on  $C_l$  (see Fig. 17). A secondary benefit of the open loop optimal flap schedule is reduction in BVI induced pressure peak at various locations along the chord as seen in Figs. 22 through 26. Figure 27 presents controlled airload variation for the case with  $w_1=1$ ,  $w_2=1$ ,  $w_3=1$  and  $w_4=0$ . Note that in this case, complete suppression of BVI effect on  $C_l$  is not achieved due to non-zero weightings on  $C_m$  and  $C_d$ .

As the development of a dynamic model of BVI which is tractable to control design would involve several approximations, active control based on fuzzy logic principles has been investigated as an alternative. Rules for the controller are formulated using CFD simulations. A genetic algorithm is used to optimize for input membership functions, fuzzification and defuzzification weights. In order for the controller to be effective over a range of flight conditions, adaptation of fuzzification and defuzzification weights with flight condition using a neural network is considered. Preliminary results from CFD simulations indicate that an active controller based on fuzzy logic is effective in reducing the BVI induced pressure pulse. A block diagram representation of the fuzzy logic controller is shown as Fig. 28 and a comparison of simulation results of uncontrolled and controlled pressure variation near the leading edge of the airfoil is shown in Fig. 29.

## External Interactions

1. Discussions with Drs. F. Straub and A. Hassan of McDonnell Douglas Helicopter Systems.
2. Briefings to Drs. Y. Yu of AFDD at NASA Ames and to Dr. J. Berry of Structures Directorate at NASA Langley.
3. Work on this project has partially lead to a separate grant from Sikorsky to Dr. Sankar for a study on oscillating airfoils.
4. Work related to this project has partially lead to a patent given to personnel from McDonnell Douglas Helicopter Company and to Dr. L.N. Sankar.



## **Publications**

1. Swaminathan, R., Prasad, J.V.R. and Sankar, L.N., "Active Control of Blade-Vortex Interactions Using a Neuro-Fuzzy Controller," Proceedings of the Third International Conference on Intelligent Materials, Lyon, France, June 1996.
2. Sankar, L.N., "A First Principles Based Methods for Prediction of Loading Over Fixed and Rotating Geometries," Tenth National Computational Fluid Dynamics Symposium, Chuo University, Tokyo, Japan, December 19-21, 1996.

## **M.S. Special Problems**

1. Sheng-Yu Yi, M.S., Special Problem on "Active Control of Blade Vortex Interaction."
2. Robert Norris, M.S., Special Problem on "A Two-Dimensional Finite State Model Simulation of Unsteady Aerodynamics."
3. Sang Bae, M.S.(in progress), Special Problem on "Active Control of Blade-Vortex Interaction."

## **Ph.D. Students:**

Sheng-Yu Yi, Ph.D. (in progress)

Fig. 1 : Comparison of steady  $C_l$  between finite-state model and CFD code

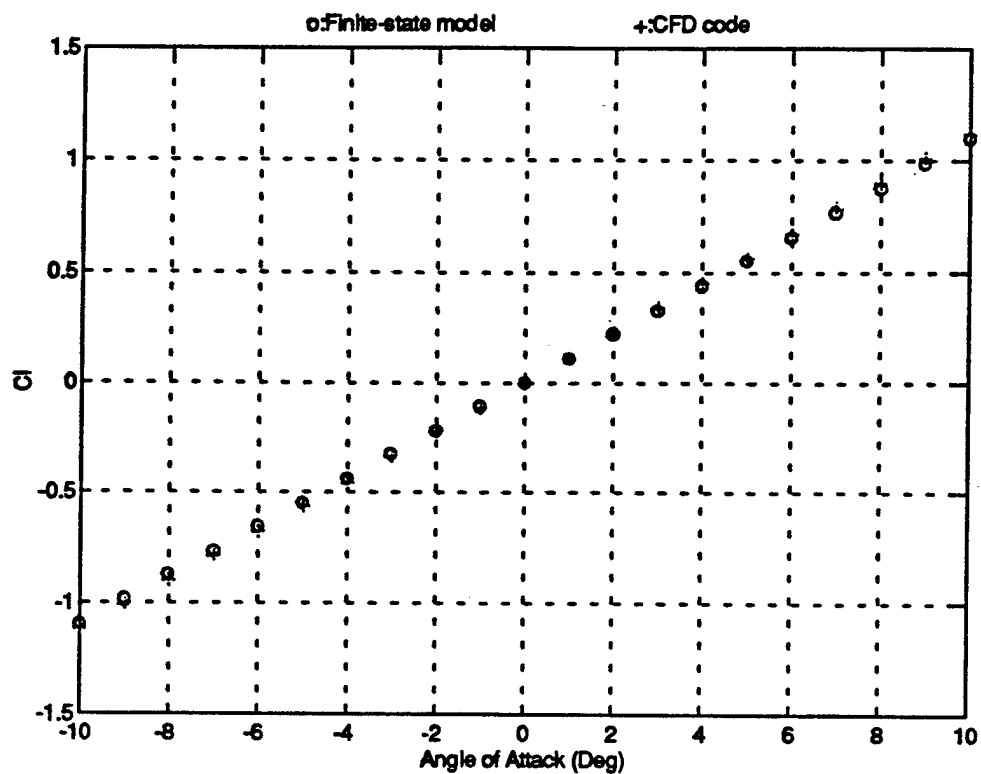


Fig. 2 : Comparison of steady  $C_m$  between finite-state model and CFD code

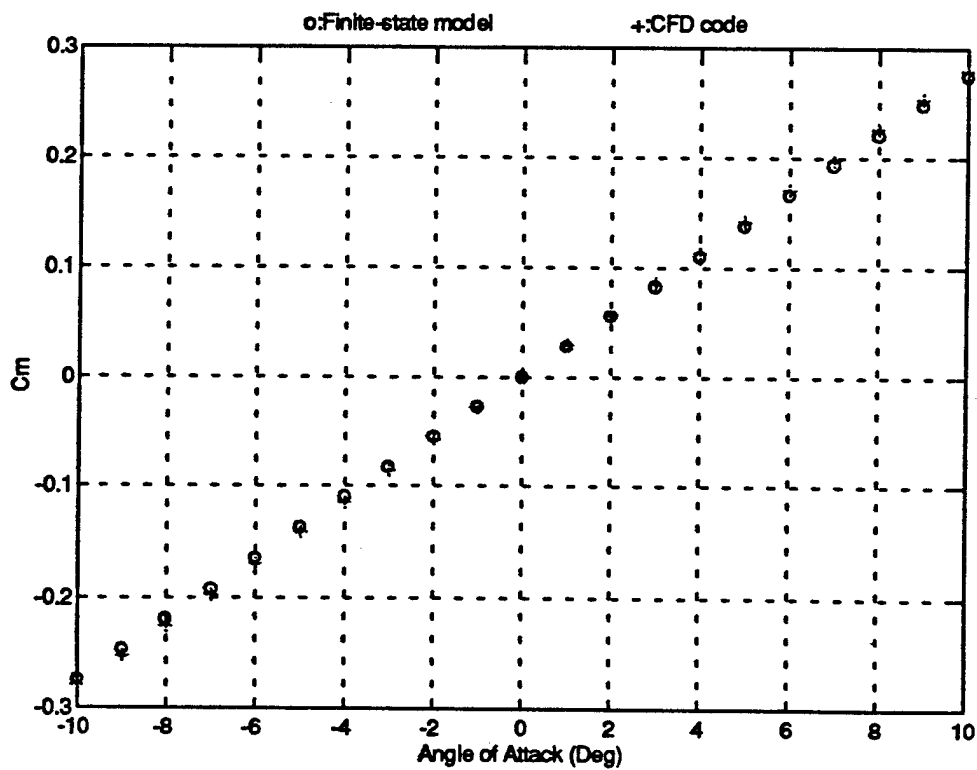


Fig. 3 : Comparison of steady Cd between finite-state model and CFD code

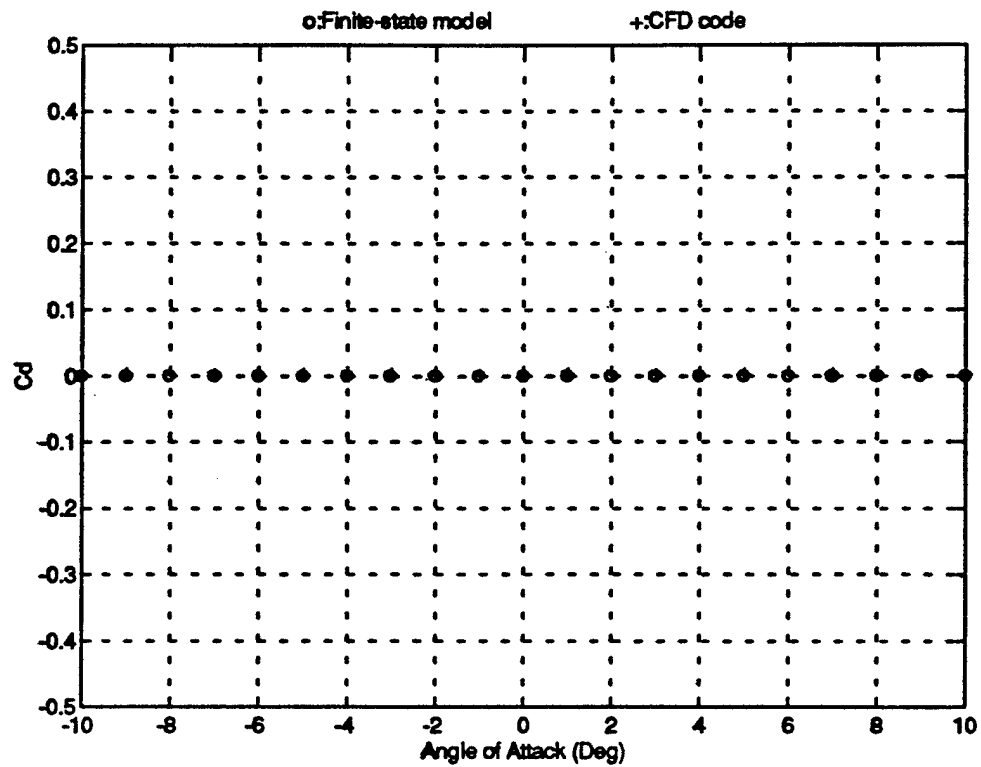


Fig. 4 : Comparison of steady Cp distributions between finite-state model and CFD code

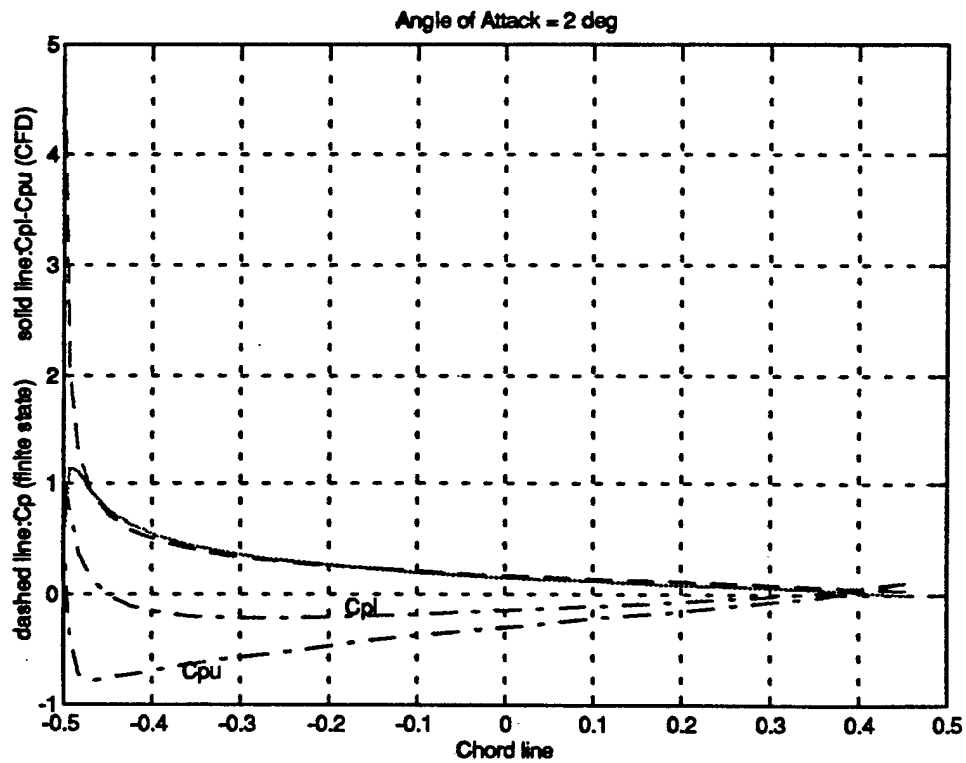


Fig. 5 : Comparison of unsteady  $C_p$  between finite-state model and CFD code  
(Panel 1 ~ 4)

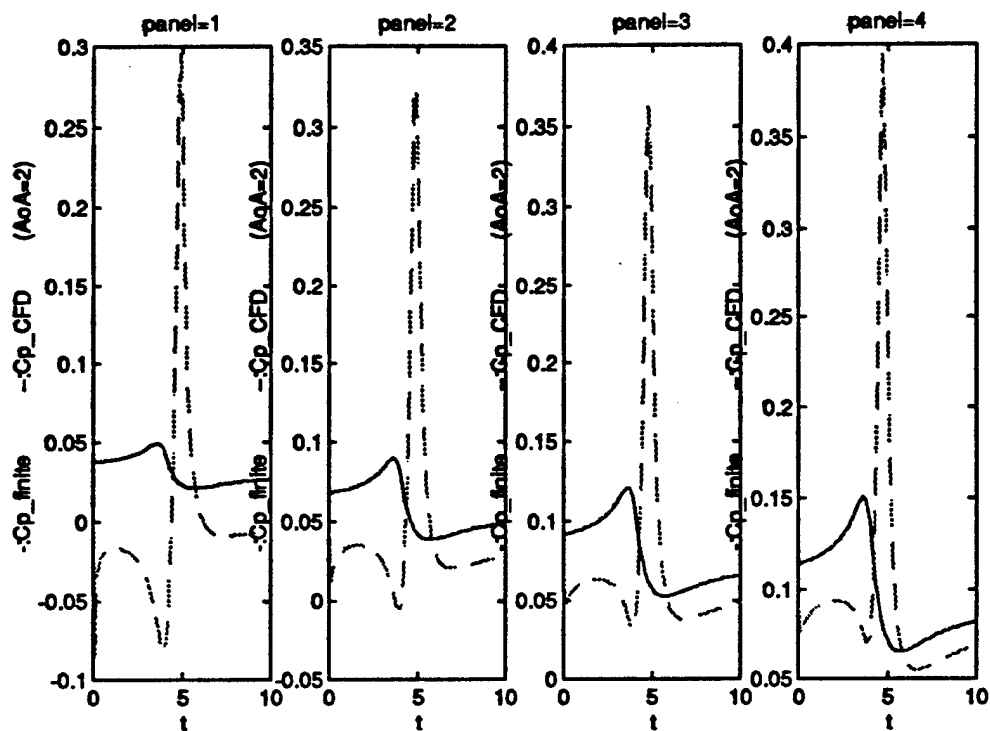


Fig. 6 : Comparison of unsteady  $C_p$  between finite-state model and CFD code  
(Panel 5 ~ 8)

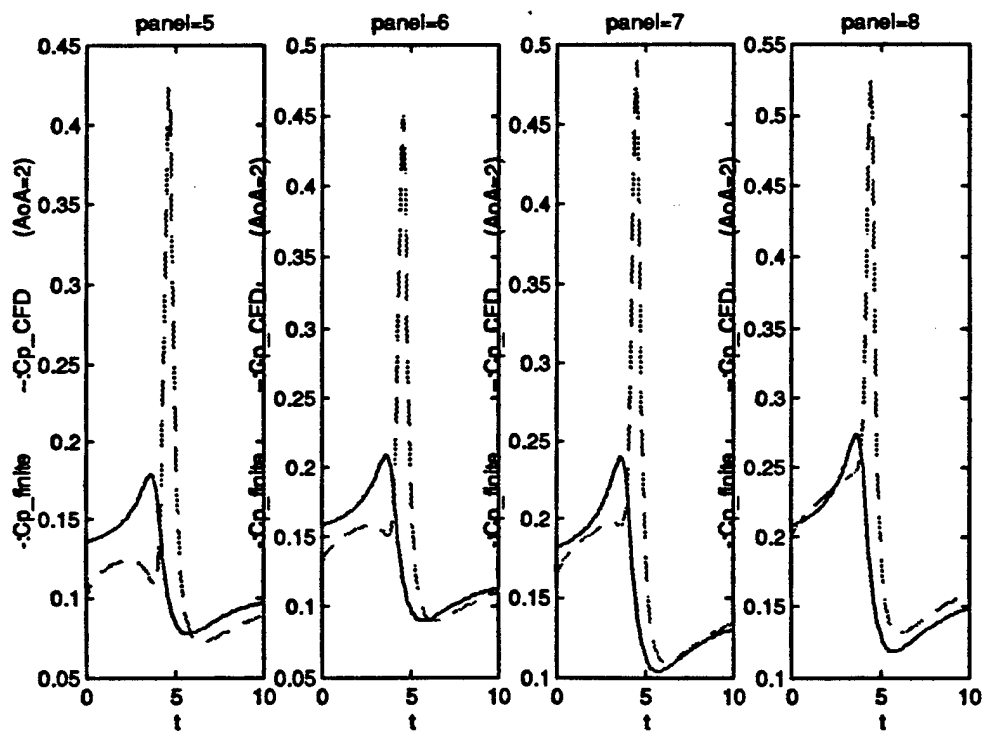


Fig. 7 : Comparison of unsteady  $C_p$  between finite-state model and CFD code  
(Panel 9 ~ 12)

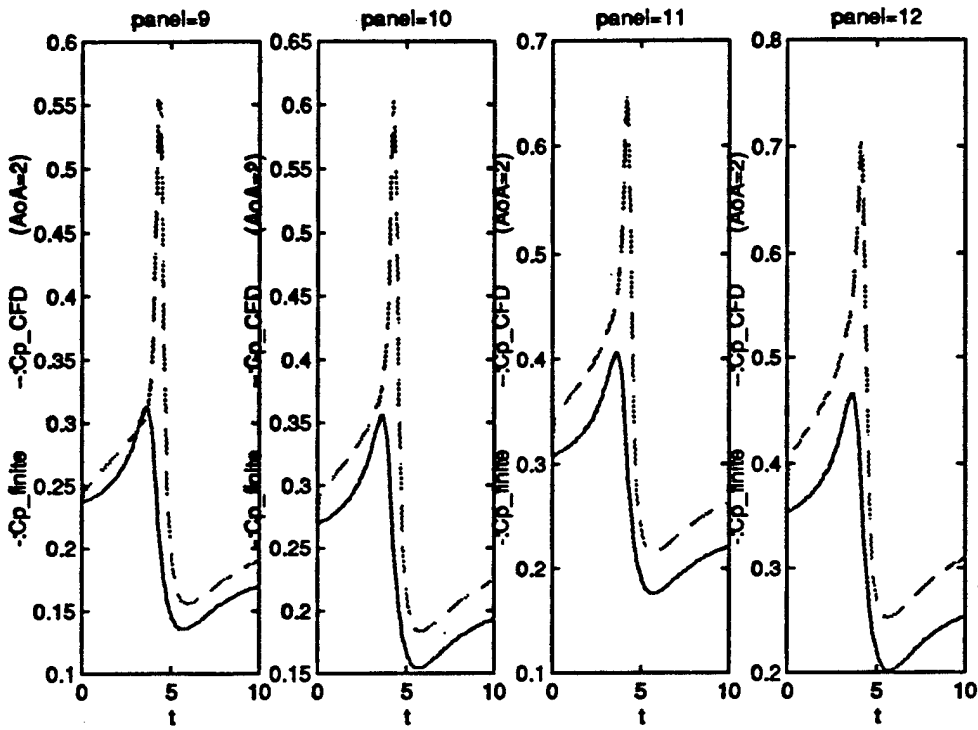


Fig. 8 : Comparison of unsteady  $C_p$  between finite-state model and CFD code  
(Panel 13 ~ 16)

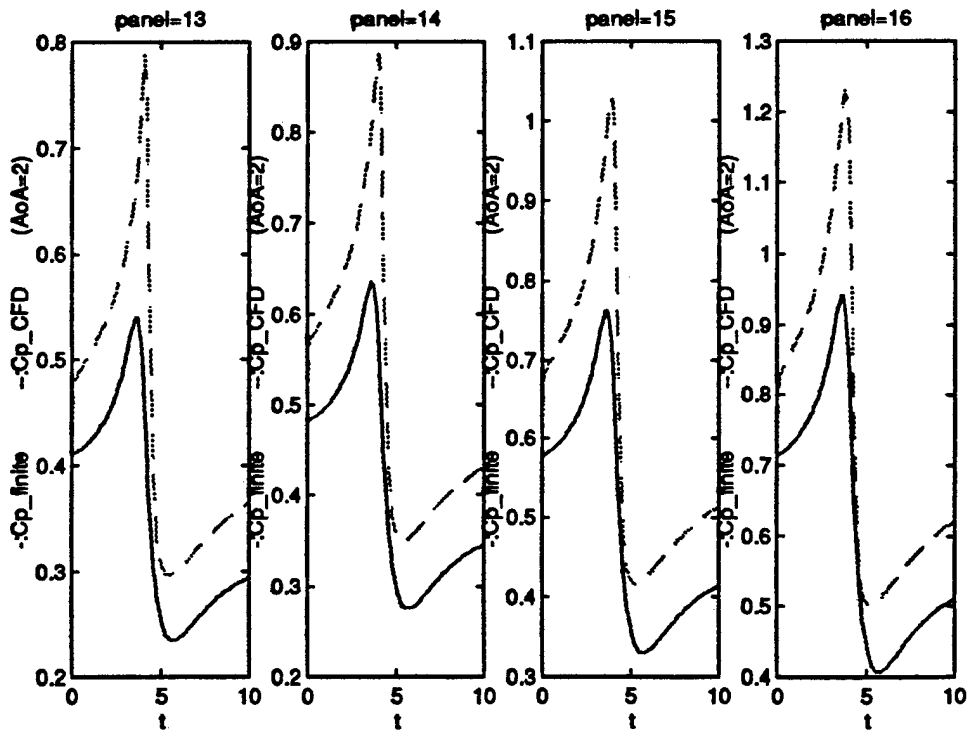


Fig. 9 : Comparison of unsteady  $C_p$  between finite-state model and CFD code  
(Panel 17 ~ 20)

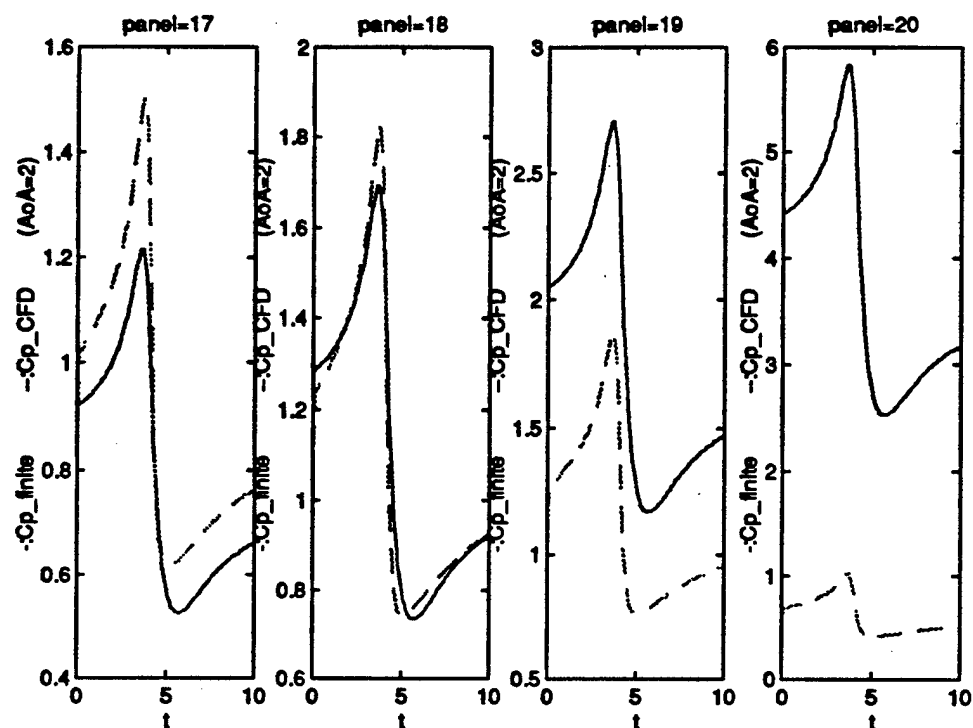


Fig. 10 : Comparison of unsteady  $C_l$  between finite-state model and CFD code  
at  $\alpha=4^\circ, 2^\circ, 0^\circ, -2^\circ, -4^\circ$

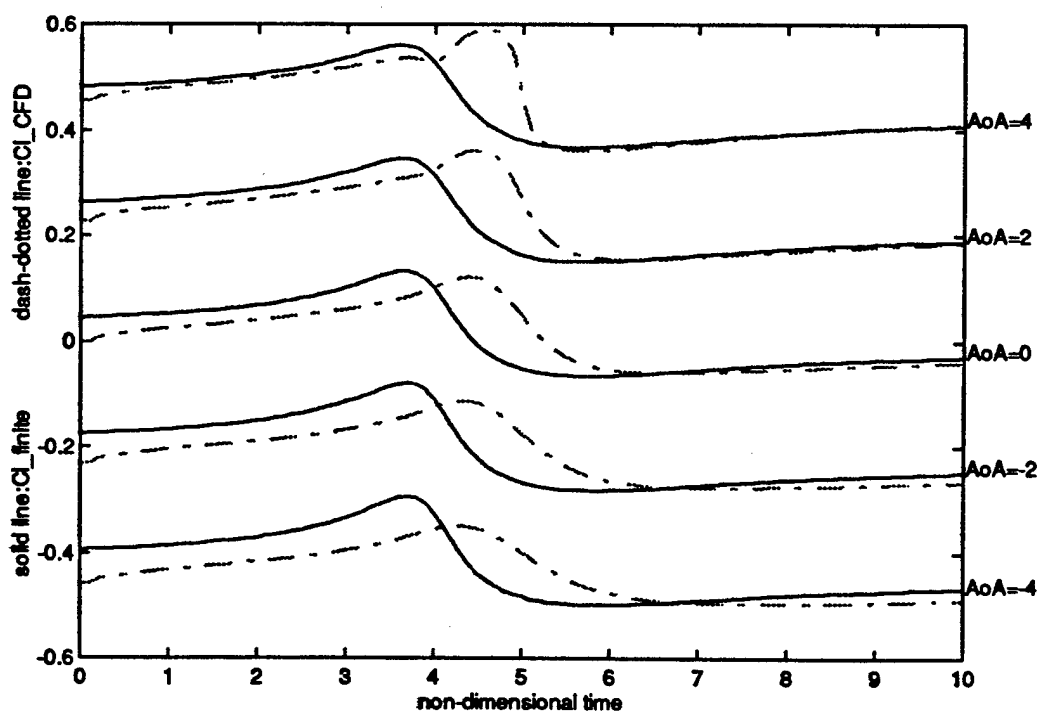


Fig. 11 : Comparison of unsteady  $C_m$  between finite-state model and CFD code  
at  $\alpha = 4^\circ, 2^\circ, 0^\circ, -2^\circ, -4^\circ$

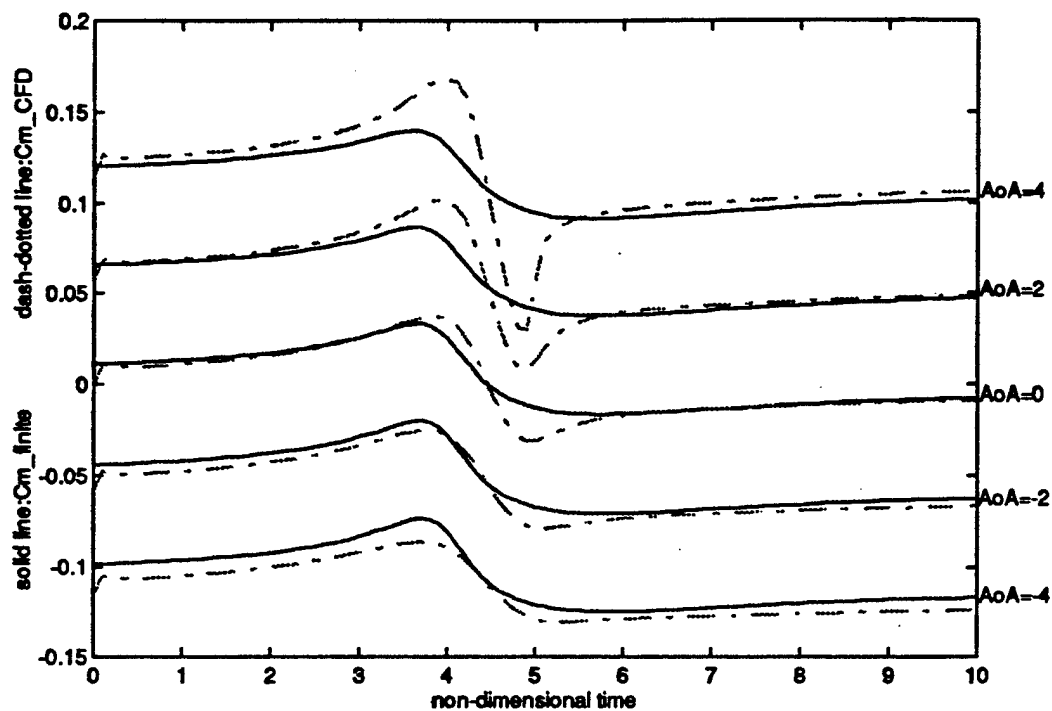


Fig. 12 : Unsteady  $C_l$  from finite-state model for  $\alpha = 10^\circ \sim -10^\circ$

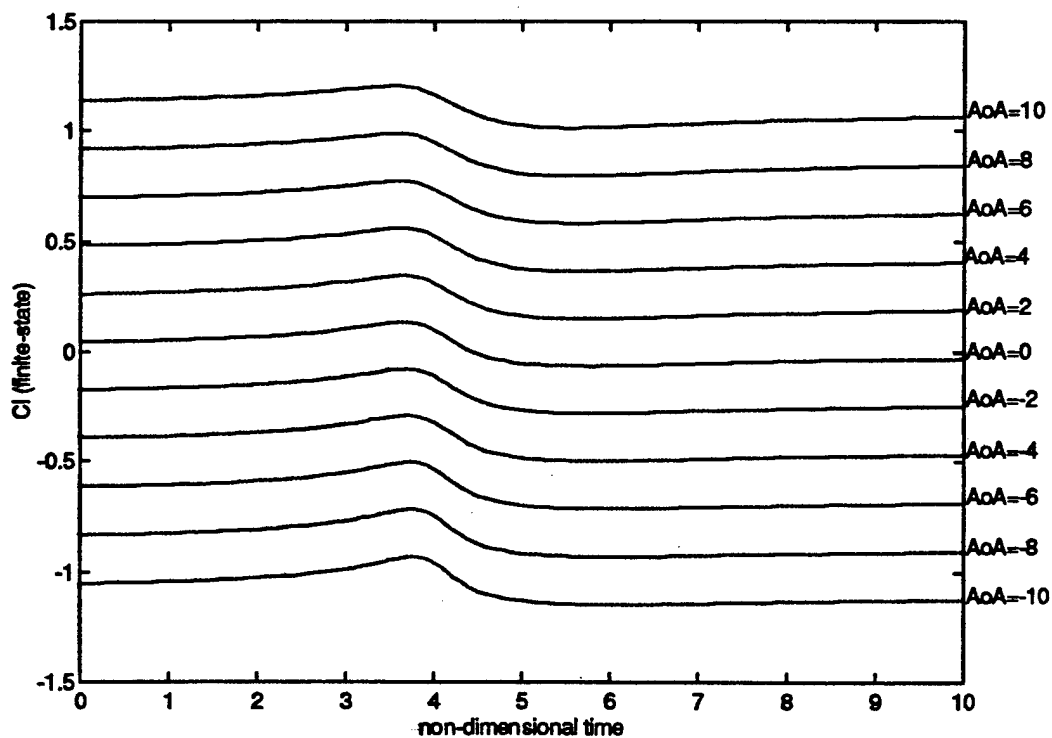


Fig. 13 : Unsteady  $C_l$  from CFD code for  $\alpha = 10^\circ \sim -10^\circ$

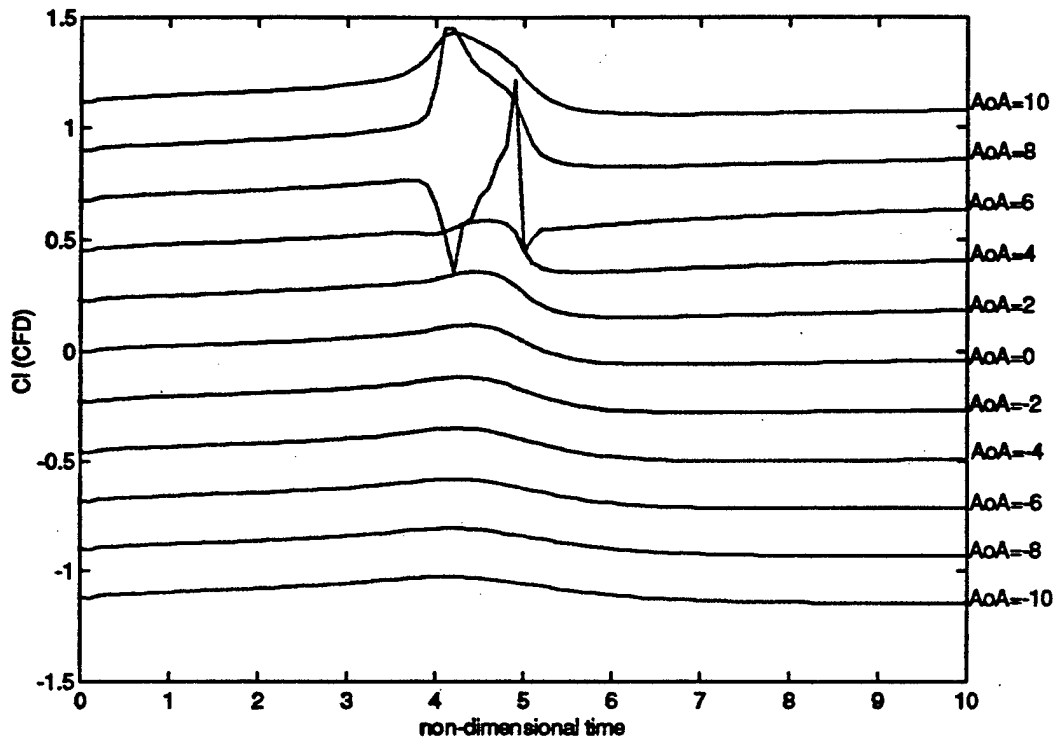


Fig. 14 : Unsteady  $C_m$  from finite-state model for  $\alpha = 10^\circ \sim -10^\circ$

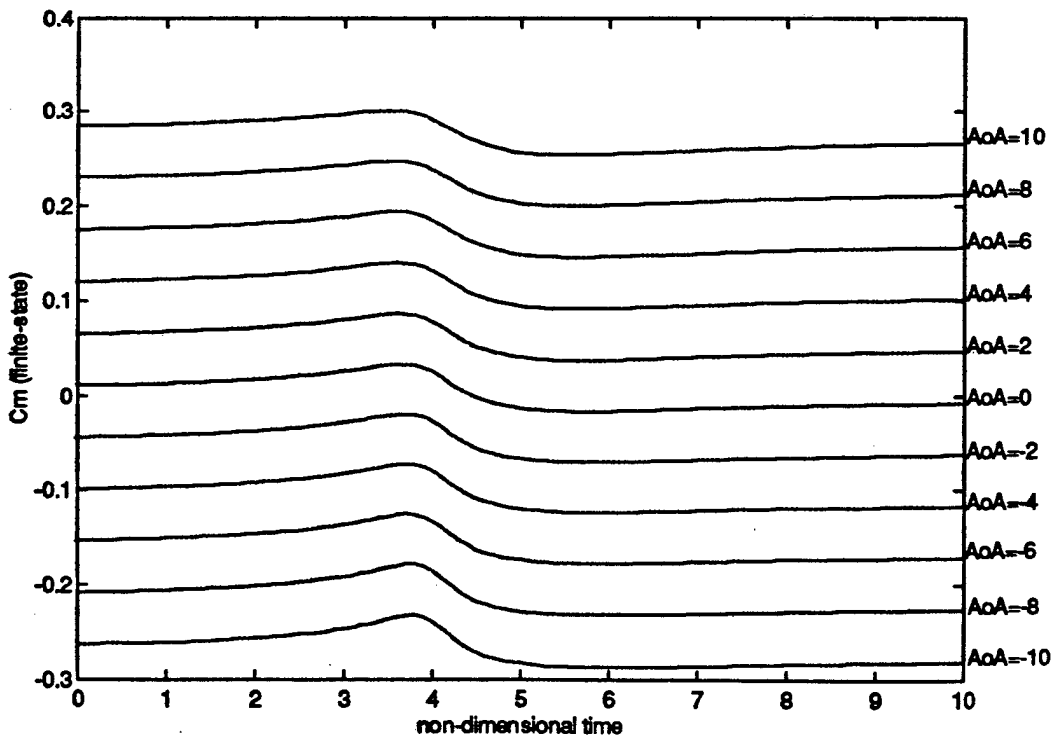




Fig. 15 : Unsteady  $C_m$  from CFD code for  $\alpha = 10^\circ \sim -10^\circ$

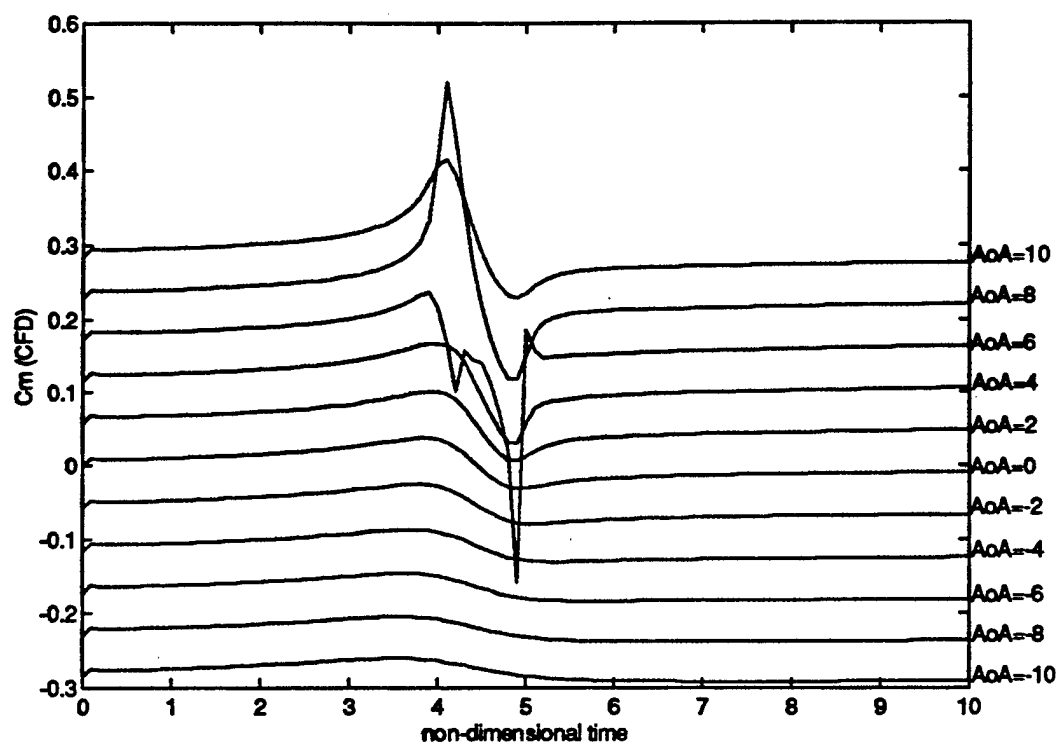


Fig. 16 : Unsteady  $C_l$ ,  $C_m$ , and  $C_d$  from finite-state model at  $\alpha = 10^\circ$

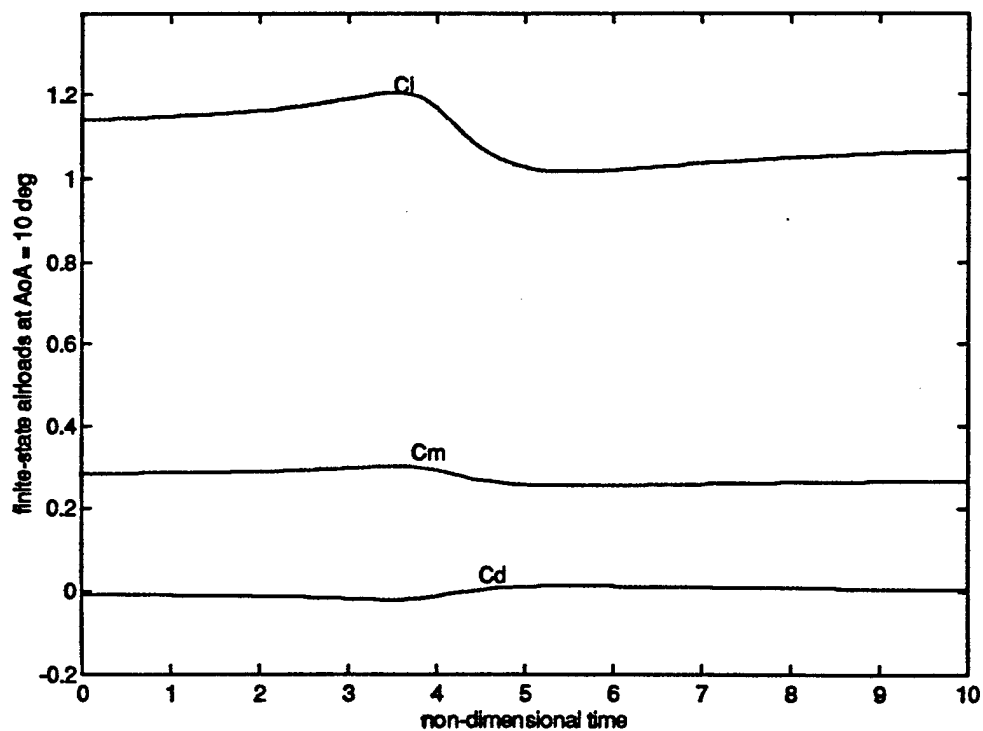


Fig. 17 : Comparison of controlled and uncontrolled Cl

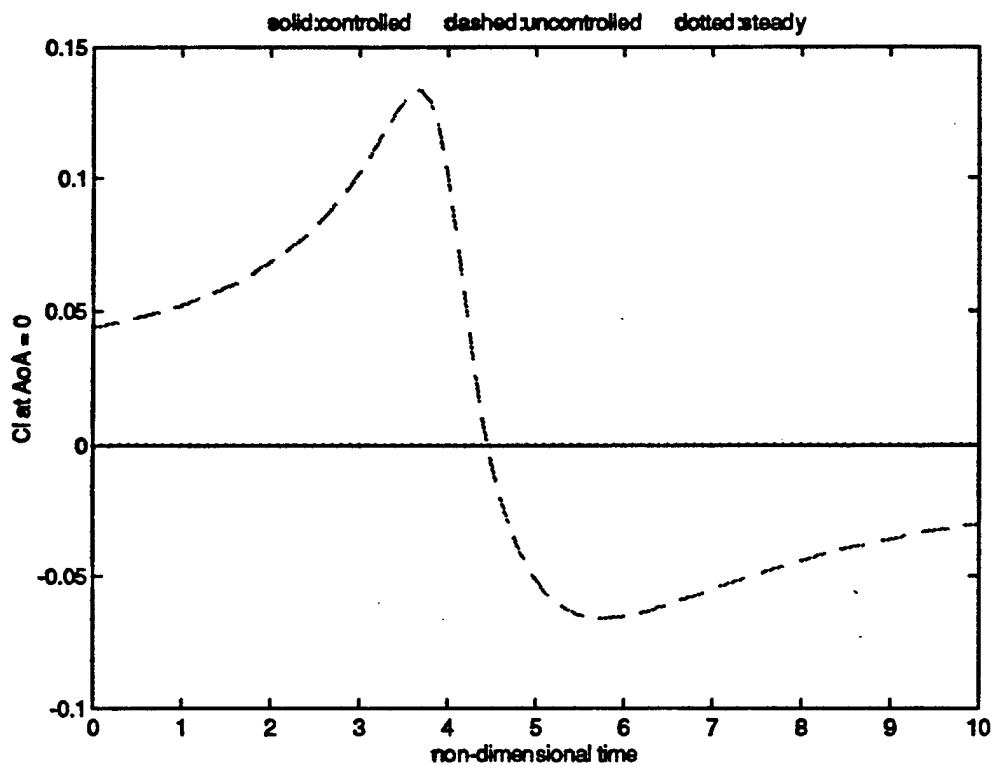


Fig. 18 : Optimal flap deflection scheme

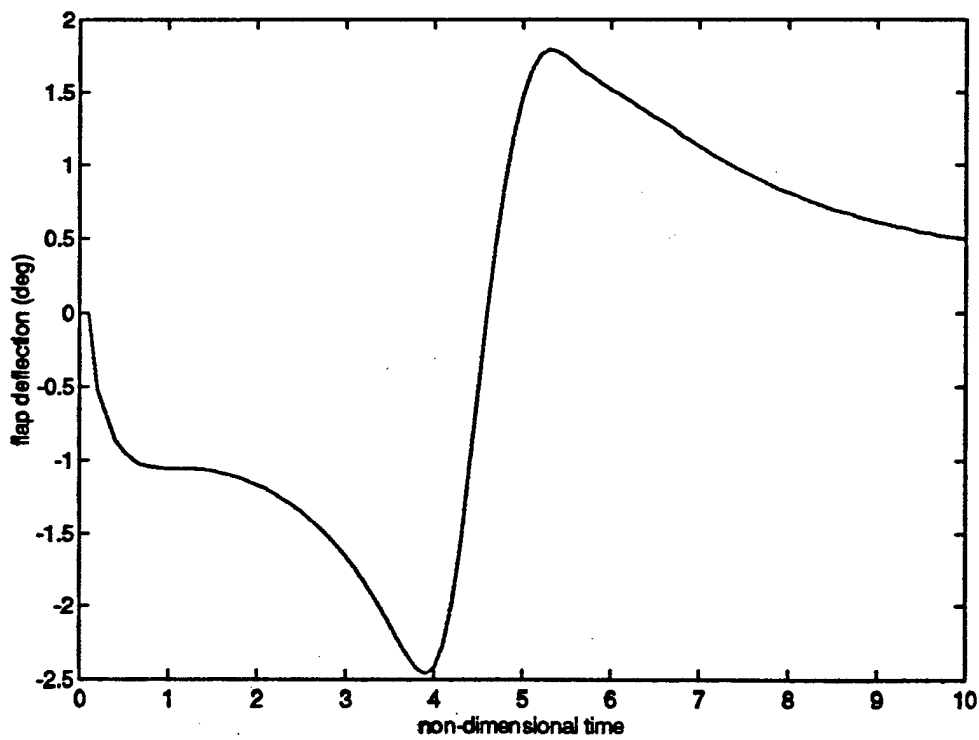


Fig. 19 : Optimal flap angular rate scheme

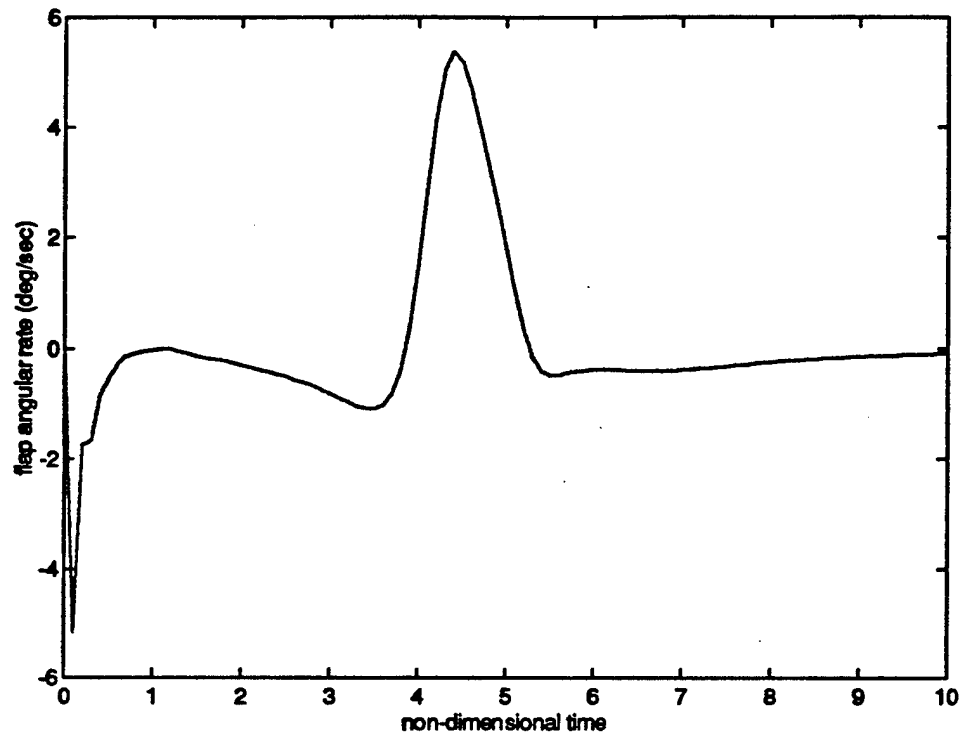


Fig. 20 : Optimal flap angular acceleration scheme

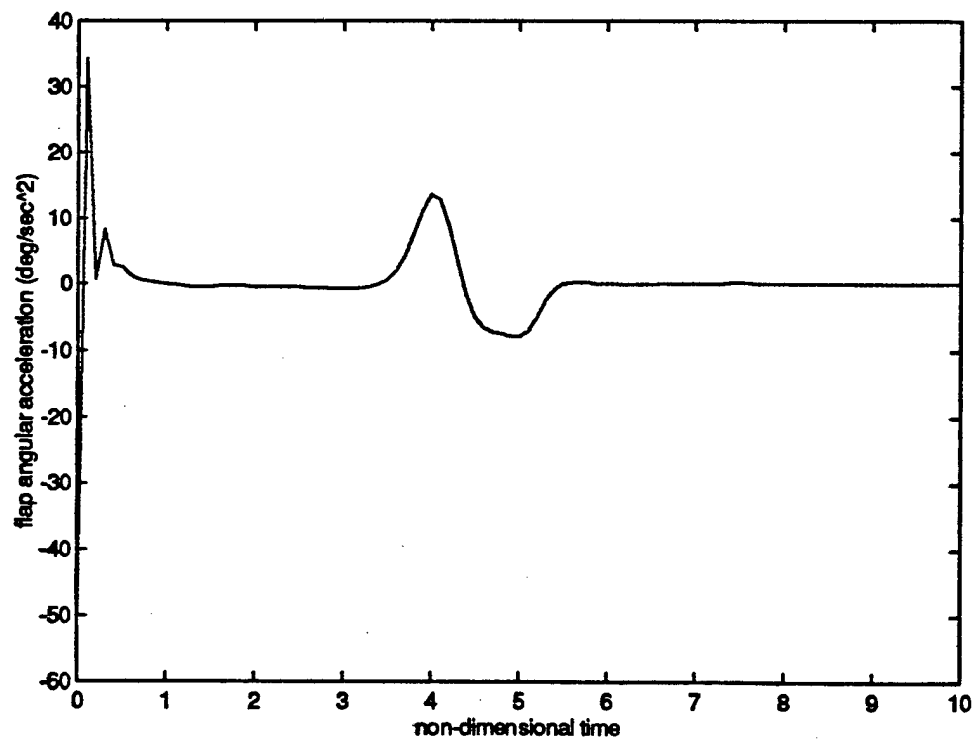


Fig. 21 : Optimal control input scheme

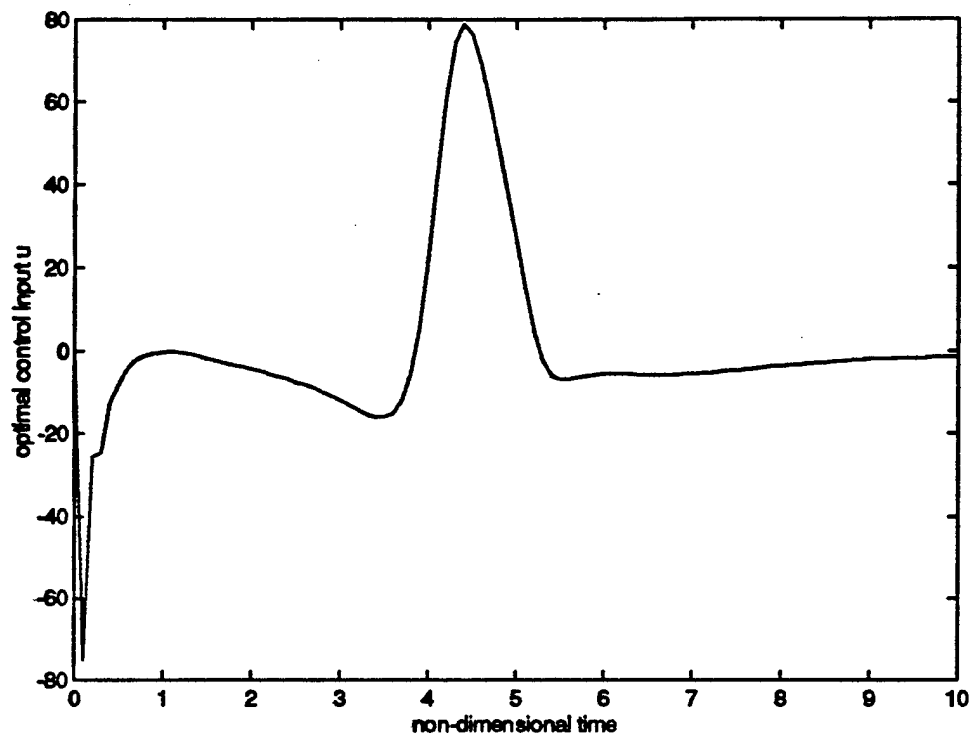


Fig. 22 : Comparison of controlled and uncontrolled  $C_p$  (Panel 1 ~ 4)

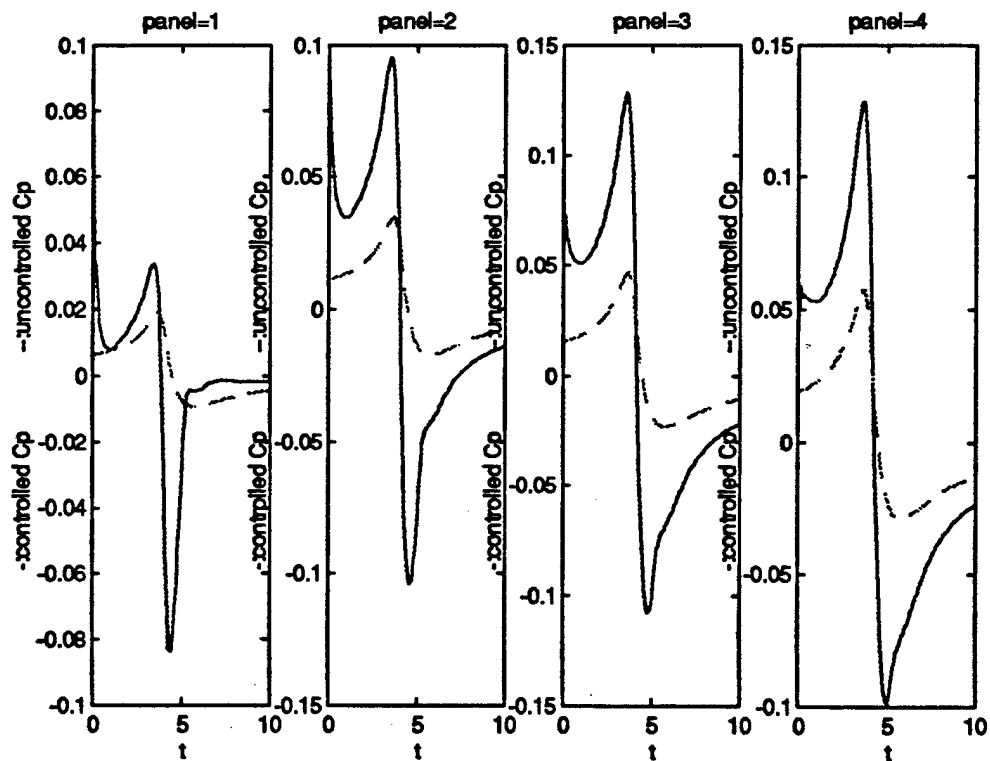


Fig. 23 : Comparison of controlled and uncontrolled  $C_p$  (Panel 5 ~ 8)

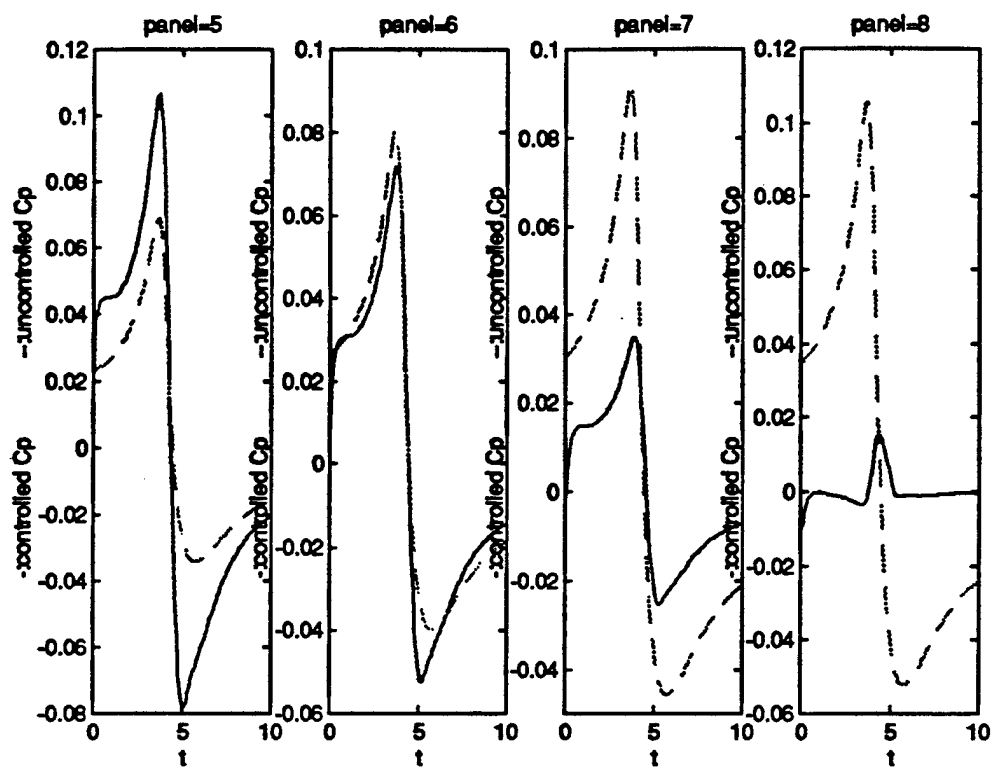


Fig. 24 : Comparison of controlled and uncontrolled  $C_p$  (Panel 9 ~ 12)

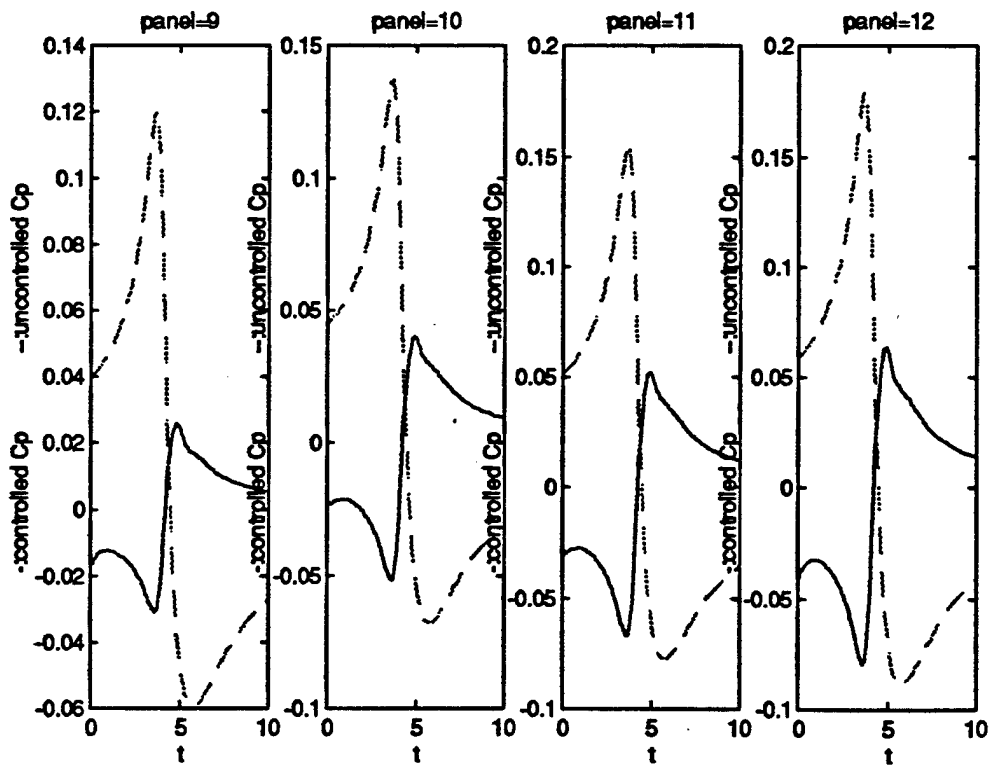


Fig. 25 : Comparison of controlled and uncontrolled  $C_p$  (Panel 13 ~ 16)

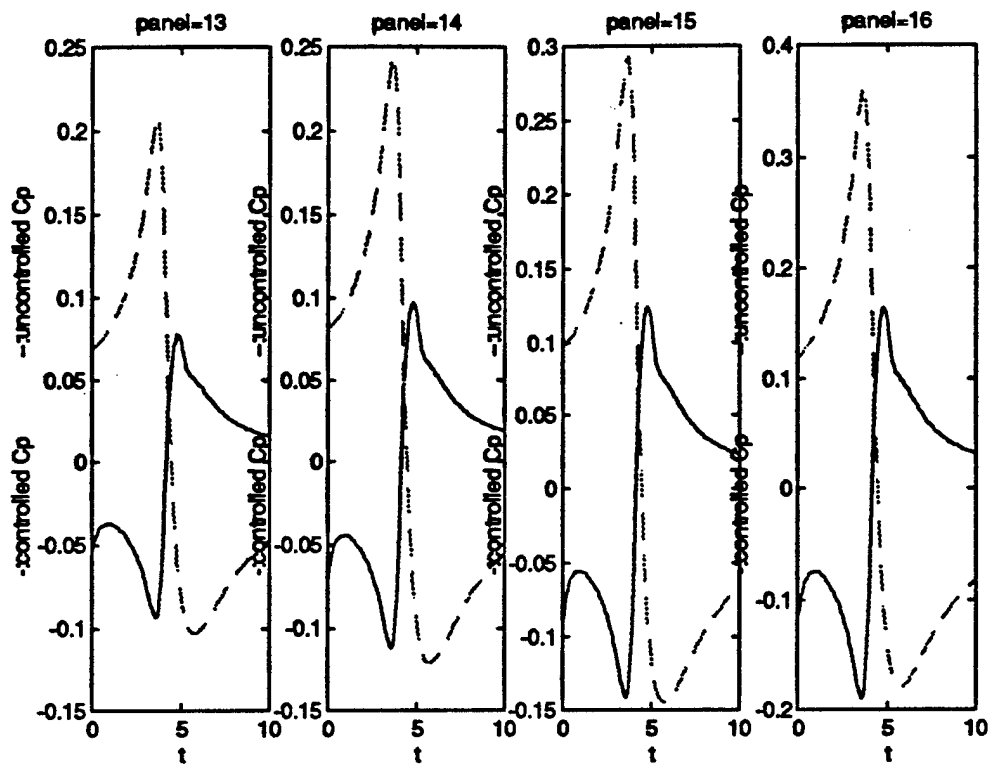


Fig. 26 : Comparison of controlled and uncontrolled  $C_p$  (Panel 17 ~ 20)

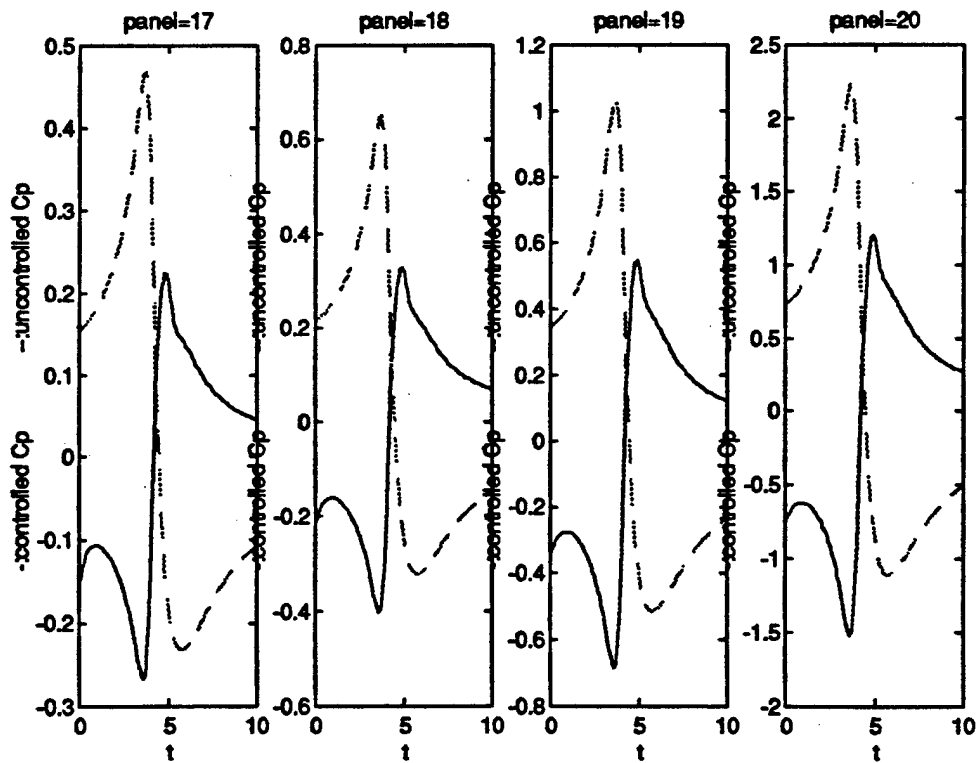


Figure 27. Open-loop and Closed-loop Response

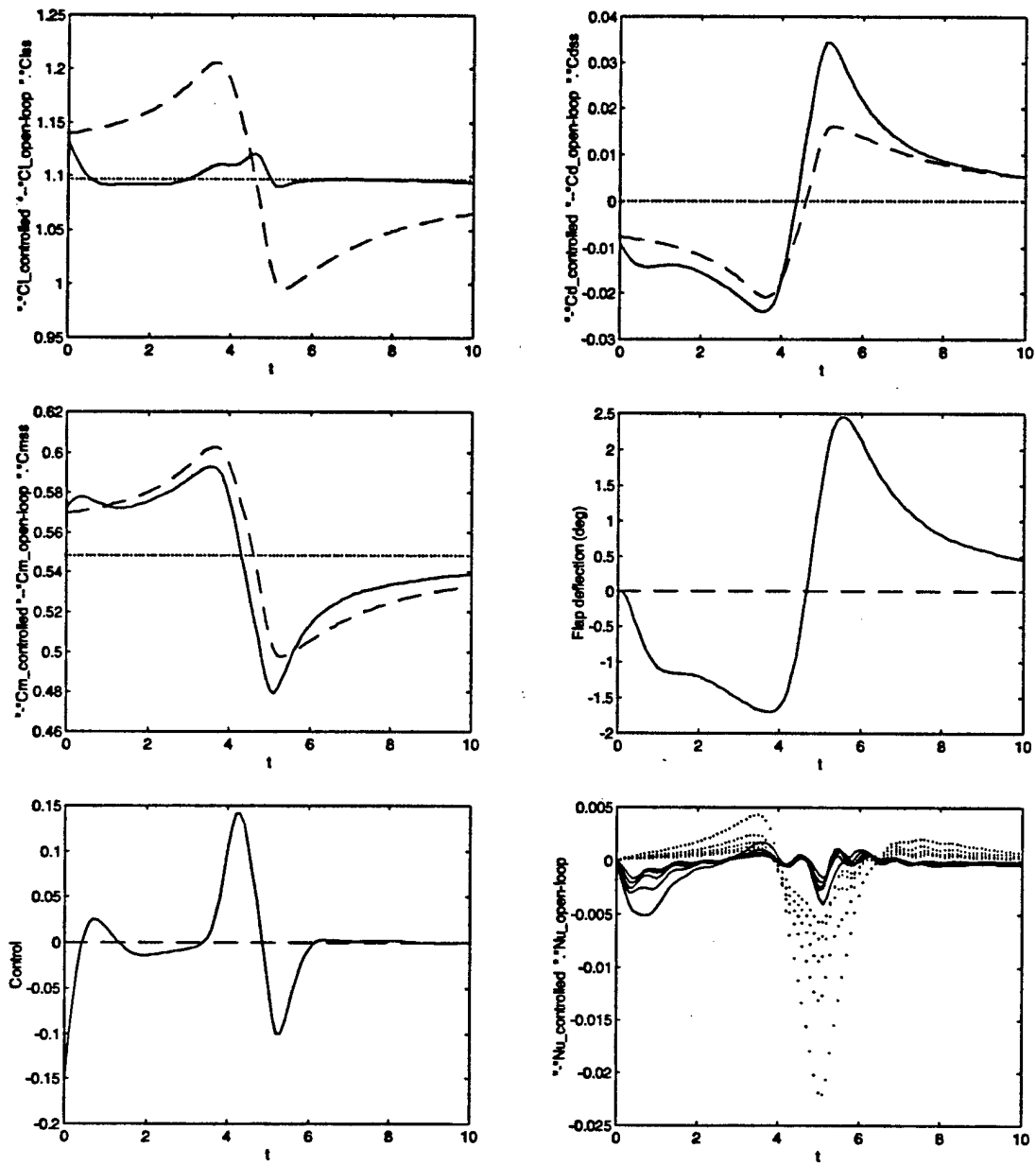


Figure 28. Block Diagram Representation of a Neuro-Fuzzy Controller for BVI

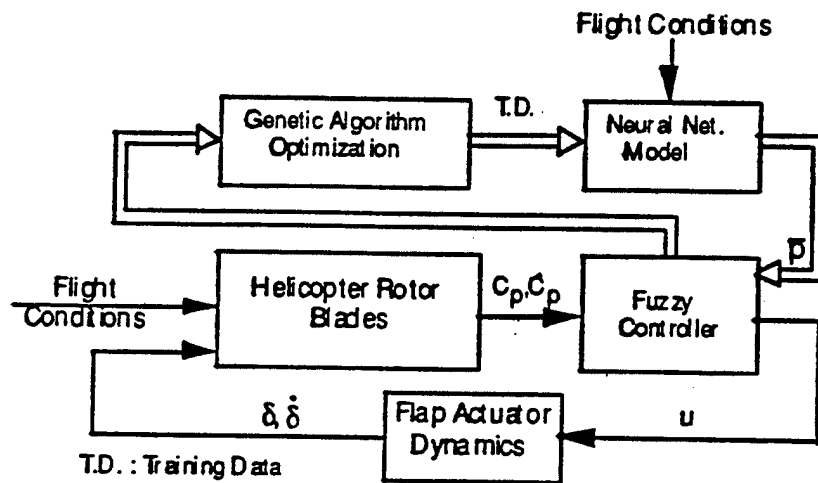
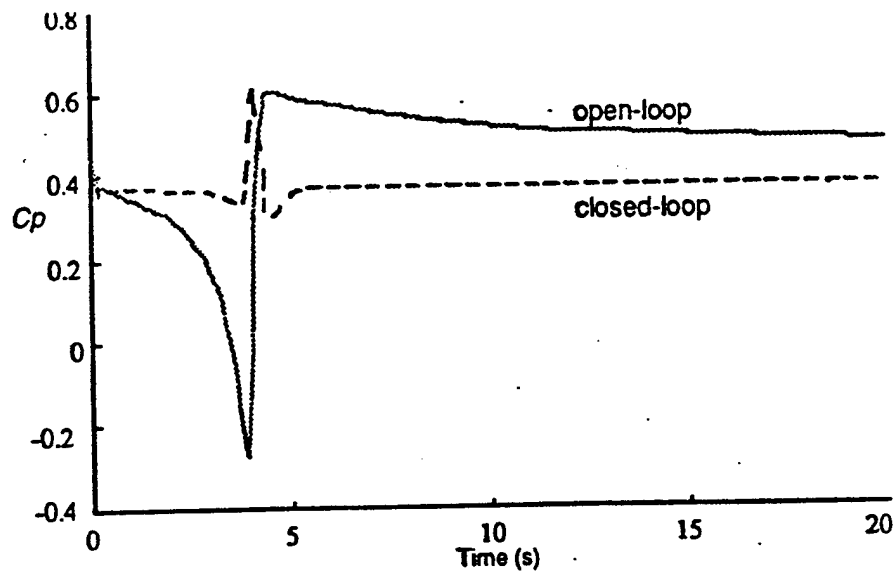


Figure 29. BVI induced pressure variation with a fuzzy logic controller.





## **RTI 5: ACTIVE AIRFOIL FOR ROTORCRAFT**

(CoPIs: S. Hanagud and R. G. Lowey;

Other investigators: Y. Yillicki, R. Roglin)

### **I. Problem Studied**

The principal objective of the task is to conduct basic research that will lead to improved control of rotorcraft. The control can be the collective control, cyclic control or the vibration control. In this task, these controllers are formulated by the use of smart structures to activate the trailing edge flap.

### **II. Accomplishments**

As a first objective, we developed a shape memory alloy based (SMA) trailing edge flap and demonstrated its applicability to collective control by analysis and flight tests on a remotely piloted small vehicle. These SMA based flaps do not have the needed frequency response for the forward flight and vibration control. For this purpose, we have developed a hybrid SMA-piezoelectric transducer based actuator. This actuator has been demonstrated as a bread board model.

The next step was to develop techniques and concepts to use smart structures based trailing edge flaps in forward flight before designing vibration controllers. For forward flight, we need to determine the amount of trailing edge flap deflection needed as a function of the azimuth angle selected advance ratio. The concept used consists of a pre-set angle of attack, a shape memory alloy induced angle of attack and the additional cyclic angle of attack provided by the piezo actuators. With this concept, we have formulated a mathematical model to obtain the cyclic flap deflection with flap deflection varying as a function of the radius. The model has been developed first by using rigid blade/hinge concept to develop the trim conditions to calculate the dynamics of the hinge-less blade/flap by using finite difference equations.

The future work will be to replace the rigid blade/flap trim equations with elastic blade/flap trim equations. Next, we will introduce the dynamics of the flap and flap controllers. Following this

we will design the blades, test these blades and demonstrate the forward flight of a small helicopter.

In this report, we have first described the collective control with the SMA actuators. Then we have described the design concepts for a smart helicopter blade for forward flight with trailing edge flap control. The third part of the report describes our analysis of trailing edge flap control to determine the needed flap angle and flap angle control equations.

### **III. Smart Helicopter for Collective Control**

#### **3.1 Introduction:**

An intelligent structure requires three components. These components are sensors to determine the current state of the structure, actuators to alter the structure from the current state to a desired state, and an algorithm to determine what the desired state of the structure should be. When these three components are present and functional in a structure this structure will have the ability to interact with its environment as the environment is perturbed. The key being the ability to interact according to a predetermined set of rules. An example is an aeroelastically tailored wing. Where the torsional stiffness of the wing is coupled with the bending stiffness to increase the speed when torsional divergence will occur.

The development of an adaptive airfoil presented in this paper includes only the actuator portion of the three components required for an intelligent structure. The actuator drives a trailing edge flap which changes the camber of a portion of the main rotor blade. The initial sensor package will consist of four strain gages located along the span of the blade and the algorithm will compare the output from the sensors on blade 1 and blade 2. Based on this comparison the power distribution to the actuator will be altered to increase the camber of one blade and decrease the camber of the other blade. This comparison / distribution loop is repeated till the blade sensors have the same output.

#### **3.2 Shape Memory Alloys**

In 1965 at the U.S. Naval Ordnance Laboratory Beuhler and Wiley received a United States Patent for a series of engineering alloys that possessed a unique mechanical "memory",

generically named 55-Nitinol due to the fact that the material contains approximately 55 weight percent nickel in chemical composition. The Naval Ordnance Laboratory now called the Naval Surface Warfare Center has been very active in characterization of this material. Other laboratories including Battelle-Memorial Institute and National Aeronautics and Space Administration have also made major contributions toward understanding the mechanism associated with shape memory alloys (SMA).

Figure 1 illustrates the formation of Martensite in a shape memory alloy and the relationship between temperature and the geometric properties of length and volume and the material property of electrical resistance.

Fundamental to the shape memory effect is the occurrence of a martensitic phase transformation and its subsequent reversal. During the martensitic phase the material is soft and easy to deform. The shape memory effect occurs when the specimen is heated and undergoes the phase transformation to its parent or austenitic state. Relatively large strains (6% to 10%) can be achieved with these alloys making them a candidate for actuation type applications.

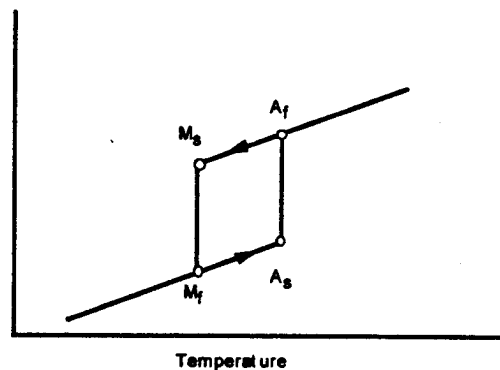


Figure 1. Strain vs. Temperature

This phenomenon of shape memory or the shape memory effect (SME) is illustrated in Figure 2. Let us consider a wire made of SMA (Step 1). Let us also assume that this wire is stretched and deformed inelastically at low temperature (Step 2). The wire is then heated to a temperature above a certain critical temperature (Step 3) to determine the shape that is to be remembered and then cooled. A mechanical stress is then applied to deform the cool wire (STEP 4). Then heat the wire and it returns to its remembered geometric shape (Step 5).

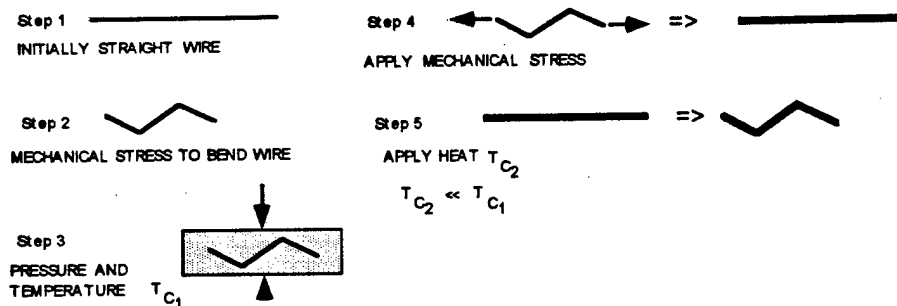


Figure 2. The shape memory effect

Although the shape memory phenomena was first investigated in the 1960's and the shape memory effect has been seen in different alloys only three alloys which exhibit this phenomena are presently in commercial use CuZnAl, CuAlNi, and NiTi

Many researchers were involved in determining the mechanism which explains these alloys unique abilities. These alloys have the mechanical ability to accommodate plastic strains of typically six to eight percent and when restrained from regaining their original shape they can generate stresses in the range of 100,000 psi. These force and displacement capabilities make shape memory alloys an attractive material for electromechanical actuators.

The shape memory effect results from the formation of martensitic plates. Figure 3 illustrates a single plane of shape memory alloy. In the austenitic phase or parent phase the plane has the shape of a square (this is the shape which has been memorized by the material as described in figure 2).

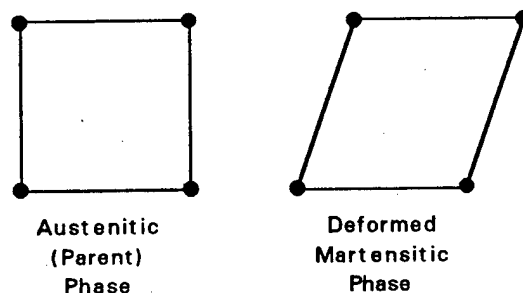


Figure 3. Austenitic / Martensitic planes

When the alloy is at a temperature below  $M_f$  it is deformed into a rhombus. When the alloy is cooled below  $M_f$  martensitic plates form which are self-accommodating and cause no macroscopic deformations. the plane is then deformed into a rhombus under a mechanical load

which is subsequently removed. When the alloy is then heated the martensitic plates begin to disappear starting at  $A_S$  and by the time the alloy has reached  $A_f$  all the martensitic plates are gone and the shape of the plane is back to that of a square.

In two dimensions there are four ways the square can be deformed into the rhombus illustrated in Figure 4. Once a path of deformation has been established for deforming the plane from a square to a rhombus this is the only path that can be followed. This means that if the square has been deformed by application of a shear along the top surface as seen in Figure 4a the reverse process will be for the top to slide back to the left.

The characteristic of self-accommodation demonstrated by the martensitic plates causes four of the rhombic variants to group together. Figure 5 illustrates this grouping in the large scale picture of a specimen ABCD under a load acting to the upper right. In this orientation three of the rhomboids are unstable (1, 3, and 4) with respect to the stress. These three will be consumed by the growth of martensitic plates in rhombus number 2. When this specimen is subsequently heated the martensitic plates formed will disappear and the shape will follow the reverse of the deformation path to return to its original square shape.

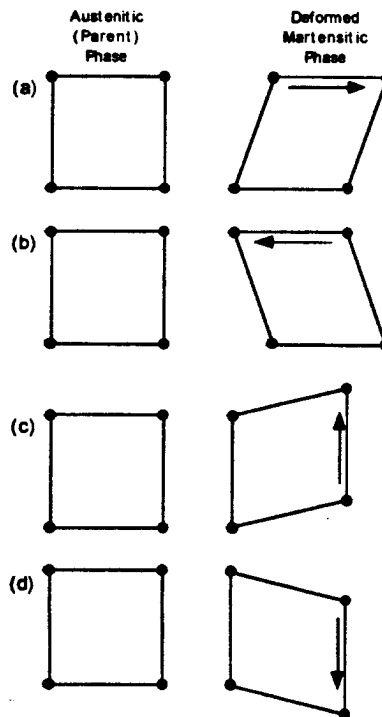


Figure 4. Deformation paths

This phenomena is described as the one way shape memory effect because after the specimen is heat and returns to it's original shape it will remain in this shape under temperature cycling. The specimen can be deformed again in the martensitic phase and will return to the parent shape when heated above the austenitic start temperature. Therefore as long as there is a stress to deform the specimen in the martensitic phase the material can be cycled.

The temperature deformation relationship is illustrated in Figure 1. In this figure there is a transition temperature where the alloy undergoes a material phase transformation from austenite to martensite it is this phase transformation which is responsible for the shape memory effect. The effect of the end conditions is illustrated in Figure 6. As the end condition stiffness change from free to fixed the deformation of a wire specimen decreases and internal specimen stress increases this can lead to a phenomenon known as stress induced martensitic transformation of the alloy.

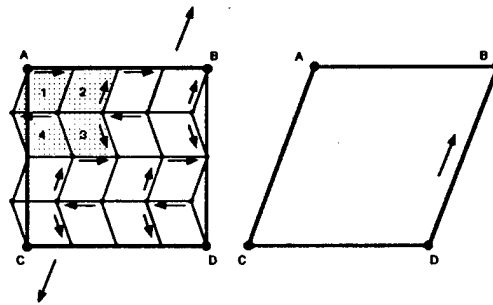
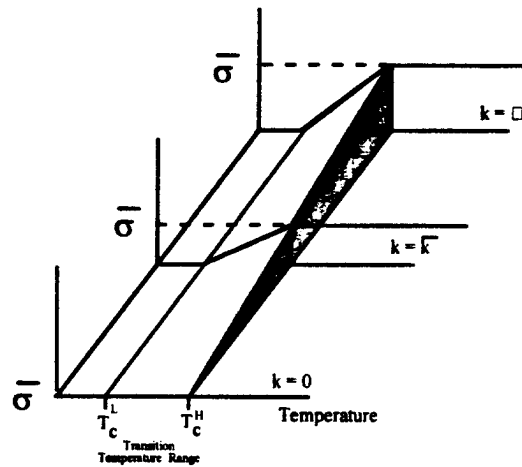


Figure 5. Self-accommodation of martensitic plates

The fabrication of SMA hybrid composites are an example of a material with "*Intelligence at the most primitive levels*". These composite materials contain a lamina of SMA fibers. There is still much to be learned about the interaction of stress and temperature in relation to the extent, reliability and fatigue life of shape memory alloy dynamic actuators. Composite materials which incorporate shape memory fibers have tremendous potential for creating structures which can adapt to changes in their loading environment. When these composite materials are heated they can demonstrate stiffness increases of as much as three times that of the unheated material. There are many applications for such an actuator. These include vibration control through the processes of active stiffness tuning or active strain energy tuning.

Active stiffness tuning is a method of steady state vibration control. The vibration characteristics, frequencies and mode shapes, of a structure or mechanical component can be

Active stiffness tuning is a method of steady state vibration control. The vibration characteristics, frequencies and mode shapes, of a structure or mechanical component can be altered in a controlled fashion by heating the embedded or bonded shape memory alloy fibers associated with the structure. As the fibers heat the alloy experiences a phase change when it transforms from the martensitic state to an austenitic state. Associated with this phase transformation is an increase in Young's



Temperature Relationship

$$\sigma = \bar{\sigma} \left( \frac{T - T_c^L}{T_c^H - T_c^L} \right)$$

Deformation Relationship

$$\delta = 0 \Rightarrow k = \infty : \bar{\sigma} = \sigma_{\max}$$

$$\delta = \delta_{\max} \Rightarrow k = 0 : \bar{\sigma} = 0$$

$$\bar{\sigma} = \sigma_{\max} \left( \frac{\delta_{\max} - \delta}{\delta_{\max}} \right)$$

Figure 6. End condition effect

modulus by a factor of three and an increase in yield strength by a factor of ten. Since the natural frequencies of any structure are proportional to the Young's modulus these increases will result in a stiffer structure with higher natural frequencies.

Active strain energy tuning is a process in which a shape memory lamina is located and oriented in such a way that upon heating it will not deform the structure but instead will impose a residual state of strain. The resulting stored strain energy (compression or tension) changes the total energy distribution and modifies the modal response of the structure.

relaxation is solely due to cooling. To achieve the maximum frequency response requires an active control loop which will monitor the material temperature. The minimum temperature must not be allowed to be less than the martensite finish temperature and the maximum temperature must not be allowed to exceed the austenite finish temperature. This means the temperature must be kept in a range of  $40^{\circ}\text{C}$  for material with a transition temperature of  $90^{\circ}\text{C}$ . The other limitation is the inertia effect. This effect is present when the material is rapidly contracted with an external load such as in the case of a wire actuator. Under these conditions the inertia effect associated with the load which the actuator is attempting to move can overstress the wire actuator. A practical frequency response of 4 hertz can be achieved for a wire with a diameter of 0.010 inches if the wire is heated using short (millisecond) high bursts of current and cooled using a water with glycol bath. This type actuator will require very high values of current to heat the wire since an active cooling mechanism (a water with glycol bath) is being used to continuously remove heat from the wire.

The application to structural mechanics problems of these hybrid shape memory alloy composites is far greater than just the control of vibrations. The ability of the material to change modulus of elasticity would allow discretely placed shape memory alloy fibers to increase the critical buckling load of flexible structures or alter the critical speed of a flexible drive shaft. Another area where shape memory alloys will excel is in shape control of flexible structures. This application will include both motion and shape control. To accomplish this a controller must simultaneously employ force actuators and stiffness actuators for transition to occur from one predetermined shape to another similar to the way the human muscular system works.

### 3.3 Control Problems:

The environment in which a helicopter must operate is extremely complex due to the interaction between the vehicle dynamics and the aerodynamic loading. The low natural frequencies associated with the rotor blades result in severe dynamic loading of the fuselage through the rotor hub. In addition to the aerodynamic loading of the rotor system there are also the additional forces associated with any rotating system. These include centrifugal, coriolis, and gyroscopic forces. In forward flight the rotational system is also subject to an asymmetrical lift



the additional forces associated with any rotating system. These include centrifugal, coriolis, and gyroscopic forces. In forward flight the rotational system is also subject to an asymmetrical lift due to differences in the airflow over the advancing and retreating blades. The aeroelastic phenomena described above combine to result in an aerodynamic flow around the rotor disk which is unsteady and asymmetric with airloads changing periodically along the span due to variations in blade section velocity and deformation.

Solutions to reduce the impact of asymmetrical loads and the resulting rotor blade vibration have been proposed and implemented in the following three areas.

- Alterations to blade and hub systems
- Passive vibration control schemes
- Active vibration control schemes

The first area is to improve the blade and hub systems. These include new blade airfoil sections or tips and elastomeric rotor hubs. With these solutions engineers are attempting to eliminate the unwanted vibratory effects before they enter the fuselage. There are drawbacks associated with this solution. First, they are applicable in a limited portion of the flight envelope and second, it is extremely expensive to manufacture a blade in which the cross section (airfoil shape) varies from root to tip.

The second area is to incorporate passive devices to isolate the pilot, passengers, or cargo from the effects associated with the vibratory loading. The problem with this solution is there is usually a weight penalty associated with these isolation devices and the devices usually have a narrow range of vibratory loading for which they are effective.

The third area is the employment of active vibration control schemes. These schemes can be developed to have flexibility in how they modify the rotor system response characteristics. Higher harmonic control and individual blade control are two examples of active control schemes.

The higher harmonic control scheme is based on the fact that the vibratory loads acting on the blade are harmonic in nature and contain an infinite number of harmonic components. Normally, the swash-plate inputs (changes in rotor blade pitch or angle of attack) which are applied to the rotor system only address the phenomena associated with the lower harmonics such

additional higher harmonic inputs which interact with the airloads to reduce vibration of the rotor system. The drawbacks of this scheme are:

- There must be sufficient control force to overcome the mass inertia effect associated with the swash-plate and pitch links.
- The swash-plate must be stiffer to transfer the forces associated with a smaller stroke or tilt of the plate as would occur when transmitting a higher harmonic inputs.
- Each blade at a given azimuthal location is constrained to follow the same pitch variation.

The individual blade control scheme differs from the higher harmonic control scheme in that the control mechanism is now associated with each rotor blade at the blade level rather than at the rotor hub level. This means that each blade has the ability to act independently of the other blades thus allowing the implementation of more complex control inputs to the rotating system. Alterations of the rotor blade dynamic characteristics now have another degree of freedom associated with the problem of reducing vibratory loads before they enter the rotor hub. The current method of swash-plate stroke and tilt for collective and cyclic control inputs can now be eliminated if these basic rotor functions of lift, thrust generation, and trim are moved to the rotor blade.

### 3.4 Current Work:

The objective of this research was to investigate the application of an adaptive material as an actuation mechanism for individual blade collective control. This actuator was employed to change the camber of a portion of the main rotor blade. The primary function of this camber change was to generate thrust and replace the collective control currently used to generate thrust. The unique features of this work are:

- The use of an ADAPTIVE MATERIAL as the actuation element of the electromechanical actuator in an individual blade collective control scheme which will change the camber of an airfoil
- Employment of camber change as the PRIMARY thrust generating mechanism in a powered lift vehicle

- Employment of camber change as the PRIMARY thrust generating mechanism in a powered lift vehicle

The motivations for pursuing this problem were the potential improvement to performance by implementation of individual blade control to alter of the cross section shape and blade twist, the potential improvements to reliability through reduction in the number of moving parts and maintainability through a reduction in the mechanical complexity of the actuation system.

The accomplishments associated with the research are the design, fabrication and testing of a flight vehicle. The design tasks dealt with how to modify the power plant of an existing internal combustion powered helicopter and the design of a control surface to be incorporated into the main rotor blades. The fabrication task was then the manufacturing of the required parts to transfer the design concept from paper to hardware. The testing task involved both ground and flight test of the modified vehicle to insure the structure integrity of the modifications. Finally the feasibility of the idea was demonstrated in flight test when a deflection of the control surface by an adaptive material resulted in vertical climb of the helicopter.

3.4.1 Helicopter: This project started with a generic radio controlled helicopter. A three view of the helicopter and the characteristic data associated with the helicopter are shown in Figure 7. The recommended internal combustion motor to be used with a helicopter of this size has an output of 1.8 horsepower and can generate 17,000 rpm under load.

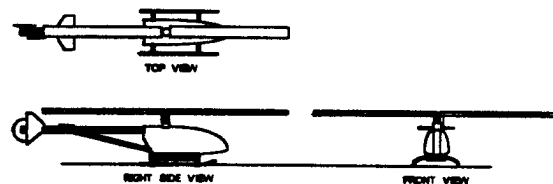


FIGURE 7 Three View

Fuselage Length	35 in
Fuselage Width	8 in
Helicopter	108 oz
Weight	

PARAMETERS	MAIN	TAIL
Radius	28 in	6 in
Chord	2.5 In	0.75 in
Solidity	0.0568	0.0796
No. of Blades	2	2
Tip Speed	4693 in/sec	4023 in/sec
Airfoil Section	NACA 0012	NACA 0012
Collective Range	+8° -> -8°	+8° -> -8°
Long      Cyclic	+5° -> -5°	N/A
Range		
Lateral    Cyclic	+5° -> -5°	N/A
Range		

Control of this helicopter is achieved with five small servo actuators. These function as follows:

- Longitudinal Cyclic
- Lateral Cyclic
- Collective Main Rotor
- Collective Tail Rotor
- Throttle

There is mechanical coupling between the main rotor collective and lateral cyclic and electronic coupling between the main rotor collective, tail rotor collective and throttle.

**3.4.2 Helicopter Modifications:** This baseline helicopter was then modified to remove the internal combustion power plant and incorporate an electric power plant. The reason for this modification was to improve the reliability and repeatability of helicopter flights. The internal combustion motors are sensitive to many factors such as fuel content and carburetor adjustments. This sensitivity results in many hours of downtime spent diagnosing and correcting power plant problems. This sensitivity also leads to variations in the power available and the associated performance of the helicopter which adversely effect the repeatability of the experimental results. There is also the problem of testing the helicopter indoors with an internal combustion power plant. Since volatile liquid fuels are used there is a real possibility of fire or explosion and the problem of venting the exhaust.

plant. Since volatile liquid fuels are used there is a real possibility of fire or explosion and the problem of venting the exhaust.

The first step was to determine the required input and output of an electric motor to be used as the helicopter power plant. The first analysis was done using just the momentum method. This method calculates the power based on an exchange of energy between the rotor disk and the wake. The thrust required to hover the helicopter is related to this change in momentum between the rotor disk and the wake below. First the expression for the thrust is presented in equation 1. This equation related the thrust to the change in mass flow rate from above the rotor disk  $v_0$  (equal to zero) to below the rotor disk  $v_2$ .

$$\begin{aligned}
 \text{Thrust} &= (\text{mass/sec}) * (\text{Change in Flow Velocity}) \\
 \text{Thrust} &= (\rho v_1 A) * (v_2 - v_0) \\
 v_2 &= \text{Velocity below the rotor disk} \\
 v_1 &= \text{Velocity at the rotor disk} \\
 v_0 &= \text{Velocity above the rotor disk} \Rightarrow 0
 \end{aligned}
 \tag{Eq (1)}$$

Once, the expression for thrust has been determined the relationship between the flow velocity at the disk  $v_1$  and the flow velocity below the rotor in the wake  $v_2$  must be established. This relationship is established by equating the energy absorbed by the wake to the energy dissipated by the rotor.

$$\begin{aligned}
 \text{Energy Dissipated by Rotor} &= \\
 &\quad \text{Energy Absorbed by Wake} \\
 \frac{E_R}{\text{sec}} &= \frac{E_W}{\text{sec}} \\
 T * v_1 &= \frac{1}{2} \left( \frac{\text{mass}}{\text{sec}} \right) (v_2)^2 \\
 (\rho v_1 A v_2) v_1 &= \frac{1}{2} (\rho v_1 A) (v_2)^2 \\
 v_2 &= 2 v_1
 \end{aligned}
 \tag{Eq (2)}$$

The expression for the inflow velocity  $v_1$  in equation 2 is then substituted into the thrust expression in equation 1. Since the thrust to hover must equal the weight of the helicopter the thrust value is a known quantity and the only unknown is the inflow velocity  $v_1$ . Rearranging the terms and solving for the inflow velocity (equation 3) illustrates the relationship of inflow to disk loading.

$$\begin{aligned}
T &= 2 \rho (v_1)^2 A \\
v_1 &= \sqrt{T / 2 \rho A} \\
v_1 &= (\sqrt{T / 2 \rho}) (\sqrt{DL}) \\
DL &= \frac{T}{A}
\end{aligned}
\tag{Eq (3)}$$

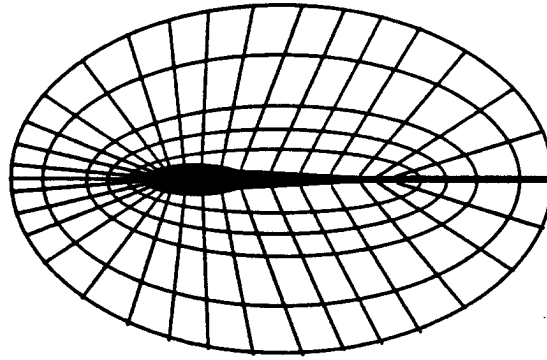
The inflow velocity is related to the square root of the disk loading. For the helicopter used in this program the disk loading is 0.75 pound per square foot and the inflow velocity is 12.6 feet per second.

$$\begin{aligned}
T &= 12 \text{ [lbs]} \\
A &= 15.9 \text{ [ft}^2\text{]} \\
DL &= 0.75 \text{ [} \frac{\text{lbs}}{\text{sqft}} \text{]} \\
v_1 &= 12.6 \text{ [} \frac{\text{ft}}{\text{sec}} \text{]} \\
v_2 &= 25.2 \text{ [} \frac{\text{ft}}{\text{sec}} \text{]}
\end{aligned}
\tag{Eq (4)}$$

The induced power required which is equal to the product of thrust and inflow velocity can then be calculated. The power value based on a figure of merit or efficiency of 60% for this helicopter is 341 watts (watts will be the unit for power since the power plant for this helicopter is an electric motor )

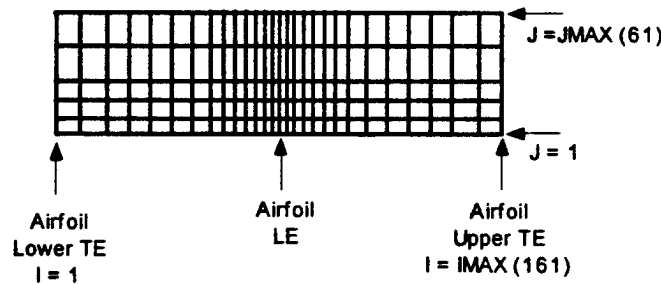
$$\begin{aligned}
h_{pi} &= \frac{T \sqrt{DL}}{550 \sqrt{2 \rho}} = 0.2743 \text{ hp} = 205 \text{ watts} \\
h_{pa} &= \frac{h_{pi}}{\text{Figure of Merit}} \\
h_{pa} &= \frac{205}{0.6} = 341 \text{ watts}
\end{aligned}
\tag{Eq (5)}$$

The blade element method was then applied to the rotor system to improve the prediction of power required by the electric power plant. In this method the rotor blade is divided into segments.



Lift and drag are calculated on each section using 2D airfoil coefficients which were found using a CFD method.

The model employed a control volume which has a 161 by 61 grid. The grid is closely spaced at the leading edge and then becomes wider as it progresses to the trailing edge. The above illustration is for a typical grid of this form. This grid illustration is not to scale and the numbers given above for the grid are 61 ellipses with 161 radial lines emanating from the airfoil. This grid is then unfolded to the following form



A finite difference scheme is then applied to this grid to solve the Navier-Stokes equations which are listed below

$$\vec{q}_t + \vec{E}_x + \vec{F}_y = \frac{(\vec{R}_x + \vec{S}_y)}{R_e}$$

$q = \{\rho, \rho u, \rho v, e\}^T$  Conserved Flow Properties

$\rho$  = Fluid Density

$u, v$  = Inertial Cartesian Velocity Components

$e$  = Total Energy of the Fluid / Volume

$\vec{E} = \{\rho u, \rho u^2 + p, \rho uv, u(e + p)\}^T$

$\vec{F} = \{\rho v, \rho uv, \rho v^2 + p, v(e + p)\}^T$

$\vec{R} = \{0, \tau_{xx}, \tau_{xy}, R_4\}$

$\vec{S} = \{0, \tau_{xy}, \tau_{yy}, S_4\}$

Where the components of the R and S vectors are viscous terms

From this data the lift curve slope was calculated and substituted into equation 6. The results are then summed from the blade root to the blade tip to determine the thrust. The first quantity needed in the lift equation 6 is an expression for the lift on a single blade element.

$$\begin{aligned}
 \Delta L &= q c_l c \Delta r \\
 q &= \text{Local Dynamic Pressure} \\
 q &= \frac{1}{2} \rho (\Omega r)^2 \\
 c_l &= a \alpha \\
 \alpha &= \theta - \phi \\
 c_l &= a (\theta - \frac{v_l}{\Omega r}) \\
 \Delta L &= \frac{1}{2} \rho (\Omega r)^2 a (\theta - \frac{v_l}{\Omega r}) c \Delta r
 \end{aligned}
 \tag{Eq (6)}$$

This expression is then integrated (equation 7) over the blade span to determine the thrust. The blades used in this program have no twist ( $q = q_0$  "Collective Input") and have no taper.

$$\text{Thrust} = b \int_{R_1}^{R_2} \left\{ \frac{1}{2} \rho (\Omega r)^2 a \left( \theta - \frac{v_l}{\Omega r} \right) c \right\} dr
 \tag{Eq (7)}$$

In coefficient form the thrust for this helicopter is given in equation 8. To non-dimensionalize the thrust is divided by the air density ( $\rho$ ) the rotor disk area ( $A$ ) and the tip speed squared ( $\Omega R^2$ ). The thrust coefficient base on the effective rotor disk area ( $\sigma A$ ) is also given. Where  $s$  is the rotor solidity.

$$\begin{aligned}
 \rho &= 0.002378 \left[ \frac{\text{slugs}}{\text{sec}^3} \right] \\
 \Omega &= 146.61 \left[ \frac{\text{Rad}}{\text{sec}} \right] \\
 C_T &= \frac{\text{Thrust}}{\rho A (\Omega R)^2} \\
 \sigma &\equiv \text{Solidity} = \frac{AB}{A} = \frac{bc}{\pi R} \text{ (Constant Chord)} \\
 \sigma &= 0.0589 \\
 C_T / \sigma &= 0.0526
 \end{aligned}
 \tag{Eq (8)}$$

Once the expression for thrust has been determined it can be rearranged to show the function relationship between thrust and collective (equation 9). In this equation the term  $f$  is defined as the square root of one half the trust coefficient. The term  $f$  is



$$\begin{aligned}
\text{Thrust} &= b [\rho/2 (\Omega R)^2] a [\theta(R/2) - \phi_T(R/2)] c \\
\phi_T &= \frac{v_1}{\Omega R} \\
v_1 &= \sqrt{\eta_2 \rho A} \\
\phi_T &= \sqrt{C_{T_2}} \\
T &= c b [\rho/2 (\Omega R)^2] a (R/2) [\theta(\eta_3) - \sqrt{C_{T_2}}] \\
C_{T_\sigma} &= (\eta_4) [\theta(\eta_3) - \sqrt{(\eta_2)(C_{T_\sigma})}] \\
\theta &= (\eta_2) [(\eta_4)(C_{T_\sigma}) + \sqrt{(\eta_2)(C_{T_\sigma})}] \quad \text{Eq (9)}
\end{aligned}$$

physically the reduction in pitch angle  $q$  due to the orientation of the inflow velocity. Based on the thrust of 12 pounds the collective angle would have to be  $6.5^\circ$ .

The torque and power relationships are the final equation (equation 10). Where power is just the torque times the angular velocity. The torque is composed of two part one due to induced drag effects and one due to profile drag effects.

$$\begin{aligned}
\Delta P &= \Delta Q \Omega \\
\Delta Q &= r (\Delta L \phi + \Delta D_o) \\
\Delta Q &= r ( \{ [ \frac{1}{2} \rho (\Omega r)^2 ] a (\theta - \phi) c \} \phi \\
&\quad + \{ [ \frac{1}{2} \rho (\Omega r)^2 ] c_d c \} ) \Delta r \\
C_{Q_\sigma} &= (\eta_4) [\theta(\eta_3) - \phi] \phi + \eta_8 \\
C_Q &= C_T \sqrt{C_{T_2}} + \sigma \eta_8 \\
C_P &= C_Q = 0.0002 \quad \text{Eq (10)} \\
P &= C_P \rho A (\Omega r)^3 \\
P &= 275.1 \left[ \frac{\text{lbs} \cdot \text{ft}}{\text{sec}} \right] = 373 \text{ watts} \\
P &= \frac{373}{0.6} = 622 \text{ watts (Actual power req)}
\end{aligned}$$

From this equation the required power is 622 watts which is almost double that calculated by the momentum method. The calculation of power required by both these methods assumed a constant chord blade with no twist and no control surface.

The final method used to calculate the power required was a combined momentum - blade element method. There are two basic equations associated with the approach. These equations are

$$\Delta T = b (\rho/2) (\Omega r)^2 a (\theta - \phi) c \Delta r \quad \text{Eq (11)}$$

$$\Delta T = 4 \rho (v_1)^2 r \Delta r \quad \text{Eq (12)}$$

Equation 11 is the thrust developed according to the blade element theory and equation 12 is the thrust developed according to the momentum theory. These two are then set equal to each other and the result is a formula for the induced velocity. The lift curve slope calculated above by the two dimensional CFD analysis is also substituted into equation 13 before the induced velocity can be formed.

$$4 \rho (v_1)^2 r \Delta r = b (\rho/2) (\Omega r)^2 a (\theta - \phi) c \Delta r$$

$$\phi = \frac{v_1}{\Omega r} = \frac{a\sigma}{16(\gamma_R)} \left[ -1 + \sqrt{1 + \frac{32 \theta (\gamma_R)}{a\sigma}} \right]$$

For cambered airfoils :  $\theta = \theta_o + \alpha_{0L}$   
 $\theta_o \equiv$  Collective Input  
 $\alpha_{0L} \equiv$  Angle of Attack @ Zero Lift

Eq (13)

Once the induced velocity is known the inflow angle can be determined

$$\phi = \frac{v_1}{\Omega r} \quad \text{Eq (14)}$$

and then substitution of equation 14 into equation 11 and integration from the blade root to the effective blade tip results in the thrust being developed by the rotor system.

$$T = b \int_{R_1}^{R_2} (\gamma_2) (\Omega r)^2 a (\theta - \phi) c dr$$

$R_1 \equiv$  Start of Blade span accounting for root cutout  
 $R_2 \equiv$  End of Blade span accounting for tip loss  
 $B \equiv$  Tip loss  $= 1 - 0.0\gamma_b = 0.97$

$$Q = b \int_{R_1}^{R_2} r \{ [(\gamma_2) (\Omega r)^2 a (\theta - \phi) c] \phi + [(\gamma_2) (\Omega r)^2 c_d c] \} dr \quad \text{Eq (15)}$$

$P = Q \Omega$

Using these equations a parametric study was performed where the parameters were motor rpm (1300 rpm to 1500 rpm) and collective setting ( $3^\circ$  to  $7^\circ$ ) to determine if an electric motor could be found for this application. The results of this parametric study are listed in Table 1.

Based on these results and the size of the current internal combustion motor an electric motor with an output of 1200 watts (1.6 Horsepower) was selected. Although from Table 1 it would appear that this motor is very conservative it was selected because an actual value for the losses associated with the drive train and the power required for the tail rotor are unknown.

The helicopter airframe had to be modified and a mounting block had to be designed and fabricated to integrate the electric motor into the airframe. The motor mount was a rectangular block of aluminum with two orthogonal set screws to hold the electric motor and four mounting screws to mate with the mounting holes on the airframe. To achieve the proper alignment of the motor and the drive train the mounting holes located on the helicopter were elongated to allow longitudinal adjustment of the mounting block. In addition to the motor mount a coupler was also fabricated which

Rotor Angular Velocity (RPM)											
	1300		1350		1400		1450		1500		
	THRUST	POWER	THRUST	POWER	THRUST	POWER	THRUST	POWER	THRUST	POWER	
3.0	3.4	2.2	3.6	2.4	4.0	2.7	4.2	3.0	4.5	3.3	
3.5	4.2	2.4	4.6	2.7	4.9	3.0	5.3	3.3	5.6	3.7	
4.0	5.1	2.7	5.6	3.0	6.0	3.3	6.4	3.7	6.8	4.1	
4.5	6.1	3.0	6.5	3.3	7.0	3.7	7.5	4.1	8.1	4.6	
5.0	7.0	3.3	7.5	3.7	8.1	4.1	8.7	4.6	9.3	5.1	
5.5	8.0	3.7	8.6	4.1	9.2	4.6	9.9	5.1	10.6	5.7	
6.0	9.0	4.1	9.7	4.6	10.4	5.1	11.2	5.7	12.0	6.3	
6.5	10.0	4.5	10.8	5.1	11.6	5.7	12.5	6.3	13.4	6.9	
7.0	11.1	4.9	11.9	5.6	12.8	6.2	13.8	6.9	14.7	7.7	

UNITS: THRUST = LBS POWER = WATTS/100

TABLE 1 Thrust and Power Output

allowed the motor to mate with the existing centrifugal clutch which is the first component of the drive train. These two components and the modification of the airframe mounting holes allowed the electric motor to be mated to the airframe.

Unlike the internal combustion motor which uses a throttle the electric motor requires an electronic speed controller. This device regulates the motor speed by adding or subtracting resistance from the input circuit which then decreases or increases voltage to the electric motor. The problem with this device is the removal of the heat generated by the electronics. This was not a trivial problem and during early ground tests of the helicopter a speed controller caught on fire and was destroyed. This problem was solved by locating the speed controller in the down wash of the main rotor. The device was moved and then a series of tests were performed where

the speed setting was varied and using a temperature probe the controller temperature was measured after each test. This helped to locate the speed controller in the downwash where it would get sufficient cooling to run at any speed indefinitely. In addition to the new location a heat sink was added with fins to remove heat from the controller. The speed controller also was subject to overload once because of a voltage potential induced in the power tether cord. The voltage was a result of the long (60 foot) tether power cord used to provide power to the electric motor. This problem was solved by including a large capacitor ( $2200\ \mu\text{f} \setminus 50\ \text{volt}$ ) in the input power line to drain off the AC voltage before it could get to the speed controller. There also was a thermal problem with the electric motor. This problem is not present when these motors are used in an airplane application because the downwash from the propeller is used to cool the motor but in our application the downwash is obstructed from cooling the motor. This problem was solved by attaching a cooling fan to the bottom output shaft of the motor and sucking air through the motor to provide sufficient cooling to keep the motor core below  $300^{\circ}\text{F}$ .

**3.4.3 Rotor Blade:** A NACA 0012 is a standard main rotor blade cross section for this size helicopter. The blade span is 28 inches and the blade chordwise dimension is 2.5 inches resulting in a solidity of 0.0568. The design goal was to match the thrust generated at a collective setting greater than that required to hover the helicopter by changing the camber of a portion of the rotor blade. The helicopter has an assumed weight of 12 pounds (actual weight 8 lbs.) therefore the cambered portion of the blade must generate thrust greater than 12 pounds of thrust for the helicopter to climb vertically. Assuming an increase in thrust of 4 pound what would be the required camber change of the airfoil? Blade element and momentum theory aerodynamics were used to determine the required collective setting to hover at 12 pounds. This value is  $7^{\circ}$  at 1450 rpm. Conservation of momentum was then used to determine the climb velocity  $V_n$  and is illustrated in Figure 8

Once the climb velocity had been established, the size and location of the control surface had to be determined. The design methodology was to set the collective such that the helicopter would generate a

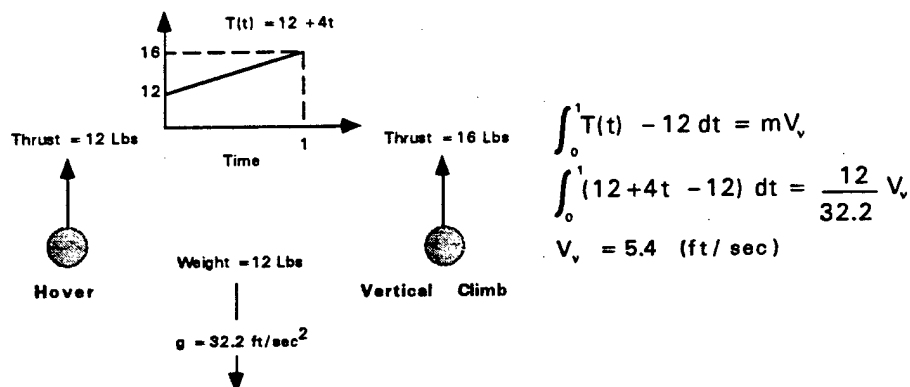


FIGURE 8 Vertical Climb Velocity

thrust equal to the weight of the vehicle. The thrust generated by the control surface would then be employed for vertical climb or descent. Based on this methodology the collective was set at  $7^\circ$  which would generate 12 pounds of thrust which is enough for the helicopter to hover. Based on discussion with engineers at Kaman Aerospace Company the control surface was located at 75% of the span of the rotor blade. The dimensions of the control surface are 8 inches in the spanwise direction (28% of the total span) and 1 inch in the chordwise direction (40% of the total chord).

A two dimensional computational fluid dynamic airfoil analysis was performed to determine upper and lower airfoil section pressure distributions as well as sectional lift and drag coefficients. These coefficients were used to determine the incremental lift associated with rotor blade segments and the resultant pressure distribution on the airfoil. The resultant pressure distribution is illustrated in Figure 9. From the pressure distribution illustrated in Figure 9 the effect of the deflected control surface can be seen as a sharp increase in the pressure differential at approximately 55% of the chord.

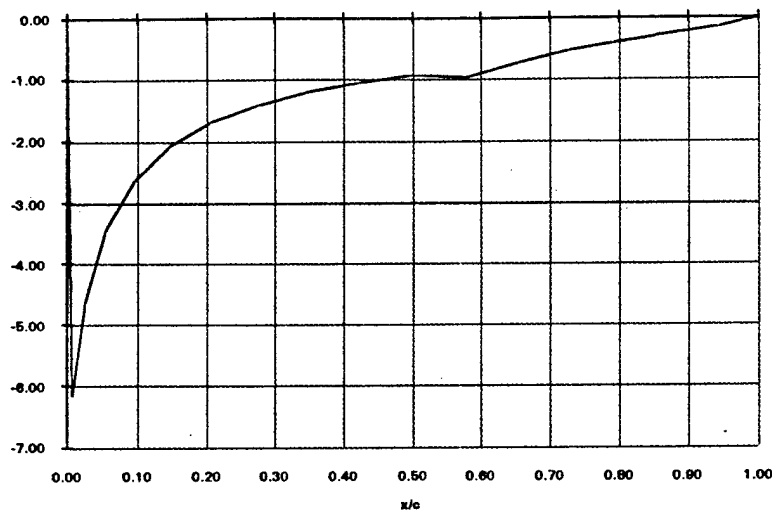


FIGURE 9 Airfoil Pressure Distribution

The area under this portion of the curve is the airload on the control surface and is used to calculate the required moment for deflecting the surface. Equation 16 is the integral for calculating the area and is equal to the lift coefficient for the control surface.

$$c_l = \frac{1}{c} \int_0^c C_{p_{lo}} - C_{p_{up}} dx \Rightarrow 0.08 \quad \text{Eq (16)}$$

Table 2 tabulates the incremental airloads on the control surface from the inside edge radius 1.5 feet to the outside edge at radius 2.08 feet.

Radius (Ft)	Velocity (Ft/Sec)	Dynamic Pressure (Lbs/SqFt)	Lift (Lbs)
1.42	215.33	55.13	0.03
1.50	228.00	61.81	0.03
1.58	240.67	68.87	0.04
1.67	253.33	76.31	0.04
1.75	266.00	84.13	0.05
1.83	278.67	92.33	0.05
1.92	291.33	100.92	0.06
Total Lift =>			0.30

TABLE 2 Control Surface Airload

The airload on the control surface is then the sum of the incremental airloads. This total lift then was assumed to act at the chordwise station of 1.83 inches from the leading edge or 0.33 inches aft of the hinge line. Based on these numbers the moment due to airloads to be overcome

is 0.10 inch-pounds or 1.60 inch-ounces. Once the airload has been overcome the control surface must be deflected  $4^\circ$  for the effective angle of attack to be the required  $9.88^\circ$ . The geometric relationship between control surface angle and effective angle of attack is illustrated in Figure 10.

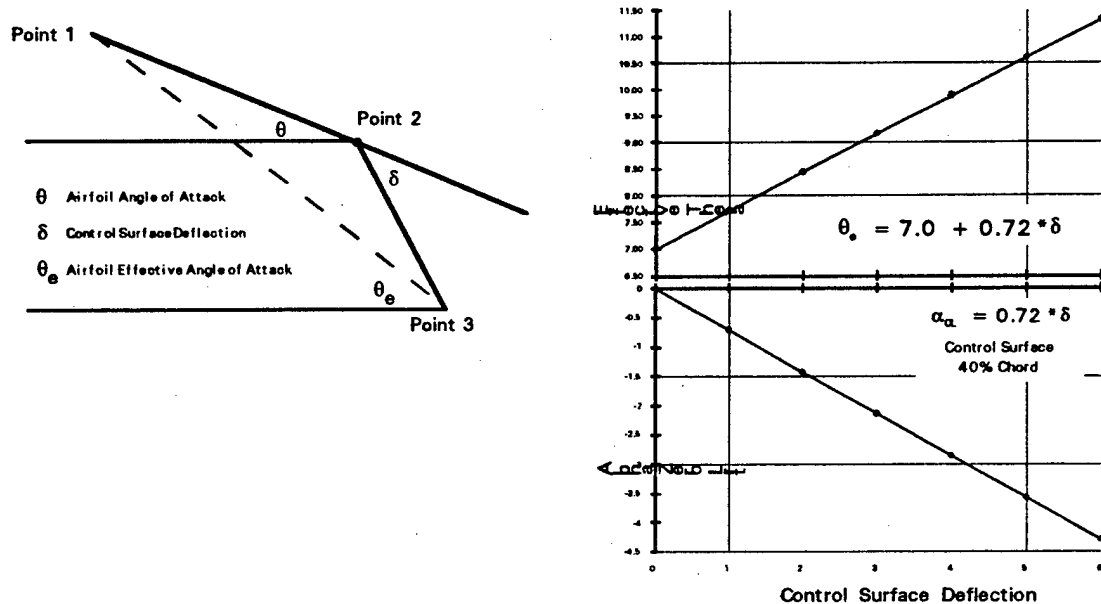


FIGURE 10 Effective Angle of Attack

Again estimating the lift by the combined blade element and momentum theories the total lift for this rotor system would be 16.5 pounds. Where the blades are set to a collective pitch of  $7^\circ$  and the control surface described above is deflected by  $4^\circ$  and the rotor is spinning at 1450 rpm. The actuation element used to manifest this deflection is a Shape Memory Alloy.

The next issue to resolve was the power requirement for the SMA actuator element. Figure 11 illustrates the power required to activate a 2 inch long strand of 0.01 inch diameter SMA wire. This figure also illustrates that the shape memory effect can be used to deflect the flap.

This figure also illustrates that the shape memory effect can be used to deflect the control surface with a reasonable amount of electric power. Even though the time responses that one encounters when shape memory alloys are used for shape changes (1 hertz) are not as fast as the time responses with piezoelectric transducers a shape memory alloy can maintain the changed shape for a prescribed time duration. This makes the shape memory alloy an ideal smart or adaptive material for collective control.

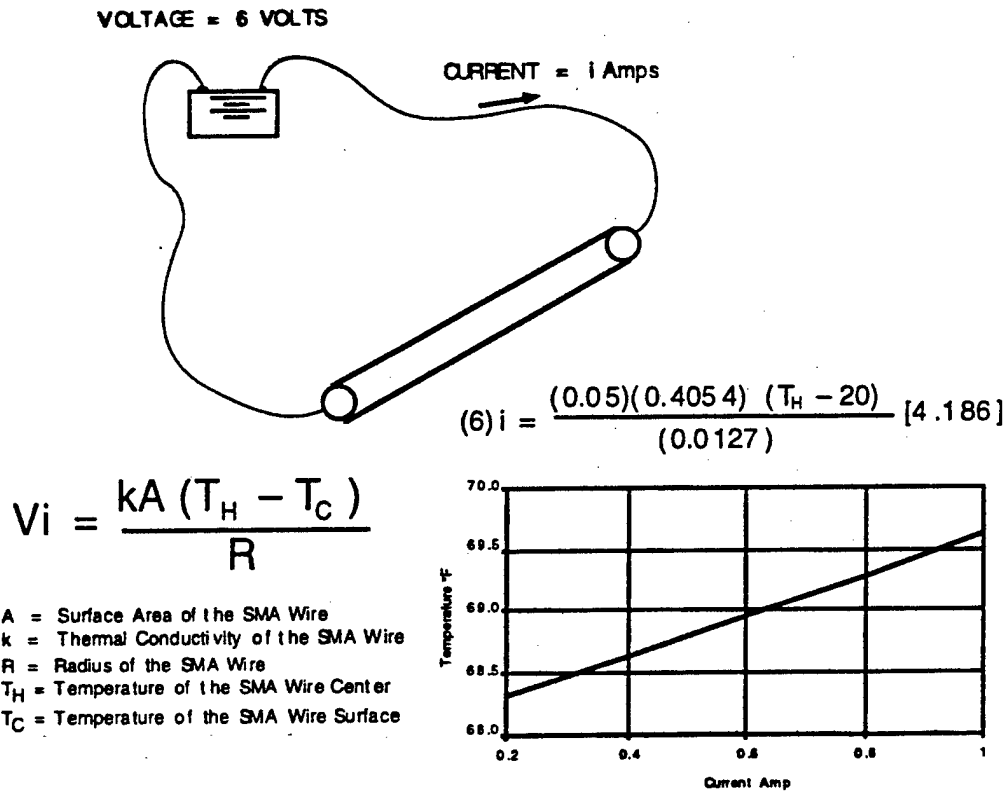


FIGURE 11 SMA Power vs. Temperature Relationship

Figure 12 illustrates the design configuration of the control surface and the shape memory alloy actuation element. Based on this figure when the SMA wire is heated it will contract pulling free end point "A" of the actuator lever arm forward. As the free end of the actuator lever arm moves forward the portion between points "B" and "C" will rotate clockwise and the embedded end point "D" of the control surface lever arm will move downward. The length of the actuator lever arm was based on the amount of strain recovery and force associated with this work. The amount of strain allowed in an application is a function of the number of cycles the material will experience this strain.

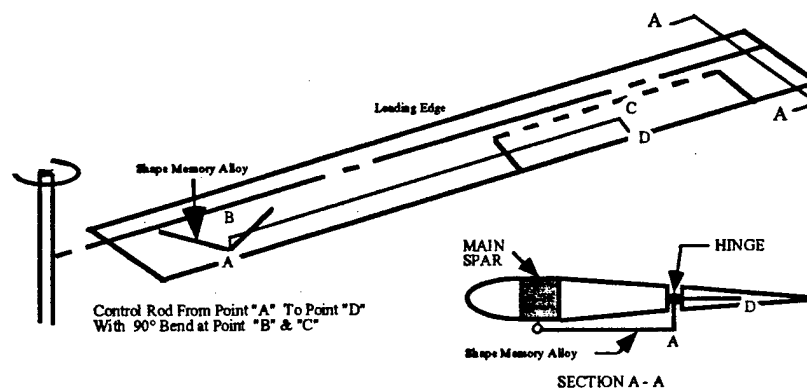


FIGURE 12 Adaptive Airfoil with Shape Memory Alloy



The manufacturers recommended strain for applications such as this is 4% and the available force is 6.5 ounces for SMA wire with a diameter of 0.010 inches. Since the required moment to be overcome is 5.44 inch-ounces the actuator lever arm (point "A" to "B") must be 0.84 inches in length. The 4% strain and a right angle pull orientation were then used to calculate the amount of SMA wire required and the voltage required. Figure 13 illustrates the layout of the SMA wire.

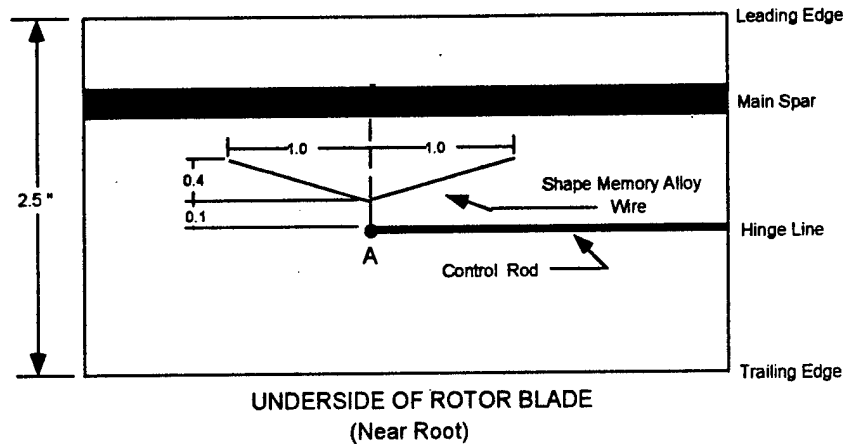


FIGURE 13 Actuator Wire Layout

The 0.1" dimension shown in this figure represents the actual magnitude of the displacement at point "A" (free end of the actuator lever arm). The required displacement from the calculations is 0.022" ( $0.84 \cdot \tan 1.5^\circ$ ) which is a 0.9% strain.

$$R = r \cdot L \Rightarrow 0.5 \text{ W/in} \cdot 2.24 \text{ in} = 1.12 \text{ W}$$

$$V = R \cdot i \Rightarrow 1.12 \text{ W} \cdot 1 \text{ A} = 1.12 \text{ V}$$

$$P = V \cdot i \Rightarrow 1.12 \text{ V} \cdot 1 \text{ A} = 1.12 \text{ W}$$

The above calculation based on 4% strain being developed indicates that 1.12 watts per blade of power are required

Since only 0.9% strain is required and a 0.9% strain corresponds to a temperature of 60°F, the curve in Figure 11 would indicate that only 0.6 amps are required to power the actuator mechanism.

**3.4.4 Helicopter Testing:** A number of ground tests were performed on the basic system in order to determine electrical power requirements and limitations on the electric motor and motor speed control unit. Ground tests were also used to track and balance the main rotor blades. The process of balancing the blades is begun during fabrication of the blades when mass is added to the blades till they are of equal weight and spanwise center of gravity. The blades are then mounted in the blade cuffs of the rotor head and spun to see if they track in the same plan (tip path plan). The blades can be out of track for two reasons (1) improper balance (This will not be the reason if the balancing task was done correctly) and (2) there is a difference in pitch link length. These tests also were used to setup and make preliminary adjustments to the radio control unit and programming the radio to insure the proper spinup rate. The spinup rate is important to avoid ground resonance modes which can damage the helicopter electronics and to load the electric motor properly to avoid overheating the electric motor core. All these tests were performed using an unmodified blade (NACA 0012 with a 2.5 inch chord). The next series of tests were flight tests of the helicopter system with unmodified blades. The purpose of these tests were to provide the pilot with flight time with an electric powered helicopter and to refine the radio control unit setup. In addition to this, many mechanical problems were encountered which were not present during the ground spin tests. An example of one problem was the tendency for the gear teeth on the tail rotor drive gear to strip during flights when the electric motor rpm would be slightly above the rpm developed by an internal combustion motor. This is a recurring problem since the motor speed control unit is very sensitive.

Results from these tests were an electric helicopter of this size can generate sufficient lift with the unmodified blades but care must be taken not to overheat the electric motor or the motor speed control unit. The main rotor speed during spinup on the ground was 1500 rpm and the hover rpm was 1400 rpm. The required battery voltage was 36 volts and there was a 10 volt drop in the 60 foot tether line between the batteries and the helicopter. The temperature developed by

the electric motor was 150° F and the motor speed control was 120° F. These temperatures are near the upper operating limits for both these components.

The next test was a wind tunnel test to insure the structural integrity of the modified helicopter rotor blade. The standard blade was first modified by cutting a control surface into the blade. The control surface was located 4 inches from the tip of the blade, the spanwise length of the control surface was 8 inches and the chordwise length of the control surface was 40 percent of the airfoil chord or 1 inch. A plastic hinge was glued to the top surface of both the control surface and the blade to attach the two pieces. This configuration was then placed in the wind tunnel in a vertical orientation. The blade was subjected to a series of dynamic pressures minimum of 0 psi maximum of 50 psi. The pressure was increased to this maximum in 10 psi increments and was subjected to each dynamic pressure increment for approximately 10 minutes.

The results of this test were the modified blade demonstrated sufficient structural integrity for dynamic pressures from 0 to 50 psi and the control surface did not flutter.

The next test was to subject the modified rotor blade to a ground spin test to evaluate the structural integrity to centrifugal load. For this test the helicopter was weighted with approximately 12 pounds of lead. The rotor was spun to 1600 rpm with zero collective input and was kept at this speed for approximately 5 minutes. Examination of the blade during the test showed no sign of vibration or flutter even though the blades did not track very well. After the test examination of the blades showed no structural integrity problems. The rotor was then spun up again and collective was applied in a controlled manner till the helicopter actually lifted off with the 12 pounds of ballast.

The results of this test were the modified blade demonstrated sufficient structural integrity for dynamic pressures from 0 to 180 psi and centrifugal loads associated with a rotational speed of 1600 rpm. Also under these conditions the control surface did not flutter.

The next flight tests were done with the modified blade using the conventional control system. In these tests the aircraft was hovered at 6 to 8 feet off the ground for approximately 5 minutes. This test was performed 8 times and in all flights the helicopter experienced only mechanical failures in the drive system. The major failure being the tendency for the gear teeth on the tail rotor drive gear to strip and we had one tail rotor blade strike on a hard landing during a

gust. The purpose of these tests were also to provide the pilot with flight time with an electric powered helicopter with modified rotor blades.

The results of these test flights again emphasized the sensitivity of the drive system to overspeed problems. But the major outcome was the modified blades are able to lift the helicopter and can be controlled with conventional control inputs.

Ground tests of the helicopter with the modified blade activated to a camber change were the next set of tests performed. The objective of these was to demonstrate that a camber change could be maintained using the shape memory alloy actuation system. These tests also gave the pilot some practice at activating and deactivating the control surface. The conditions for these tests were similar to the other ground tests where the rpm was varied from 0 to 1600 in increments of 100 and each increment was maintained for 5 minutes. Since the actuator wire was not directly exposed to the airstream, there was minimal aerodynamic cooling of the wire actuator and power requirements were low 1 amp at 3 volts.

The results of this test demonstrated the structural integrity of the shape memory alloy and the control surface actuation system.

The final test was a flight test of the helicopter where the shape memory actuator was activated and resulted in a vertical climb of the helicopter. This test was performed in the following sequence (1) the helicopter was hovered at 6 feet off the ground, (2) once a stable hover was achieved the actuator was activated and the helicopter climbed vertically with the pilot maintaining stability through cyclic and increased tail rotor pitch to overcome the additional torque placed on the main rotor system, (3) after a climb of 3 feet the pilot deactivated the actuator and varied the collective to land the helicopter.

The results of this test demonstrated the ability of the shape memory alloy actuator system to change blade camber. This camber change generated enough thrust to result in a vertical climb of the 8 pound helicopter. Therefore a shape memory alloy actuator system has the ability to effect the magnitude of camber changes required to replace the current collective control system on the helicopter.

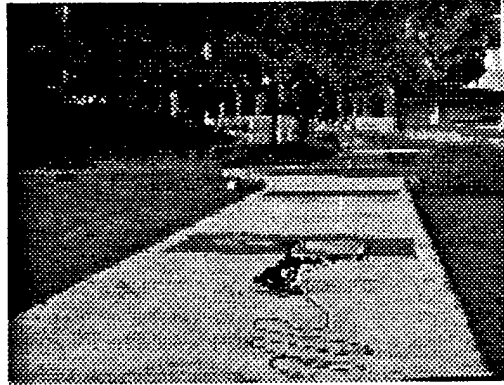


Figure 14. Startup

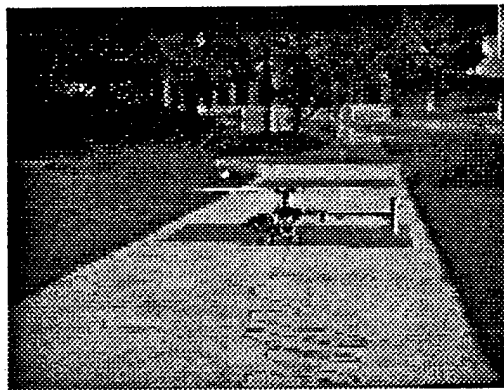


Figure 15. Hover with collective



Figure 16. Vertical climb

### 3.5 Deflection Of Surface:

The scheme for providing a linear proportional control of the control surface had to be accomplished. The transmitter used in this project has four channels which have proportional control and one channel which has on / off control. The four proportional controls are as follows:

1. A mixed channel which controls motor speed and collective pitch
2. A channel which controls lateral cyclic pitch
3. A channel which controls longitudinal cyclic pitch
4. A channel which controls tail rotor collective pitch

Originally the on / off control channel transmitted a signal to a switch on the aircraft to provide power to the Shape Memory Alloy actuator. The power level was determined prior to the flight to be the amount of additional thrust needed for the vehicle to climb vertically. The next step was to devise a scheme by which the power to the actuator could be varied and thus change the control surface deflection in a proportional fashion while the vehicle was in flight.

The method devised to control the deflection of the control surface included the use of the on / off switch and the signal from the collective proportional channel. A relay was employed to switch the signal from the channel which normally controls the collective pitch and make it the channel which controlled the deflection of the control surface. Figure 17 illustrates the relay switch.

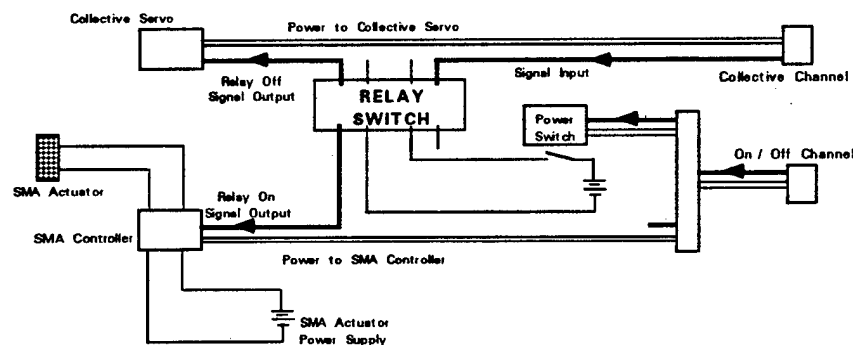


Figure 17. Relay switch

The relay switch illustrated above is the device which directs the signal from the collective channel. When the relay switch is in the off position the signal is passed to the collective servo for changing the rotor blade pitch. When the relay switch is in the on position the signal from the collective channel is directed to a controller which limits the power supplied to the SMA actuator.

The other component of this circuit is the power switch which turns the power on / off to the relay switch. This power switch is controlled by the on / off channel of the transmitter. Power from the on / off channel is divided some being sent to the servo which activates the power

switch and some being sent to the SMA controller. There are also two additional battery pack in the above figure. The first one provides power to the relay switch and is a 6 volt battery pack. The second provides power to the SMA actuator and is a 4.8 volt battery pack. The 4.8 volt battery pack was used in the original design to power the SMA actuator through the power switch which is controlled by the on / off channel.

The circuit now allows the operator to vary the control surface deflection by moving the stick which is normally associated with the collective control of the vehicle. Uninterrupted separate power sources are present to hold the position of the collective servo when the signal is directed to the SMA actuator or to maintain the control surface deflection when the signal is directed to the collective servo.

### 3.6 SUMMARY:

This research completes the preliminary design and proof of concept for a rotor which generates thrust through camber change. The design and testing of the new controller which allows the selection of any desired amount of control surface deflection has been completed and will be flown on the test helicopter soon. With the completion of the phase of work the next phase is ready to begin. The next phase will address the development of a sensor package to monitor the spanwise strain of the rotor blade. These two components are the basis for an intelligent rotor system which is the ultimate goal of this research.

### 3.7 REFERENCES:

- 1 Schetky,L.. "Shape Memory Alloys." *Scientific American*, 1 November 1979
- 2 Brown,W.. *Technical Characteristics of FLEXINOL*. Irvine California: Dynalloy,Inc.
- 3 Rogers,C.A. and Barker,D.K.. "Experimental Studies of Active Strain Energy Tuning of Adaptive Composites." In *31st AIAA Structures, Structural Dynamics and Materials Conference.* , 1990.

- 4 Rogers, C.A.. "Novel Design Concepts Utilizing Shape Memory Alloy Reinforced Composites." In *American Society of Composites 3rd Technical Conference on Composite Materials*. Lancaster, Pennsylvania: Technomic, 1988.
- 5 Rogers, C.A. and Robertshaw, H.H.. "Shape Memory Alloy Reinforced Composites." *Engineering Science Reprints* 25, ESP25.88027, (1988).
- 6 Nagaya, K., Takeda, S., Tsukui, Y. and Knmaido, Y.. "Active Control Method for Passing Through Critical Speeds of Rotating Shafts by Changing Stiffness of the Supports with Use of Memory Metals." *Journal of Sound & Vibration*, 113 (1987).
- 7 Baz, A., Ro, J., Poh, S. and Gilheany, J.. "Control of Smart Traversing Beam." In *Active Materials & Adaptive Structures*. Philadelphia, Pennsylvania: IOP Publishing Ltd., 1991.
- 8 Lagoudas, D.C. and Tadjbakhsh, I.G.. "Active Flexible Rods with Embedded SMA Fibers." In *Active Materials & Adaptive Structures*. Philadelphia, Pennsylvania: IOP Publishing Ltd., 1991.
- 9 Baz, A., Inman, K. and McCoy, J.. "Active Control of Flexible Beams using Shape Memory Actuators." *Journal of Sound & Vibration*, 140 (1990).
- 10 Johnson, W., *Helicopter Theory*, Princeton University Press, New Jersey, 1980.
- 11 Gessow, A. and Myers, G.C., Jr., *Aerodynamics of the Helicopter 8th Edition*, pp 29, Fredrick Ungar Publishing Co., New York, 1985.
- 12 Roglin, R.L. and Hanagud, S.V., 1992, Shape Memory Alloy Camber Control, Patent Issued.
- 13 Hanagud, S.V. and Roglin, R.L., "Adaptive Airfoils", Southeastern Conference of Theoretical and Applied Mechanics, 1992.
- 14 Hanagud, S.V., Roglin, R.L. and Nagesh Babu, G.L., "Smart Airfoils for Helicopter Control", Eighteenth European Rotorcraft Forum, 1992.



#### IV. Adaptive Airfoils for Forward Flight

The SMA based actuator can not provide the needed frequency response and the associated one per rev. changes of the flap angle. We have designed and demonstrated an elastic beam piezo actuator combination to produce the needed flap angle variations of  $5^{\circ}$ ~ $7^{\circ}$  per revolution. The next step is to incorporate this in a rotor blade. This is accomplished by a hybrid system that consists of a pre-set angle of attack, SMA to augment the fixed angle of attack and piezo actuators to provide the cyclic variations as shown in Figure 4.1

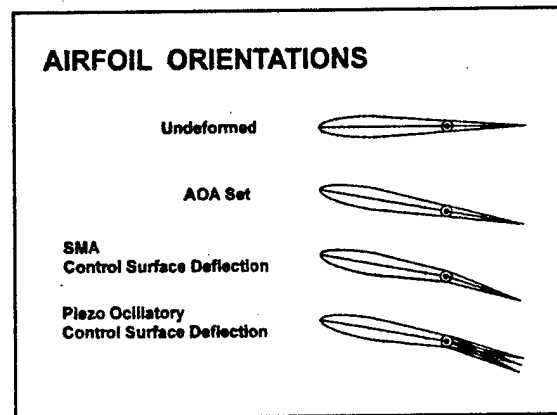


Figure 4.1

We have studied different mechanisms to implement the bread-board system in a rotor blade. One such system is illustrated in Figure 4.2 with fix beams. The system that will be incorporated will be similar to the system illustrated in Figure 4.3. Our preliminary calculations indicated that we would also need a spatial variation of the induced flap angle.

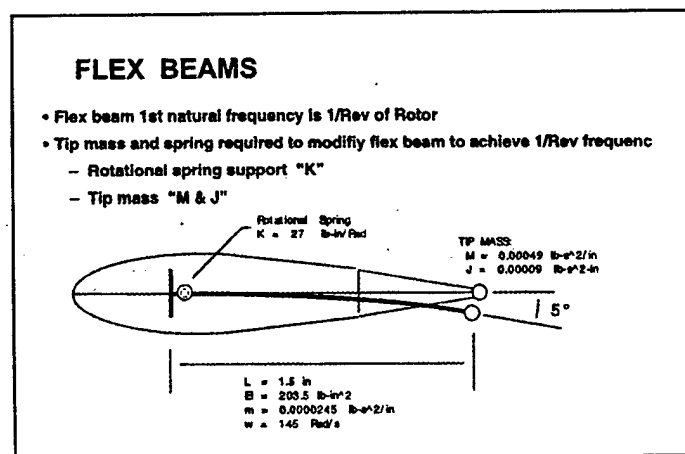


Figure 4.2

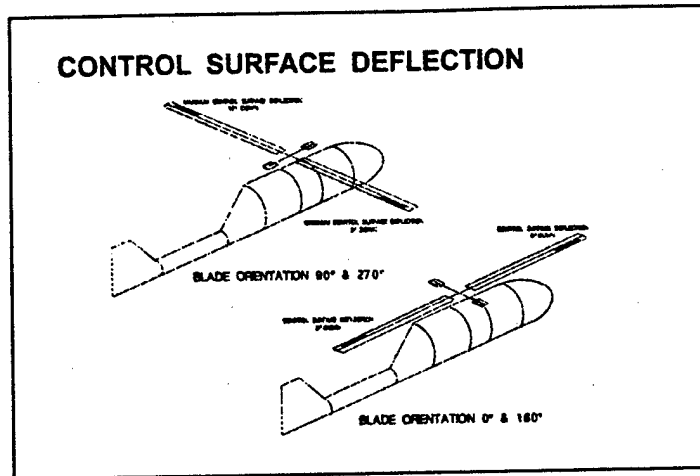


Figure 4.3

Our next step is to calculate the required flap angle variations as a function of the azimuth. This is discussed in the next section.

## V. Nonlinear Dynamics of Flap Controlled Rotor Blades

### 5.1 Flap Controlled Rotor Blade Concept

The use of swash-plate systems for applying collective and cyclic pitch change has been the primary element of helicopter controls since the earliest phases of its development. Almost all rotorcraft of today use swash-plate system as the main control device for adjusting the blade pitch angle to balance the total thrust variation which results from the aerodynamic lift and moment distributions along the blades as changed significantly by the azimuthal position.

Total sectional lift of an lifting surface can be written as

$$L = \frac{1}{2} \rho S U^2 C_L \quad (5-1)$$

where  $\rho$  is density of flowing air,  $C_L$  is profile lift coefficient,  $U$  is profile resultant of air velocity on lifting surface and  $S$  is the area of the aerodynamic surface. Profile sectional lift coefficient is written in the simplest form as;

$$C_L = a\alpha \quad (5-2)$$

where  $a$  is the lift curve slope of the profile which basically defines the lift generating capability and  $\alpha$  is the effective angle of attack. The angle of attack " $\alpha$ " has been conventionally changed by cyclic pitch change applicator to change the lifting capability " $C_L$ " of the blade section.

The idea of changing the lift curve slope " $a$ " instead of the blade section angle of attack " $\alpha$ " is the basic idea behind the "trailing edge flap control" concept for the rotor blades. A downward motion of an hinged trailing edge flap can significantly change the camber of the blade which eventually changes lift generating capability of the airfoil

Trailing edge flap control concept was first introduced by Charles Kaman, a distinguished helicopter pioneer, and the concept called *servo-flap* was successfully used in several Kaman helicopters for many years. For helicopter rotors the use of trailing edge flaps on the blades has found use only for 1/rev. cyclic pitch control, e.g. the Kaman servo-flap. On the other hand, with the newly developing smart materials/structures and high bandwidth active control technologies, it is now becoming increasingly feasible to use compliant airfoil surfaces or trailing edge mounted flaps on rotor blades as a means of individual blade control (IBC). Coupled with real time adaptive feedback strategies, active controlling of the blade lift distribution offers several possibilities for the improvement of the rotor performance, as well as for the reduction of blade loads and vibrations.

Formulation of aeroelastic analysis of rotor blades with flap controls consists of three major steps. The first step is the formulation of the new aerodynamic environment around the rotor blade due to the time dependent trailing edge motion. The second step of the problem is the formulation of flap control trim settings for a chosen helicopter configuration. The new set of rotor blade nonlinear partial differential equations which govern the thrust and aeroelastic response of the rotor blade system are solved numerically as the third step.

## 5.2 Aerodynamic Formulation

The nonconservative generalized forces which come as a result of the new aerodynamic environment are presented in this section. In present formulation, the aerodynamic terms are determined from Greenberg's extension of Theodeorsen's theory as presented in reference [11] for thin, two-dimensional airfoils undergoing unsteady motion. in a time-varying incompressible free-

thin, two-dimensional airfoils undergoing unsteady motion. in a time-varying incompressible free-stream. As formulated in references [11, 13]. Theodorsen theory facilitates chordwise rigid airfoil with aerodynamically unbalanced trailing edge flap or control surface hinged at  $x=(c/2)*C_{cf}$ . The airfoil may have moved in vertical translation  $h(t)$  and rotate about an axis at  $x=a*c/2$  through an angle  $\alpha(t)$ ;  $\Lambda(t)$  donates the angular displacement of the flap relative to the chordline of the airfoil. The positive direction of these variables are as illustrated in Figure 5.1

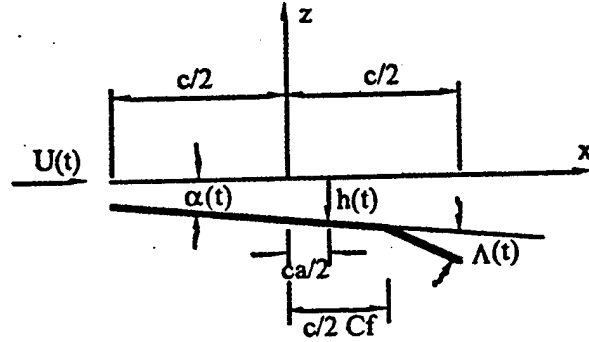


Figure 5.1 2-D Oscillating airfoil representation.

A quasi-steady aerodynamic approximation is employed Where Theodorsen's lift deficiency function  $C(k)$  is taken as equal to unity. The circulatory and noncirculatory lift and moment per unit span, assuming pitch occurs about the quarter chord can be written based on the derivation given in reference [11] as;

$$L_c = \frac{1}{2} \rho a c U \left[ -\dot{U}_p + \frac{c}{2} \dot{\alpha} \right] + \rho c U \left[ U \Lambda f_1 + \frac{c}{4} \dot{\Lambda} f_2 \right] \quad (5-1)$$

$$L_{nc} = \frac{1}{2} \rho a \frac{c^2}{4} \left[ -\ddot{U}_p + \frac{c}{4} \ddot{\alpha} \right] + \rho \frac{c^2}{4} \left[ U \dot{\Lambda} f_3 + \frac{c}{2} \ddot{\Lambda} f_4 \right] \quad (5-2)$$

and the aerodynamic pitching moment is also expressed as,

$$M_\theta = \frac{c^3}{16} \rho a \left[ \left( \frac{\dot{U}_p}{2} - \frac{U \dot{\alpha}}{2} - \frac{3c}{16} \ddot{\alpha} \right) - \left( \frac{U \dot{\Lambda}}{\pi} \left( \frac{f_2}{2} + f_1 \right) + \frac{c}{2\pi} \ddot{\Lambda} f_8 \right) \right] \\ + \frac{1}{2} \rho a \frac{c^2}{4\pi} \left[ -U^2 \Lambda (f_1 + f_3) \right] \quad (5-3)$$

Specifically for the rotary wing aerodynamic representation,  $U_p$  is related to  $h$  and  $U\alpha$  in reference [12] as

$$U_p \equiv -(\dot{h} + U\alpha), \quad U^2 = U_T^2 + U_p^2 \quad (5-4)$$

$U_T$  and  $U_p$  are given in reference [13] as In nondimensional form in terms of the elastic deflection variables  $v$ ,  $w$ ,  $\phi$  spanwise and azimuthal location, pitch, inflow ratio  $\lambda$ , rotor rotational velocity and advance ratio as,

$$U_T = \dot{v} + (x + \mu \sin \psi) + \mu v^+ \cos \psi \quad (5-5)$$

$$U_p = \dot{w} - \mu(\theta + \phi)v^+ \cos \psi + \mu(w^+ + \beta_{pc}) \cos \psi - \lambda + (w^+ v + v\beta_{pc}) - \dot{v}(\theta + \phi) - (\theta + \phi + v^+ w^+)(x + v \sin \psi) \quad (5-6)$$

Finally the lift components in lead-lag and flap directions are expressed in terms of the circulatory and noncirculatory lift components in reference [13] as

$$L_v = -(\theta + \phi)(L_c \cos \rho + L_{nc} - D \sin \rho) + (-L_c \sin \rho - D \cos \rho) \quad (5-7)$$

$$L_w = (L_c \cos \rho + L_{nc} - D \sin \rho) - (\theta + \phi)(L_c \sin \rho + D \cos \rho) \quad (5-8)$$

The two dimensional airfoil sectional drag is approximated as

$$D = \frac{1}{2} \rho_0 c C_{D0} U^2 \quad (5-9)$$

along with the geometric relations illustrated in Figure 5.2 where  $C_{D0}$  is the sectional drag coefficient and  $c$  is the chord length.

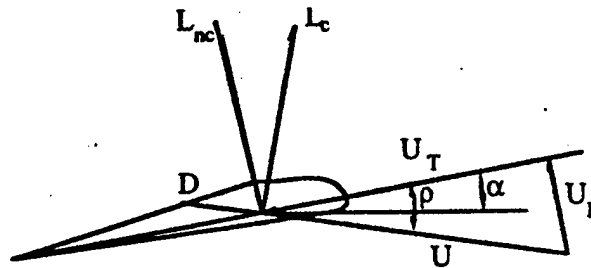


Figure 5.2 Blade sectional velocities and lift components. Details of the formulation is given in Reference [13]

### 5.3 Trim Formulations

Trim conditions for the pitch control with the same blade and vehicle configuration are first calculated by the use of standard trim equations given by Johnson [14]. As the first step, parameters directly related with flap control case are recalculated along with the replacement of pitch control with flap control varying along the radius as

$$\Lambda(\xi, \psi) = f(\xi) \{ \Lambda_0 + \Lambda_{1s} \sin \psi + \Lambda_{1c} \cos \psi + \Lambda_{2s} \sin 2\psi + \Lambda_{2c} \cos 2\psi \} \quad (5-10)$$

where  $\Lambda_0$  is the collective flap  $\Lambda_{tw}$  is the pre-twist, and  $\Lambda_{1s}$ ,  $\Lambda_{1c}$ ,  $\Lambda_{2s}$ , and  $\Lambda_{2c}$  are first and second harmonics which give 1/rev and 2/rev variations of the blade trailing edge flap angle.

Sectional blade lift for two-dimensional strip aerodynamic formulation is written as;

$$\frac{F_z}{\sigma a} = \frac{1}{2} [U_T^2 \theta_n - U_p U_T] + \left[ \frac{c}{4a} (f_2 - f_3) U_T \dot{\Lambda} - \frac{c^2}{8a} f_4 \ddot{\Lambda} + \frac{1}{a} f_1 U_T^2 \Lambda \right] \quad (5-11)$$

where  $\theta_n$  is the rigid pitch angle of the blade,  $c$  is the nondimensional blade chord,  $\Lambda$  is the trailing edge flap angle given by equation 13,  $a$  is the blade lift curve slope and  $\sigma$  is the blade solidity ratio. Parameters  $f_1$ ,  $f_2$ ,  $f_3$  and  $f_4$  are related with flap hinge offset geometry which have been introduced by Theodorsen's two-dimensional unsteady aerodynamic formulation for the oscillating airfoils. Detailed expressions of these parameters are given in reference [7].

First term in  $F_z$  formulation is related with blade profile lift with a rigid pitch angle  $\theta_n$ . Blade sectional velocities  $U_T$  and  $U_p$  are given in non-dimensional form for a rigid blade with only rigid blade flapping motion;

$$U_T = x + \mu \sin \psi \quad (5-12)$$

$$U_p = \lambda + \dot{\beta} r + \beta \mu \cos \psi \quad (5-13)$$

For forward flight trim conditions, rigid blade flapping motion  $\beta$  is represented up to its 1st harmonics as:

$$\bar{\beta}(\psi) = \bar{\beta}_0 + \bar{\beta}_{1s} \sin \psi + \bar{\beta}_{1c} \cos \psi \quad (5-14)$$

As similar with the conventional single main rotor helicopter trim formulations  $\Lambda_{1s}$ ,  $\Lambda_{1c}$  first harmonic contents of the blade flap control inputs and the blade coning angle  $\theta_0$  are calculated from the rigid flapping dynamics of the rotor blade given as;

$$\ddot{\beta} + v^2 \beta = \frac{1}{2} \gamma \int_0^l F_z dx \quad (5-15)$$

Resultant blade cross-sectional velocity is approximated as  $U=U_T$ . Mean of the total rotor thrust is derived from equation 5-11 as,

$$\begin{aligned} \frac{C_{T0}}{\sigma a} = & \frac{1}{2} \left( C_{12} + C_{10} \frac{\mu^2}{2} \right) \theta_0 - \frac{1}{2} C_{11} \lambda + \left( d_{3k2} + d_{3k0} \frac{\mu^2}{2} \right) \Lambda_0 \\ & + \left( d_{3k3} + d_{3k1} \frac{\mu^2}{2} \right) \Lambda_{tw} + d_{3k1} \mu \Lambda_{1s} - d_{1k0} \frac{\mu}{2} \Lambda_{1c} - d_{3k0} \frac{\mu^2}{4} \Lambda_{2c} \end{aligned} \quad (5-16)$$

Parameters  $C_{10}$ ,  $C_{11}$ , .....,  $d_{3k3}$  are related with blade chord and flap geometries and are given in reference [5]. Equation 5-16 gives the amount of  $\Lambda_0$  control input required to maintain the mean of the rotor thrust  $C_{T0}$ .

Rotor blade flapping dynamic equilibrium must be also considered to calculate the required cyclic flap angle inputs  $\Lambda_{1s}$ ,  $\Lambda_{1c}$  zeroth harmonic of blade flapping,  $\beta_0$ . Flapping dynamics of a rigid rotor can be written as;

$$\ddot{\beta} + v^2 \beta = \frac{1}{2I} \rho c a R^4 \int r F_z dr \quad (5-17)$$

where blade flapping motion is expressed as up to its first harmonics,

$$\beta = \beta_0 + \beta_{1s} \sin \psi + \beta_{1c} \cos \psi \quad (5-18)$$

Harmonic balance of equation 5-17 up to its second harmonics gives five equilibrium condition.

First equilibrium equation is given as

$$\begin{aligned}
& \frac{v^2 \mu \Lambda_{1s}}{\gamma} \beta_0 - \left( d_{3k3} + d_{3k1} \frac{v^2}{2} \right) \Lambda_0 + C_{12} \frac{\lambda}{2} - \left( d_{3k4} + d_{3k2} \frac{\mu^2}{2} \right) \Lambda_{tw} \\
& - \left( \frac{C_{13}}{2} + C_{11} \frac{\mu^2}{4} \right) \theta_n + d_{1k1} \frac{\mu}{2} \Lambda_0 - d_{3k2} \mu \Lambda_{1s} + d_{3k1} \frac{\mu^2}{4} \Lambda_{1c} = 0
\end{aligned} \tag{5-19}$$

The other four equilibrium equations are also written to calculate first and second harmonics of the flap control input.

#### 5.4 Compound Helicopter Basic Trim Formulation

The operating condition of the helicopter rotor system is determined by force and moment equilibrium of the entire vehicle. Since additional canard and tail wing lifts along with a tail propulsion are included in the vehicle configuration, longitudinal and lateral equilibrium of the new helicopter must be considered for trim calculations. At this initial stage only the effects on the longitudinal equilibrium equations are considered whereas canard and tail wing lifts are assumed to be symmetric or have canceling effects in the lateral direction. This approximate trim formulation is based on the standard helicopter trim formulations given by Johnson [13].

Longitudinal force equilibrium considers the forces in the vertical longitudinal plane of the helicopter as seen in Figure 5.3. The helicopter has speed  $V_H$  and a flight path angle  $\theta_{fp}$ , so that climb and descent conditions can also be considered. The acceleration effects of rotor slowing down transition are neglected and steady unaccelerated flight conditions are assumed for the formulation.

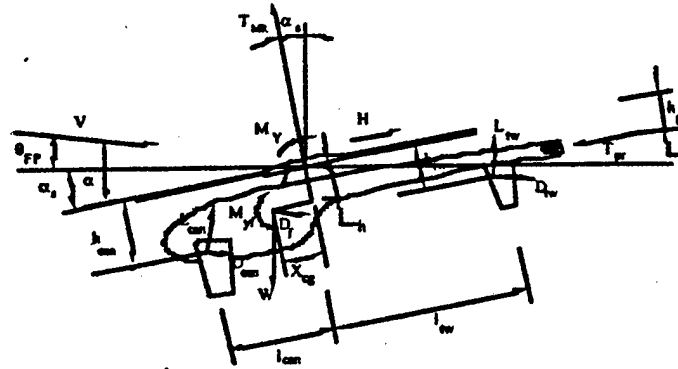


Figure 5.3 Compound Helicopter Longitudinal Equilibrium



The force on the rotor which are the main rotor thrust  $T_{mr}$ , and the rotor drag  $H$  are defined relative to the reference rotor hub plane. This reference plane has angle of attack  $\alpha$  with respect to the forward speed. The forces acting on the helicopter are the weight  $W$  of the helicopter, canard and tail wing lifts,  $L_{can}$ ,  $L_{tw}$ , aerodynamic drags of fuselage  $D_f$  as well as canard and tail wing drags  $D_{can}$ ,  $D_{tw}$  respectively. A tail propulsion,  $T_{pr}$ , is also applied in the direction of the hub reference plane from aft rear end of the tail boom. Forces and moments acting on the helicopter are also illustrated in Figure 5.3. Vertical force equilibrium requirements is written as

$$W = T_{mr} \cos \alpha_s + H \sin \alpha_s - D_T \sin \theta_{fp} + L_T \cos \theta_{fp} - T_{pr} \sin \alpha_s \quad (5-20)$$

and the horizontal force equilibrium can be written as;

$$D_T \cos \theta_{fp} + H \cos \alpha_s = T_{mr} \sin \alpha_s - L_T \sin \theta_{fp} - T_{pr} \cos \alpha_s \quad (5-21)$$

where

$$D_T = D_f + D_{can} + D_{tw}$$

$$L_T = L_{can} + L_{tw}$$

$$\alpha_s = \alpha - \theta_{fp}$$

Next, the equilibrium of pitch moments on the helicopter which determines the angle of attack of the rotor shaft relative to the vertical,  $\alpha_s$  is considered. Moments are taken about the rotor hub so that the rotor forces are not involved and the rotor reference plane is not entered into the problem. The rotor hub moment  $M_y$  must be included and the pitching moment equilibrium about the rotor hub, for small angles, can be written as,

$$\begin{aligned} M_Y + M_{YF} + W(h \sin \alpha_s - x_{cg} \cos \alpha_s) - h D_f \cos \alpha_s - x_{cg} D_f \sin \alpha_s \\ + L'_{can} l_c - D'_{can} h_{can} - L'_{tw} l_{tw} - D'_{tw} h_{tw} + T_{pr} h_{pr} = 0 \end{aligned} \quad (5-22)$$

## 5.5 Solution Method

Several methods have been developed for the solution of nonlinear coupled partial differential equations representing the flap-lag-torsion motions of hingeless and bearingless rotor blades. A conditionally stable, explicit finite difference scheme to numerically integrate the nonlinear partial differential equations in space and time are employed to obtain the aeroelastic response of elastic

hingeless rotor blades with flap control inputs.

For purposes of numerical integration by the proposed approach which is based on explicit finite difference methods, it is convenient to express the coupled nonlinear partial differential equations of rotor blade system in terms of first order time and second order space derivatives. This reduction is performed by introducing the following variables.

$$\begin{aligned}
 v_t &= \dot{v}, w_t = \dot{w}, \phi_t = \dot{\phi}, \\
 \text{and} \\
 m_v &= v^{++}, m_w = w^{++}, \\
 \text{similarly} \\
 \dot{m}_v &= v_t^{++}, \dot{m}_w = w_t^{++}
 \end{aligned} \tag{5-23}$$

where  $( )^*$  and  $( )^+$  are the partial derivatives with respect to nondimensional time variable ( $\psi$ = azimuth angle) and nondimensional spanwise location variable ( $x=r/R$ ), respectively. In terms of these variables, rotor blade nonlinear, coupled partial differential equations and the trailing terms given in reference [14] are reorganized in reference [15] matrix form as follows,

$$\begin{aligned}
 \dot{u}_t &= A(u, \psi)u_m^{++} + B(u, \psi)u_d^{++} + C(u, \psi)u_d^+ + Du_t \\
 &\quad + E(u, \psi)u_m + F(\psi)u_d + G(u, \psi) \\
 \dot{u}_m &= I_{23}u_t^{++} \\
 \dot{u}_d &= I_{33}u_t
 \end{aligned} \tag{5-24}$$

where  $u_d$  and  $u_t$  are displacement and velocity vectors respectively and the matrices A, B, ..., F and G given in reference [15]. The quantity  $u_m$  is vector defined in the following set of equations.

$$u_t = \{v_t, w_t, \phi_t\}^T, u_m = \{m_v, m_w\}^T, u_d = \{v, w, \phi\}^T \tag{5-25}$$

Details of the Explicit Finite Difference method is given in reference [15].

## 5.6 Result and Discussions

In this section numerical results are presented to illustrate the application of the approximate method to solve rotor blade aeroelastic equations. Since the objective of this paper is primarily to illustrate the application of the approximate method to find transient and steady-state response of

rotor blades with cyclic flap controls in hover and forward flight conditions, certain simplifications and assumptions are made as follows.

- A uniform inflow model is used for forward flight condition.
- Hub and tip losses are not included.
- A two dimensional, strip type, quasi-steady aerodynamic model is used where Theodorsen lift deficiency function  $C(k)$  is set equal to unity.
- Structural and mass properties of the blade are assumed to be uniform along the blade. All offsets from the elastic axis are also neglected.
- Reverse flow effects are not included.

Solutions of forward flight are initiated by setting all elastic deformation to zero and they are increased by a linear incremental procedure until their trim solution values are reached.

## 5.7 Flap Control Concept Validation Results

First set of results are obtained both for pitch and flap control cases where identical rotor blade and helicopter configurations are considered for both control cases. Basic rotor and vehicle parameters of the considered 700lb micro-helicopter configuration are given in Table 1 and 2 respectively and rotor angular speed is taken as  $\Omega=70\text{rad/sec}$  for this configuration.

Table 1.: Helicopter and Rotor Parameters

Number of blades	$b = 2$
Main rotor radius	$R_{MR} = 7.0\text{ft}$
Main rotor angular speed	$\Omega_{MR} = 70 \text{ rad/sn}$
Main rotor chord	$c_{MR} = 1.0 \text{ ft}$
Flap width ratio	$c_f = 0,43 \ c_{MR}$
Hub- $c_g$ offsets	$x_{cg} = 0,125\text{ft}$ $h = 1,8\text{ft}$
Gross weight	$W_g = 700 \text{ lb}$
Sectional Inertias	$\left(\frac{k_A}{k_M}\right)^2 = 1,0$ $\left(\frac{k_M}{R}\right) = 0,025$ $\left(\frac{k_{m1}}{k_{m2}}\right) = 0,0$

Blade drag coefficient	$C_{D0} = 0,01$
Solidity ratio	$\sigma = 0,073$
Lock number	$\gamma = 6.$
2-D lift curve slope	$a = 2\pi$
Blade rigid pitch angle	$\theta_{ri} = 0,10 \text{ rad}$
Blade pre-twist angle	$\theta_{tw} = 0,0 \text{ rad}$

Nondimensional bending and torsion stiffness are written as follows:

$$\Lambda_y = \frac{EI_y}{m\Omega^2 R^4}, \Lambda_z = \frac{EI_z}{m\Omega^2 R^4}, \Lambda_t = \frac{GJ}{m\Omega^2 R^4}$$

Table 2.: Blade Stiffness Parameters.

	Ay Flap	Az Lag	A <sub>t</sub> Torsion
1. Case	0.01079	0.1474	0.0100
2. Case	0.01079	0.1474	0.0625

Parameters related to the chosen configuration are obtained by a simplified preliminary design approach since they are necessary inputs for the present analysis. The considered rotor blade has a rectangular planform with chord width  $c=1.0 \text{ ft}$ , and uniform flap along the rotor span with nondimensional flap hinge offset from center chord,  $c_f=0.4$ . Rotor blade pre-twist  $\theta_{tw}$  is neglected for both control cases and a rigid pitch settings is taken as,  $\theta_{ri}=0.10$ . Trim settings for the pitch and flap control cases are compared. As seen from results identical patterns of variations for corresponding control inputs are observed in general. The difference in magnitudes of collective pitch and flap inputs is found to be in the range of the rigid pitch setting which is included for the flap control case. The comparison of the corresponding pitch and flap inputs indicates that flap control has the identical effect for generating the required lift variation as of conventional pitch control.

Corresponding trim values for pitch and flap control cases are given in Table 3 for the forward flight condition,  $\mu=0.25$ . Trim solutions yield inflow ratio  $\lambda_0 = -0.03198$  and vehicle angle of attack  $\alpha_v = 0.07858$  for both control cases. Elastic rotor tip deflections are compared for conventional pitch and flap controls for forward flight condition  $\mu=0.25$ .

Table 3.: Trim values of corresponding pitch and flap controls for  $\mu=0.25$ .

$\theta_0$	$\theta_{1s}$	$\theta_{1c}$
------------	---------------	---------------

0.12989	-0.02635	0.00062
$\Lambda_0$	$\Lambda_{1s}$	$\Lambda_{1c}$
0.04522	-0.03971	0.003165

## 5.8 Contoured Flap Concept Results

The second set of results are presented to represent the effect of second harmonics of the flap controlled inputs for blades with different flap contour shapes.

Basic vehicle and rotor blade configuration parameters for the considered 220 lb model (test-in-flight) helicopter configuration are given in Table 4 from reference 10. Main rotor with radius  $R_{mr}=3.8$  ft with blade chord  $C=0.36C_{mr}$  effective between  $r=0.2R_{mr}$  to  $r=0.95R_{mr}$  is considered.

Average blade chord is  $C_{av}=0.28$  ft for the selected rotor configuration.

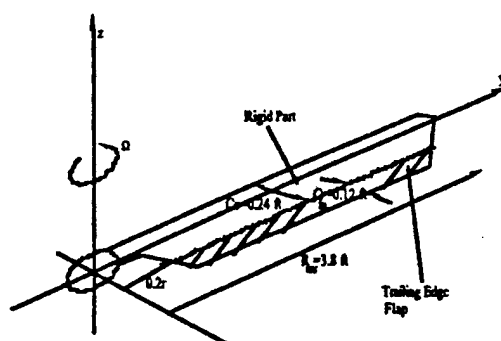


Figure 5.4 Flap geometry for contours flap, Case 2

Table 4.: Selected Helicopter and Rotor Parameters.

Number of blades	$b=2$
Main rotor radius	$R_{MR} = 3.8$ ft
Main rotor angular speed	$\Omega_{MR} = 180$ rad/sn
Chord length	$c_{MR} = 0.36$ ft
Flap width	$c_f = 0.333 c_{MR}$
Hub-c~ aspect length	$x_{cg} = 0.08$ ft
	$h = 1.1$ ft
Gross weight	$W_g = 220$ lb
Section Inertia	$\left(\frac{k_A}{k_M}\right)^2 = 1,0$

	$\left(\frac{k_M}{R}\right) = 0,025$
	$\left(\frac{k_{m1}}{k_{m2}}\right) = 0,0$
Blade zero drag coefficient	$C_{D0} = 0.01$
Solidity ratio	$\sigma = 0.066$
lock number	$\gamma = 6.$
2-D lifting curve slope	$a = 2\pi$
Advancing ratio	$\mu, \text{ de } I_{\text{ken}}$
Rigid blade angle	$\theta_{ri} = 0.16 \text{ rad}$
Blade pretwist angle	$\theta_{tw} = -0.04 \text{ rad}$

Table 5.: Blade Stiffness Parameters for case 2.

$\Lambda_v$	$\Lambda_z$	$\Lambda_t$
Flap	Lag	Torsion
0.0041	0.24	0.004

Vehicle trim and rotor response calculations are initiated from hover condition ( $\mu=0$ ) and increased with increments  $\Delta\mu=0.0125$  up to  $\mu=0.20$ . Results are presented for two blade revolutions for forward flight increase from  $\mu=0.1875$  to  $\mu=0.20$ . Five different rectangular flap surfaces considered for comparison defined by equation 5-10 and illustrated in Figure 5.4 are outlined in Table 6.

Table 6 Flap Contours.

	Flat	$\text{Sin}\pi\psi/L_f$	$\text{Sin}2\pi\psi/L_f$	$\text{Cos}\pi\psi/L_f$	$\text{Cos}2\pi\psi/L_f$
n	0	1	2	1	2
$S_{ns}$	0	1	1	0	0
$S_{nc}$	1	0	0	1	1
	Flat	$\text{Sin}\pi$	$\text{Sin}2\pi$	$\text{Cos}\pi$	$\text{Cos}2\pi$

Figure 5.5 represents the time dependent portion of the flap controls with contents of second harmonics which depicts the control input change due to flight condition change from  $\mu=0.1875$  to  $\mu=0.20$ . As seen from Figures 5.6 and 5.7 blade lead-lag and flap tip deflections are not affected significantly for different flap contours. On the other hand the blade torsional tip

deflections are significantly changed for different blade shapes (Figure 5.8), which affected the total lift of each blade as illustrated in Figure 5.9.

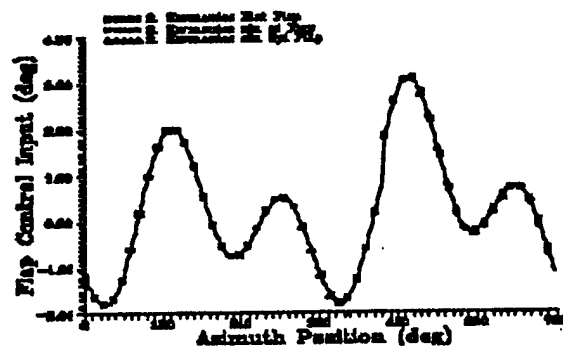


Figure 5.5 Flap control input variation

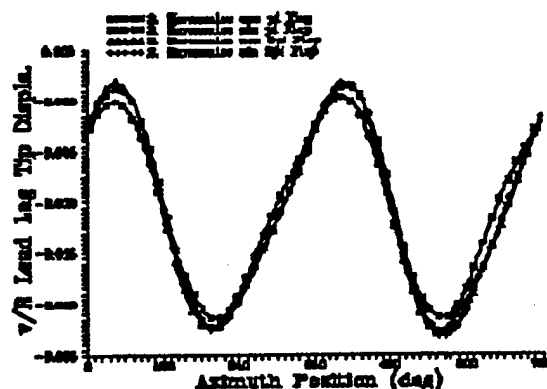


Figure 5.6 Lead-lag tip response for different flap geometries

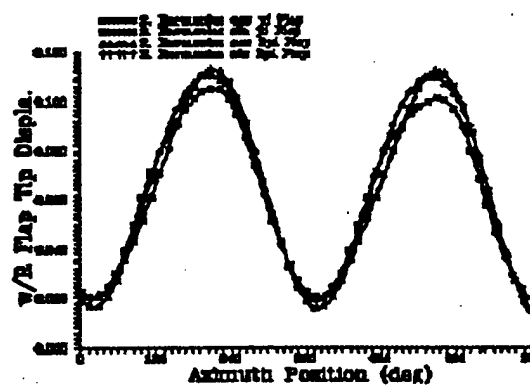


Figure 5.7 Flap tip response for different geometries

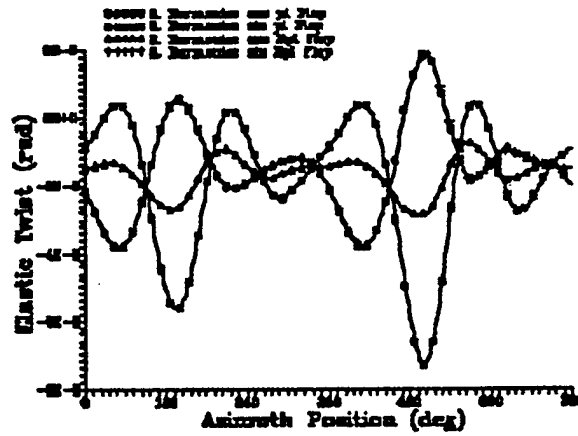


Figure 5.8 Elastic tip twist of different flap geometries

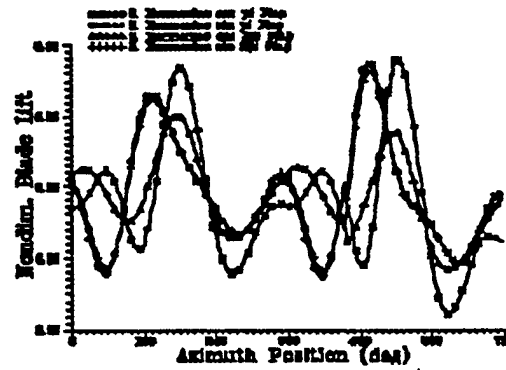


Figure 5.9 Blade lift (nondim.)

The shaft moment required to rotate each blade has not been affected in magnitude but the location of peak values are shifted for different blade shapes (Figure 5.10).

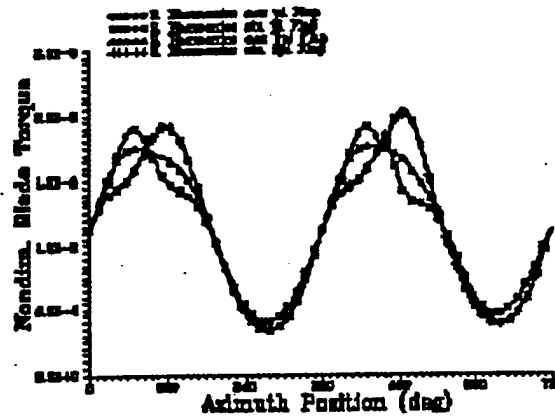


Figure 5.10 Blade required torque (nondim.)



## 5.9 References

- [1] Proudly, R. W., Smart Materials and Helicopters, Rotor & Wing, May, 1996
- [2] S. Hanagud, J. V. R. Prasad, T. Boules and G. L. Nagesh Babu, Smart structures in the active control of blade vortex interaction, Pre 17<sup>th</sup> European Rotorcraft Forum, Sept 1991, Berlin, Germany
- [3] Hanagud, S., Roglin, R. L. and Nagesh Babu, G. L., Smart airfoils for helicopter control, 18<sup>th</sup> European Rotorcraft Forum, Sept 15-18, 1992, Avignon, France
- [4] Hanagud, S. and Nagesh Babu, G. L., Smart structures in the control of airframe vibrations, Journal of American Helicopter Society, April 1994, pp.69-72
- [5] Streblow, H. and Rapp, H., Smart materials for helicopter active control, AGARD CP-531, April 5, 1993
- [6] Chandra, R. and Chopra, I., Structural modeling of composite beams with induced strain actuators, AD-Vol. 30, Recent Advances in the Structural Dynamic Modeling of Composite Rotor Blades and Thick Composites, ASME 1992
- [7] Yillikci, Y. K., Hanagud, S., Schrage, D. P. and Hijman, J., Aeroelastic analysis of rotor blades with flap control, 18<sup>th</sup> European Rotorcraft Forum, Sept. 15-18, 1992, Avignon, France
- [8] Leisman, J. G., Unsteady lift of an airfoil with a trailing edge flap based on indicial concepts, 18<sup>th</sup> European Rotorcraft Forum, Sept. 15-18, 1992, Avignon, France
- [9] Yillikci, Y. K., Prasad, J. V. R., and Schrage, D. P., Transient response of flap controlled stopped rotor, proceedings of the 19<sup>th</sup> ICAS Conference, pp. 2812-2822, Sept. 1994, Anaheim, USA
- [10] Yillikci, Y. K. and Hanagud, S., Modeling contoured trailing edge flap controls, Proceedings of the 20<sup>th</sup> European Rotocraft Forum, October 4-6, 1994, Amsterdam, Holland
- [11] Bishlinghoff, R. L., Ashley, H. and Holfman, R. L., Aeroelasticity, Addison Wesley Publication Co., 1975
- [12] Kaza, K. R. V. and Kuatarnik, R. G., Engineering Notes - Application of unsteady airfoil theory to rotary wings, J. of Aircraft, Vol. 18, No. 7, 1981
- [13] Johnson, W., Helicopter Theory, Princeton University, 1980
- [14] Taylor, D. J., A method for the efficient calculation of elastic rotor blade dynamic response in forward flight, Doctoral Dissertation, School of Aerospace Engineering, Georgia Institute of Technology, Atlanta, USA, March, 1987
- [15] Yillikci, Y. K. and Hanagud, S., Finite Difference Techniques and rotor blade aeroelastic partial differential equation: An explicit time-space finite element approach for P. D. E., 15<sup>th</sup> European Rotorcraft Forum, Sept 12-15, 1989, Amsterdam, Holland
- [16] Roglin, R. L. and Hanagud, S., A helicopter with adaptive rotor blades for collective control, Smart Structures and Materials Journal, Vol.5, 1996
- [17] Yillikci, Y. K. and Hanagud, S., Modeling nonlinear response of hingeless rotor blades with

flap control, European Rotorcraft Forum, 1996

[18] Hanagud, S., Roglin, R. L. and Luo, H., Adaptive rotor blades for forward flight, Society of Engineering Mechanics Conference, Phoenix, Arizona, November, 1996

## **VI. Future Work**

Future work needed to implement the cyclic and vibration control are as follows;

- Elastic trim in flap controlled rotor blade with spatial variation of the flap angle
- Dynamics of the flap system and controllers of the flap angle in trim conditions
- Design of the rotor blade
- Wind tunnel testing of the rotor blade
- Forward flight test demonstration in a small model helicopter
- Vibration controllers to suppress high harmonic with and without flaps
- Shape changes by the use of out-of-plane bending in piezo actuated helical springs

## **VII. External Interactions**

Our external interactions are with the Army Research Facilities in NASA Langley Research Facilities, NASA Ames Research Facilities, Sikorsky Aircraft, and MDHC Helicopter Systems.